UNIVERSITY OF SOUTHAMPTON

Faculty of Social Sciences
School of Mathematics

Building Mountains on Neutron stars

by

Yashaswi Gangwar

ORCiD: 0000-0002-2930-3801

A thesis for the degree of
Doctor of Philosophy

February 2026

University of Southampton

Abstract

Faculty of Social Sciences
School of Mathematics

Doctor of Philosophy

Building Mountains on Neutron stars

by Yashaswi Gangwar

The first detection of gravitational waves in 2015, along with the many subsequent detections, has provided profound insights into theories of gravity and the nature of compact objects such as black holes and neutron stars. The signals detected so far have been transient, originating from events like binary mergers. However, we also expect quasi-monochromatic signals, known as continuous gravitational waves, to be emitted by rapidly rotating neutron stars with non-axisymmetric quadrupole moments, for instance, neutron stars with a "mountain." Such continuous signals will offer an independent probe of neutron star physics, complementing electromagnetic and neutrino observations.

In this thesis, we investigate elastic mountains, in which the non-zero quadrupole ellipticity is supported by the elastic properties of the crust, under two distinct models: the starquake model and the superfluid vortex pinning model.

In the starquake model, originally developed to explain pulsar glitches, we extend the symmetric analysis of Baym and Pines (1971) to the general case of both symmetric and asymmetric crust breaking, where the latter gives rise to a mountain. We apply this framework to the spin-up of an initially non-rotating star and estimate the maximum mountain that can be formed, subject only to energy and angular momentum conservation. We find that the creation of a mountain in this scenario necessarily requires a simultaneous change in the axisymmetric shape too.

In the latter half of the thesis, we investigate the formation of a "Magnus mountain," arising from the non-axisymmetric Magnus force acting on the elastic crust through pinned superfluid vortices. We numerically solve the coupled perturbed equations of motion for the elastic and fluid components of the star, and compute the associated displacement field corresponding to a non-axisymmetric shape change. We begin with the simplified case of an infinitely long cylindrical star, with the aim of extending the model to a more realistic spherical configuration in future work.

Contents

List of Figures

List of Tables

Declaration of Authorship

I declare that this thesis and the work presented in it is my own and has been generated by me as the result of my own original research.

I confirm that:

1. This work was done wholly or mainly while in candidature for a research degree at this University;
2. Where any part of this thesis has previously been submitted for a degree or any other qualification at this University or any other institution, this has been clearly stated;
3. Where I have consulted the published work of others, this is always clearly attributed;
4. Where I have quoted from the work of others, the source is always given. With the exception of such quotations, this thesis is entirely my own work;
5. I have acknowledged all main sources of help;
6. Where the thesis is based on work done by myself jointly with others, I have made clear exactly what was done by others and what I have contributed myself;
7. Parts of this work have been published in Gangwar and Jones (2024):
    - Chapter 2: Section 2.2
    - Chapter 3: Sections 3.3, 3.4.1, 3.5, 3.6
    - Chapter 4
    - Chapter 9: Section 9.1

Signed:..... Date:.....

Acknowledgements

My deepest gratitude goes to my supervisor, Prof. Ian Jones. I feel truly fortunate to have begun my research journey under his mentorship. Throughout my research, I made my fair share of mistakes—some so spectacular that physics itself might have considered disowning me—but he never gave up on me. I don't think I will ever again forget Christoffel symbols when taking derivatives for as long as I live. His kindness, generosity, and steady encouragement have left an indelible impression on me. If I ever have the privilege of mentoring students in the future, I hope to extend to them the same patience, insight, and support that he has so generously offered to me.

I will always remember Ian's reassuring words before my very first group meeting presentation: "You don't have to worry about being judged; this is your academic home." He—and all the members of our research group—truly made me feel that way. I am deeply grateful to all the professors in the group for their constructive feedback during work update presentations, as well as for the helpful practice sessions for the conference talks. I would like to thanks Nils, whose wit, humour, and brilliant insights enriched our group meetings.

I am also indebted to my office-mates for the lively, memorable conversations that brightened the gloomy winter days. Big thanks to Marcus for always stopping by my desk to say hello—it never failed to lift my spirits. My special thanks to Shanshan for being a constant source of both academic and personal support. From untangling difficult research problems to navigating life's twists and turns, she have been a trusted confidant.

I want to thank my family for believing in me even in moments when I doubted myself. While they may not yet fully understand exactly what I do, I am grateful that they have never confused it with astrology. Thank you, my beloved Gullu Rani (Ginnie, my furbaby), for being the most beautiful soul and for lifting my spirits every day from 7,000 km away. To maa (mother) and baba(father), thank you for guiding me out of the existential maze I was once lost in, and for setting me on a path of clarity, purpose, wonder, and peace. With your belief in me and your blessings, I know I will one day unravel all the mysteries of existence.

Chapter 1

Introduction

Neutron stars (NSs) are among the densest objects in the Universe, typically containing around 1–2 solar masses within a radius of about 10–15 km (Nättilä and Kajava, 2022). Their density is so extreme that they cause significant distortions in the very fabric of spacetime. Neutron stars are born when a medium-sized star, with a progenitor mass of about 8–10 times the mass of the Sun, undergoes core-collapse supernova. There also exists an upper limit of $\gtrsim$ 25 solar masses for the progenitor mass, above which the collapse of the star produces a black hole instead (Heger et al., 2003).

Neutron stars were first hypothesised by Baade and Zwicky in 1934 (Baade and Zwicky (1934)), interestingly just two years after the discovery of the neutron in 1932 by James Chadwick. A timeline of major historical events in the study of neutron stars and gravitational waves is shown in Figure 1.1. It then took more than three decades for neutron stars to be observationally confirmed, when Jocelyn Bell discovered the first pulsar in 1967 (Hewish et al.). She observed a radio signal repeating every few seconds with remarkable regularity. The pulses were so precise that the team initially nicknamed the source "little green men," speculating about an extraterrestrial origin. However, once additional sources were discovered with similar behavior, the extraterrestrial hypothesis was ruled out, and the objects were recognised as pulsars. Pulsars are rotating neutron stars that emit beams of electromagnetic radiation from their magnetic poles (Lyne and Graham-Smith, 2012). Although the discovery was revolutionary, it was also controversial, since Jocelyn Bell was not included in the 1974 Nobel Prize that was awarded for the discovery. Since 1967, neutron stars have been studied across the entire electromagnetic (EM) spectrum, from radio to X-rays and gamma-rays (Menezes, 2021).

Neutron stars provide scientists with a unique laboratory to study matter under conditions inaccessible on Earth. In terrestrial laboratories, matter can be studied at low density and high temperature, whereas neutron stars allow direct investigation of matter at extremely high densities and relatively low temperatures. Although their interior

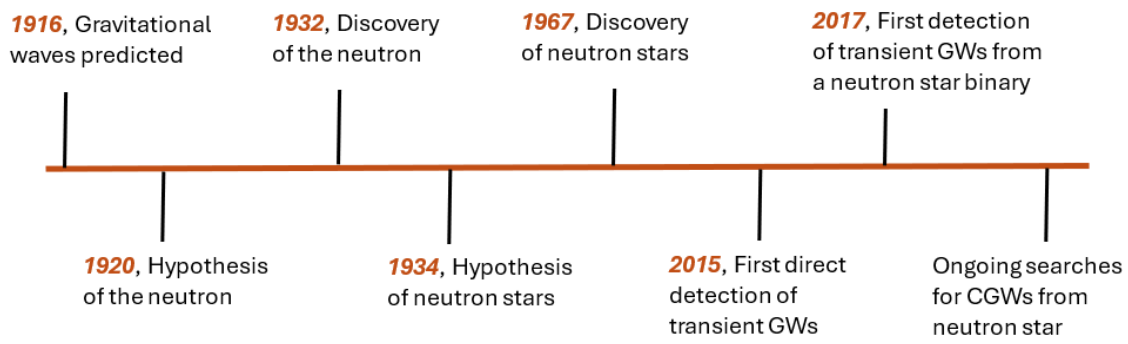

FIGURE 1.1: Historical timeline of key milestones in the fields of gravitational waves and neutron stars.

temperatures are of order 10^8 K, neutron stars are still considered extremely cold objects due to the very high Fermi energy which is a consequence of their extreme density. This suggests that matter inside many neutron stars may exist in macroscopic quantum states, such as superfluidity and superconductivity. Indeed, it is widely believed that neutrons in the core form a superfluid, while protons may form a type-II superconductor (Haskell and Sedrakian, 2018).

In this thesis, we focus on models that describe quadrupolar deformations, commonly referred to as mountains, which can emit continuous gravitational waves. In Sections 1.1 and 1.2, we will briefly discuss gravitational waves and the different types of mountains that can form on neutron stars.

1.1 Gravitational waves

In general relativity, a time-varying quadrupole moment gives rise to gravitational waves. Broadly, there are four classes of gravitational waves that can, in theory, be produced by astrophysical sources:

1. **Compact binary coalescence:** These are transient signals produced during the merger of compact binaries, such as binary black holes, binary neutron stars, or black hole–neutron star systems.

2. **Continuous gravitational waves:** These are emitted by isolated, spinning compact objects such as neutron stars, arising from long-lived, non-axisymmetric quadrupole deformations, often referred to as "mountains." In this thesis, we focus on modelling such mountains on neutron stars.

3. **Burst gravitational waves:** These form a subclass of transient signals, as they are short-lived and sudden. Potential sources include core-collapse supernovae, magnetar flares, or cosmic string cusps (Lasky, 2015). To date, they remain the most poorly modelled type of gravitational-wave signal.

4. **Stochastic background:** One possible origin of these signals is the Big Bang itself. Over cosmic time, however, the background is expected to include contributions from a large population of unresolved binary inspirals. In mid-2023, Pulsar Timing Array (PTA) collaborations reported evidence for the detection of a stochastic background (EPTA Collaboration and InPTA Collaboration, 2023). If, in the future, a primordial relic signal from the Big Bang can be disentangled from the astrophysical background, this would provide a direct observational probe of the physics of the early Universe.

Gravitational waves were first predicted by Einstein in 1916 (Einstein, 1916). It took nearly a century before the first direct detection was achieved in 2015, from the merger of two black holes observed by LIGO (Abbott and et al, 2016). That signal was transient, lasting only a few hundred milliseconds. On 17 August 2017, the Advanced LIGO and Virgo detectors observed GW170817, a gravitational-wave signal from the merger of two neutron stars. This event was historic, not only for gravitational-wave astronomy but also for neutron-star physics. With GW170817, the era of multi-messenger astronomy began, combining gravitational-wave and electromagnetic observations(Abbott et al., 2017). Neutrinos were not detected from GW170817; however, this non-detection provided upper limits on the neutrino emission during the merger (Abe et al., 2018).

Gravitational waves provide a new and independent probe of neutron-star physics, offering constraints on the stellar mass–radius relation and hence the equation of state (EoS) of ultra-dense matter (Vivanco et al., 2019). So far, all gravitational-wave detections involving neutron stars have come from binary coalescences. In principle, however, isolated neutron stars can emit continuous gravitational waves (CGWs), arising from long-lived "mountains" or from stellar oscillations. The detection of such signals will likely require next-generation detectors, such as the Einstein Telescope (ET) (Maggiore et al., 2020) and Cosmic Explorer (et al, 2017; Sieniawska and Bejger, 2019).

1.2 Neutron star mountains

A compact object such as a neutron star, when departing from its axisymmetric shape, gives rise to a non-zero quadrupole ellipticity (for simplicity we will use the term "ellipticity" for "quadrupole ellipticity"). This non-zero ellipticity is referred to as a "mountain", which, when spinning, produces CGWs (see e.g. Glampedakis and Gualtieri (2018)). The ellipticity can be quantified as

$$\epsilon_{22} = \frac{|I_{xx} - I_{yy}|}{I_{zz}}, \tag{1.1}$$

where I_{xx}, I_{yy}, and I_{zz} are the moments of inertia of the star along the x, y, and z-axes respectively, with the rotation occurring along the z-axis. The subscript (22) reflects the

fact that the corresponding non-axisymmetric mass distortion is described by an $(l = 2, m = 2)$ spherical harmonic. Since the centrifugal forces generated by the rotation give rise to a symmetrical distortion, corresponding to an $(l = 2, m = 0)$ perturbation, they do not contribute to the generation of CGWs (Glampedakis and Gualtieri, 2018).

There are different classes of mountains depending on the physical process that supports these non-axisymmetric deformations. We describe them briefly below.

Magnetic mountains

In magnetic mountains, the non-zero ellipticity is induced by the magnetic field of the star. The shape of the star depends on the type of magnetic field structure present in the star (poloidal or toroidal). Such mountains can also be produced in an accreting system (Glampedakis and Gualtieri, 2018; Haskell et al., 2015). Theory suggests that if the core of the neutron star consists of quark matter instead of normal hadronic matter, the star can sustain larger ellipticities (Glampedakis et al., 2012). Currently, the presence of a quark matter core is considered highly uncertain, but if future GW detections confirm such sources, it would provide valuable information on the existence of exotic states of matter.

Elastic mountains

As the name suggests, the non-zero ellipticity is sustained by the elastic strain of the star's crust. We will discuss the formation of these mountains under the starquake model in detail in the first half of the thesis, spanning Chapters 2 to 4. The nature of the neutron star core remains uncertain, but some theories suggest the presence of a solid core. If such a core exists, it could also support non-zero ellipticity.

Thermal mountains

These fall under the broader class of elastic mountains, since the deformation is sustained by the elastic crust. We mention thermal mountains separately, as in this work we focus on elastic mountains specifically under the starquake model. Thermal mountains are believed to form in accreting systems. When accreted matter becomes buried in the crust, nuclear reactions occur that heat the crust. We expect accretion to be asymmetric to a small degree, and consequently the resulting temperature gradients to be asymmetric as well, giving rise to thermal mountains (Osborne and Jones (2020); Glampedakis and Gualtieri (2018); Haskell et al. (2015); Bildsten (1998); Ushomirsky et al. (2000)).

Magnus mountains

These mountains arise from the non-axisymmetric Magnus force acting on pinned superfluid vortices in the neutron star. The interior of the neutron star is believed to be superfluid and superconducting. The Magnus force is produced by the spin lag between the pinned superfluid vortices and the superfluid flow. To generate a quadrupole deformation, the Magnus force must be asymmetric. If vortices are pinned to magnetic fluxtubes, any asymmetry in the internal magnetic field structure will give rise to an asymmetric Magnus force (Jones (2010); Glampedakis and Gualtieri (2018); Haskell et al. (2022)). Similarly, any asymmetry in vortex pinning at crustal nuclei may also produce an asymmetric Magnus force. Such asymmetry in crustal pinning could result from composition variations introduced during asymmetric accretion in the star's accretion phase. Magnus mountains are also classified as elastic mountains, since the quadrupole moment is sustained by the elastic crust. We will discuss the formation of Magnus mountains in detail in the second half of the thesis, spanning Chapters 5 to 8.

1.3 Focus of this thesis

In this thesis, we examine two different models for the formation of elastic mountains on spinning neutron stars. The first half of the thesis considers the starquake model, while the second half explores the Magnus mountain model. A chapter-wise outline of the thesis is presented in Figure 1.2.

Many spinning neutron stars are observed as radio pulsars. Observations show occasional sudden increases in their spin rates, termed as *glitches*; see e.g. Ruderman (1969); Haskell and Melatos (2015). The *starquake* theory was proposed by Baym and Pines (1971) to explain the glitches observed in the Crab and Vela pulsars, with the glitches being caused by sudden fractures in the star's elastically strained crust. This model was not able to explain the large glitches observed in Vela (Flanagan (1996)). The currently preferred model of glitches now involves unpinning of superfluid vortices (Anderson et al. (1981)), but starquakes may nevertheless still occur.

In the past, a few attempts were made to study the formation of elastic mountains at glitches using the starquake model. Fattoyev et al. (2018) explained the formation of the elastic mountain by considering a portion of the crust moving radially, with the rest of the crust remaining unchanged. As noted by the authors themselves, this is an overly simplistic depiction of the formation of the mountain. We do not expect such radial movement of a part of the crust due to crust break. A more globally consistent model is needed.

A more quantitative description was given by Giliberti and Cambiotti (2022), who modelled the formation of elastic mountain on an *accreting* NS. They also argued that the

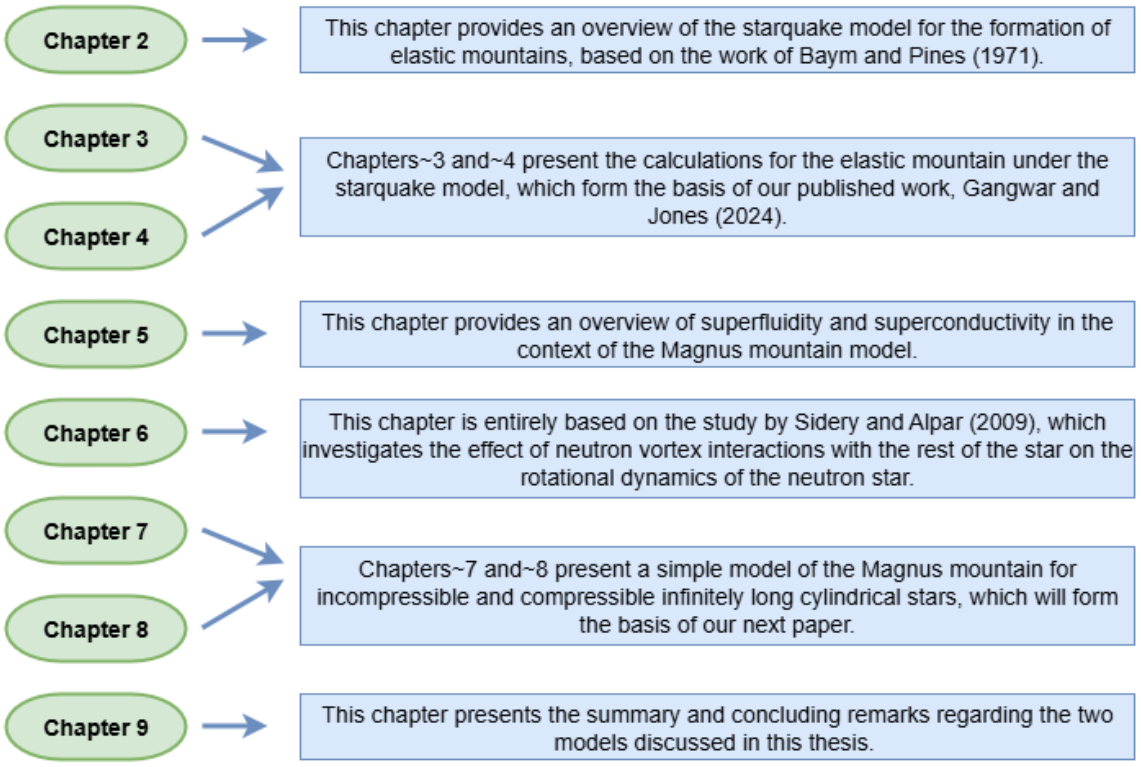

FIGURE 1.2: Chapter-wise outline of this thesis.

centrifugal force acting on the spinning-up NS can be strong enough to break the crust, and that the fracture may itself occur in a non-axisymmetric way. By making some specific assumptions about the nature of the fracture process, they calculated the range of the starquake-induced ellipticity to be $10^{-9} - 10^{-5}$.

A detailed study of the non-axisymmetric crust failure on macroscopic scales based on tectonic processes was performed by Kerin and Melatos (2022), who considered a spinning down NS. To model the micro-structure and dynamics of the crust failure, they constructed a cellular automaton. They predicted the rate of crust failure and found that typically the last failure event occurs when the NS spins down to ≈ 1 per cent of its birth frequency. They also calculated the ellipticity and gravitational wave strain as a function of the star's age.

In this thesis, we revisit the problem of mountain formation caused by starquakes in spinning-up stars. We use as our fundamental tool the simple energy minimisation methods first employed by Baym and Pines (1971), which allow one to gain intuitive insights into possible NS deformations. The original Baym and Pines (1971) analysis specialised to axisymmetric ($m = 0$) deformations, as that was the most relevant to the glitch phenomena that they studied. We extend their analysis to the non-axisymmetric ($m = 2$) case, allowing for both axisymmetric and non-axisymmetric deformations simultaneously.

Our parameter space is two-dimensional (2-d), with one parameter controlling the change in axisymmetric shape of the star, and the other the degree to which it becomes triaxial. We enforce angular momentum and energy conservation, and examine how large a mountain can be formed, subject only to these constraints. We also use our model to describe a specific mountain building scenario proposed recently in Giliberti and Cambiotti (2022).

The structure of the first half of the thesis is as follows. In Chapter 2, we review the starquake model. In Chapter 3, we calculate the energy contributions for both symmetric and asymmetric crust breaking during a starquake. Since we did not find a derivation of the symmetric crust breaking energies in the literature, we provide these explicitly before moving to the asymmetric case. We then test whether cross-terms appear in the total energy expression when both symmetric and asymmetric perturbations are present. Chapter 3 concludes with a relation between the post-starquake equilibrium shape and the relaxed zero-strain shape of the star in the purely asymmetric case.

In Chapter 4, we estimate the change in the star's total energy during a starquake and map the region of parameter space where this change is negative, i.e. where mountain formation is energetically allowed. We then calculate the maximum mountain that can be formed, and compare our results with the scenario of Giliberti and Cambiotti (2022). A paper based on the results of Chapters 3 and 4 has been published in *Monthly Notices of the Royal Astronomical Society* (Gangwar and Jones, 2024).

In the second half of this thesis, we examined another model for the formation of elastic mountains, in which the asymmetry arises from the Magnus force. We therefore refer to this as the *Magnus mountain* model.

It is widely accepted in the scientific community that the neutron fluid inside a neutron star exists in a state of superfluidity. Many models also suggest that the proton fluid in the core is in a state of superconductivity. Theory and experiment both support the existence of superfluid vortices in rotating superfluids and of flux tubes in superconductors.

The idea of a Magnus mountain was first proposed by Jones (2002a), who argued that if the neutron superfluid vortices are pinned non-axisymmetrically, either to flux tubes or to crustal nuclei, this will generate a non-axisymmetric Magnus force acting on the pinned vortices. This force, transmitted to the elastic crust through the vortices, may deform the crust and thereby give rise to a Magnus mountain. In recent times, Haskell et al. (2022) investigated the effect of pinned superfluid vortices at the flux tubes in the outer core on both the mass and current multipoles.

The structure of the second half of the thesis is as follows. In Chapter 5, we briefly review the physics of superfluidity and superconductivity. In Chapter 6, we investigate how both symmetric and non-axisymmetric interactions of superfluid vortices

with crustal nuclei and flux tubes influence the rotational dynamics of the neutron star under different scenarios. This analysis is entirely based on the study presented in Sidery and Alpar (2009). In particular, we consider whether the time evolution of non-axisymmetric interactions can lead to non-axisymmetric pinning of the vortices. This step is crucial for developing a self-consistent model of Magnus mountain formation, since the associated dynamics must be understood.

In Chapter 7, we present a simplified model of an infinitely long cylindrical star in which we impose, by hand, a non-axisymmetric neutron superfluid velocity field. This field gives rise to a non-axisymmetric Magnus force acting on the pinned vortices. We solve the coupled elastic and fluid equations of motion and calculate the resulting shape change of the star. In Chapter 7, we consider the incompressible case, while in Chapter 8 we extend the analysis to a compressible star. Finally, in Chapter 9, we present concluding remarks regarding both the starquake and Magnus mountain models for elastic mountain formation.

Chapter 2

Starquake model overview

In this chapter, we present the theory of the starquake model and discuss how it can be used to study the formation of elastic mountains. We summarise the calculations of Baym and Pines (1971) for the equilibrium shape of a star in the case of an $l = 2, m = 0$ perturbation, and extend the discussion to the $l = 2, m = 2$ perturbation, which is responsible for mountain formation. The calculations for the relevant energies involved in extending this idea are performed in Chapter 3. The logic developed here will then be applied in Chapter 4 to estimate the maximum size of a mountain, along with a discussion of results from a recent study that addresses the maximum size of an elastic mountain on a spinning-up neutron star.

The starquake model was first proposed by Baym and Pines (1971) to explain the glitches observed in the Crab and Vela pulsars. Pulsars are among the most stable clocks in the Universe, rivaling the precision of terrestrial atomic clocks over long timescales (Becker et al., 2018). However, observations reveal sudden increases in their spin frequency, known as *glitches* (Haskell and Melatos, 2015; Ruderman, 1969). The starquake model can explain small glitches but fails to account for the large glitches observed in Vela (Flanagan, 1996). Subsequently, a more promising theory, involving the pinning and unpinning of superfluid vortices, became the widely accepted explanation for glitches. Starquakes may still play a role in glitches, as they can accompany or even trigger the unpinning of vortices in the superfluid model for glitches (Epstein and Link, 2000). Nevertheless, the starquake model remains useful for studying the formation of elastic mountains on neutron stars (Fattoyev et al., 2018; Giliberti and Cambiotti, 2022).

The starquake model states that when a star spins down or spins up, its equilibrium shape changes: in the former case it becomes less oblate, and in the latter case it becomes more oblate, due to variations in the centrifugal force. This behaviour is illustrated in Figs. 2.1 and 2.2. However, because the crust is elastic, it resists this shape

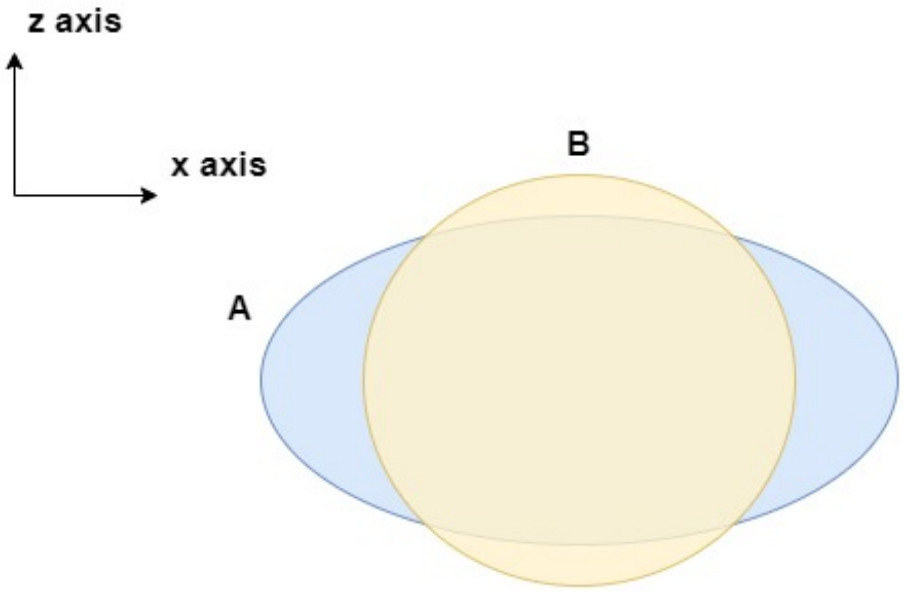

FIGURE 2.1: Spinning-down star. A represents the initial configuration with rotation along the z-axis. As the star spins down, it tries to readjust its shape to become less oblate, moving to configuration B.

change, and strain develops. The strain is described by the strain tensor:

$$\Sigma_{ij} = \frac{1}{2}\left(\frac{\partial \xi_i}{\partial x_j} + \frac{\partial \xi_j}{\partial x_i}\right), \tag{2.1}$$

where $\xi_i(\boldsymbol{r})$ is the displacement field (Franco et al., 2000). When the strain reaches a critical limiting value, the crust breaks. Glitch models typically consider only axisymmetric crust breaking, as they are primarily concerned with changes in the moment of inertia. However, crust breaking is a non-linear phenomenon and may also result in non-axisymmetric failure, which can lead to a non-zero quadrupole ellipticity (Giliberti and Cambiotti, 2022).

We divide this chapter into two sections. In Section 2.1, we present the starquake model under the assumption of axisymmetric crust breaking. In Section 2.2, we extend the analysis to include non-axisymmetric crust breaking.

2.1 Axisymmetric crust breaking

The energy analysis of the equilibrium shape under the starquake model was first performed by Baym and Pines (1971), who computed the displacement field ξ_i for an incompressible uniform-density, uniform-shear-modulus stellar model (see also Franco et al. (2000)). They assumed whole star to be elastic. They considered purely axisymmetric ($m = 0$) shape changes during starqauke. For a spinning-down star, the transition is from the zero-strain configuration with oblateness $\epsilon_{20,0}$ to a strained equilibrium

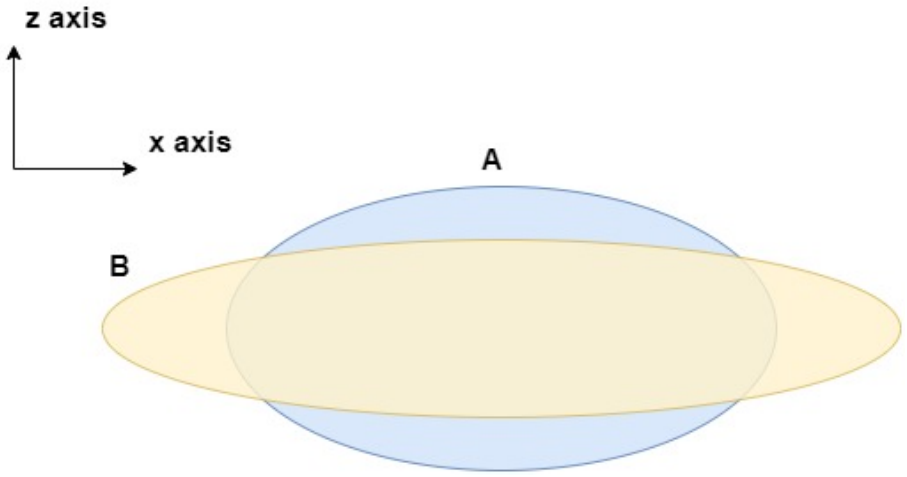

FIGURE 2.2: Spinning-up star. A is the initial configuration with rotation along the z-axis. As the star spins up, it tries to readjust its shape to become more oblate, moving to configuration B.

configuration ϵ_{20}. The oblateness parameter is defined as:

$$\epsilon_{20} = \frac{I_{zz} - I_{zz,s}}{I_{zz,s}}, \tag{2.2}$$

where I_{zz} is the moment of inertia about the rotation axis (chosen to be the z-axis) and $I_{zz,s}$ is the moment of inertia in the spherical configuration.

To find the equilibrium shape, one must balance the rotational and strain energies—which favour a more oblate shape—against the gravitational energy, which favours a more spherical configuration. The total energy is written as:

$$E_{\mathrm{T}} = E_{\mathrm{grav}} + E_{\mathrm{rot}} + E_{\mathrm{strain}}, \tag{2.3}$$

where E_{grav} is the gravitational potential energy, E_{rot} is the rotational kinetic energy, and E_{strain} is the strain energy.

For small departures from sphericity, the gravitational potential energy can be written as:

$$E_{\mathrm{grav}} = E_{\mathrm{grav,s}} + \delta E_{\mathrm{g}}, \tag{2.4}$$

where $E_{\mathrm{grav,s}}$ is the gravitational potential energy of the spherical configuration of the star, and δE_{g} represents the change in gravitational energy due to the deformation. Since the gravitational energy must reach a minimum when $\epsilon_{20} = 0$, this motivates the quadratic dependence

$$\delta E_{\mathrm{g}} = A_{20}\epsilon_{20}^2. \tag{2.5}$$

Here A_{20} acts like a gravitational stiffness, resisting shape changes. For a uniform density star of mass M and radius R:

$$A_{20} = \frac{3}{25}\frac{M^2 G}{R}. \tag{2.6}$$

This expression for A_{20} is mentioned in Baym and Pines (1971). They did not derive this expression, but instead gave the reference Love (1944). Since we did not find the derivation in Love (1944), we derived the expression for A_{20} explicitly in chapter 3.

The rotational kinetic energy is:

$$E_{\text{rot}} = \frac{L^2}{2I_{zz}}, \tag{2.7}$$

where L is the angular momentum.

The elastic strain energy is minimised when the actual shape, ϵ_{20}, matches the shape $\epsilon_{20,0}$ at which the strain vanishes, leading to the relation

$$E_{\text{strain}} = B_{20}(\epsilon_{20} - \epsilon_{20,0})^2, \tag{2.8}$$

where B_{20} is a constant representing the elastic stiffness of the crust. For an incompressible star with uniform density and uniform shear modulus μ, we have

$$B_{20} = \frac{57}{50}\mu V_s, \tag{2.9}$$

where $V_{\text{s}} = \frac{4\pi R^3}{3}$ is the total volume of the star (Baym and Pines, 1971).

In a realistic neutron star, only the crust is elastic. In this case, the expression for B_{20} can be written as

$$B_{20} = \frac{57}{50}\mu\left(\frac{4\pi}{3}(R^3 - R_c^3)\right), \tag{2.10}$$

where R_c is the inner radius of the crust.

Although the value of B_{20} is quoted by Baym and Pines (1971), the derivation is not provided in their work. In the following chapter, we explicitly calculate the constant B_{20}.

Collecting the above contributions, the total energy of the star can be written as

$$E_{\text{T}} = E_{\text{grav,s}} + \frac{L^2}{2I_{zz,s}(1+\epsilon_{20})} + A_{20}\epsilon_{20}^2 + B_{20}(\epsilon_{20} - \epsilon_{20,0})^2. \tag{2.11}$$

To determine the equilibrium shape ϵ_{20}, we minimise Eq. (2.11) with respect to ϵ_{20}, keeping the angular momentum L fixed. This yields

$$\epsilon_{20} = \frac{I_{zz,s}\,\Omega^2}{4\,(A_{20}+B_{20})} + \frac{B_{20}}{A_{20}+B_{20}}\,\epsilon_{20,0}, \tag{2.12}$$

where Ω is the angular velocity of the star. This equation gives the relation between the equilibrium shape (ϵ_{20}) and the elastically relaxed shape ($\epsilon_{20,0}$) of the star. The first term, proportional to Ω^2, can be identified as the centrifugal distortion. The second term, which remains when Ω is set to zero, is the (axisymmetric) distortion supported by the elastic strains in the crust.

We can rewrite Eq. (2.12) in the form

$$\epsilon_{20} = \epsilon_{\Omega} + b_{20}\,\epsilon_{20,0}, \tag{2.13}$$

where

$$\epsilon_{\Omega} = \frac{5}{6}\frac{R^3\Omega^2}{GM} = 1.76 \times 10^{-3}\left(\frac{f}{100\,\mathrm{Hz}}\right)^2 \frac{R_6^3}{M_{1.4}}, \tag{2.14}$$

using $\Omega = 2\pi f$, and

$$b_{20} \;=\; \frac{B_{20}}{A_{20}+B_{20}} \;\approx\; \frac{B_{20}}{A_{20}} \;=\; \frac{38\pi\,\mu\,R^3\Delta R}{M^2 G} \;\approx\; 2.28 \times 10^{-5}\,\frac{\mu_{30}\,R_6^3\,\Delta R_5}{M_{1.4}^2}. \tag{2.15}$$

In Eqs. (2.14) and (2.15), the quantities have been scaled to canonical values: $M_{1.4}$ is the mass in units of $1.4M_{\odot}$, R_6 is the stellar radius in units of 10^6 cm, μ_{30} is the shear modulus in units of 10^{30} erg cm^{-3}, and ΔR_5 is the crust thickness in units of 10^5 cm.

2.2 Non-axisymmetric crust breaking

The analysis presented in the previous section applies only to the axisymmetric $l = 2, m = 0$ perturbation and is therefore not directly applicable to mountain building, which is associated with the non-axisymmetric $l = 2, m = 2$ perturbations. However, the same approach can be straightforwardly adapted.

Neglecting rotation, we can modify Eq. (2.11) to express the total energy for the $m = 2$ case as

$$E_{\mathrm{T}} = E_{\mathrm{grav,s}} + A_{22}\epsilon_{22}^2 + B_{22}(\epsilon_{22} - \epsilon_{22,0})^2, \tag{2.16}$$

where ϵ_{22} and $\epsilon_{22,0}$ describe, respectively, the actual equilibrium configuration and the relaxed zero-strain configuration, both non-axisymmetric. In the $l = 2, m = 2$ case we allow for a non-vanishing relaxed configuration $\epsilon_{22,0}$. In a neutron star crust, failure is a nonlinear and localized process: due to spatial inhomogeneities in temperature, composition, and magnetic stresses, the breaking strain is reached first in limited regions rather than globally. Consequently, after crustal break, the relaxed shape of the star could evolve into a non-axisymmetric configuration. Motivated by this physically plausible symmetry breaking during crustal failure, we therefore allow for a non-zero $\epsilon_{22,0}$ in the present model.

Minimising Eq. (2.16) with respect to ϵ_{22} gives

$$\epsilon_{22} = \frac{B_{22}}{A_{22} + B_{22}} \epsilon_{22,0}. \tag{2.17}$$

This expression relates the equilibrium non-axisymmetric deformation ϵ_{22} to the corresponding relaxed shape $\epsilon_{22,0}$.

In much of the literature, A_{22} and B_{22} are assumed to be identical to A_{20} and B_{20}, respectively. Since $A_{20} \gg B_{20}$, we may approximate Eq. (2.17) as

$$\epsilon_{22} = \frac{B_{22}}{A_{22} + B_{22}} \epsilon_{22,0} \approx \frac{B_{22}}{A_{22}} \epsilon_{22,0} \approx \frac{B_{20}}{A_{20}} \epsilon_{22,0} \approx 10^{-5} \epsilon_{22,0}, \tag{2.18}$$

where the last step follows from Eq. (2.15). This indicates that the actual equilibrium mountain size is much smaller than the relaxed $m = 2$ shape. This outcome is not very favourable for mountain formation, as it implies that even if the crust attempts to sustain a significant deformation, gravity, being much stronger, will flatten almost all of it, leaving only a small residual ellipticity.

In Chapter 3, we will explicitly calculate B_{22} and A_{22} to verify the scaling given in Eq. (2.18).

In the most general case, both $l = 2, m = 0$ and $l = 2, m = 2$ perturbations may be present simultaneously. The total energy can then be expressed as

$$E_T = E_{\text{grav},0} + \frac{L^2}{2I_{zz}} + B_{20}(\epsilon_{20} - \epsilon_{20,0})^2 + A_{20}\epsilon_{20}^2 + B_{22}(\epsilon_{22} - \epsilon_{22,0})^2 + A_{22}\epsilon_{22}^2. \tag{2.19}$$

In Chapter 3, we will show explicitly that no cross-energy terms appear in Eq. (2.19) when the two perturbations coexist.

Chapter 3

Energy Calculations for Elastic Mountains

In this chapter, we explicitly compute the strain and perturbed gravitational potential energy of a star subject to a non-axisymmetric $l = 2, m = 2$ perturbation, which corresponds to the non-axisymmetric deformation of the crust in the starquake model. We subsequently evaluate the constants B_{22} and A_{22}, which are associated with the strain energy and gravitational energy, respectively.

As the derivations of B_{20} and A_{20} for the axisymmetric $l = 2, m = 0$ perturbation are not available in the existing literature, we begin by deriving these quantities before proceeding to the $m = 2$ case. Once the expressions for B_{22} and A_{22} are established, we use them to quantify the numerical relationship between the relaxed (zero-strain) shape and the equilibrium shape of the star within the starquake framework. This, in turn, allows us to estimate the size of a mountain that would result from a given zero-strain configuration.

Additionally, we examine whether cross-terms arise in the energy expression when both axisymmetric and non-axisymmetric perturbations are present simultaneously. The results obtained in this chapter will be utilised in Chapter 4, where we compute the maximum possible mountain size on a spinning neutron star.

To facilitate analytical calculations, we adopt a highly idealised stellar model following Baym and Pines (1971). The star is assumed to be incompressible and of uniform density, with the entire star treated as elastic with a uniform shear modulus. The total stellar radius is R.

Treating the neutron star as incompressible is a good approximation for elastic mountain formation in starquake models because the deformation is dominated by shear rather than compression. Neutron star matter is extremely stiff, with a very large bulk modulus, so volume changes are negligible compared to shape distortions for the

stresses involved in crustal failure. This approximation therefore captures the relevant physics while providing analytically tractable estimates of the maximum quadrupole.

3.1 Calculation of B_{20}

In this section, we derive the strain energy coefficient B_{20}, as given in Equation (2.9), for the $l = 2, m = 0$ perturbation. The general expression for calculating the strain energy of an elastic medium is

$$E_{\text{strain}} = \int U_{\text{strain}}\, dV = \int \mu\, \Sigma_{ij}\Sigma^{ij}\, dV, \tag{3.1}$$

where U_{strain} is the strain energy density, μ is the shear modulus, and Σ_{ij} is the strain tensor. We first compute the strain tensor Σ_{ij} for the displacement field assumed for the neutron star, and then evaluate the strain energy density U_{strain}. Finally, we perform the volume integral to obtain the total strain energy E_{strain} (Thorne and Blandford, 2017).

The total strain energy after the starquake process is then equated to the phenomenological expression for the strain energy, given by Equation (2.8):

$$B_{20}(\epsilon_{20} - \epsilon_{20,0})^2 = \int \mu\, \Sigma_{ij}\Sigma^{ij}\, dV. \tag{3.2}$$

By computing the difference between the zero-strain and equilibrium oblateness parameters, $(\epsilon_{20} - \epsilon_{20,0})$, we can determine B_{20} from Equation (3.2).

We begin by calculating the strain tensor Σ_{ij} using the covariant derivative form Thorne and Blandford (2017), which is a generalisation of Equation (2.1):

$$\Sigma_{ij} = \frac{1}{2}(\nabla_j \xi_i + \nabla_i \xi_j). \tag{3.3}$$

To evaluate the strain tensor, we first need to specify a displacement field $\vec{\xi}$ for the star. We adopt the displacement field given in Baym and Pines (1971) (Equation 29). The derivation of this displacement is found in Chapter 4 (Equation 4.100) of Lucy Keer's thesis (Keer, 2014). This displacement corresponds to the difference between two configurations: the initial relaxed configuration, rotating with angular velocity Ω_A, and the strained configuration, rotating with angular velocity Ω. It is expressed as

$$\vec{\xi} = U(r)P_2(\cos\theta)\,\hat{\boldsymbol{r}} + V(r)\,\boldsymbol{\nabla} P_2(\cos\theta), \tag{3.4}$$

where the Legendre polynomial of degree 2 is

$$P_2(\cos\theta) = \frac{1}{2}(3\cos^2\theta - 1). \tag{3.5}$$

Equation (3.4) represents the general form of any $l = 2, m = 0$ displacement field. The functions $U(r)$ and $V(r)$ are radial eigenfunctions that encode the amplitude of the displacement associated with the quadrupolar ($\ell = 2$) perturbation. For a uniform-density elastic star (i.e., the entire star is elastic) with uniform shear modulus, Baym and Pines (1971) and Keer (2014) provide the following expressions for $U(r)$ and $V(r)$:

$$U(r) = \frac{1}{5R^2}\frac{\lambda}{1+b_{20}}(\Omega^2 - \Omega_A^2)(3r^3 - 8R^2 r), \tag{3.6}$$

$$V(r) = \frac{1}{5R^2}\frac{\lambda}{1+b_{20}}(\Omega^2 - \Omega_A^2)\left(\frac{5}{2}r^4 - 4R^2 r^2\right), \tag{3.7}$$

with

$$\lambda = \frac{5}{8\pi G\rho}. \tag{3.8}$$

and

$$b_{20} = \frac{57\mu}{8\pi G\rho^2 R^2}. \tag{3.9}$$

Substituting Equations (3.6) and (3.7) into Equation (3.4), we obtain:

$$\vec{\xi} = \frac{1}{5R^2}\frac{\lambda}{1+b_{20}}(\Omega^2 - \Omega_A^2)(3r^3 - 8R^2 r)P_2(\cos\theta)\,\hat{\boldsymbol{r}} - \frac{3}{2}\frac{1}{5R^2}\frac{\lambda}{1+b_{20}}(\Omega^2 - \Omega_A^2)\left(\frac{5}{2}r^3 - 4R^2 r\right)\sin(2\theta)\,\hat{\boldsymbol{\theta}}. \tag{3.10}$$

For convenience, let us define

$$k = \frac{1}{5R^2}\frac{\lambda}{1+b_{20}}(\Omega^2 - \Omega_A^2). \tag{3.11}$$

With this definition, Equation (3.10) can be rewritten as

$$\vec{\xi} = k(3r^3 - 8R^2 r)P_2(\cos\theta)\,\hat{\boldsymbol{r}} - \frac{3}{2}k\left(\frac{5}{2}r^3 - 4R^2 r\right)\sin(2\theta)\,\hat{\boldsymbol{\theta}}. \tag{3.12}$$

For analytical calculations, it is convenient to write the displacement vector in a compact form as

$$\vec{\xi} = \xi_r\,\hat{\boldsymbol{r}} + \xi_\theta\,\hat{\boldsymbol{\theta}}, \tag{3.13}$$

where the radial and polar components are given by

$$\xi_r = U(r)P_2(\cos\theta) = k(3r^3 - 8R^2 r)P_2(\cos\theta), \tag{3.14}$$

$$\xi_\theta = V(r)\,\nabla P_2(\cos\theta) = -\frac{3}{2}\frac{V(r)}{r}\sin(2\theta) = -\frac{3}{2}k\left(\frac{5}{2}r^3 - 4R^2 r\right)\sin(2\theta). \tag{3.15}$$

Next, we calculate the different components of the strain tensor using the displacement field $\vec{\xi}$ defined in Eq. (3.13). The expressions for the strain tensor components in spherical coordinates are taken from Thorne and Blandford (2017).

We evaluate each non-zero component of the strain tensor:

$$\Sigma_{rr} = \frac{2}{3}\frac{\partial \xi_r}{\partial r} - \frac{2}{3r}\xi_r - \frac{\cot\theta}{3r}\xi_\theta - \frac{1}{3r}\frac{\partial \xi_\theta}{\partial \theta} - \frac{1}{3r\sin\theta}\frac{\partial \xi_\phi}{\partial \phi} = 4kP_2r^2 + \frac{V(r)}{r^2}(3\cos^2\theta - 1), \tag{3.16}$$

$$\Sigma_{\theta\theta} = \frac{2}{3r}\frac{\partial \xi_\theta}{\partial \theta} + \frac{1}{3r}\xi_r - \frac{1}{3r}\frac{\partial \xi_r}{\partial r} - \frac{\cot\theta}{3r}\xi_\theta - \frac{1}{3r\sin\theta}\frac{\partial \xi_\phi}{\partial \phi} = \frac{V(r)}{r^2}(2 - 3\cos^2\theta) - 2P_2kr^2, \tag{3.17}$$

$$\Sigma_{\phi\phi} = \frac{2}{3r\sin\theta}\frac{\partial \xi_\phi}{\partial \phi} + \frac{2}{3r}\cot\theta\xi_\theta + \frac{\xi_r}{3r} - \frac{1}{3}\frac{\partial \xi_r}{\partial r} - \frac{1}{3r}\frac{\partial \xi_\theta}{\partial \theta} = -2P_2kr^2 + \frac{V(r)}{r^2}, \tag{3.18}$$

$$\Sigma_{\phi\theta} = \Sigma_{\theta\phi} = \frac{1}{2r}\frac{\partial \xi_\phi}{\partial \theta} - \frac{\cot\theta\xi_\phi}{2r} + \frac{1}{2r\sin\theta}\frac{\partial \xi_\theta}{\partial \phi}, \tag{3.19}$$

$$\Sigma_{\phi r} = \Sigma_{r\phi} = \frac{1}{2r\sin\theta}\frac{\partial \xi_r}{\partial \phi} + \frac{1}{2}\frac{\partial \xi_\phi}{\partial r} - \frac{\xi_\phi}{2r}. \tag{3.20}$$

We assume that the displacement does not depend on ϕ and that $\xi_\phi = 0$. Furthermore, since ξ_θ and ξ_r are independent of ϕ, their partial derivatives with respect to ϕ vanish. This gives:

$$\Sigma_{\phi\theta} = \Sigma_{\theta\phi} = \Sigma_{\phi r} = \Sigma_{r\phi} = 0.$$

The remaining non-zero off-diagonal components are:

$$\Sigma_{r\theta} = \Sigma_{\theta r} = \frac{1}{2}\frac{\partial \xi_\theta}{\partial r} - \frac{\xi_\theta}{2r} + \frac{1}{2r}\frac{\partial \xi_r}{\partial \theta} = 6k\sin 2\theta(R^2 - r^2). \tag{3.21}$$

We now summarise the full strain tensor:

$$\Sigma_{ij} = \begin{bmatrix} 4kP_2r^2 + \frac{V(r)}{r^2}(3\cos^2\theta - 1) & 6k\sin 2\theta(R^2 - r^2) & 0 \\ 6k\sin 2\theta(R^2 - r^2) & \frac{V(r)}{r^2}(2 - 3\cos^2\theta) - 2P_2kr^2 & 0 \\ 0 & 0 & -2P_2kr^2 - \frac{V(r)}{r^2} \end{bmatrix} \tag{3.22}$$

To calculate the total strain energy E_{strain}, we first compute the strain energy density U_{strain}, given by

$$U_{\text{strain}} = \mu \Sigma_{ij} \Sigma^{ij}. \tag{3.23}$$

Expanding Eq. (3.23) yields:

$$U_{\text{strain}} = \mu \left[\Sigma_{rr}^2 + \Sigma_{\theta\theta}^2 + \Sigma_{\phi\phi}^2 + 2(\Sigma_{r\theta})^2 \right]. \tag{3.24}$$

Substituting the expressions from Eq. (3.22), we obtain:

$$\begin{aligned} \Sigma_{ij}\Sigma^{ij} = &\left[4kP_2 r^2 + \frac{V(r)}{r^2}(3\cos^2\theta - 1) \right]^2 + \left[\frac{V(r)}{r^2}(2 - 3\cos^2\theta) - 2P_2 k r^2 \right]^2 \\ &+ \left[-2P_2 k r^2 - \frac{V(r)}{r^2} \right]^2 + 2\left[6k \sin 2\theta (R^2 - r^2) \right]^2. \end{aligned} \tag{3.25}$$

Inserting Eq. (3.25) into Eq. (3.23) and simplifying gives:

$$U_{\text{strain}} = \mu k^2 \left(96R^4 + \frac{117}{2} r^4 + \frac{3}{2} r^4 \cos^2\theta (9\cos^2\theta + 33) - 72 r^2 R^2 (2 + \cos^2\theta) \right). \tag{3.26}$$

We now perform the volume integration of U_{strain} over the entire star to obtain the total strain energy:

$$E_{\text{strain}} = \int U_{\text{strain}} \, dV = 38 \mu k^2 R^7 \pi. \tag{3.27}$$

The final step in obtaining the value of B_{20} is the evaluation of

$$\epsilon_{20} - \epsilon_{20,0} = \frac{I_{zz}^{20} - I_{zz,s}}{I_{zz,s}} - \frac{\delta I_{zz}^{20,0} - I_{zz,s}}{I_{zz,s}} = \frac{\delta I_{zz}}{I_{zz,s}}. \tag{3.28}$$

Here, we assume that the rotation occurs about the z-axis. The quantity $I_{zz,s}$ denotes the moment of inertia of a spherical, non-rotating star about the rotation axis, while δI_{zz} is the change in moment of inertia as the star transitions from the relaxed, zero-strain shape to the equilibrium shape. The expressions for I_{zz} and δI_{zz} are given by:

$$I_{zz} = \int_V \rho (x^2 + y^2) \, dV, \tag{3.29}$$

$$\delta I_{zz} = \delta \int_V \rho (x^2 + y^2) \, dV. \tag{3.30}$$

To evaluate δI_{zz}, we make use of the identity

$$\delta \int_V \rho f \, dV = \int_V \rho \Delta f \, dV, \tag{3.31}$$

as noted in Friedman and Schutz (1978), Eq. (B12). The Lagrangian perturbation Δf of a fluid variable f is defined as

$$\Delta f(x,t) = f(x+\xi,t) - f_0(x,t). \tag{3.32}$$

The corresponding Eulerian perturbation δf is related to the Lagrangian perturbation by

$$\Delta f = \delta f + \xi \cdot \nabla f_0. \tag{3.33}$$

Applying Eq. (3.31) to Eq. (3.30) gives:

$$\delta I_{zz} = \int_V \rho \Delta(x^2 + y^2) \, dV. \tag{3.34}$$

Now, using the definition of the Lagrangian perturbation of a tensor quantity,

$$\Delta(x_i x_j) \equiv (x_i + \xi_i)(x_j + \xi_j) - x_i x_j = \xi_i x_j + \xi_j x_i + \xi_i \xi_j, \tag{3.35}$$

and keeping only terms linear in ξ, we obtain

$$\delta I_{zz} = 2\rho \int_V (\xi_x x + \xi_y y) \, dV. \tag{3.36}$$

Since the calculations are carried out in spherical coordinates, we express the displacement vector in the form $\boldsymbol{\xi} = \xi_r \hat{r} + \xi_\theta \hat{\theta}$. Projecting this displacement onto the Cartesian basis yields the Cartesian components

$$\xi_x = \xi_r \sin\theta \cos\phi + \xi_\theta \cos\theta \cos\phi, \tag{3.37}$$

$$\xi_y = \xi_r \sin\theta \sin\phi + \xi_\theta \cos\theta \sin\phi. \tag{3.38}$$

Substituting Eqs. (3.37) and (3.38) into Eq. (3.36) and performing the angular integrations over the stellar volume, we obtain

$$\delta I_{zz} = \frac{8}{3} k R^7 \pi \rho. \tag{3.39}$$

The expression for the moment of inertia of a spherical star is:

$$I_{zz,s} = \frac{8\rho\pi R^5}{15}. \tag{3.40}$$

Substituting Eqs. (3.39) and (3.40) into Eq. (3.28), we obtain:

$$\epsilon_{20} - \epsilon_{20,0} = 5kR^2. \tag{3.41}$$

Now, substituting Eq. (3.27) and Eq. (3.41) into Eq. (3.1), we get:

$$E_{\text{strain}} = 38\mu k^2 R^7 \pi = 25 B_{20} k^2 R^4, \tag{3.42}$$

which yields:

$$B_{20} = \frac{57}{50}\mu \left(\frac{4\pi R^3}{3}\right). \tag{3.43}$$

Thus, we reproduce the expression for the constant B_{20} as given in Baym and Pines (1971) in Eq. (2.9).

In the above derivation, we have assumed the entire star to be elastic. In a realistic neutron star, however, only the crust is elastic, with a fluid core in the interior. In that case, the same method could be applied to obtain the expression for B_{20} as given in Eq. (2.10), adopting the same displacement field (3.4) as the correct eigenfunction for a star with finite crust thickness. This approximation is justified since elasticity is much weaker than gravity. Baym et al. (1969) followed this approach and provided values of B_{20} for varying crust thicknesses in Table 1 of their work.

Later, in the calculation of B_{22} for the non-axisymmetric perturbation, we will assume the star to consist of a fluid core surrounded by an elastic crust.

3.2 Calculation of A_{20}

In this section, we calculate the perturbed gravitational potential energy, δE_g, which appears in Equation (2.4). We again assume an incompressible star with uniform density. Two different methods are employed: (1) the Friedman and Schutz formalism, which is a perturbative approach that expresses δE_g in terms of the displacement vector field (Friedman and Schutz, 1978), and (2) the Maclaurin spheroids method (Shapiro and Teukolsky, 1983), which involves solving Poisson's equation using Green's functions expressed in terms of spherical harmonics to compute E_g for an ellipsoid. The latter method is general for any ellipsoid and can be applied to the biaxial case considered here.

3.2.1 Method: Friedman and Schutz

We use the formalism provided in Friedman and Schutz (1978) to compute the perturbed gravitational potential energy (equation B56 in Friedman and Schutz (1978)).

The expression for δE_g is given by

$$\delta E_g = \int_V [\rho \xi^i \nabla_i \Phi + \rho \xi^i \nabla_i \delta\Phi + \frac{1}{8\pi G} \nabla_i \delta\Phi \nabla^i \delta\Phi + \frac{1}{2} \rho \xi^i \xi^j \nabla_i \nabla_j \Phi] dV. \tag{3.44}$$

We use the displacement field from Eq. (3.13), previously employed in the calculation of B_{20}. The gravitational potential Φ is obtained by solving Poisson's equation:

$$\nabla^2 \Phi = 4\pi G \rho, \tag{3.45}$$

which yields:

$$\Phi(r) = \begin{cases} \frac{2}{3}\pi G\rho(r^2 - 3R^2), & r \leq R \\ -\frac{4\pi G \rho R^3}{3r}, & r > R. \end{cases} \tag{3.46}$$

Note that the integration domain in Eq. (3.44) is infinite. Therefore, to compute the third term in Eq. (3.44), one has to consider both $\delta\Phi_{\text{int}}(0 \leq r \leq R)$ and $\delta\Phi_{\text{ext}}(r > R)$ as given below:

$$\delta\Phi^{\text{int}} = 4\pi G R^2 \rho k r^2 P_2(\cos\theta), \tag{3.47}$$

$$\delta\Phi^{\text{ext}} = \frac{4\pi G R^7 \rho k P_2(\cos\theta)}{r^3}, \tag{3.48}$$

from Keer (2014). We now evaluate the four contributions appearing in Eq. (3.44). The first term is given by

$$\int_V \rho \xi^i \nabla_i \phi \, dV = \int_V \rho \xi^r \nabla_r \phi \, dV. \tag{3.49}$$

This term vanishes identically after performing the angular integration and therefore does not contribute to the energy variation. The second term evaluates to

$$\int_V \rho \xi^i \nabla_i \delta\phi \, dV = -16 \rho^2 k^2 \pi^2 G R^9. \tag{3.50}$$

The third term represents the self-energy associated with the gravitational potential perturbation and is given by

$$\int_V \frac{1}{8\pi G} \nabla_i \delta\phi \nabla^i \delta\phi \, dV = 8 \rho^2 k^2 \pi^2 G R^9. \tag{3.51}$$

The fourth term, which is quadratic in the displacement field, takes the form

$$\int_V \frac{1}{2} \rho \xi^i \xi^j \nabla_i \nabla_j \phi \, dV = \frac{316}{45} \rho^2 k^2 \pi^2 G R^9. \tag{3.52}$$

Adding the non-vanishing contributions from the second, third, and fourth terms, we obtain the total change in gravitational energy

$$\delta E_g = -\frac{44}{45} \rho^2 k^2 \pi^2 G R^9. \tag{3.53}$$

This result implies a negative change in gravitational energy, which contradicts physical expectations. The background star is initially spherical and non-rotating, representing a configuration of minimum gravitational energy. Upon the introduction of rotation, the star becomes deformed. However, the result given in Eq. (3.53) incorrectly suggests that the deformed, rotating star possesses a lower gravitational energy than the original spherical configuration. This is unphysical, as rotational deformation should increase the total gravitational energy compared to the non-rotating, spherically symmetric state.

To assess the full picture, we also compute the change in internal energy δU, using Eq. (B48) from Friedman and Schutz (1978):

$$\delta U = \frac{1}{2}\int_V \xi^i \xi^j \nabla_i \nabla_j P \, dV. \tag{3.54}$$

In order to evaluate this, we first require the pressure profile $P(r)$, which can be obtained from the static Euler equation:

$$\rho \frac{dv}{dt} = -\nabla P - \rho \nabla \Phi. \tag{3.55}$$

Since the background star is static and time-independent, equation (3.55) reduces to the time-independent Euler equation:

$$0 = -\nabla P - \rho \nabla \Phi. \tag{3.56}$$

Using Eqs. (3.46) and (3.56), we find:

$$P(r) = \begin{cases} \frac{2}{3}\pi G \rho^2 (R^2 - r^2), & r \leq R \\ 0, & r > R. \end{cases} \tag{3.57}$$

At the surface, the pressure gradient can be expressed via a Heaviside function (Yim and Jones, 2022):

$$\nabla_j P(r) = -\frac{4}{3}\pi G \rho^2 r_j H(R - r). \tag{3.58}$$

Differentiating Eq. (3.58) gives:

$$\nabla_i \nabla_j P(r) = -\frac{4}{3}\pi G \rho^2 [\delta_{ij} H(R - r) - r_j \hat{r}_i \delta(r - R)]. \tag{3.59}$$

Inserting Eq. (3.59) into Eq. (3.54):

$$\delta U = -\frac{2}{3}\pi G\rho^2 \int_V \xi^i \xi_i \, dV + \frac{2}{3}\pi G\rho^2 R \int_{\partial V} [\xi^r(R)]^2 \, dS. \tag{3.60}$$

Evaluating Eq. (3.60) using the displacement field given in Eq. (3.13), we find

$$\delta U = \frac{284}{45}\rho^2 k^2 \pi^2 G R^9. \tag{3.61}$$

Since we are considering an incompressible star, the change in internal energy should vanish. However, Equation (3.61) yields a positive change in internal energy.

If we proceed with the calculated values of δU and δE_g, and sum them, we obtain

$$\delta U + \delta E_g = \frac{248}{45}\rho^2 k^2 \pi^2 G R^9 - \frac{44}{45}\rho^2 k^2 \pi^2 G R^9 = \frac{16}{3}\rho^2 k^2 \pi^2 G R^9. \tag{3.62}$$

Equating this with $A_{20}\epsilon^2$:

$$\delta U + \delta E_g = \frac{16}{3}\rho^2 k^2 \pi^2 G R^9 = A_{20}\epsilon^2, \tag{3.63}$$

and using $\rho = \frac{3M}{4\pi R^3}$, we obtain:

$$A_{20} = \frac{3}{25}\frac{GM^2}{R}. \tag{3.64}$$

We reproduce the value of A_{20} as given in Baym and Pines (1971), but only after combining the change in internal energy, δU, with the change in gravitational energy, δE_g. However, this is not correct, since A_{20} is defined as the coefficient associated only with the perturbed gravitational energy.

There are two main issues with the calculation above: (1) the incorrect negative value of δE_g in Eq. (3.53), and (2) the non-zero internal energy δU despite the star being incompressible, for which δU should ideally vanish. These problems were previously identified in Yim and Jones (2022).

We find that the source of the discrepancy noted above is that the displacement field given in Equation (3.4) enforces incompressibility only to first order, whereas the leading-order contributions to δE_g and δU arise at second order. A more accurate displacement field, which ensures incompressibility to second order, should resolve this issue. If we compute the Lagrangian perturbation in density, we may identify the second-order correction that should be added to the displacement field so that the incompressibility condition is satisfied up to second order. We calculate the Lagrangian perturbation in density using the formalism described in Friedman and Schutz (1978):

$$\frac{\Delta\rho}{\rho} = -\nabla_i\xi^i + \frac{1}{2}(\nabla_i\xi^i\nabla_j\xi^j + \nabla_i\xi^j\nabla_j\xi^i) + \mathcal{O}(\xi^3), \tag{3.65}$$

Using this expression, we obtain a second-order perturbation to the density in powers of k^2, which takes a rather complicated form:

$$\frac{\Delta\rho}{\rho} = k^2\left(-\frac{207}{4}r^4\cos^4\theta + \frac{333}{4}r^4\cos^2\theta + \frac{117r^4}{4} + 360r^2R^2\cos^4\theta - 396r^2R^2\cos^2\theta \right.$$
$$\left. -72r^2R^2 + 48R^4 + 144\cos^2\theta R^4 - 144\cos^4\theta R^4\right). \tag{3.66}$$

Here, k is a small parameter defined in equation (3.11) in terms of the angular velocity Ω. From the form of the density perturbation, it is not straightforward to deduce the second-order correction to the displacement field in equation (3.4) that would render it incompressible to this order. Although it is possible to construct such a field, the derivation would be lengthy and cumbersome. Instead, we employ an alternative displacement field that suffices for calculating δE_g, since the gravitational energy depends only on the shape of the star and not on how the individual fluid elements inside the star are rearranged. We therefore proceed with the analysis by choosing the Kelvin mode displacement, which represents a family of vector fields defined as follows:

$$\vec{\xi_{lm}} = \frac{\alpha_{lm}}{R^{l-2}}\nabla(r^l Y_{lm}(\theta,\phi)). \tag{3.67}$$

For a perturbation with $l = 2$ and $m = 0$, equation (3.67) becomes:

$$\vec{\xi_{20}} = 2\alpha_{20}rY_{20}\hat{e_r} + \alpha_{20}r\frac{dY_{20}}{d\theta}\hat{e_\theta}, \tag{3.68}$$

where the spherical harmonic is given by

$$Y_{20} = \frac{1}{4}\sqrt{\frac{5}{\pi}}(3\cos^2\theta - 1). \tag{3.69}$$

The components of the displacement field are:

$$\xi^r = \alpha_{20}r\frac{1}{2}\sqrt{\frac{5}{\pi}}(3\cos^2\theta - 1), \tag{3.70}$$

$$\xi^\theta = -\alpha_{20}r\frac{3}{4}\sqrt{\frac{5}{\pi}}(\sin 2\theta). \tag{3.71}$$

Using equations (3.44) and (3.54), we compute δE_g and δU for this displacement field. We find:

$$\delta E_g = -\frac{3}{20}\frac{GM^2}{\pi R}\alpha_{20}^2, \tag{3.72}$$

$$\delta U = \frac{3}{4}\frac{GM^2}{\pi R}\alpha_{20}^2. \tag{3.73}$$

We again observe that the same two issues persist: a negative perturbed gravitational potential energy and a positive change in internal energy. These results were first noted in Yim and Jones (2022), where the authors also employed the Kelvin mode displacement field in their analysis. We further note that Equation (3.68) too enforces incompressibility only to first order. To verify this, we again compute the density perturbation using Equation (3.65):

$$\frac{\Delta\rho}{\rho} = \frac{15}{4\pi}\alpha_{20}^2. \tag{3.74}$$

This result shows that the star is not incompressible to second order. Unlike Equation (3.66), this expression for the density perturbation is simpler, allowing us to easily identify a second-order correction term that can be added to the Kelvin mode displacement field to ensure incompressibility up to second order.

We also compute the volume perturbation by evaluating the stellar radii along the principal axes:

$$a_1 = R + \xi^r(r = R, \theta = \frac{\pi}{2}, \phi = 0) = R\left(1 + \frac{1}{2}\alpha_{20}\sqrt{\frac{5}{\pi}}\right), \tag{3.75}$$

$$a_2 = R + \xi^r(r = R, \theta = \frac{\pi}{2}, \phi = \frac{\pi}{2}) = R\left(1 + \frac{1}{2}\alpha_{20}\sqrt{\frac{5}{\pi}}\right), \tag{3.76}$$

$$a_3 = R + \xi^r(r = R, \theta = 0) = R\left(1 - \alpha_{20}\sqrt{\frac{5}{\pi}}\right). \tag{3.77}$$

The volume of the resulting triaxial ellipsoid is given by:

$$V_{\text{per}} = \frac{4\pi}{3}a_1 a_2 a_3. \tag{3.78}$$

The fractional change in volume is then:

$$\frac{\Delta V}{V} = -\frac{15}{4\pi}\alpha_{20}^2. \tag{3.79}$$

This shows that the reduction in volume is exactly balanced by the increase in density, as expected from mass conservation. The Kelvin mode introduces a uniform radial contraction ($l = 0$ mode), so we counterbalance it with an expansion. To restore incompressibility to second order, we introduce a corrective radial term by hand, which appears as a second-order addition to the displacement field:

$$\vec{\xi_{20}} = \alpha_{20}\nabla(r^2 Y_{20}(\theta,\phi)) + \frac{5r}{4\pi}\alpha_{20}^2\hat{e_r}. \tag{3.80}$$

One can verify that this modified displacement field yields zero second-order density and volume perturbations using Equations (3.65) and (3.78), respectively.

Now, we have a displacement field given in Equation (3.80) that ensures incompressibility to second order. Continuing with the calculation of the perturbed gravitational potential energy, we substitute Equation (3.80) into Equation (3.44), which yields:

$$\delta E_g = \frac{3}{5}\frac{GM^2}{\pi R}\alpha_{20}^2. \tag{3.81}$$

We now obtain a positive perturbed gravitational potential energy. Furthermore, with the modified displacement field, the internal energy perturbation vanishes, as can be verified by substituting Equation (3.80) into the expression given in Equation (3.60).

Next, to evaluate the constant A_{20}, we compute the ellipticity using Equation (2.2). The unperturbed moment of inertia is given by:

$$I_{zz,0} = \frac{2}{5}MR^2, \tag{3.82}$$

while for a uniform density ellipsoid:

$$I_{zz} = \frac{M}{5}(a_1^2 + a_2^2). \tag{3.83}$$

Substituting the values of a_1 from Equation (3.75) and a_2 from Equation (3.76), we obtain:

$$I_{zz} = \frac{2}{5}MR^2\left(1 + \alpha_{20}\sqrt{\frac{5}{\pi}}\right), \tag{3.84}$$

which is valid to first order in α_{20}.

Substituting Equations (3.82) and (3.84) into the definition of ellipticity given in Equation (2.2), we obtain:

$$\epsilon_{20} = \alpha_{20}\sqrt{\frac{5}{\pi}}. \tag{3.85}$$

Next, inserting Equation (3.85) into the phenomenological expression for the perturbed gravitational energy given in Equation (2.5), and comparing with the perturbed gravitational energy in Equation (3.81) derived in this section, we find:

$$A_{20} = \frac{3GM^2}{25R}. \tag{3.86}$$

Thus, we reproduce the value of A_{20} found in the literature using a second-order incompressible displacement field. Baym and Pines (1971) present the result for A_{20} and cite the book by Love (1944) as the source. However, we were unable to find an explicit derivation of this result in that reference and have therefore carried out the calculation independently.

3.2.2 Method: Maclaurin spheroids

To gain further confidence in the value of A_{20} calculated in the previous section, we now compute the perturbed gravitational potential energy using an alternative method based on Maclaurin spheroids. This approach is outlined in Shapiro and Teukolsky (1983), Section 7.3, "Rotating Configurations: The Maclaurin Spheroids" (Shapiro and Teukolsky, 1983). The gravitational potential energy of a Maclaurin spheroid, representing an oblate spheroid formed when a uniformly dense self-gravitating fluid rotates at a constant angular velocity, is given as an exercise in Shapiro and Teukolsky (1983) (Eq. 7.3.23).

The calculation begins with the gravitational potential Φ, obtained from the Green's function solution of Poisson's equation, given by

$$\Phi = -2\pi G\rho\left[-\tfrac{1}{3}r^2 + \int_0^1 \frac{dx}{\frac{1}{a_1^2} + \left(\frac{1}{a_3^2} - \frac{1}{a_1^2}\right)x^2} - (3\cos^2\theta - 1)\,\tfrac{r^2}{4}\int_0^1 dx\,(3x^2-1)\,\log\left[\frac{1}{a_1^2} + \left(\frac{1}{a_3^2} - \frac{1}{a_1^2}\right)x^2\right]\right], \tag{3.87}$$

where a_1 and a_3 denote the equatorial and polar radii of the spheroid, respectively. This expression for the gravitational potential Φ is given in Equation (7.3.5) of Shapiro and Teukolsky (1983).

The gravitational potential energy is then obtained by taking the volume integral of Eq. (3.87):

$$E_{\text{grav}} = \frac{1}{2}\rho \int \Phi \, d^3x. \tag{3.88}$$

Carrying out this integration yields

$$E_{\text{grav}} = -\frac{3}{5}\left(\frac{4\pi}{3}\right)^2 G\rho^2 a_1^5 \frac{\sin^{-1} e}{e}(1-e^2), \tag{3.89}$$

where e is the eccentricity of the spheroid, defined as

$$e^2 = 1 - \frac{a_3^2}{a_1^2}. \tag{3.90}$$

To compute δE_{grav}, we Taylor expand Eq. (3.89) in terms of e. The expression for the mass M of the star in terms of a_1 and e is given by Shapiro and Teukolsky (1983) (Eq. 7.3.20):

$$M = \frac{4}{3}\pi a_1^3 (1-e^2)^{1/2}\rho. \tag{3.91}$$

Rearranging Eq. (3.91) allows us to express a_1 in terms of e:

$$a_1 = R(1-e^2)^{-1/6}, \tag{3.92}$$

where

$$R = \left(\frac{3M}{4\pi\rho}\right)^{1/3}. \tag{3.93}$$

To express e^2 in terms of Ω, we use the following expression from Shapiro and Teukolsky (1983) (Eq. 7.3.18):

$$\Omega^2 = 2\pi\rho G\left[\frac{(1-e^2)^{1/2}}{e^3}(3-2e^2)\sin^{-1} e - \frac{3(1-e^2)}{e^2}\right]. \tag{3.94}$$

Linearising Eq. (3.94), we get:

$$\frac{5\Omega^2}{8\pi\rho G} = \frac{1}{3}e^2 + \frac{1}{21}e^4. \tag{3.95}$$

Let us define $\gamma = -\frac{5\Omega^2}{8\pi\rho G}$. Then Eq. (3.95) becomes:

$$-\gamma = \frac{1}{3}e^2 + \frac{1}{21}e^4. \tag{3.96}$$

Assuming a perturbative expansion of the form:

$$e^2 = k_0\gamma + k_1\gamma^2, \tag{3.97}$$

and substituting into Eq. (3.96), we get:

$$-\gamma = \frac{1}{3}k_0\gamma + \left(\frac{1}{3}k_1 + \frac{1}{21}k_0^2\right)\gamma^2. \tag{3.98}$$

Matching coefficients, we find:

$$k_0 = -3, \tag{3.99}$$

$$k_1 = -\frac{9}{7}. \tag{3.100}$$

Substituting these into Eq. (3.97) gives:

$$e^2 = -3\gamma - \frac{9}{7}\gamma^2. \tag{3.101}$$

Now substitute Eq. (3.92) into the gravitational energy expression Eq. (3.89):

$$E_{\text{grav}} = -\frac{3}{5}\left(\frac{4\pi}{3}\right)^2 G\rho^2 R^5 (1-e^2)^{-5/6}\frac{\sin^{-1}e}{e}(1-e^2). \tag{3.102}$$

Linearising this in e, we find:

$$\delta E_{\text{grav}} = \frac{3}{5}\left(\frac{4\pi}{3}\right)^2 G\rho^2 R^5 \cdot \frac{1}{45}e^4. \tag{3.103}$$

Substituting Eq. (3.101) into Eq. (3.103) gives:

$$\delta E_{\text{grav}} = \frac{3}{5}\left(\frac{4\pi}{3}\right)^2 G\rho^2 R^5 \cdot \frac{1}{5}\gamma^2. \tag{3.104}$$

In order to calculate A_{20}, we require ϵ_{20} in terms of γ. In the calculation of the constant B_{20} (which is related to the strain energy), we previously obtained $\epsilon_{20} - \epsilon_{20,0} = 5kR^2$.

Here, we are considering a fluid star. In this case, only the surface shape of the star affects the gravitational potential energy; the nature of the stellar matter, whether fluid or elastic, does not influence the calculation. For a fluid star, the shear modulus vanishes ($\mu = 0$), and we can set $\Omega_A = 0$ in equation (3.41). Physically, this corresponds to taking a non-rotating spherical star as the initial configuration and then spinning it up to an angular velocity Ω, thereby making it oblate. With these substitutions into equation (3.41), we obtain

$$\epsilon_{20} = 5 \cdot \frac{\lambda}{5R^2}\Omega^2 R^2, \tag{3.105}$$

where λ is a constant defined in Eq. (3.8).

Finally, inserting the expression for λ into equation (3.105) yields

$$\epsilon_{20} = \frac{5\Omega^2}{8\pi G\rho} = -\gamma. \tag{3.106}$$

Inserting Eqs. (3.104) and (3.106) into Eq. (2.5) yields:

$$\frac{3}{5}\left(\frac{4\pi}{3}\right)^2 G\rho^2 R^5 \cdot \frac{1}{5}\gamma^2 = A_{20}\gamma^2, \tag{3.107}$$

which implies:

$$A_{20} = \frac{3}{25}\frac{GM^2}{R}. \tag{3.108}$$

Thus, using the Maclaurin spheroids method, we successfully reproduce the value of A_{20} as found in Baym and Pines (1971). This provides further confidence in the correctness of the value of A_{20} cited in the literature.

So far, our energy calculations have focused on the $l = 2$, $m = 0$ perturbation. In the next section, we extend our analysis to the case of $l = 2$, $m = 2$.

3.3 Calculation of B_{22}

In this section, we calculate the strain energy for the $l = 2, m = 2$ case to evaluate the corresponding constant B_{22}. We follow a method analogous to that used in the calculation of B_{20}. The expression for the strain energy is given by:

$$E_{\text{strain}} = B(\epsilon_{22} - \epsilon_{22,0})^2 = \int U_{\text{strain}}\, dV = \int \mu \Sigma_{ij}\Sigma^{ij}\, dV. \tag{3.109}$$

We begin by calculating the strain tensor Σ_{ij} using equation (3.3). In the axisymmetric perturbation ($l = 2, m = 0$), rotation acted as the physical deforming process, providing an exact expression for the displacement field in the strained star (Keer, 2014). However, for the non-axisymmetric case ($l = 2, m = 2$), no such physical process exists, so we must choose a one-parameter family of solutions $\vec{\xi}$ ourselves. We consider an incompressible elastic star with a uniform shear modulus and choose $\vec{\xi}$ in the form of Kelvin modes as defined in equation (3.67).

For $l = 2$ and $m = 2$, equation (3.67) becomes:

$$\vec{\xi_{22}} = \alpha_{22} \nabla (r^2 Y_{22}(\theta, \phi)), \tag{3.110}$$

where the spherical harmonic Y_{22} is given by:

$$Y_{22} = \frac{1}{4}\sqrt{\frac{15}{2\pi}} \sin^2\theta e^{i2\phi}. \tag{3.111}$$

The components of the displacement vector field are then:

$$\xi^r = \frac{1}{2}\sqrt{\frac{15}{2\pi}} \alpha_{22} r \sin^2\theta \cos(2\phi), \tag{3.112}$$

$$\xi^\theta = \frac{1}{2}\sqrt{\frac{15}{2\pi}} \alpha_{22} r \sin\theta \cos\theta \cos(2\phi), \tag{3.113}$$

$$\xi^\phi = -\frac{1}{2}\sqrt{\frac{15}{2\pi}} \alpha_{22} r \sin\theta \sin(2\phi). \tag{3.114}$$

Using this displacement field, we compute the components of the strain tensor Σ_{ij}. The relevant expressions in spherical coordinates are taken from Thorne and Blandford (2017), Box 11.4. Following the same procedure as in Section 3.1, we find the full strain tensor:

$$\Sigma_{ij} = \frac{1}{2}\sqrt{\frac{15}{2\pi}} \alpha_{22} \begin{bmatrix} \sin^2\theta\cos 2\phi & \sin\theta\cos\theta\cos 2\phi & -\sin\theta\sin 2\phi \\ \sin\theta\cos\theta\cos 2\phi & \cos^2\theta\cos 2\phi & -\cos\theta\sin 2\phi \\ -\sin\theta\sin 2\phi & -\cos\theta\sin 2\phi & -\cos 2\phi \end{bmatrix} \tag{3.115}$$

With the strain tensor known, we calculate the strain energy density U by inserting equation (3.115) into equation (3.23). After simplification, we obtain:

$$U_{\text{strain}} = \mu \alpha_{22}^2 \frac{15}{4\pi}. \tag{3.116}$$

Next, we integrate the strain energy density over the volume of the crust to obtain the total strain energy:

$$E_{\text{strain}} = 5(R^3 - R_c^3)\mu\alpha_{22}^2. \tag{3.117}$$

The final step is to calculate $\epsilon_{22} - \epsilon_{22,0}$ to evaluate B_{22}. This is defined by:

$$\epsilon_{22} - \epsilon_{22,0} = \frac{\Delta I_{xx} - \Delta I_{yy}}{I_{zz}}, \tag{3.118}$$

where ΔI_{xx} and ΔI_{yy} are the changes in the moments of inertia along the x and y axes, respectively, with respect to the relaxed zero-strain configuration. I_{zz} is the moment of inertia along the z-axis, given by equation (3.40).

We have:

$$\Delta I_{xx} = \int_V \rho\Delta(y^2 + z^2)\, dV, \tag{3.119}$$

$$\Delta I_{yy} = \int_V \rho\Delta(x^2 + z^2)\, dV. \tag{3.120}$$

Using the relation given in equation (3.35), we rewrite the above as:

$$\Delta I_{xx} = \int_V 2\rho(\xi_y y + \xi_z z)\, dV, \tag{3.121}$$

$$\Delta I_{yy} = \int_V 2\rho(\xi_x x + \xi_z z)\, dV. \tag{3.122}$$

We retain only the terms linear in ξ. To evaluate these integrals, we convert to spherical coordinates, using the relations from equations (**??**)–(**??**):

$$\xi_x = \xi_r \sin\theta\cos\phi + \xi_\theta \cos\theta\cos\phi - \xi_\phi \sin\phi, \tag{3.123}$$

$$\xi_y = \xi_r \sin\theta\sin\phi + \xi_\theta \cos\theta\sin\phi + \xi_\phi \cos\phi, \tag{3.124}$$

$$\xi_z = \xi_r \cos\theta - \xi_\theta \sin\theta. \tag{3.125}$$

Substituting equations (**??**), (**??**), (3.124), and (3.125) into equation (3.121) and integrating, we find:

$$\Delta I_{xx} = -\frac{4}{15}\sqrt{\frac{15}{2\pi}}\rho\alpha_{22}\pi R^5. \tag{3.126}$$

Similarly, inserting equations (**??**), (**??**), (3.123), and (3.125) into equation (3.122) and integrating yields:

$$\Delta I_{yy} = \frac{4}{15}\sqrt{\frac{15}{2\pi}}\rho\alpha_{22}\pi R^5. \tag{3.127}$$

Using equations (3.40), (3.126), and (3.127) in equation (3.118), we obtain:

$$\epsilon_{22} - \epsilon_{22,0} = -\alpha_{22}\sqrt{\frac{15}{2\pi}}. \tag{3.128}$$

Finally, substituting equations (3.117) and (3.128) into equation (3.109) gives:

$$B_{22} = \frac{1}{2}V_c\mu, \tag{3.129}$$

where V_c is the volume of the star's crust. This expression provides the value of the constant B_{22}. We note that its magnitude is approximately half to that of B_{20}, as is often assumed in the literature.

Comparing equations (3.43) and (3.129), we obtain the following relation between B_{20} and B_{22}:

$$B_{22} = \frac{25}{57}B_{20}. \tag{3.130}$$

We will make use of this result in subsequent sections.

3.4 Calculation of A_{22}

In this section, we calculate the perturbed gravitational potential energy for the perturbation mode $l = 2, m = 2$. During this analysis, we discovered a third method, introduced by Chandrasekhar in Chandrasekhar (1969), for computing the perturbed gravitational energy. We will elaborate on this later in the section. First, we evaluate δE_g using two established methods provided by Friedman and Schutz (1978), and Shapiro and Teukolsky (1983), as done previously.

3.4.1 Method 1: Friedman and Schutz

The authors in Friedman and Schutz (1978) derived the expression for perturbed gravitational energy to second order in perturbations (see Equation (B56) in their appendix). We once again employ the Kelvin mode displacement field $\vec{\xi}$ in this calculation. Since the domain of integration is infinite, both $\delta\Phi_{\text{int}}$ (for $0 \leq r \leq R$) and $\delta\Phi_{\text{ext}}$ (for $r > R$) must be considered. These potentials are given by Yim and Jones (2022) as:

$$\delta\Phi_{\text{int}} = -\frac{4\pi\rho G l}{2l+1}\alpha_{lm}\frac{r^l}{R^{l-2}}Y_{lm}(\theta,\phi), \tag{3.131}$$

$$\delta\Phi_{\text{ext}} = -\frac{4\pi\rho G l}{2l+1}\alpha_{lm}\frac{R^{l+3}}{r^{l+1}}Y_{lm}(\theta,\phi). \tag{3.132}$$

Using the Kelvin mode displacement field yields a negative value for the change in gravitational energy:

$$\delta E_g = -\frac{1}{8}\alpha_{22}^2\rho\omega_2^2R^5, \tag{3.133}$$

which appears physically inconsistent, as it implies that the spherical configuration does not correspond to the minimum gravitational potential energy.

In addition, the change in internal energy, δU, is found to be non-zero:

$$\delta U = \frac{5}{8}\alpha_{22}^2\rho\omega_2^2R^5. \tag{3.134}$$

Both of these results are obtained directly from equations (3.44) and (3.54). As we are considering an incompressible star, we expect $\delta U = 0$. The authors in Yim and Jones (2022) suggest that this discrepancy arises because the Kelvin mode solution is derived only to first order in $\vec{\xi}$.

To rectify this, we introduce a second-order radial correction to enforce incompressibility. The Lagrangian density perturbation (using Equation (3.65)) gives:

$$\frac{\Delta\rho}{\rho} = \frac{15}{8\pi}\alpha_{22}^2. \tag{3.135}$$

We compute the volume perturbation using the perturbed radii along the x, y, and z axes:

$$a_1 = R + \xi^r(r = R, \theta = \frac{\pi}{2}, \phi = 0) = R(1 + \alpha_{22}\frac{1}{2}\sqrt{\frac{15}{2\pi}}), \tag{3.136}$$

$$a_2 = R + \xi^r(r = R, \theta = \frac{\pi}{2}, \phi = \frac{\pi}{2}) = R(1 - \alpha_{22}\frac{1}{2}\sqrt{\frac{15}{2\pi}}), \tag{3.137}$$

$$a_3 = R + \xi^r(r = R, \theta = 0) = R, \tag{3.138}$$

The fractional volume change is then:

$$\frac{\Delta V}{V} = -\frac{15}{8\pi}\alpha_{22}^2. \tag{3.139}$$

We see once again that the decrease in the stellar volume is exactly compensated by the corresponding increase in the density, implying that the total mass of the star is conserved. The calculated density and volume perturbations indicate that the star is incompressible only to first order. To ensure incompressibility to second order, we introduce an additional radial second-order term in the displacement field, given by

$$\vec{\xi_{22}} = \alpha_{22}\nabla(r^2 Y_{22}(\theta, \phi)) + \frac{5r}{8\pi}\alpha_{22}^2\,\hat{e_r}. \tag{3.140}$$

This can be interpreted as the presence of a Y_{00} (spherically symmetric) perturbation in addition to the Y_{22} component, resulting in a uniform radial expansion of the star. The radii of the star along the x, y, and z axes then become:

$$a_1 = R(1 + \frac{5}{8\pi}\alpha_{22}^2)(1 + \alpha_{22}\frac{1}{2}\sqrt{\frac{15}{2\pi}}), \tag{3.141}$$

$$a_2 = R(1 + \frac{5}{8\pi}\alpha_{22}^2)(1 - \alpha_{22}\frac{1}{2}\sqrt{\frac{15}{2\pi}}), \tag{3.142}$$

$$a_3 = R(1 + \frac{5}{8\pi}\alpha_{22}^2). \tag{3.143}$$

This modification ensures second-order incompressibility. Using Equation (3.44), the perturbed gravitational energy becomes:

$$\delta E_g = \frac{3}{10\pi R}GM^2\alpha_{22}^2. \tag{3.144}$$

We thus obtain a positive value for the perturbed gravitational potential energy. To determine the constant A_{22}, we equate δE_g from equation (3.144) with the phenomenological expression for the perturbed gravitational energy, $\delta E_g = A_{22}\,\epsilon_{22}^2$. The equatorial

ellipticity ϵ_{22} is calculated using equation (1.1). Here, I_{zz} is given by equation (3.82), while I_{xx} and I_{yy} for a uniform-density ellipsoid are given by

$$I_{xx} = \frac{M}{5}(a_2^2 + a_3^2), \tag{3.145}$$

$$I_{yy} = \frac{M}{5}(a_1^2 + a_3^2), \tag{3.146}$$

we compute the moments of inertia using Equations (3.141)–(3.143):

$$I_{xx} = \frac{M}{5}R^2(1 + \frac{5}{8\pi}\alpha_{22}^2)^2[(1 - \alpha_{22}\frac{1}{2}\sqrt{\frac{15}{2\pi}})^2 + 1], \tag{3.147}$$

$$I_{yy} = \frac{M}{5}R^2(1 + \frac{5}{8\pi}\alpha_{22}^2)^2[(1 + \alpha_{22}\frac{1}{2}\sqrt{\frac{15}{2\pi}})^2 + 1], \tag{3.148}$$

$$I_{zz} = \frac{2M}{5}R^2(1 + \frac{5}{8\pi}\alpha_{22}^2)^2[1 + (\alpha_{22}\frac{1}{2}\sqrt{\frac{15}{2\pi}})^2]. \tag{3.149}$$

Inserting these into Equation (1.1) yields:

$$\epsilon_{22} = -\sqrt{\frac{15}{2\pi}}\alpha_{22}. \tag{3.150}$$

Then, using Equations (3.144) and (3.150) in $\delta E_g = A_{22}\epsilon_{22}^2$:

$$\frac{3}{10\pi R}GM^2\alpha_{22}^2 = A_{22}\epsilon_{22}^2, \tag{3.151}$$

we get:

$$A_{22} = \frac{GM^2}{25R}. \tag{3.152}$$

This yields the required value of the constant A_{22}. Taking the ratio of A_{20} (from Equation (3.108)) and A_{22} gives:

$$A_{22} = \frac{1}{3}A_{20}. \tag{3.153}$$

We will use this result in the subsequent analysis. In the following subsections, we derive A_{22} via two additional methods found in the literature.

3.4.2 Method 2: Maclaurin Spheroids

We used the Maclaurin spheroids method in Section (3.2.2). In the case of $l = 2, m = 0$ perturbation, the expression for the total gravitational potential energy was given by Equation (3.89). For the $l = 2, m = 2$ case, we will now calculate the total gravitational potential energy using the method described in Section 7.3 of Shapiro and Teukolsky (1983).

We begin by solving Poisson's equation:

$$\nabla^2\Phi = 4\pi G\rho, \tag{3.154}$$

where ρ is the matter density of the star and Φ is the gravitational potential. We solve Equation (3.154) using Green's function,

$$\Phi = -G\rho \int \frac{d^3x'}{|x - x'|}. \tag{3.155}$$

In spherical coordinates, the expression $\frac{1}{|x-x'|}$ can be expanded in terms of spherical harmonics Y_l^m as follows:

$$\frac{1}{|x - x'|} = 4\pi \sum_{l=0}^{\infty} \frac{1}{2l+1} \frac{r_<^l}{r_>^{l+1}} \sum_{m=-l}^{l} Y_l^m(\theta, \phi) Y_l^m(\theta', \phi'), \tag{3.156}$$

where $r_<$ is the lesser of r and r', and $r_>$ is the greater. Substituting Equation (3.156) into Equation (3.155) gives

$$\Phi = -G\rho \int_V 4\pi \sum_{l=0}^{\infty} \frac{1}{2l+1} \frac{r_<^l}{r_>^{l+1}} \sum_{m=-l}^{l} Y_l^m(\theta, \phi) Y_l^m(\theta', \phi') d^3V, \tag{3.157}$$

which can be written as

$$\Phi = -G\rho 4\pi \int_0^{2\pi} \int_0^{\pi} \sum_{l=0}^{\infty} \frac{1}{2l+1} \left(\int_0^r \frac{(r')^{l+2} dr'}{r^{l+1}} + \int_r^{R'} \frac{r^l dr'}{(r')^{l-1}} \right) \sum_{m=-l}^{l} Y_l^m(\theta, \phi) Y_l^m(\theta', \phi') \sin\theta' d\theta' d\phi'. \tag{3.158}$$

The domain of integration is the volume of the triaxial ellipsoid. The polar equation of the ellipsoid's surface is given by

$$\frac{\cos^2\phi \sin^2\theta}{a_1^2} + \frac{\sin^2\phi \sin^2\theta}{a_2^2} + \frac{\cos^2\theta}{a_3^2} = \frac{1}{R'^2}, \tag{3.159}$$

where a_1, a_2, and a_3 are the radii along the x, y, and z axes respectively:

$$a_1 = R\left(1 + \frac{\epsilon_{22}}{2}\right), \qquad a_2 = R\left(1 + \frac{\epsilon_{22}^2}{4}\right), \qquad a_3 = R\left(1 - \frac{\epsilon_{22}}{2}\right). \tag{3.160}$$

Here, ϵ_{22} is a small, dimensionless parameter that describes deviations from spherical symmetry. One can show that ϵ_{22} corresponds to the equatorial ellipticity of the star by calculating the moments of inertia I_{xx}, I_{yy}, and I_{zz} using a_1, a_2, and a_3, and then substituting these into the definition of the equatorial ellipticity given in Equation (1.1). The incompressibility assumption requires that the volume of the triaxial ellipsoid matches that of a spherical star, but this condition needs to be enforced only up to second order in ϵ, which suffices for calculating the leading-order change in gravitational potential energy E_{grav}.

We start by computing the $l = 0, m = 0$ contribution to the potential in Equation (3.158):

$$\Phi_{00} = -G\rho 4\pi \int_0^{2\pi} \int_0^{\pi} \left(\int_0^r \frac{(r')^2 dr'}{r} + \int_r^{R'} r' dr' \right) Y_0^0(\theta, \phi) Y_0^0(\theta', \phi') \sin\theta' d\theta' d\phi', \tag{3.161}$$

where

$$Y_0^0 = \frac{1}{2}\sqrt{\frac{1}{\pi}}. \tag{3.162}$$

After integrating over the radial coordinate, we obtain

$$\Phi_{00} = 2\pi G\rho \frac{r^2}{3} - G\rho \int_0^{2\pi} \int_0^{\pi} \frac{R'^2}{2} \sin\theta' d\theta' d\phi'. \tag{3.163}$$

To evaluate the integral over the polar angle θ', we use Equation (3.159) to express the angular dependence of R'. This gives:

$$\Phi_{00} = 2\pi G\rho \frac{r^2}{3} - \frac{G\rho}{2} \int_0^{2\pi} \int_0^{\pi} \frac{\sin\theta'}{\frac{\cos^2\phi' \sin^2\theta'}{a_1^2} + \frac{\sin^2\phi' \sin^2\theta'}{a_2^2} + \frac{\cos^2\theta'}{a_3^2}} d\theta' d\phi'. \tag{3.164}$$

Define the following:

$$A(\phi') = \frac{\cos^2\phi'}{a_1^2} + \frac{\sin^2\phi'}{a_2^2}, \qquad B(\phi') = \frac{1}{a_3^2} - \frac{\cos^2\phi'}{a_1^2} - \frac{\sin^2\phi'}{a_2^2}. \tag{3.165}$$

Then Equation (3.164) becomes:

$$\Phi_{00} = 2\pi G\rho \frac{r^2}{3} - \frac{G\rho}{2} \int_0^{2\pi} \int_0^{\pi} \frac{\sin\theta'}{A(\phi') + B(\phi')\cos^2\theta'} d\theta' d\phi'. \tag{3.166}$$

Now let

$$x = \cos\theta' \quad \Rightarrow \quad dx = -\sin\theta' d\theta', \tag{3.167}$$

which implies that

$$\Phi_{00} = 2\pi G\rho \frac{r^2}{3} - G\rho \int_0^{2\pi} \int_0^{1} \frac{dx}{A(\phi') + B(\phi')x^2} d\phi'. \tag{3.168}$$

Carrying out the integral with respect to x, we get

$$\Phi_{00} = 2\pi G\rho\frac{r^2}{3} - G\rho\int_0^{2\pi}\frac{\arctan\left(\sqrt{\frac{B(\phi')}{A(\phi')}}\right)}{A(\phi')\sqrt{\frac{B(\phi')}{A(\phi')}}}d\phi'. \tag{3.169}$$

Inserting (3.160) into the expressions for A and B and linearising, we obtain:

$$\frac{B(\phi')}{A(\phi')} = (\cos^2\phi' + 1)\epsilon_{22} + (4\cos^4\phi' - \cos^2\phi' + 5)\left(\frac{\epsilon_{22}}{2}\right)^2 + \mathcal{O}(\epsilon^3) \tag{3.170}$$

$$\frac{1}{A(\phi')} = R^2\left(1 + 2\cos^2\phi'\frac{\epsilon_{22}}{2} + (4\cos^4\phi' - 5\cos^2\phi' + 2)\left(\frac{\epsilon_{22}}{2}\right)^2 + \mathcal{O}(\epsilon^3)\right) \tag{3.171}$$

Since $\frac{B(\phi')}{A(\phi')}$ is proportional to ϵ, we can use the series expansion $\frac{\tan^{-1}x}{x} = 1 - \frac{1}{3}x^2 + \frac{1}{5}x^4$ in the expression for Φ_{00} given in (3.169). After linearising equation (3.169), we obtain:

$$\Phi_{00} = 2\pi G\rho\frac{r^2}{3} - G\rho R^2\int_0^{2\pi}\frac{1}{A(\phi')}\left(1 - \frac{1}{3}\frac{B(\phi')}{A(\phi')} + \frac{1}{5}\frac{B(\phi')^2}{A(\phi')^2}\right)d\phi'. \tag{3.172}$$

Inserting (3.170) and (3.171) into (3.172) and integrating over the azimuthal angle ϕ', we find:

$$\Phi_{00} = \frac{2}{3}\pi G\rho[r^2 - 3R^2] + R^2G\rho\frac{8\pi}{15}\epsilon^2. \tag{3.173}$$

We have thus obtained the expression for the gravitational potential for the $l = 0, m = 0$ perturbation. Next, we compute the corresponding gravitational potential energy $E_{g,00}$ using the formula:

$$E_{g,00} = \frac{\rho}{2}\int_V \Phi_{00}\, d^3x. \tag{3.174}$$

Substituting (3.173) into (3.174) yields:

$$E_{g,00} = \frac{\rho}{2}\int_0^{2\pi}\int_0^{\pi}\int_0^{R'}\left(\frac{2}{3}\pi G\rho r^2 - 2\pi G\rho R^2 + R^2G\rho\frac{8\pi}{15}\epsilon^2\right)r^2\sin\theta dr d\theta d\phi. \tag{3.175}$$

Since the second and third terms in (3.175) are constants, their volume integrals yield factors of $\frac{M}{2}$, giving:

$$E_{g,00} = \frac{\rho}{2}\int_0^{2\pi}\int_0^{\pi}\int_0^{R'}\frac{2}{3}\pi G\rho r^4\sin\theta dr d\theta d\phi - \frac{3GM^2}{4R} + \frac{GM^2}{5R}\epsilon^2. \tag{3.176}$$

We integrate the first term with respect to r:

$$E_{g,00} = \frac{\rho^2\pi G}{15}\int_0^{2\pi}\int_0^{\pi}R'^5\sin\theta d\theta d\phi - \frac{3GM^2}{4R} + \frac{GM^2}{5R}\epsilon^2 \tag{3.177}$$

Using the angular dependence of R' from equation (3.159), we integrate over θ to obtain:

$$E_{g,00} = \frac{\rho^2\pi G}{15}\int_0^{2\pi}\int_0^{\pi}\frac{\sin\theta}{\left(\frac{\cos^2\phi\sin^2\theta}{a_1^2}+\frac{\sin^2\phi\sin^2\theta}{a_2^2}+\frac{\cos^2\theta}{a_3^2}\right)^{\frac{5}{2}}}d\theta d\phi - \frac{3GM^2}{4R}+\frac{GM^2\epsilon^2}{5R}. \tag{3.178}$$

We simplify the integral in (3.178) using (3.165) and the substitution (3.167):

$$E_{g,00} = \frac{2\rho^2\pi G}{15}\int_0^{2\pi}\int_0^{1}\frac{1}{(A(\phi')+B(\phi')x^2)^{\frac{5}{2}}}dxd\phi - \frac{3GM^2}{4R}+\frac{GM^2\epsilon^2}{5R}. \tag{3.179}$$

Integrating with respect to x yields:

$$E_{g,00} = \frac{2\rho^2\pi G}{15}\int_0^{2\pi}\frac{2B(\phi')+3A(\phi')}{3A(\phi')^2(A(\phi')+B(\phi'))^{3/2}}d\phi - \frac{3GM^2}{4R}+\frac{GM^2\epsilon^2}{5R}. \tag{3.180}$$

Substituting the expressions for $A(\phi')$ and $B(\phi')$ into (3.180) and simplifying, we obtain:

$$E_{g,00} = \frac{2\rho^2\pi G}{45}\int_0^{2\pi}\frac{a_1^2a_2^2a_3(2a_1^2a_2^2+a_3^2a_1^2+(a_3^2a_2^2-a_3^2a_1^2)\cos^2\phi)}{(a_1^2+(a_2^2-a_1^2)\cos^2\phi)^2}d\phi - \frac{3GM^2}{4R}+\frac{GM^2\epsilon^2}{5R}. \tag{3.181}$$

Inserting the expressions for a_1, a_2, and a_3 and linearising (3.181), we get:

$$E_{g,00} = \frac{2\rho^2\pi GR^5}{45}\int_0^{2\pi}\left(3+5(2\cos^2\phi-1)\epsilon+(28\cos^4\phi-39\cos^2\phi+13)\epsilon^2\right)d\phi - \frac{3GM^2}{4R}+\frac{GM^2\epsilon^2}{5R}. \tag{3.182}$$

Integrating over the azimuthal angle ϕ gives:

$$E_{g,00} = -\frac{3GM^2}{5R}+\frac{GM^2}{10R}\epsilon_{22}^2. \tag{3.183}$$

We have now determined the gravitational potential energy for the $l=0$, $m=0$ case. Similarly, the potential energies for other $l=2$ modes are:

$$E_{g,20} = -\frac{9GM^2}{200R}\epsilon_{22}^2, \tag{3.184}$$

$$E_{g,21} = 0, \tag{3.185}$$

$$E_{g,22} = -\frac{3GM^2\epsilon_{22}^2}{400R}. \tag{3.186}$$

Adding the contributions from all the gravitational potential energy terms:

$$E_{g,\text{total}} = E_{g,00} + E_{g,20} + 2E_{g,21} + 2E_{g,22}, \tag{3.187}$$

$$E_{g,\text{total}} = -\frac{3GM^2}{5R} + \frac{GM^2\epsilon_{22}^2}{25R}. \tag{3.188}$$

Defining the leading order and perturbed gravitational energies as:

$$E_0 = -\frac{3GM^2}{5R}, \qquad \Delta E_g = \frac{GM^2}{25R}\epsilon_{22}^2, \tag{3.189}$$

we can write:

$$\Delta E_g = \frac{GM^2}{25R}\epsilon_{22}^2 = A_{22}\epsilon_{22}^2, \tag{3.190}$$

$$A_{22} = \frac{GM^2}{25R}. \tag{3.191}$$

This yields the value of the constant A_{22}, which matches the result previously obtained using the Friedman and Schutz method.

3.4.3 Method 3: Chandrasekhar's Method

In this section, we calculate the perturbed gravitational potential energy using the formalism given in Chandrasekhar (1969). This method provides a way to compute the gravitational potential energy of a triaxial ellipsoid through the potential energy tensor E_{ij}, given by (equation 128 in Chandrasekhar (1969)):

$$E_{ij} = -2\pi G\rho\, A_{(i)}\, Q_{ij}, \tag{3.192}$$

where $A_{(i)}$ $(i = 1, 2, 3)$ are dimensionless coefficients associated with the principal axes. Here, the subscript (i) is a label corresponding to the i-th direction and is not a tensor index.

We have

$$Q_{ij} = \frac{1}{5}Ma_{(i)}^2\delta_{ij}, \qquad M = \frac{4}{3}\pi a_1 a_2 a_3 \rho, \tag{3.193}$$

where Q_{ij} is the quadrupole moment tensor and a_1, a_2, a_3 are the radii along the x, y, and z axes, respectively. The total potential energy E_g is obtained by contracting the indices ij as follows:

$$E_g = -\frac{2\pi G\rho M}{5}[A_1a_1^2 + A_2a_2^2 + A_3a_3^2]. \tag{3.194}$$

The coefficients A_1, A_2, and A_3 are defined as:

$$A_1 = \frac{2a_2a_3}{a_1^2 \sin^3\phi \sin^2\theta}[F(\theta,\phi) - E(\theta,\phi)], \tag{3.195}$$

$$A_2 = \frac{2a_2a_3}{a_1^2 \sin^3\phi \sin^2\theta \cos^2\theta}[E(\theta,\phi) - F(\theta,\phi)\cos^2\theta - \frac{a_3}{a_2}\sin^2\theta \sin\phi], \tag{3.196}$$

$$A_3 = \frac{2a_2a_3}{a_1^2 \sin^3\phi \cos^2\theta}\left[\frac{a_2}{a_3}\sin\phi - E(\theta,\phi)\right], \tag{3.197}$$

where the elliptic integrals $E(\theta,\phi)$ and $F(\theta,\phi)$ are given by:

$$E(\theta,\phi) = \int_0^\phi (1 - \sin^2\theta \sin^2\Phi)^{\frac{1}{2}} d\Phi, \tag{3.198}$$

$$F(\theta,\phi) = \int_0^\phi (1 - \sin^2\theta \sin^2\Phi)^{-\frac{1}{2}} d\Phi. \tag{3.199}$$

These are the standard incomplete elliptic integrals. Additionally, the geometrical relations are:

$$\sin\theta = \left(\frac{a_1^2 - a_2^2}{a_1^2 - a_3^2}\right)^{\frac{1}{2}}, \qquad \cos\phi = \frac{a_3}{a_1}. \tag{3.200}$$

The expressions (3.195–3.200) correspond to equations (31–35) in Chandrasekhar (1969). It is noted therein that these formulas are valid under the condition $a_1 > a_2 > a_3$. The quantities a_1, a_2, and a_3 are given in equation (3.160).

In our case, we consider a triaxial star whose volume is conserved up to second order. This assumption is necessary because we are interested in evaluating the second-order perturbation in the gravitational potential energy. Under these conditions, we have

$$\sin\theta = \sqrt{\frac{2 - \frac{\epsilon_{22}}{2} - \left(\frac{\epsilon_{22}}{2}\right)^3}{4}}. \tag{3.201}$$

$$\cos\theta = \sqrt{\frac{2 + \frac{\epsilon_{22}}{2} + \left(\frac{\epsilon_{22}}{2}\right)^3}{4}}, \tag{3.202}$$

$$\sin\phi = \frac{2\sqrt{\frac{\epsilon_{22}}{2}}}{1 + \frac{\epsilon_{22}}{2}}, \tag{3.203}$$

$$\cos\phi = \frac{1 - \frac{\epsilon_{22}}{2}}{1 + \frac{\epsilon_{22}}{2}}. \tag{3.204}$$

Since $\sin\phi$ is small, we can expand equations (3.203) and (3.204) using the following series expansions:

$$(1-x)^{1/2} = 1 - \frac{x}{2} - \frac{x^2}{8} - \frac{x^3}{16} + ..., \tag{3.205}$$

$$(1-x)^{-1/2} = 1 + \frac{x}{2} + \frac{3x^2}{8} + \frac{5x^3}{16} + ... \tag{3.206}$$

Using these, the expressions for $E(\theta,\phi)$ and $F(\theta,\phi)$ become:

$$E(\theta,\phi) \approx \int_0^{\phi} \left(1 - \frac{\sin^2\theta\sin^2\Phi}{2} - \frac{\sin^4\theta\sin^4\Phi}{8} - \frac{\sin^6\theta\sin^6\Phi}{16}\right) d\Phi, \tag{3.207}$$

$$F(\theta,\phi) \approx \int_0^{\phi} \left(1 + \frac{\sin^2\theta\sin^2\Phi}{2} + \frac{3\sin^4\theta\sin^4\Phi}{8} + \frac{5\sin^6\theta\sin^6\Phi}{16}\right) d\Phi. \tag{3.208}$$

Integrating and simplifying equations (3.207) and (3.208), we obtain:

$$\begin{aligned} E(\theta,\phi) = \phi - \frac{\sin^2\theta}{4}(\phi - \sin\phi\cos\phi) - \frac{\sin^4\theta}{64}(3\phi - 2\sin^3\phi\cos\phi - 3\sin\phi\cos\phi) \\ - \frac{\sin^6\theta}{768}(15\phi - 15\sin\phi\cos\phi - 2\sin^3\phi\cos\phi(5 + 4\sin^2\phi)), \end{aligned} \tag{3.209}$$

$$\begin{aligned} F(\theta,\phi) = \phi + \frac{\sin^2\theta}{4}(\phi - \sin\phi\cos\phi) + \frac{3\sin^4\theta}{64}(3\phi - 2\sin^3\phi\cos\phi - 3\sin\phi\cos\phi) \\ + \frac{5\sin^6\theta}{768}(15\phi - 15\sin\phi\cos\phi - 2\sin^3\phi\cos\phi(5 + 4\sin^2\phi)). \end{aligned} \tag{3.210}$$

For negative integer n, the binomial expansion gives

$$(1+x)^{-n} = \sum_{k=0}^{\infty} (-1)^k \binom{n+k-1}{k} x^k, \tag{3.211}$$

valid for $|x| < 1$. This will be useful later in this section for calculating A_1, A_2, and A_3.

We now compute the expressions for A_1, A_2, and A_3. Substituting equations (3.209) and (3.210) into the expression for A_1 and simplifying, we obtain:

$$A_1 = \frac{a_2 a_3}{a_1^2 \sin^3\phi}\left[1 + \frac{3\sin^2\theta}{8} + \frac{15\sin^4\theta}{64}\right]\phi - \frac{a_2 a_3 \cos\phi}{a_1^2 \sin^2\phi}\left[1 + \frac{\sin^2\theta}{8}(2\sin^2\phi + 3) + \frac{\sin^4\theta}{64}(15 + 2\sin^2\phi(5 + 4\sin^2\phi))\right]. \quad (3.212)$$

We recall:

$$\sin\phi = \frac{2\sqrt{\frac{\epsilon_{22}}{2}}}{1 + \frac{\epsilon_{22}}{2}}, \quad (3.213)$$

and thus,

$$\phi = \sin^{-1}\left(\frac{2\sqrt{\frac{\epsilon_{22}}{2}}}{1 + \frac{\epsilon_{22}}{2}}\right). \quad (3.214)$$

We expand equation (3.214) using the Taylor series:

$$\sin^{-1}(x) = x + \frac{x^3}{6} + \frac{3x^5}{40} + \frac{5x^7}{112} + ... \quad (3.215)$$

Substituting, we obtain:

$$\phi = \sin^{-1}\left(\frac{2\sqrt{\frac{\epsilon_{22}}{2}}}{1 + \frac{\epsilon_{22}}{2}}\right) = \frac{2\sqrt{\frac{\epsilon_{22}}{2}}}{1 + \frac{\epsilon_{22}}{2}} + \frac{4}{3}\left(\frac{\left(\frac{\epsilon_{22}}{2}\right)\sqrt{\frac{\epsilon_{22}}{2}}}{\left(1 + \frac{\epsilon_{22}}{2}\right)^3}\right) + \frac{12}{5}\left(\frac{\left(\frac{\epsilon_{22}}{2}\right)^2\sqrt{\frac{\epsilon_{22}}{2}}}{\left(1 + \frac{\epsilon_{22}}{2}\right)^5}\right) + \frac{40}{7}\left(\frac{\left(\frac{\epsilon_{22}}{2}\right)^3\sqrt{\frac{\epsilon_{22}}{2}}}{\left(1 + \frac{\epsilon_{22}}{2}\right)^7}\right). \quad (3.216)$$

Substituting equations (3.201)–(3.204) and (3.216) into equation (3.212), and linearising using series expansion (3.211), we obtain:

$$A_1 = \frac{2}{3} - \frac{2}{5}\epsilon_{22} + \frac{9}{70}\epsilon_{22}^2. \quad (3.217)$$

Similarly, we find:

$$A_2 = \frac{2}{3} - \frac{9\epsilon_{22}^2}{35}, \tag{3.218}$$

$$A_3 = \frac{2}{3} + \frac{2\epsilon_{22}}{5} + \frac{9\epsilon_{22}^2}{70}. \tag{3.219}$$

According to Lemma 4 (Chapter 3, Equation 24) in Chandrasekhar (1969), the sum of A_1, A_2, and A_3 should equal 2. The values of A_i we calculated indeed satisfy this condition,

$$A_1 + A_2 + A_3 = 2. \tag{3.220}$$

We now have the values of the constants A_1, A_2, and A_3. Substituting equations (3.160), (3.217), (3.218), and (3.219) into the expression for the gravitational potential energy in equation (3.194), we obtain:

$$E_g = -\frac{3GM^2}{5R} + \frac{4GM^2\epsilon_{22}^2}{25R}, \qquad [\rho = \frac{3M}{4\pi a^3}], \tag{3.221}$$

$$E_0 = -\frac{3GM^2}{5R}, \qquad \Delta E_g = \frac{4GM^2\epsilon_{22}^2}{25R}. \tag{3.222}$$

Here, E_0 is the leading-order gravitational potential energy, and ΔE_g is the perturbation in gravitational potential energy. To calculate A_{22}, we equate ΔE_g with $A_{22}\epsilon_{22}^2$:

$$\Delta E_g = \frac{GM^2\epsilon_{22}^2}{25R} = A_{22}\epsilon_{22}^2, \tag{3.223}$$

$$A_{22} = \frac{GM^2}{25R}. \tag{3.224}$$

We thus arrive at the same value of the constant A_{22} using three different methodologies. This consistency lends confidence to the derived value of A_{22}.

3.5 Are There Cross Terms?

In a realistic neutron star (NS), there are both axisymmetric strains, arising from spin-up/spin-down, and non-axisymmetric ones, associated with the presence of a mountain. Therefore, we need to model both $(l = 2, m = 0)$ and $(l = 2, m = 2)$ deformations *simultaneously*.

The expression for the energy of such a star will naturally include the separate contributions given by equations (2.11) and (2.16). However, one may ask whether there are also cross terms, i.e., terms proportional to the product of the small parameters describing each type of perturbation. In this section, we show that such cross terms do not arise.

The total energy of the spinning star can be written as:

$$E_{\text{total}} = E_{\text{grav,s}} + \frac{L^2}{2I} + B_{20}(\epsilon_{20} - \epsilon_{20,0})^2 + A_{20}\epsilon_{20}^2 + B_{22}(\epsilon_{22} - \epsilon_{22,0})^2 + A_{22}\epsilon_{22}^2 + B_{20,22}(\epsilon_{20} - \epsilon_{20,0})(\epsilon_{22} - \epsilon_{22,0}) + A_{20,22}\epsilon_{20}\epsilon_{22}, \quad (3.225)$$

where ϵ_{20} and ϵ_{22} represent the equilibrium oblateness and equatorial ellipticity, respectively, as discussed in previous sections. The parameters $\epsilon_{20,0}$ and $\epsilon_{22,0}$ denote the zero-strain configurations, which are mapped from the background spherical configuration using the Kelvin mode displacement field $\vec{\xi}$.

Note that we have included potential cross terms in both the gravitational potential energy (via $A_{20,22}$) and the elastic energy (via $B_{20,22}$).

When both perturbations $l = 2, m = 0$ and $l = 2, m = 2$ are present, the total displacement field is a linear combination of the individual displacement fields:

$$\vec{\xi} = \alpha_{20}\vec{\xi_{20}} + \alpha_{22}\vec{\xi_{22}}. \quad (3.226)$$

Using equation (3.3), the strain tensor becomes:

$$\Sigma_{ij} = \alpha_{20}\Sigma_{ij}^{20} + \alpha_{22}\Sigma_{ij}^{22}. \quad (3.227)$$

3.5.1 Check for $B_{20,22}$

The methodology here mirrors that used for calculating B_{20} in Section 3.1. We write the strain energy in the presence of both perturbations as

$$E_{\text{strain}} = \mu \int \left[\Sigma_{ij}^{20}\Sigma^{20\,ij} + \Sigma_{ij}^{22}\Sigma^{22\,ij} + \Sigma_{ij}^{20}\Sigma^{22\,ij} + \Sigma_{ij}^{22}\Sigma^{20\,ij}\right] dV, \quad (3.228)$$

where Σ_{ij}^{20} and Σ_{ij}^{22} are the strain tensors corresponding to the $l = 2, m = 0$ and $l = 2, m = 2$ perturbations, respectively. Due to the orthogonality of the spherical harmonics Y_{20} and Y_{22} on the 2-sphere, the cross-terms $\Sigma_{ij}^{20}\Sigma^{22\,ij}$ integrate to zero. Hence,

the total strain energy separates neatly as

$$E_{\text{strain}} = E^{20}_{\text{strain}} + E^{22}_{\text{strain}}. \tag{3.229}$$

This shows that $B_{20,22} = 0$.

3.5.2 Check for $A_{20,22}$

Similarly, the perturbed gravitational energy in the presence of both $l = 2, m = 0$ and $l = 2, m = 2$ deformations can be written formally in terms of the corresponding displacement fields:

$$E_{\text{g}} = E^{20}_{\text{g}} + E^{22}_{\text{g}} + \text{cross-terms}. \tag{3.230}$$

By the same orthogonality argument, the cross-terms vanish upon integration over the sphere, leaving

$$E_{\text{g}} = E^{20}_{\text{g}} + E^{22}_{\text{g}}. \tag{3.231}$$

Thus, we find $A_{20,22} = 0$. Owing to the orthogonality of the spherical harmonics Y_{20} and Y_{22} on the 2-sphere, there are no cross-terms proportional to $B_{20/22}$ or $A_{20/22}$ in the total energy when both perturbations are present simultaneously.

3.6 Ellipticity at Equilibrium

Given the absence of cross terms in the star's total energy, equation (3.227) reduces to the sum of the separate contributions:

$$E_{\text{T}} = E_{\text{grav,s}} + \frac{L^2}{2I_{zz}} + B_{20}(\epsilon_{20} - \epsilon_{20,0})^2 + A_{20}(\epsilon_{20})^2 + B_{22}(\epsilon_{22} - \epsilon_{22,0})^2 + A_{22}(\epsilon_{22})^2, \tag{3.232}$$

The $l = 2, m = 2$ perturbations do not contribute to the kinetic energy since $\delta I^{22}_{zz} = 0$ (see Section 8.5.1 of Yim (2022)).

It follows that the axisymmetric ($m = 0$) and non-axisymmetric ($m = 2$) deformations behave independently and can be analysed separately. Minimising E_{T} with respect to ϵ_{20}, while keeping L, $\epsilon_{20,0}$, ϵ_{22}, and $\epsilon_{22,0}$ fixed, reproduces equation (2.12). Similarly, minimising with respect to ϵ_{22} yields equation (2.17).

From equations (3.130) and (3.153), we find that $B_{20} \ll A_{20}$ and $B_{22} \ll A_{22}$. Using these relations, we obtain:

$$\frac{B_{22}}{A_{22}} = \frac{25}{19}\frac{B_{20}}{A_{20}}. \tag{3.233}$$

This ratio determines the actual deformation (ϵ_{20} or ϵ_{22}) that results from a given zero-strain reference shape ($\epsilon_{20,0}$ or $\epsilon_{22,0}$). For both deformation modes, elasticity plays a minor role compared to gravity, making the actual deformation small. The numerical factor in equation (3.233) is specific to our simple stellar model, but the general trend $B_{22}/A_{22} \sim B_{20}/A_{20}$ is expected to hold in more realistic cases.

Using representative values, we find:

$$A_{22} = \frac{1}{25R}GM^2 = 2.091 \times 10^{52}\mathrm{erg}\frac{\mathrm{M}_{1.4}^2}{\mathrm{R}_6}. \tag{3.234}$$

Expressing B_{22} in terms of ΔR, we obtain:

$$B_{22} = \frac{1}{2}\mu V_c = 2\pi\mu R^2\Delta R = 0.628 \times 10^{48}\mu_{30}R_6^2\Delta R_5 \text{ erg}. \tag{3.235}$$

The equilibrium mountain size is given by:

$$\epsilon_{22} = b_{22}\epsilon_{22,0}, \tag{3.236}$$

where

$$b_{22} = \frac{B_{22}}{A_{22}+B_{22}} \approx \frac{B_{22}}{A_{22}} = \frac{50\pi\mu R^3\Delta R}{M^2G} \approx 3.005 \times 10^{-5}\frac{\mu_{30}R_6^3\Delta R_5}{M_{1.4}^2}. \tag{3.237}$$

Substituting equation (3.237) into equation (3.236), we find:

$$\epsilon_{22} \approx 3.005 \times 10^{-5}\epsilon_{22,0}\frac{\mu_{30}R_6^3\Delta R_5}{M_{1.4}^2}. \tag{3.238}$$

This result quantifies the fact that the equilibrium ellipticity is significantly smaller than the relaxed (zero-strain) ellipticity of the star.

In this chapter, we derived the expressions for the constants B_{20} and A_{20}, which are associated with the strain energy and gravitational potential energy of the star under the starquake model for axisymmetric shape deformations. Although these expressions are known in the literature, their derivation's are not explicitly provided. We therefore carried out the full derivation to independently verify their validity. We then proceeded to

derive the expressions for the constants B_{22} and A_{22}, corresponding to the strain energy and gravitational potential energy associated with non-axisymmetric deformations.

Subsequently, we considered the scenario in which both $l = 2, m = 0$ and $l = 2, m = 2$ perturbations are present simultaneously. We found that the total energy expression contains no cross terms proportional to mixed coefficients such as $A_{20,22}$ or $B_{20,22}$. Finally, we established a relation between the equilibrium shape and the relaxed zero-strain shape of the star within the starquake framework.

All results obtained in this chapter will be applied in the following chapter, where we construct a simple model of a spinning-up neutron star undergoing a starquake, and estimate the maximum possible mountain that can be formed.

Chapter 4

Energy Changes During Starquake

In this chapter, we apply our starquake model to a specific scenario, similar to those considered by Fattoyev et al. (2018) and Giliberti and Cambiotti (2022), and illustrated schematically in Figure 4.1.

We begin with a non-rotating, spherically symmetric, and elastically relaxed star, denoted by S. The star is then spun up to a pre-quake equilibrium configuration, denoted by E. This spin-up process is modelled as a perturbation. At equilibrium E, the crust fractures, and the star transitions to a new equilibrium configuration Q. The relaxed (zero-strain) configuration associated with Q is denoted by Q_0.

To build physical intuition, we begin in Section 4.1 by considering fractures described purely by $m = 0$ perturbations. In Section 4.2, we turn to fractures described purely by $m = 2$ perturbations. Finally, in Section 4.3, we consider the most realistic scenario, where both $m = 0$ and $m = 2$ perturbations are present simultaneously.

A crucial part of our modelling involves the enforcement of both angular momentum and energy conservation. Angular momentum conservation is imposed by requiring that the angular momentum of star Q is equal to that of star E. Energy conservation is imposed by requiring that the total energy of star Q is less than or equal to that of star E. This condition accounts for the fact that a realistic fracture will generate internal heat and emit gravitational waves—both of which are not explicitly included in our energy budget. It is important to note that if the starquake is axisymmetric, the associated gravitational wave emission does not carry angular momentum (see, e.g., Yim and Jones (2022)).

In our analysis, we treat star E as a fixed initial configuration. This leaves us with a two-parameter family of possible starquakes, corresponding to perturbations in the $m = 0$ and $m = 2$ modes. We take as our free parameters the changes in the relaxed shapes, $\Delta\epsilon_{20,0}$ and $\Delta\epsilon_{22,0}$. Our goal is to identify the allowed region in this parameter space for

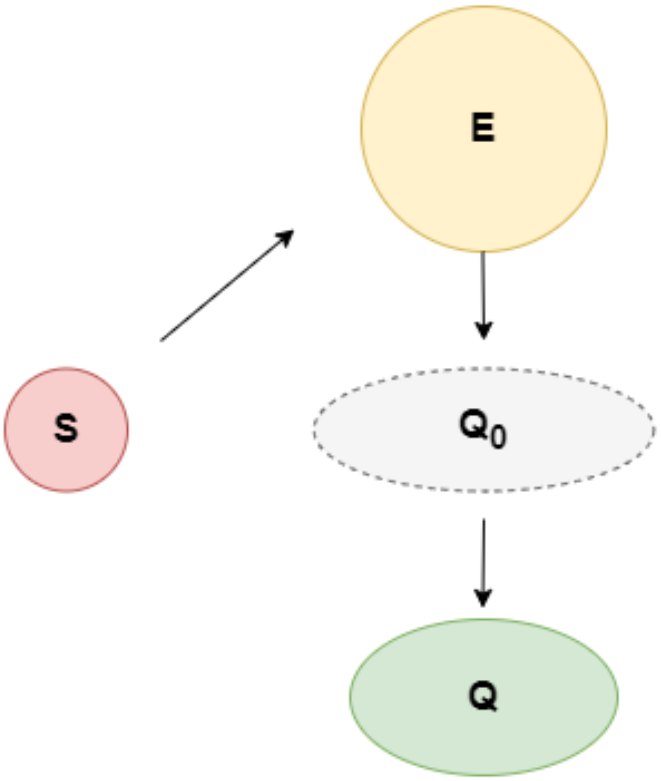

FIGURE 4.1: Schematic illustration of the proposed starquake model. The figure shows the stellar configurations in the x-y plane, with the rotation axis aligned along the z-axis. Star S (red) is the initial, non-rotating, elastically relaxed spherical star. It spins up to configuration E (yellow). At this point, the crust fractures and the star assumes a new equilibrium configuration Q (green). The relaxed configuration corresponding to Q is denoted by Q_0 (grey).

which starquakes are energetically and dynamically consistent, and to determine the maximum size of the resulting mountain.

4.1 Perturbation $l = 2, m = 0$

The expression for the total energy of star E, in the case of a pure $m = 0$ perturbation, is given by equation (2.11). To determine the shape of star E, we minimise this energy as described previously, keeping both the angular momentum L and the reference shape $\epsilon_{20,0}$ fixed. This leads to the standard relation (2.12) between the equilibrium shape and the elastically relaxed shape.

However, in this case, we have $\epsilon_{20,0} = 0$, since star E is obtained by spinning up the initially spherical and relaxed star S. Equation (2.12) therefore reduces to

$$\epsilon_{20} = \frac{I_{zz,s}\Omega^2}{4(A_{20} + B_{20})}. \tag{4.1}$$

When the crust fractures, the axisymmetric perturbation ϵ_{20} changes relative to the star in configuration E. The moment of inertia and angular velocity of star E transform as $I \to I + \Delta I$ and $\Omega \to \Omega + \Delta\Omega$, respectively. Over the short timescale of the quake, we assume conservation of angular momentum and neglect energy losses due to internal dissipation and gravitational-wave emission. Under these assumptions,

$$L = (I + \Delta I)(\Omega + \Delta\Omega) = I\Omega. \tag{4.2}$$

Rearranging equation (4.2) yields

$$\frac{\Delta I}{I} = -\frac{\Delta\Omega}{\Omega} - \frac{\Delta I}{I}\frac{\Delta\Omega}{\Omega}. \tag{4.3}$$

The change in the moment of inertia is given by

$$\Delta I = \Delta\left(I_{zz,s}(1 + \epsilon_{20})\right) = I_{zz,s}\Delta\epsilon_{20}. \tag{4.4}$$

Using equations (4.3) and (4.4) gives

$$\frac{\Delta\Omega}{\Omega} = -\frac{\Delta\epsilon_{20}}{1 + \epsilon_{20} + \Delta\epsilon_{20}}. \tag{4.5}$$

To relate the actual change in shape, $\Delta\epsilon_{20}$, going from star E to star Q, to the change in reference shape $\Delta\epsilon_{20,0}$, we perturb equation (2.12), yielding

$$\Delta\epsilon_{20} = \frac{2I_{zz,s}\Omega\Delta\Omega}{4(A_{20} + B_{20})} + \frac{B_{20}}{A_{20} + B_{20}}\Delta\epsilon_{20,0}. \tag{4.6}$$

Using equations (4.1) and (4.5) in equation (4.6), we obtain

$$\Delta\epsilon_{20} = -\frac{2\epsilon_{20}\Delta\epsilon_{20}}{1 + \epsilon_{20} + \Delta\epsilon_{20}} + \frac{B_{20}}{A_{20} + B_{20}}\Delta\epsilon_{20,0}. \tag{4.7}$$

The above expression is a quadratic in $\Delta\epsilon_{20}$. Solving this using the standard quadratic formula and then linearising to leading order in b_{20}, we obtain

$$\Delta\epsilon_{20} = b_{20}\Delta\epsilon_{20,0}(1 - 2\epsilon_{20}). \tag{4.8}$$

The change in kinetic energy between the two equilibrium configurations, E and Q, is given by

$$\Delta E_{\mathrm{k}} = \Delta\left(\frac{L^2}{2I_{zz,s}(1 + \epsilon_{20})}\right) = -\frac{(I_{zz}\Omega)^2}{2I_{zz,s}(1 + \epsilon_{20})^2}\Delta\epsilon_{20}. \tag{4.9}$$

The moment of inertia about the rotation axis, I_{zz}, can be written in terms of the oblateness parameter using equation (2.2):

$$I_{zz} = I_{zz,s}(1 + \epsilon_{20}). \tag{4.10}$$

Inserting the expression for the moment of inertia (4.10) and using equation (4.1) for ϵ_{20}, equation (4.9) simplifies to

$$\Delta E_{\mathrm{k}} = -\frac{I_{zz,s}\Omega^2}{2}\Delta\epsilon_{20} = -2(A_{20} + B_{20})\epsilon_{20}\Delta\epsilon_{20}. \tag{4.11}$$

The change in gravitational potential energy between the two equilibrium configurations is given by

$$\Delta E_{\mathrm{g}} = \Delta(A_{20}\epsilon_{20}^2) = 2A_{20}\epsilon_{20}\Delta\epsilon_{20}. \tag{4.12}$$

We then find that the combined change in gravitational and kinetic energy is

$$\Delta E_{\mathrm{g}} + \Delta E_{\mathrm{k}} = -2B_{20}\epsilon_{20}\Delta\epsilon_{20}. \tag{4.13}$$

To calculate the change in strain energy, we cannot use the perturbative method employed so far, as we now allow for order-unity changes in the strain energy. This corresponds to the star releasing all or most of its strain energy in a single, large fracture event. Therefore, to evaluate the change in strain energy between the two equilibrium configurations, we compute the strain energy of configurations E and Q separately and take the difference:

$$\Delta E_{\mathrm{s}} = E_{\mathrm{s}}^Q - E_{\mathrm{s}}^E = B_{20}(\epsilon_{20}^Q - \epsilon_{20,0}^Q)^2 - B_{20}(\epsilon_{20}^E - \epsilon_{20,0}^E)^2. \tag{4.14}$$

We have,

$$\epsilon_{20}^Q = \epsilon_{20} + \Delta\epsilon_{20}, \tag{4.15}$$

and

$$\epsilon_{20,0}^Q = \epsilon_{20,0} + \Delta\epsilon_{20,0} = \Delta\epsilon_{20,0}. \tag{4.16}$$

Inserting equations (4.15) and (4.16) into equation (4.14), we obtain

$$\Delta E_{\mathrm{s}} = B_{20}(\epsilon_{20} + \Delta\epsilon_{20} - \Delta\epsilon_{20,0})^2 - B_{20}\epsilon_{20}^2. \tag{4.17}$$

Substituting equation (4.8) into equation (4.17) and simplifying gives

$$\Delta E_{\rm s} = B_{20}\Delta\epsilon_{20,0}^2 - 2B_{20}\epsilon_{20}\Delta\epsilon_{20,0} + 2B_{20}\epsilon_{20}\Delta\epsilon_{20} + B_{20}\Delta\epsilon_{20}^2 - 2B_{20}\Delta\epsilon_{20}\Delta\epsilon_{20,0}. \quad (4.18)$$

The total change in energy for the $m = 0$ perturbation is given by

$$\Delta E_{\rm T} = \Delta E_{\rm k} + \Delta E_{\rm g} + \Delta E_{\rm s} = B_{20}\Delta\epsilon_{20,0}^2 - 2B_{20}\epsilon_{20}\Delta\epsilon_{20,0} + B_{20}\Delta\epsilon_{20}^2 - 2B_{20}\Delta\epsilon_{20}\Delta\epsilon_{20,0}. \quad (4.19)$$

The change in the energy, corresponding to $\Delta E_{\rm k} + \Delta E_{\rm g}$ (4.13), gets completely cancelled by the third term in the expression of $\Delta E_{\rm s}$ (4.18). Also, (4.13) is b_{20} times smaller than the leading order terms in $\Delta E_{\rm s}$. Since, the third and fourth term in (4.19) are order of magnitude smaller than first two terms, we can ignore them. This gives,

$$\Delta E_{\rm T} = B_{20}\Delta\epsilon_{20,0}^2 - 2B_{20}\epsilon_{20}\Delta\epsilon_{20,0}. \quad (4.20)$$

This implies that the leading-order contribution to the total energy change $\Delta E_{\rm T}$ arises solely from the change in strain energy. In equation (4.20), the free parameter is $\Delta\epsilon_{20,0}$. The total energy change will be negative as long as the following condition is satisfied:

$$\Delta\epsilon_{20,0} < 2\epsilon_{20}. \quad (4.21)$$

This has a simple physical interpretation. For very small values of $\Delta\epsilon_{20,0}$ the strain energy is guaranteed to decrease, as some of the strain created by spinning up the spherical star is relieved. All of this strain would be relieved if $\Delta\epsilon_{20,0} = \epsilon_{20}$, as the new reference shape would match the actual shape of the star. If the star "overshoots", less energy is relieved. In the case of overshooting as far as $\Delta\epsilon_{20,0} < 2\epsilon_{20}$, the new strain is equal in magnitude to the pre-quake strain , but is acting to make the star more, not less, oblate, and the change is energetically neutral, in terms of strain energy.

For a given ϵ_{20}, the variation of $\Delta E_{\rm T}/B_{20}$ with respect to $\Delta\epsilon_{20,0}$ is shown in Figure 4.2. We have chosen $\epsilon_{20} = 0.1$, corresponding to the fastest known rotating pulsar (716 revolutions per second). One can choose any other value of ϵ_{20}, and the curve in Figure 4.2 will scale accordingly.

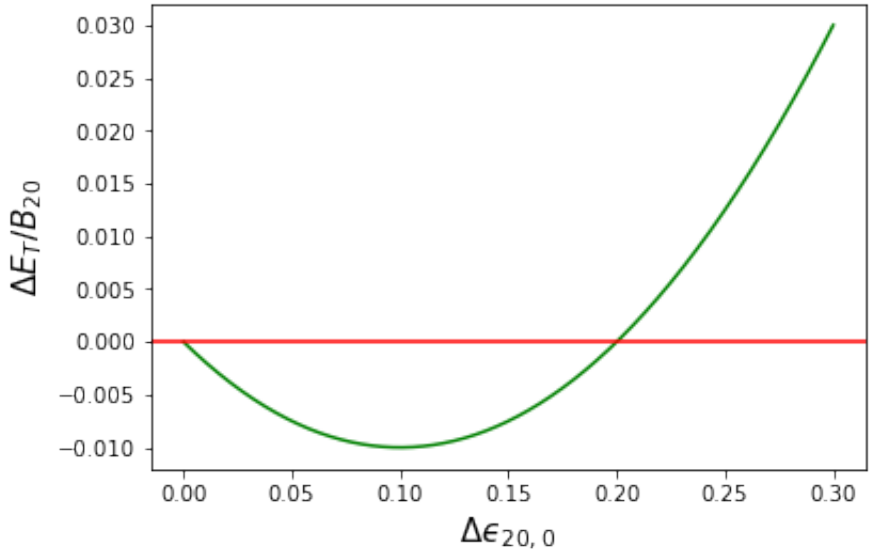

FIGURE 4.2: This curve shows the variation of the total change in energy with the free parameter $\Delta\epsilon_{20,0}$ for $\epsilon_{20} = 0.1$. The result is independent of Ω, since we do not perform an expansion in Ω, but rather in b_{20}.

We also verified that including third-order terms in the total energy expression,

$$E_{\mathrm{T}} = E_{\mathrm{grav,s}} + \frac{L^2}{2I_{zz,s}(1+\epsilon_{20})} + A_{20}\epsilon_{20}^2 + B_{20}(\epsilon_{20}-\epsilon_{20,0})^2 + A'_{20}\epsilon_{20}^3 + B'_{20}(\epsilon_{20}-\epsilon_{20,0})^3, \quad (4.22)$$

introduces only higher-order corrections to ΔE_{T}. To show this, we minimise equation (4.22), obtaining

$$0 = -\frac{L^2}{2I_{zz,s}(1+\epsilon_{20})^2} + 2A_{20}\epsilon_{20} + 2B_{20}(\epsilon_{20}-\epsilon_{20,0}) + 3A'_{20}\epsilon_{20}^2 + 3B'_{20}(\epsilon_{20}-\epsilon_{20,0})^2. \quad (4.23)$$

Solving equation (4.23), which is quadratic in ϵ_{20}, we obtain the following relation between ϵ_{20} and $\epsilon_{20,0}$:

$$\epsilon_{20}(A_{20}+B_{20}-3B'_{20}\epsilon_{20,0}) = \frac{I_{zz,s}\Omega^2 + 4B_{20}\epsilon_{20,0} - 6B'_{20}\epsilon_{20,0}^2}{4}. \quad (4.24)$$

Next, we perturb equation (4.24) to relate $\Delta\epsilon_{20}$ to $\Delta\epsilon_{20,0}$, obtaining

$$\Delta\epsilon_{20}(A_{20}+B_{20}-3B'_{20}\epsilon_{20,0}) + \epsilon_{20}(-3B'_{20}\Delta\epsilon_{20,0}) = \frac{I_{zz,s}\Omega\Delta\Omega}{2} + B_{20}\Delta\epsilon_{20,0} - 3B'_{20}\epsilon_{20,0}\Delta\epsilon_{20,0}. \quad (4.25)$$

Setting $\epsilon_{20,0} = 0$ in equation (4.25) and using equations (4.1) and (4.5), we obtain

$$\Delta\epsilon_{20} = \frac{3B'_{20}\epsilon_{20}\Delta\epsilon_{20,0}}{A_{20}+B_{20}} - \frac{2\epsilon_{20}\Delta\epsilon_{20}}{1+\epsilon_{20}+\Delta\epsilon_{20}} + \frac{B_{20}\Delta\epsilon_{20,0}}{A_{20}+B_{20}}. \tag{4.26}$$

Solving and linearising equation (4.26), which is again quadratic in $\Delta\epsilon_{20}$, we find

$$\Delta\epsilon_{20} = \left(\frac{B_{20}}{A_{20}+B_{20}} - \frac{2B_{20}\epsilon_{20}}{A_{20}+B_{20}} + \frac{3B'_{20}\epsilon_{20}}{A_{20}+B_{20}} - \frac{(3B_{20}+6B'_{20})\epsilon_{20}^2}{A_{20}+B_{20}}\right)\Delta\epsilon_{20,0}. \tag{4.27}$$

Let $b = \frac{B_{20}}{A_{20}+B_{20}}$ and $b' = \frac{B'_{20}}{A_{20}+B_{20}}$. Ignoring the second-order term in ϵ_{20} in equation (4.27), we obtain

$$\Delta\epsilon_{20} = (b - 2b\epsilon_{20} + 3b'\epsilon_{20})\Delta\epsilon_{20,0}. \tag{4.28}$$

Substituting equation (4.28) into the expression for the total energy change (4.19), we find

$$\Delta E_T = B_{20}\Delta\epsilon_{20,0}^2 - 2B_{20}\epsilon_{20}\Delta\epsilon_{20,0} \underbrace{-2bB_{20}\Delta\epsilon_{20,0}^2 + (4b-6b')B_{20}\epsilon_{20}\Delta\epsilon_{20,0}^2}_{\text{higher-order terms}}. \tag{4.29}$$

We observe that the correction terms in ΔE_T are of higher order in b and b'. Therefore, for a leading-order analysis, we can safely neglect these higher-order contributions. This justifies the use of the simpler total energy model given in equation (2.11) for the remainder of our analysis.

4.2 Perturbation $l = 2, m = 2$

We now calculate the change in the total energy associated with a pure $m = 2$ perturbation of star E. The total energy of the pre-quake equilibrium star E is given by equation (2.11). When the starquake occurs, star E transitions to a new equilibrium configuration Q. At the starquake, we superpose only a non-axisymmetric perturbation (ϵ_{22}) on top of the configuration E. The total energy of the new equilibrium configuration Q is given by

$$E_{\mathrm{T}} = E_{\mathrm{grav,s}} + \frac{L^2}{2I_{zz,s}(1+\epsilon_{20})} + A_{20}\epsilon_{20}^2 + B_{20}(\epsilon_{20}-\epsilon_{20,0})^2 + A_{22}\epsilon_{22}^2 + B_{22}(\epsilon_{22}-\epsilon_{22,0})^2. \tag{4.30}$$

Here, $\epsilon_{22,0}$ denotes the relaxed (zero-strain) ellipticity of star Q_0. To obtain the relationship between the new equilibrium shape Q and its corresponding relaxed shape Q_0, we

minimise equation (4.30) with respect to ϵ_{22}, holding L, ϵ_{20}, $\epsilon_{20,0}$, and $\epsilon_{22,0}$ fixed. This gives

$$\epsilon_{22} = \frac{B_{22}}{A_{22} + B_{22}} \epsilon_{22,0} \approx \frac{B_{22}}{A_{22}} \epsilon_{22,0}. \tag{4.31}$$

Perturbing equation (4.31) to describe the change from E to Q gives

$$\Delta\epsilon_{22} = \frac{B_{22}}{A_{22} + B_{22}} \Delta\epsilon_{22,0} = b_{22} \Delta\epsilon_{22,0}, \tag{4.32}$$

The change in the strain energy stored in the crust, between configurations E and Q, for a pure $m = 2$ perturbation is given by

$$\Delta E_{\rm s} = B_{22}(\epsilon_{22} - \epsilon_{22,0})^2. \tag{4.33}$$

Since there is no mountain before the starquake, we can write the equilibrium shape (ϵ_{22}) and the relaxed shape ellipticity ($\epsilon_{22,0}$) of star Q as the change in the equilibrium ($\Delta\epsilon_{22}$) and relaxed shape ellipticity ($\Delta\epsilon_{22,0}$) between star E and Q, i.e.,

$$\Delta\epsilon_{22} = \epsilon_{22}^{Q} - \epsilon_{22}^{E} = \epsilon_{22} - 0 = \epsilon_{22} \tag{4.34}$$

and

$$\Delta\epsilon_{22,0} = \epsilon_{22,0}^{Q} - \epsilon_{22,0}^{E} = \epsilon_{22,0} - 0 = \epsilon_{22,0}. \tag{4.35}$$

Substituting equations (4.34) and (4.35) into equation (4.33), we find

$$\Delta E_{\rm s} = B_{22}(\Delta\epsilon_{22} - \Delta\epsilon_{22,0})^2 \approx B_{22} \Delta\epsilon_{22,0}^2. \tag{4.36}$$

The change in the gravitational potential energy, between the two equilibrium configurations E and Q, for pure $m = 2$ perturbation is given as,

$$\Delta E_{\rm g} = A_{22}\epsilon_{22}^2 = A_{22}\Delta\epsilon_{22}^2. \tag{4.37}$$

Using equation (4.32), this becomes

$$\Delta E_{\rm g} = B_{22} b_{22} \Delta\epsilon_{22,0}^2. \tag{4.38}$$

The change in the gravitational potential energy $\Delta E_{\rm g}$ is b_{22} order of magnitude smaller than $\Delta E_{\rm s}$. Therefore, the change in the total energy is given as,

$$\Delta E_{\rm T} \approx \Delta E_{\rm s} \approx B_{22} \Delta\epsilon_{22,0}^2. \tag{4.39}$$

Since the change in total energy is positive, it follows that a starquake consisting solely of a pure $m = 2$ perturbation is energetically forbidden. Hence, any $m = 2$ perturbation must necessarily be accompanied by an axisymmetric $m = 0$ perturbation. We consider this more general and physically realistic case in the next Section 4.3.

4.3 Perturbation $m = 0$ and $m = 2$ Present Together

As shown previously in Section 3.5, when both $m = 0$ and $m = 2$ perturbations are present, the corresponding energy changes are independent of each other. Therefore, to obtain the expression for the total change in energy, we can simply add the results from Sections 4.1 and 4.2, namely equations (4.20) and (4.39). This yields:

$$\Delta E_{\mathrm{T}} = B_{20}\Delta\epsilon_{20,0}^2 - 2B_{20}\epsilon_{20}\Delta\epsilon_{20,0} + B_{22}\Delta\epsilon_{22,0}^2. \tag{4.40}$$

Here, the two free parameters are $\Delta\epsilon_{20,0}$ and $\Delta\epsilon_{22,0}$. Figure 4.3 shows, in green, the curve in the 2D parameter space of $\Delta\epsilon_{20,0}$ and $\Delta\epsilon_{22,0}$ for which $\Delta E_{\mathrm{T}} = 0$. For a mountain to form, the condition is:

$$\Delta E_{\mathrm{T}} = B_{20}\Delta\epsilon_{20,0}^2 - 2B_{20}\epsilon_{20}\Delta\epsilon_{20,0} + B_{22}\Delta\epsilon_{22,0}^2 < 0, \tag{4.41}$$

i.e., the region enclosed within the green curve.

Equation (4.40) can be rewritten in the following form:

$$\frac{(\Delta\epsilon_{20,0} - \epsilon_{20})^2}{\epsilon_{20}^2} + \frac{B_{22}(\Delta\epsilon_{22,0})^2}{\epsilon_{20}^2 B_{20}} = 1. \tag{4.42}$$

This clearly shows that the curve is an ellipse. Note that, without loss of generality, we may restrict our attention to the upper half of the ellipse. Any configuration with $\epsilon_{22} < 0$ can be mapped to one with $\epsilon_{22} > 0$ by a $\pi/2$ rotation in the x-y plane; see, for example, Jones (2015).

The physical meaning of this curve can be understood as follows. As shown in Section 4.2, when $\Delta\epsilon_{20,0} = 0$, it is energetically impossible to form a mountain, and thus $\Delta\epsilon_{22,0} = 0$. Some of the strain energy stored in the axisymmetric configuration must be released in order to build a mountain. This explains why the curve starts at the origin.

As $\Delta\epsilon_{20,0}$ increases, more axisymmetric strain energy is liberated and can be used to build a mountain, so $\Delta\epsilon_{22,0}$ increases correspondingly. The maximum liberated axisymmetric strain energy occurs when $\Delta\epsilon_{20,0} = \epsilon_{20}$, as discussed in Section 4.1 (see the discussion following equation (4.21)). At this point, $\Delta\epsilon_{22,0}$ reaches its peak.

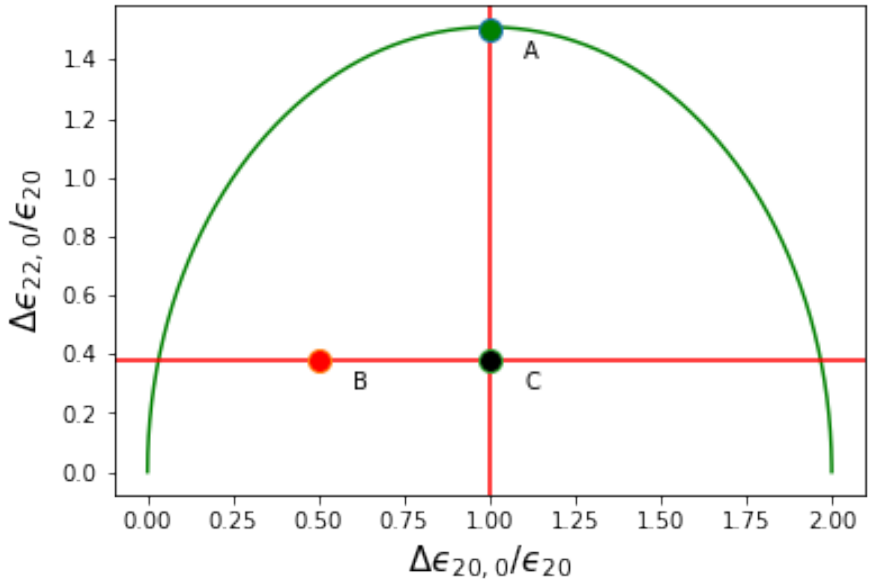

FIGURE 4.3: This figure shows the region in our $(\Delta\epsilon_{20,0}, \Delta\epsilon_{22,0})$ parameter space for which $\Delta E_{\mathrm{T}} < 0$. Green curve marks the elliptical boundary of this region, where $\Delta E_{\mathrm{T}} = 0$; energetically allowed points lie on and below this curve. It gives the position of three different configurations of the star. Point A (green) marks the position of the star with largest mountain. Point B (red) indicates the position of the star with a mountain size as discussed in a recent study Giliberti and Cambiotti (2022). Point C (black) gives the position of the star configuration with the same mountain as star B, but which requires the least energy.

As $\Delta\epsilon_{20,0}$ increases further, the amount of strain energy liberated begins to decrease, leading to a reduction in $\Delta\epsilon_{22,0}$. Eventually, when $\Delta\epsilon_{20,0} = 2\epsilon_{20}$, no strain energy is liberated, and no mountain can be formed (as per equation (4.21)).

4.4 The Maximum Mountain

We now explore some consequences of our starquake model by focusing on the maximum mountain size that can be formed. Throughout this section, we continue to consider a scenario in which we begin with a non-rotating, elastically relaxed, spherical star S, which is spun up to some angular velocity Ω, resulting in a rotating, elastically strained star E with oblateness ϵ_{20}. This star then undergoes a starquake to form a triaxial configuration Q.

As before, the two free parameters describing the quake are taken to be $\Delta\epsilon_{20,0}$ and $\Delta\epsilon_{22,0}$, representing the $m = 0$ and $m = 2$ changes in reference oblateness and ellipticity, respectively.

Before calculating the largest mountain that can form when star E undergoes a quake, we first determine the most energetically favoured change in axisymmetric configuration for a *given* mountain size ϵ_{22}. This is obtained by minimising the total energy

perturbation ΔE_{T} from equation (4.40) while holding $\Delta\epsilon_{22,0}$ fixed. The condition for minimisation is:

$$\Delta\epsilon_{20,0} = \epsilon_{20}. \tag{4.43}$$

This simply states that the most energy is liberated if the $m = 0$ reference shape increases by an amount equal to the original oblateness ϵ_{20} of star E. This condition is represented as the vertical red line $\Delta\epsilon_{20,0} = \epsilon_{20}$ in Figure 4.3.

The largest mountain that can be formed in the starquake corresponds to the topmost point of the ellipse, shown as the green point and labelled as star A in Fig. 4.3. Setting $\Delta\epsilon_{20,0} = \epsilon_{20}$ and $\Delta E_{\mathrm{T}} = 0$ in equation (4.40) gives

$$\Delta\epsilon_{22,0}^{\max} = \sqrt{\frac{B_{20}}{B_{22}}}\,\epsilon_{20}. \tag{4.44}$$

This represents the relaxed (zero-strain) shape of the mountain. To determine the actual mountain size, we use equation (4.32), which yields:

$$\Delta\epsilon_{22}^{\max} = \frac{\sqrt{B_{22}B_{20}}}{A_{22}}\,\epsilon_{20}. \tag{4.45}$$

This is one of our key results: it represents the largest mountain that can form in a starquake, under the constraints of angular momentum and energy conservation. Notably, the result involves the geometric mean of B_{20} and B_{22}, reflecting the fact that the formation of an $m = 2$ mountain necessarily requires a release of $m = 0$ strain energy, coupling the two deformation modes.

To get a rough estimate of the maximum mountain size, we can insert ϵ_Ω of equation (2.14) and (3.130) into equation (4.45), as in our model this oblateness comes from the centrifugal forces in the spinning star:

$$\epsilon_{22}^{\max} = \frac{\sqrt{57}}{5}\cdot\frac{B_{22}}{A_{22}}\,\epsilon_\Omega \approx 7.98\times10^{-8}\left(\frac{f}{100\,\mathrm{Hz}}\right)^2\frac{\mu_{30}R_6^6\Delta R_5}{M_{1.4}^3}. \tag{4.46}$$

This result should be interpreted as follows: if a non-rotating, elastically relaxed star is spun up to a rotation frequency f, and subsequently undergoes a crustquake, the expression above gives the maximum mountain that can form.

There is however a limit to the applicability of this result, as the oblateness in the spinning up star, and the mountain formed in the quake event, will be limited by the crust's finite breaking strain. The maximum mountain size imposed by the finite breaking strain has been examined many times previously (Haskell et al., 2006; Johnson-McDaniel and Owen, 2013; Gittins et al., 2020; Gittins and Andersson, 2021; Morales

and Horowitz, 2022), but in the context of our simple model, we can set the ellipticity at the time of the crustquake to the breaking strain $\sigma_{\rm break}$. Setting $\epsilon_\Omega = \sigma_{\rm break}$ in equation (2.14) then gives the maximum frequency $f_{\rm break}$ that the star can be spun up to before fracture:

$$f_{\rm break} \approx 753\,{\rm Hz}\left(\frac{\sigma_{\rm break}}{10^{-1}}\frac{M_{1.4}}{R_6^3}\right)^{1/2}. \tag{4.47}$$

We have parameterised the breaking strain using the typical value $\sigma_{\rm break} \sim 0.1$, as suggested by molecular dynamics simulations in Horowitz and Kadau (2009).

The corresponding upper limit on the mountain can be obtained by substituting this into the second equality of equation (4.46), or, more directly, by setting $\epsilon_\Omega = \sigma_{\rm break}$ in the first equality:

$$\epsilon^{\rm max}_{22,\,\rm break} = 1.13\times10^{-5}\left(\frac{\sigma_{\rm break}}{10^{-1}}\right)\frac{\mu_{30}R_6^3\Delta R_5}{M_{1.4}^2}. \tag{4.48}$$

This is the largest mountain that could be produced if an initially non-rotating star is spun up all the way to the point where the strain in its crust reaches the breaking strain, and then a curstquake occurs forming the largest possible mountain.

In the following Section 4.5, we demonstrate how the recent analysis presented by Giliberti and Cambiotti (2022) can be described within our framework.

4.5 Description of Giliberti and Cambiotti (2022)

As a further application of our model, we now use it to describe a particular mountain-building starquake scenario presented in Giliberti and Cambiotti (2022). Our formalism will allow us to explore a few things not considered in Giliberti and Cambiotti (2022). Specifically, we will show that the model of Giliberti and Cambiotti (2022) involves not only an $m = 2$ change, but necessarily also an $m = 0$ change. We will be able to calculate the corresponding reference shape the post-quake star would have, i.e. how its zero-strain configuration is reconfigured in the quake, for both the $m = 0$ and $m = 2$ perturbations. Furthermore, we will confirm that, at fixed angular momentum, the total energy of the star indeed decreases. We will also evaluate how close the mountain described by Giliberti and Cambiotti (2022) is to the maximum possible mountain allowed by the quake process, as per equation (4.45).

Giliberti and Cambiotti (2022) considered several different stellar configurations, which we now describe. These configurations are displayed schematically in Fig. 4.4, where we show cross-sections in the x-y plane, with rotation always along the z-axis. The differences in the sizes of the stars are greatly exaggerated for clarity.

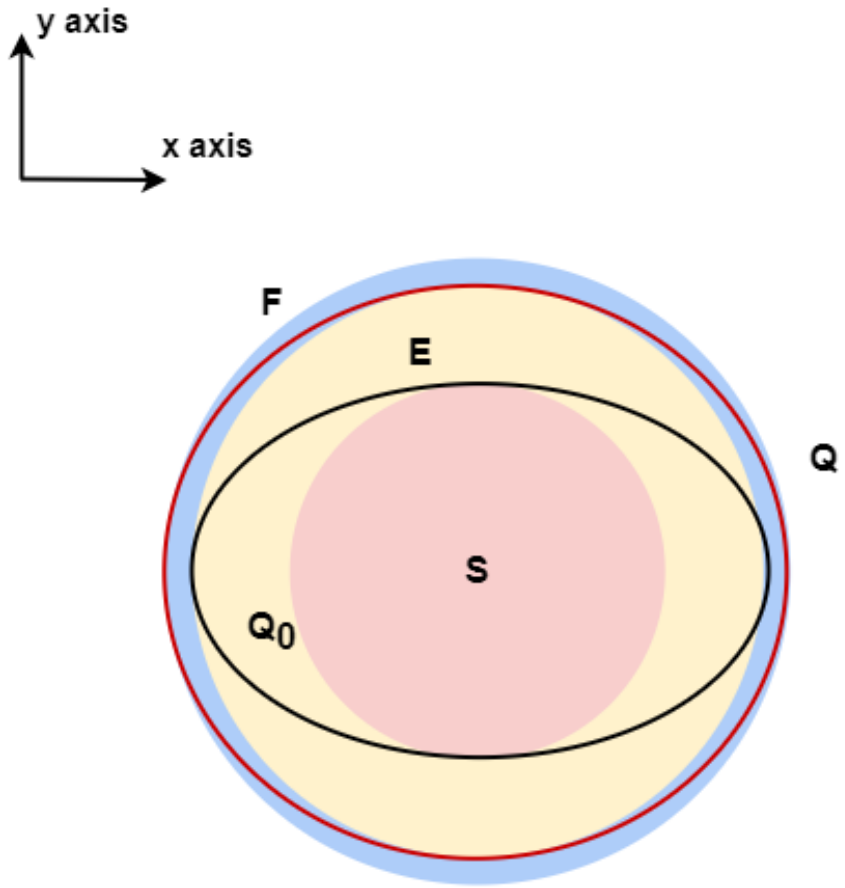

FIGURE 4.4: Schematic depiction of various configurations of the spinning up star in x-y plane, with rotation along the z-axis. The pink disk S represents the spherical non-rotating zero strain configuration. The yellow disk E represents the elastic strained axisymmetric configuration just before the starquake. The blue disk F represents a star with the same angular momentum as E, but elastically relaxed and axisymmetric (i.e. equivalent to a fluid). The red ellipse Q represents the post-starquake equilibrium shape. The black ellipse Q_0 represents the elastically relaxed shape corresponding to star Q. We assume that the moment of inertia along the x-axis is smaller than the moment of inertia along the y-axis for both Q and Q_0 configurations. The differences in shape of the various configurations are greatly exaggerated for clarity.

The non-rotating, elastically relaxed, spherical star S is shown as a pink disk. This star is spun up to form star E, which represents the configuration just prior to the starquake. Star E is rotating, elastically strained, and axisymmetric, with moment of inertia tensor $\Delta I^E = \mathrm{Diag}(\Delta I^E_{xx}, \Delta I^E_{xx}, \Delta I^E_{zz})$. It is depicted as the yellow disk in Fig. 4.4.

If all of the strain energy stored in star E is fully relieved at fixed angular momentum—either through a sequence of starquakes or via plastic creep—the star reaches a configuration corresponding to a fluid star F. This configuration has slightly larger oblateness than star E. It is shown as the blue disk and represents a rotating, unstrained, and axisymmetric star with moment of inertia tensor $\Delta I^F = \mathrm{Diag}(\Delta I^F_{xx}, \Delta I^F_{xx}, \Delta I^F_{zz})$.

Giliberti and Cambiotti (2022) expressed the post-quake configuration using the moment of inertia tensor $\Delta I^Q = \mathrm{Diag}(\Delta I^Q_{xx}, \Delta I^Q_{yy}, \Delta I^Q_{zz})$, which is illustrated by the red

ellipse Q in Fig. 4.4. Note that, simply for the sake of definiteness, we have assumed the symmetry-breaking is such that the radius along the x-axis is larger than the radius along the y-axis, so that $\Delta I^{Q}_{xx} < \Delta I^{Q}_{yy}$.

Giliberti and Cambiotti (2022) argued that the post-quake configuration is expected to lie between the elastic and fluid configurations, as sketched in Fig. 4.4, i.e. the red ellipse Q must lie between the pre-glitch elastically strained configuration E (yellow disk) and the zero-strain fluid configuration F (blue disk). The authors concluded that the maximum value of $\Delta I^{Q}_{yy} - \Delta I^{Q}_{xx}$ is $\Delta I^{E}_{xx} - \Delta I^{F}_{xx}$. This corresponds to the red ellipse of Fig. 4.4 just touching its bounding disks E and F. This was computationally useful, as the stellar configurations E and F can both be computed as perturbations away from star S. Giliberti and Cambiotti (2022) did this numerically for SLy and BSk21 equations of state, while we do so analytically, using the displacement vector field (3.10), valid for our uniform density incompressible stars.

Given (3.10), we can calculate the radii along the x, y and z axes for any uniform density spherical elastic star that is spin-up from $\Omega_A = 0$ to $\Omega_B > 0$:

$$a_1 = R + \xi^r(r = R, \theta = \frac{\pi}{2}, \phi = 0) = R(1 + \alpha_{20}\frac{1}{2}), \tag{4.49}$$

$$a_2 = R + \xi^r(r = R, \theta = \frac{\pi}{2}, \phi = \frac{\pi}{2}) = R(1 + \alpha_{20}\frac{1}{2}), \tag{4.50}$$

$$a_3 = R + \xi^r(r = R, \theta = 0) = R(1 - \alpha_{20}), \tag{4.51}$$

where ξ^r is the radial component of the displacement field (3.10) and

$$\alpha_{20} = \frac{\lambda}{1 + b_{20}}\Omega^2. \tag{4.52}$$

This gives

$$a^{\mathrm{E}}_1 = a^{\mathrm{E}}_2 = R\left[1 + \frac{1}{2}\alpha_{20}\right]. \tag{4.53}$$

The oblateness ($m = 0$) of star E is given by substituting the radii a_1 and a_2 of equations (4.49) and (4.50) into (4.59). This gives

$$\epsilon_{20} = \alpha_{20} + \frac{\alpha^2_{20}}{4}. \tag{4.54}$$

For $\alpha_{20} \ll 1$, this can be inverted:

$$\alpha_{20} \approx \epsilon_{20} - \frac{\epsilon^2_{20}}{4}. \tag{4.55}$$

The radii of star F are of the same form, but with departures from star S a factor $(1 + b_{20})$ larger:

$$a_1^{\mathrm{F}} = a_2^{\mathrm{F}} = R\left[1 + \frac{1}{2}\alpha_{20}(1 + b_{20})\right] \tag{4.56}$$

In the model of Giliberti and Cambiotti (2022), we can now immediately write down the radii of star Q. Along the x-axis, it has the radius of star F, so that

$$a_1^{\mathrm{Q}} = a_1^{\mathrm{F}} = R\left[1 + \frac{1}{2}\alpha_{20}(1 + b_{20})\right], \tag{4.57}$$

while along the y-axis, star Q has the same radius as star E:

$$a_2^{\mathrm{Q}} = a_2^{\mathrm{E}} = R\left[1 + \frac{1}{2}\alpha_{20}\right], \tag{4.58}$$

Given the radii of the equilibrium shape Q, we can straightforwardly compute the associated oblateness ϵ_{20}^{Q} and ellipticity ϵ_{22}^{Q} using the expressions derived below.

To begin with, we recall the definition of the oblateness parameter ϵ_{20} as given in equation (2.2). Using the definition of the moment of inertia I_{zz} from equation (3.83), we obtain the following expression for ϵ_{20}:

$$\epsilon_{20} = \frac{(a_1^2 + a_2^2) - 2R^2}{2R^2}. \tag{4.59}$$

Next, substituting the definitions of I_{zz} from equation (3.83), I_{xx} from equation (3.145), and I_{yy} from equation (3.146) into the definition of ϵ_{22} given in equation (1.1), we find:

$$\epsilon_{22} = \frac{a_1^2 - a_2^2}{a_1^2 + a_2^2}. \tag{4.60}$$

To compute the value of ϵ_{20}^{Q}, we insert equations (4.57) and (4.58) into equation (4.59). This yields:

$$\epsilon_{20}^{Q} = \alpha_{20} + \frac{b_{20}\alpha_{20}}{2} + \frac{\alpha_{20}^2}{4}. \tag{4.61}$$

Similarly, inserting equations (4.57) and (4.58) into equation (4.60) gives:

$$\epsilon_{22}^{\mathrm{Q}} \approx \frac{b_{20}\alpha_{20}}{2}. \tag{4.62}$$

Of most interest here are the *changes* in $\epsilon_{20}^{\mathrm{Q}}$ and $\epsilon_{22}^{\mathrm{Q}}$, in going from star E to star Q. The oblateness ($m = 0$) of star E is given by equation (4.54), so we have:

$$\Delta\epsilon_{20} = \epsilon_{20}^{\mathrm{Q}} - \epsilon_{20}^{E} = \frac{1}{2}b_{20}\alpha_{20} \approx \frac{1}{2}b_{20}\epsilon_{20}. \tag{4.63}$$

Quantity	Configuration A	Configuration B	Configuration C
$\Delta\epsilon_{20}$	$b_{20}\epsilon_{20}$	$\frac{b_{20}}{2}\left(\epsilon_{20}-\frac{\epsilon_{20}^2}{4}\right)$	$b_{20}\epsilon_{20}$
$\Delta\epsilon_{22}$	$b_{22}\epsilon_{20}\sqrt{\frac{B_{20}}{B_{22}}}$	$\frac{b_{20}}{2}\left(\epsilon_{20}-\frac{\epsilon_{20}^2}{4}\right)$	$\frac{b_{20}}{2}\left(\epsilon_{20}-\frac{\epsilon_{20}^2}{4}\right)$
$\Delta\epsilon_{20,0}$	ϵ_{20}	$\frac{1}{2}\left(\epsilon_{20}-\frac{\epsilon_{20}^2}{4}\right)$	ϵ_{20}
$\Delta\epsilon_{22,0}$	$\epsilon_{20}\sqrt{\frac{B_{20}}{B_{22}}}$	$\frac{19}{50}\left(\epsilon_{20}-\frac{\epsilon_{20}^2}{4}\right)$	$\frac{19}{50}\left(\epsilon_{20}-\frac{\epsilon_{20}^2}{4}\right)$
ΔE_{T}	0	$-\frac{1957B_{22}}{1250}\epsilon_{20}^2$	$-\frac{5339B_{22}}{2500}\epsilon_{20}^2$

TABLE 4.1: Summary of changes in oblateness, ellipticity, and total energy for the star configurations A, B, and C as illustrated in Figure 4.3. The first two rows show the changes in equilibrium oblateness ($\Delta\epsilon_{20}$) and ellipticity ($\Delta\epsilon_{22}$) for the final equilibrium configuration Q. The next two rows give the corresponding changes in the relaxed (reference) shape, $\Delta\epsilon_{20,0}$ and $\Delta\epsilon_{22,0}$, defining configuration Q_0. The final row presents the total energy change ΔE_{T} associated with each configuration during the starquake event.

The ellipticity ($m = 2$) of star E is, by assumption, zero, so we have

$$\Delta\epsilon_{22} = \epsilon_{22}^{Q} - \epsilon_{22}^{E} = \epsilon_{22}^{Q} = \frac{b_{20}\alpha_{20}}{2} \approx \frac{1}{2}b_{20}\epsilon_{20}. \tag{4.64}$$

In both equations (4.63) and (4.64) we have approximated equation (4.55) as $\alpha_{20} \approx \epsilon_{20}$.

This is a simple result: the mountain formation scenario of Giliberti and Cambiotti (2022) consists of equal increases in ϵ_{22} (creating the mountain) and in ϵ_{20} (releasing some axisymmetric strain). We record these results in the middle column of Table 4.1.

Having calculated the changes in equilibrium shape, as parameterised by $\Delta\epsilon_{20}$ and $\Delta\epsilon_{22}$, we can easily calculate the changes in the corresponding reference shapes, $\Delta\epsilon_{20,0}$ and $\Delta\epsilon_{22,0}$. For the axisymmetic change, we can use equation (4.8) to give

$$\Delta\epsilon_{20,0} = \frac{1}{2}(\epsilon_{20} - \frac{\epsilon_{20}^2}{4}) \tag{4.65}$$

while for the non-axisymmetric change we can use equation (4.32) to give

$$\Delta\epsilon_{22,0} = \frac{b_{20}}{2b_{22}}(\epsilon_{20} - \frac{\epsilon_{20}^2}{4}). \tag{4.66}$$

Using (3.130) and (3.153) we have

$$\frac{b_{20}}{b_{22}} = \frac{B_{20}A_{22}}{A_{20}B_{22}} = \frac{19}{25}. \tag{4.67}$$

Inserting (4.67) into (4.66) gives

$$\Delta\epsilon_{22,0} = \frac{19}{50}(\epsilon_{20} - \frac{\epsilon_{20}^2}{4}). \tag{4.68}$$

We record these values in column B of Table 4.1.

We can now plot the position of star B in our 2-d parameter space; see the red point in Fig. 4.3. Reassuringly, star B lies inside the green bounding ellipse, so does indeed correspond to a decrease in the star's energy. We can in fact compute the change in energy, ΔE_{T}, simply by plugging our results for $\Delta\epsilon_{20,0}$ and $\Delta\epsilon_{22,0}$ into equation (4.40). The resulting (negative) expression is given in column B, bottom row, of Table 4.1.

We can compare the size of the mountain formed in the Giliberti and Cambiotti (2022) process with the size of the maximum mountain, constrained only by angular momentum and energy conservation. Taking the ratio of the $\epsilon_{22}^{\mathrm{max}}$ of equation (4.45) with the mountain size of equation (4.64), denoted below as $\epsilon_{22}^{\mathrm{G.C.}}$:

$$\frac{\epsilon_{22}^{\mathrm{max}}}{\epsilon_{22}^{\mathrm{G.C.}}} = 2\frac{A_{20}}{A_{22}}\sqrt{\frac{B_{22}}{B_{20}}}\left(\frac{1}{1-\frac{\epsilon_{20}}{4}}\right) \approx 6\sqrt{\frac{25}{57}}\left(1+\frac{\epsilon_{20}}{4}\right) \approx 3.97. \tag{4.69}$$

This shows, to the leading order, the maximum mountain size $\epsilon_{22}^{\mathrm{max}}$ is approximately 4 times larger than the mountain $\epsilon_{22}^{\mathrm{G.C.}}$ built in the Giliberti and Cambiotti (2022) scenario.

As a final application of our model, we can consider a star C, defined to have the same mountain ϵ_{22} as that of Giliberti and Cambiotti (2022) (equation (4.64)), but lying on the red vertical maximal energy-release line of Fig. 4.3. We record its parameters in the final column of Table 4.1. Such a star has the same $\Delta\epsilon_{22}$ and the same $\Delta\epsilon_{22,0}$ as star B. However, it has $\Delta\epsilon_{20,0} = \epsilon_{20}$, as per equation (4.43). Using equation (4.8) this gives $\Delta\epsilon_{20} = b_{20}\epsilon_{20}$. These values can then be substituted into equation (4.40) to give the total energy change ΔE_{T}. Note that, as expected, the energy release in forming star C is larger (in magnitude) than that released in forming star B.

4.5.1 Summary

In this chapter, we proposed a simple model of a spinning-up neutron star undergoing a starquake. We calculated the changes in ellipticities and energies involved during the starquake process for both axisymmetric and non-axisymmetric crust-breaking scenarios. Our analysis showed that a mountain cannot form through a non-axisymmetric

shape change alone; an accompanying axisymmetric shape change is necessarily required.

We also estimated the maximum size of a mountain that can be formed within this framework. Furthermore, we applied our model to reinterpret the analysis presented by Giliberti and Cambiotti (2022), identifying where it lies in the parameter space defined by our formalism. The results presented in this chapter form a substantial part of the work published in our paper Gangwar and Jones (2024).

While this model captures the key aspects of mountain formation during crustquakes, several refinements are possible. These are discussed in detail in Chapter 9. We conclude this model here, noting that there remains significant scope for improvement and extension in future work.

In the second half of this thesis, we introduce an alternative mechanism for building elastic mountains on neutron stars, namely, *Magnus mountains*. We begin by outlining the fundamental physics of superfluid vortices and superconducting flux tubes within neutron stars in the following chapter, which forms the theoretical basis for the Magnus mountain model proposed in this thesis.

Chapter 5

Superconductivity and Superfluidity

Many theoretical models suggest that the interior matter of neutron stars (NSs) exists in a state of superconductivity and superfluidity. In this chapter, we briefly review the fundamental physics of superconductivity and superfluidity, highlighting key properties such as the formation of quantised superfluid vortices and magnetic flux tubes. This background will provide the necessary context for subsequent chapters, where we study the formation of Magnus mountains resulting from interactions between superfluid vortices, flux tubes, and crustal nuclei.

The discoveries of superconductivity and superfluidity led to some of the most remarkable and unexpected phenomena in condensed matter physics—phenomena that arise as direct consequences of quantum mechanics (QM). The theoretical frameworks developed to explain these effects are among the most significant achievements in many-body physics, with far-reaching implications spanning from large-scale engineering applications to the Higgs mechanism in the Standard Model of particle physics. While quantum effects are typically observed only at atomic or subatomic scales, superconductors and superfluids exhibit macroscopic manifestations of quantum mechanics, earning them the designation of macroscopic quantum phenomena (Annett, 2004).

Superconductivity and superfluidity typically emerge in systems at extremely low temperatures. A natural question then arises: how can neutron stars, with internal temperatures on the order of 10^8 K ($\approx 0.01\,\mathrm{MeV}$), exhibit these quantum states? The answer lies in the high degeneracy pressure and the attractive nuclear interaction that enable fermions to form Cooper pairs. The extreme density in a neutron star interior results in large Fermi energies for its constituent fermions, typically in the range $\varepsilon_F \approx 10$–$100\,\mathrm{MeV}$. This Fermi energy far exceeds the thermal energy, satisfying the condition $\varepsilon_F \gg T$, even for mature neutron stars (Haskell and Sedrakian, 2018).

Superfluidity and superconductivity have several observational manifestations in neutron stars. One of the most well-studied phenomena is that of pulsar glitches, which are

thought to result from the pinning and unpinning of superfluid vortices to the crustal nuclei. Some theoretical models also suggest that vortices may pin to flux tubes in the superconducting core; however, these models are still under active development and require further validation (Sidery and Alpar, 2009).

Beyond glitches, superfluidity may also imprint itself on timing noise, potentially arising from superfluid turbulence in the interior. Another important observational consequence is the effect of superfluidity on the cooling rate of the neutron star. A superfluid neutron star is expected to cool more rapidly than a non-superfluid one. This is because the onset of superfluidity leads to an enhanced neutrino emission mechanism, associated with the continuous formation and breaking of neutron Cooper pairs. This process—often referred to as pair-breaking and formation (PBF)—increases the neutrino emissivity and thereby accelerates the thermal evolution of the star (Chamel, 2017).

Macroscopically coherent quantum states can be broadly classified according to whether coherence arises from paired fermions or from fundamental bosons. Superconductors and superfluids correspond to phases formed via Cooper pairing of fermions, while Bose–Einstein condensates involve the condensation of elementary bosons. In this chapter, we focus on superconductors and superfluids, as they are most relevant to the physics of neutron stars.

5.1 Superconductivity

Superconductivity was discovered in 1911 by H. Kamerlingh Onnes in mercury (Hg) at a temperature of 4.1 K. Superconductors exhibit remarkable properties, including the ability to sustain persistent electrical currents without any resistance and the complete expulsion of magnetic flux effect known as the Meissner effect (Meissner and Ochsenfeld, 1933; Annett, 2004; Tinkham, 2004). Owing to their exceptional electromagnetic characteristics, superconducting materials are used in a wide range of applications, such as in MRI/NMR machines, beam-steering magnets for particle accelerators, and magnetic confinement systems in fusion devices like tokamaks (Annett, 2004). Additionally, superconductors are used in fabricating SQUIDs (Superconducting Quantum Interference Devices), which are among the most sensitive magnetometers known (Thorne and Blandford, 2017; Kleiner et al., 2004).

Despite its early discovery, it took nearly four decades to develop a comprehensive microscopic theory of superconductivity. In 1957, John Bardeen, Leon Cooper, and Robert Schrieffer proposed what is now known as the BCS theory (Schrieffer, 2018; Tinkham,

2004). According to this theory, the key dynamical mechanism involves quantised vibrations of the crystal lattice, referred to as phonons. These phonons mediate an effective long-range attractive interaction between electrons with opposite spin and momentum. The resulting bound states of these electrons are called Cooper pairs (Annett, 2004; Tinkham, 2004).

Because Cooper pairs have integer spin, they behave as bosons and can undergo Bose-Einstein condensation below a critical temperature T_c. This leads to a coherent macroscopic quantum state that flows without resistance. Thus, a superconductor can be interpreted as a charged superfluid. The same pairing mechanism also applies to fermionic systems such as superfluid ^{3}He, where atoms form similar paired states. The BCS theory has proven highly successful in explaining a broad range of experimental observations, which has encouraged its application to other areas of physics (Schrieffer, 2018; Chamel, 2017; Annett, 2004).

One of the most profound theoretical developments arising from superconductivity was its connection to the Higgs mechanism in particle physics. In 1963, Philip Anderson explained the expulsion of magnetic flux in superconductors in terms of spontaneous symmetry breaking of gauge symmetry. Building on this idea, Peter Higgs extended the concept to the field of particle physics, predicting the existence of the Higgs boson to account for the origin of mass in fundamental particles (Pimenta et al., 2013). The discovery of the Higgs boson was confirmed in 2013 by experiments at CERN, marking a major milestone in modern physics (ATLAS Collaboration, 2013) .

Despite its successes, the BCS theory has certain limitations. For instance, the highest known superconducting transition temperature at ambient pressure is 133 K, observed in mercury-based cuprate materials containing barium and calcium. The BCS framework cannot account for such high-temperature superconductivity, and the development of a complete theory for this phenomenon remains an open and active area of research (Bussmann-Holder and Keller, 2020).

Models suggest that in neutron stars, protons in the core can undergo Cooper pair formation and consequently become superconducting. In both the outer and inner core, proton superconductivity is expected to arise primarily through the singlet-state ($^1S_0$) pairing channel (Baldo and Schulze, 2007). Figure 5.1 shows how the transition temperature varies with density inside the neutron star. Proton superconductivity is represented by the dashed line. However, the estimates for these transition temperatures remain highly uncertain due to the strong influence of surrounding neutrons, whose interactions significantly modify the effective proton-proton pairing potential (Andersson et al., 2013).

This behaviour has significant implications for the magnetic and rotational dynamics of the neutron star, which will be discussed in subsequent sections. In addition to standard nuclear matter phases, theoretical models also predict the possible existence

of colour-superconducting phases in the inner core, where quark matter may exist at very high densities (Alford et al., 2008).

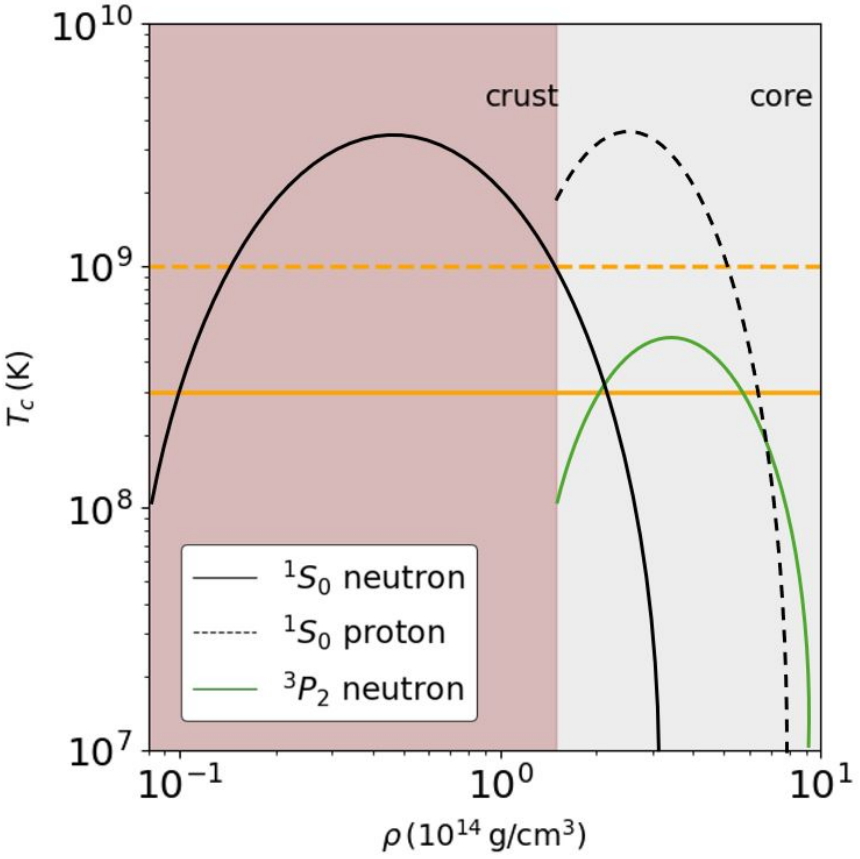

FIGURE 5.1: This figure is adapted from Andersson et al. (2013). It illustrates the variation of transition temperatures for neutron superfluidity and proton superconductivity with neutron star density, for different pairing channels. The solid black and green lines represent transition temperatures for S-wave and P-wave pairing channels, respectively, in neutron superfluidity. The dashed line indicates the transition temperature for proton superconductivity via the S-wave pairing channel. A characteristic neutron star temperature of 10^9 K is assumed here. As the temperature decreases, the regions undergoing the superfluid/superconducting transition shift: in the core, transitions occur at higher densities, while in the crust, the transitions move outward.

5.2 The Meissner Effect

One of the most striking properties of superconductors is their ability to exhibit the *Meissner effect*. When a weak external magnetic field (below a critical value H_c, which depends on the specific material) is applied to a superconducting material, the superconductor expels magnetic field lines from its interior. This phenomenon is known as the Meissner effect (Annett, 2004; Tinkham, 2004).

The expulsion of magnetic field lines is a consequence of the vanishing electric field $\mathbf{E} = 0$ inside the superconductor. As the temperature T falls below the critical temperature

T_c, the electrical conductivity tends to infinity. To ensure a finite current density, the electric field inside must vanish, i.e., $\mathbf{E} = 0$. Applying Maxwell's equation,

$$\nabla \times \mathbf{E} = -\frac{\partial \mathbf{B}}{\partial t}, \tag{5.1}$$

together with the condition $\mathbf{E} = 0$, implies

$$\frac{\partial \mathbf{B}}{\partial t} = 0, \tag{5.2}$$

at every point within the superconductor. This result shows that once a magnetic field is expelled, it remains zero inside the superconductor since the time derivative of $\mathbf{B}$ is zero. Consequently, superconductors are perfect diamagnets, exhibiting magnetic susceptibility $\chi = -1$ (Annett, 2004; Tinkham, 2004).

5.3 Type-I and Type-II Superconductivity

Superconductors are categorised as Type-I or Type-II based on their response to external magnetic fields. In Type-I superconductors, as the applied magnetic field is gradually increased, the superconducting state is abruptly destroyed at a single critical value H_c.

In contrast, Type-II superconductors exhibit two critical fields, H_{c1} and H_{c2}. When the magnetic field strength surpasses H_{c1}, superconductivity is locally suppressed by the formation of quantised *flux tubes*, allowing partial penetration of the magnetic field. As the field strength increases further, the flux tube density increases, and above H_{c2} superconductivity is entirely destroyed (Saipuddin et al., 2022; Annett, 2004). The phase diagrams for Type-I and Type-II superconductors, plotted as a function of magnetic field H and temperature T, are shown in Figure 5.2.

There are theoretical models that suggest the protons in the core of a neutron star may form either a type I or type II superconducting phase. Both scenarios have significant implications for the configuration of the magnetic field within that region. In the case of a type II superconductor, the magnetic field can penetrate the core in the form of quantised bundles of flux tubes, provided the field strength lies between the lower and upper critical values. In contrast, a type I superconducting core would expel the magnetic field entirely due to the Meissner effect. Thus, the configuration of the magnetic field in the neutron star core is determined by the local field strength and the nature of the superconducting phase.

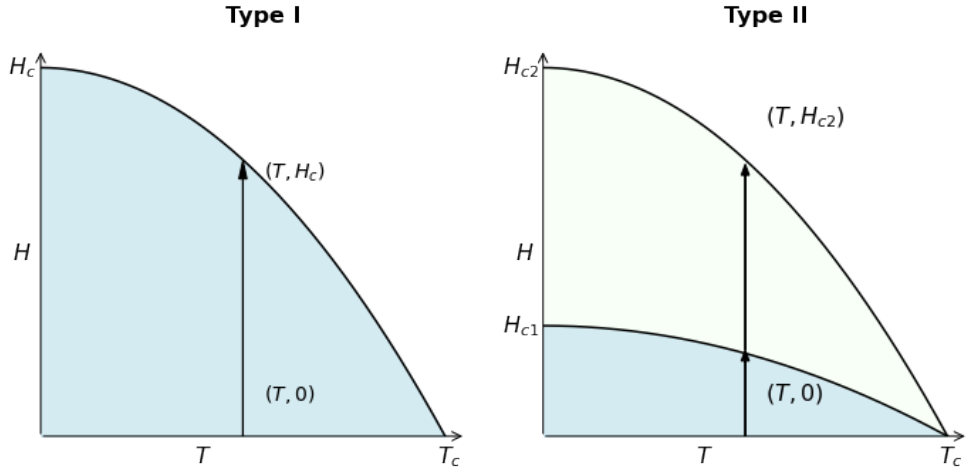

FIGURE 5.2: Adapted from Annett (2004), this figure compares magnetic behaviour of Type-I and Type-II superconductors. Left: Type-I superconductivity is destroyed beyond the critical field H_c. Right: Type-II superconductors permit partial magnetic flux penetration between H_{c1} and H_{c2} via quantised flux tubes. Beyond H_{c2}, superconductivity ceases.

5.3.1 Magnetic Flux Quantisation

The explanation for the mixed state observed between H_{c1} and H_{c2} was first provided by Abrikosov. He demonstrated that as the magnetic field exceeds H_{c1}, field lines begin to penetrate the superconductor by forming quantised flux tubes. Each flux tube has a core that exists in a normal (non-superconducting) state and is surrounded by circulating supercurrents. These supercurrents screen the magnetic field from the rest of the superconducting material.

A remarkable property of these flux tubes is that each one allows only a fixed quantum of magnetic flux, given by $\Phi_0 = \frac{h}{2e}$, to pass through. This implies that the magnetic flux is quantised within the flux tubes. For further details, see Annett (2004). If there are N flux tubes within an area A, then the average magnetic flux density is given by:

$$B = \frac{N}{A}\frac{h}{2e}. \tag{5.3}$$

If quantised magnetic flux tubes are indeed present in the neutron star core, they could have profound implications for the star's rotational dynamics, particularly through their interactions with superfluid vortices. These consequences are discussed in detail in Chapter 6.

In the next two sections, we provide a brief overview of superfluidity and the formation of quantised vortices in rotating superfluids.

5.4 Superfluidity

Superfluidity was discovered in 1938 in helium-4 (^{4}He) at temperatures below 2.17 K (Kapitza, 1938; Allen and Misener, 1938). A superfluid is a quantum fluid characterised by zero viscosity, enabling it to flow without any loss of kinetic energy. Superfluids can sustain persistent mass currents (distinct from electric currents), which remain unaffected by external perturbations. The reason why superfluids do not crystallise even at absolute zero lies in their zero-point energy, a direct consequence of the Heisenberg uncertainty principle. When the zero-point energy becomes large enough, it prevents crystallisation. To date, only two helium isotopes—^{4}He and ^{3}He—have been experimentally prepared as superfluids in laboratory conditions (Annett, 2004).

In quantum mechanics, we associate a de Broglie wavelength with particles, given by

$$\lambda_{\mathrm{dB}} = \frac{h}{p},$$

where p is the momentum of the particle. Quantum effects become significant in a liquid when the de Broglie wavelength is comparable to the characteristic interatomic separation. In most liquids, quantum effects can be neglected; however, in liquid helium, the de Broglie wavelength is $\lambda_{\mathrm{dB}} \approx 0.4\,\mathrm{nm}$, which is comparable to the typical interatomic distance $d \approx 0.27\,\mathrm{nm}$. This makes quantum mechanical effects dominant in liquid helium (Annett, 2004).

Following the development of the BCS theory, it was soon speculated that the dense fluid of neutrons in the interior of neutron stars may exhibit superfluidity (Migdal, 1959; Ginzburg, 1969). Neutrons are spin-$\frac{1}{2}$ fermions and are expected to form Cooper pairs, leading to superfluid phases analogous to those observed in ^{3}He (Haskell and Sedrakian, 2018). Neutron stars thus offer a unique astrophysical environment to investigate the behaviour of superfluids under extreme densities and temperatures that are inaccessible in terrestrial laboratories.

Theoretical models suggest that neutrons in the inner crust, where densities are relatively low compared to the core, become superfluid through singlet $^1S_0$ (S-wave) pairing. In contrast, at higher densities in the core, neutron superfluidity is expected to arise from triplet $^3P_2$ and $^3F_2$ (P- and F-wave) pairing channels (Gezerlis et al., 2014). These models further predict that the transition temperature for core superfluidity is lower than that in the crust. This is illustrated in Fig. 5.1, where the solid black curve shows the variation of the transition temperature with respect to density for the singlet pairing channel in the crust, and the solid green curve represents the transition temperature for triplet pairing in the core.

One of the most critical aspects of neutron star superfluidity is the formation of a quantised array of vortices in the rotating neutron condensate. The interaction between

these vortices and the normal fluid component gives rise to a dissipative mechanism known as mutual friction, which plays a central role in regulating the rotational dynamics of neutron stars (Haskell and Sedrakian, 2018; Sidery and Alpar, 2009). This is explored in greater detail in the next chapter. Moreover, vortices can interact with quantised magnetic flux tubes in the superconducting proton component of the core, further influencing the star's dynamics.

5.4.1 Quantised Circulation and Vortices

In this section, we review the formation of quantised superfluid vortices. We begin by defining the macroscopic wave function $\psi_0(\boldsymbol{r})$ associated with the coherent quantum state of the superfluid:

$$\psi_0(\boldsymbol{r}) = \sqrt{n_0(\boldsymbol{r})}\, e^{i\theta(\boldsymbol{r})}, \tag{5.4}$$

where $\sqrt{n_0(\boldsymbol{r})} = |\psi_0(\boldsymbol{r})|$ and $\theta(\boldsymbol{r})$ is the phase of the wave function. Here, n_0 denotes the condensate density. In the language of phase transitions, the function $\psi_0(\boldsymbol{r})$ is referred to as the order parameter.

To derive the expression for the superfluid velocity $\boldsymbol{v_s}$, we consider the standard quantum mechanical formula for the particle current density $\boldsymbol{j_0}$:

$$\boldsymbol{j_0} = \frac{\hbar}{2mi}\left[\psi_0^*(\boldsymbol{r})\,\boldsymbol{\nabla}\psi_0(\boldsymbol{r}) - \psi_0(\boldsymbol{r})\,\boldsymbol{\nabla}\psi_0^*(\boldsymbol{r})\right], \tag{5.5}$$

where the effective mass m appearing in the denominator is defined as

$$m = 2m_n, \tag{5.6}$$

with m_n denoting the mass of a single constituent particle. Thus, the effective mass corresponds to that of a Cooper pair, which is twice the mass of the underlying constituent particle. Note that $\boldsymbol{j_0}$ is not an electric current density, as it corresponds to the flow of neutral particles. Substituting Eq. (5.4) into Eq. (5.5) and simplifying, we obtain:

$$\boldsymbol{j_0} = \frac{\hbar}{m}\, n_0\, \boldsymbol{\nabla}\theta. \tag{5.7}$$

Since the current density is the product of the particle density and velocity, we identify the superfluid velocity as:

$$\boldsymbol{v_s} = \frac{\hbar}{m}\,\boldsymbol{\nabla}\theta. \tag{5.8}$$

Taking the curl of Eq. (5.8) gives:

$$\nabla \times \boldsymbol{v}_s = 0, \tag{5.9}$$

which shows that the superfluid flow is irrotational, as expected for a conservative quantum flow. The irrotational condition expressed in Eq. (5.9) implies that the circulation around any closed loop must vanish:

$$\oint \boldsymbol{v}_s \cdot d\boldsymbol{r} = 0. \tag{5.10}$$

This result would suggest that macroscopic rotation of a superfluid is forbidden. However, this holds only for regions that are free of singularities. Experiments clearly demonstrate that rotating superfluids develop a visible meniscus—indicating bulk rotation—despite the condition in Eq. (5.10). The resolution to this apparent paradox lies in the formation of *quantised vortices*: topological singularities where the phase θ becomes undefined at the vortex core, thereby allowing non-zero circulation. These vortices provide a mechanism by which the superfluid accommodates global rotation while remaining irrotational everywhere except at the cores.

To understand quantised vorticity, we consider the circulation of the superfluid velocity along a closed contour:

$$\kappa = \oint \boldsymbol{v}_s \cdot d\boldsymbol{r}. \tag{5.11}$$

Using Eq. (5.8) in Eq. (5.11), we find:

$$\kappa = \frac{\hbar}{m} \oint \nabla\theta \cdot d\boldsymbol{r}. \tag{5.12}$$

This results in:

$$\kappa = \frac{\hbar}{m}(\theta_2 - \theta_1), \tag{5.13}$$

where $\theta_2 - \theta_1$ is the net phase change along the path. For the wave function $\psi_0(\boldsymbol{r})$ to be single-valued, this phase change must satisfy:

$$\theta_2 - \theta_1 = 2\pi n, \tag{5.14}$$

where $n \in \mathbb{Z}$. Substituting Eq. (5.14) into Eq. (5.13) yields the quantised circulation:

$$\kappa = \frac{h}{m} n. \tag{5.15}$$

In practice, only $n = \pm 1$ vortices are observed as they correspond to the lowest-energy configuration. This quantisation of circulation has been experimentally verified in various systems (Rayfield and Reif, 1963; Yarmchuk et al., 1979; Tang et al., 2023).

The velocity field associated with a single vortex is expressed as

$$\boldsymbol{v_s} = \frac{\kappa}{2\pi r} \hat{e}_\phi, \tag{5.16}$$

which satisfies the irrotational condition everywhere except at $r = 0$, i.e., the vortex core. This allows rotating superfluids to support macroscopic angular momentum.

Each vortex contributes an amount of circulation h/m. For a cylindrical container of radius R rotating at angular velocity Ω_n, the total circulation at the boundary is:

$$C = \oint \boldsymbol{v_s} \cdot d\boldsymbol{r} = (2\pi R)(\Omega_n R). \tag{5.17}$$

Using the quantised circulation condition:

$$C = \frac{h}{m} N, \tag{5.18}$$

where N is the number of vortices, we equate Eq. (5.17) and Eq. (5.18) to find the vortex areal density:

$$\frac{N}{\pi R^2} = n_v = \frac{2m\Omega_n}{h}, \tag{5.19}$$

which rearranges to give:

$$\Omega_n = \frac{\kappa n_v}{2}, \tag{5.20}$$

where n_v is the number of vortices per unit area. This relation shows that the surface density of vortices in a rotating superfluid is directly proportional to the angular velocity Ω_n of the superfluid. This result has been experimentally verified in a number of laboratory systems, including superfluid helium and atomic Bose–Einstein condensates.

Changes in the rotation rate of the superfluid are governed by the radial motion of these vortices. When vortices migrate inward, the superfluid spins up; conversely, outward

motion of vortices causes the superfluid to spin down. This vortex-mediated mechanism provides a natural explanation for sudden spin-up events, known as *glitches*, observed in neutron stars. In such systems, the interplay between superfluid vortices and their environment (e.g., pinning to the crust or interactions with flux tubes) plays a key role in the dynamics of rotational evolution.

In this chapter, we briefly reviewed the concepts of superconductivity and superfluidity, including the formation of magnetic flux tubes and quantised superfluid vortices. These topological structures arise due to macroscopic quantum coherence and play a vital role in determining the internal structure and dynamics of neutron stars. In the following chapters, we will explore how the presence and interactions of these features, particularly the coupling between superfluid vortices and magnetic flux tubes or crustal nuclei, affect the internal dynamics, rotational behaviour, and crustal deformations of neutron stars.

Chapter 6

Rotational dynamics of a Neutron star

In this chapter, we review the standard model that describes how uniformly distributed vortices interact with the rest of a rotating neutron star, and then extend the discussion to the case of an asymmetric distribution of vortices. We re-derive several established results from the literature, including the expression for the coupling timescale between the neutron star's core superfluid and the crust, as well as the time evolution of the angular velocities of both the superfluid and the crust.

In theory, vortex lines moving outward may pin to flux tubes and crustal nuclei, and such pinning is energetically favoured. If the pinning of vortex lines is non-axisymmetric, it can generate a non-axisymmetric neutron superfluid velocity field, which in turn may lead to a non-zero quadrupole moment. This quadrupole moment can then act as a source of continuous gravitational waves. The foundations of this idea are presented in detail in Chapters 7 and 8.

Previously, Sidery and Alpar (2009) considered anisotropy in the pinning of vortices and studied its impact on the rotational dynamics of the star. We have carefully examined their work to understand how a non-axisymmetric distribution of vortices can arise, and how it can lead to a non-axisymmetric neutron superfluid velocity field, which in turn gives rise to the formation of a Magnus mountain.

All calculations presented in this chapter are based on Sidery and Alpar (2009). Some sections are reproduced directly from their work, while others are newly derived, though the underlying framework follows their model. A clear distinction between these cases will be made as we proceed through each section. The ideas presented in this chapter could be used for developing a self-consistent formulation of Magnus mountain formation. However, in Chapters 7 and 8 we instead adopt a simpler approach, specifying a non-axisymmetric distribution of vortices by hand.

In theory, the neutron fluid inside a neutron star is expected to exist in a superfluid state. Since the neutron fluid constitutes the bulk of the moment of inertia of the star, it has a significant influence on the rotational dynamics. The protons in the core are also expected to form a type-II superconductor. Experiments show that a type-II superconductor contains flux tubes through which quantised magnetic flux penetrates. The proton superconductor therefore interacts with the neutron superfluid, influencing the overall rotational dynamics. The coupling between the core superfluid and the crust occurs through a process known as *spontaneous magnetisation*. In this process, the circulation of the neutron superfluid around vortex lines drags the proton superconductor, thereby magnetising the vortex lines. This dragging effect is termed *entrainment*, a fundamental property of a two-fluid system in motion (Andersson, 2021). These magnetised vortex lines strongly scatter the charged component, which is itself strongly coupled to the crust via electron viscosity (Sidery and Alpar, 2009; Haskell and Sedrakian, 2018).

Observational evidence for the processes governing neutron star dynamics comes from the study of glitches. Glitches are sudden jumps in the angular velocity of the star. Since no accompanying signatures have been observed in the magnetosphere during glitches, it is believed that the mechanism responsible is internal. The most widely accepted model attributes glitches to the transfer of angular momentum from the superfluid in the inner crust to the crust itself. In this model, as the neutron star spins down, vortex lines gradually migrate outward toward the crust. These vortex lines become pinned to the crystal lattice sites of the crust. Because of this pinning, the superfluid cannot spin down while the crust continues to slow down. Once the lag between the angular velocities of the superfluid and the crust reaches a critical value, the Magnus force exceeds the pinning force, and the vortex lines unpin, moving outward and transferring angular momentum to the crust. This sudden transfer causes a measurable increase in the star's angular velocity (Anderson and Itoh, 1975; Alpar, 1977; Haskell and Melatos, 2015).

To begin, we first study the simpler case of a uniformly distributed vortex array in the absence of flux tubes in the core. We then consider the more complex scenario in which both vortex lines and flux tubes are present, investigating how they interact and how this interaction influences the rotational dynamics of the star. The different cases considered in this chapter are summarised schematically in Figure 6.1.

6.1 Local forces acting on vortex lines

We consider a two-component system. The first component is the neutron superfluid, while the second is the charged component, consisting of electrons, protons, and the solid crust. If the charged component in a neutron star were replaced with a normal

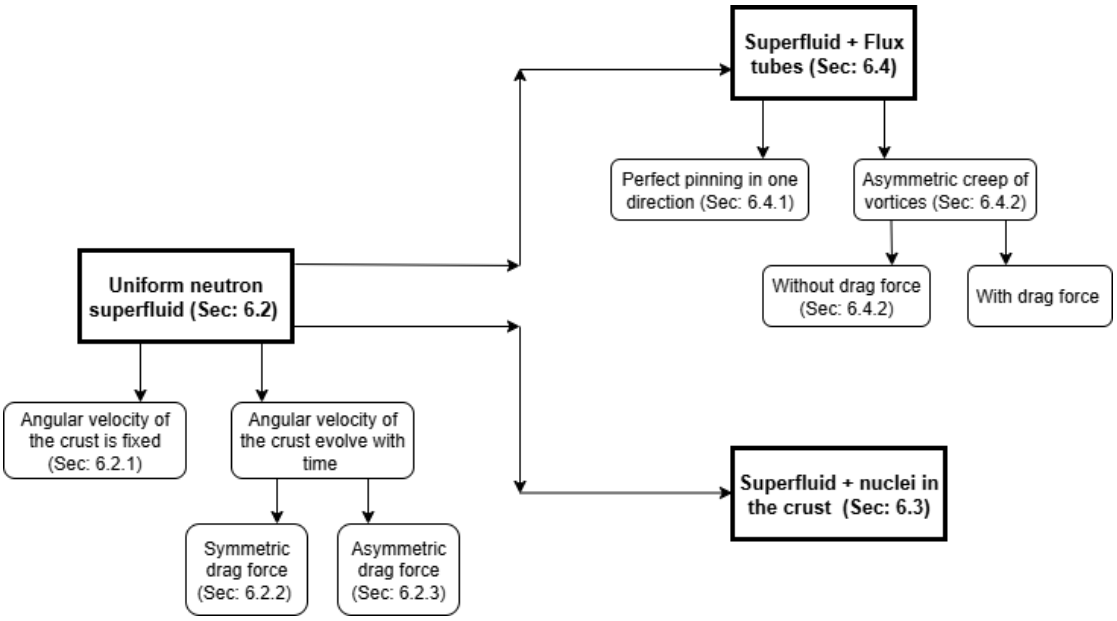

FIGURE 6.1: Map of all the different cases in which we calculate the dynamical coupling timescale.

fluid, the system would resemble superfluid helium, which can be studied in the laboratory. Since superfluid helium has been extensively investigated, it provides valuable insight into the dynamics of neutron superfluid vortices in neutron stars.

We now examine the local forces acting on vortex lines when they interact with the charged component. In this case, vortex lines are subject to two principal forces.

The first is the *Magnus force*, denoted by $\boldsymbol{F_m}$, acting per unit length of a vortex line:

$$\boldsymbol{F_m} = \rho_n \boldsymbol{\kappa} \times (\boldsymbol{v_n} - \boldsymbol{v_L}), \tag{6.1}$$

where ρ_n is the mass density of the superfluid neutrons, $\boldsymbol{v_n}$ is the neutron superfluid velocity, $\boldsymbol{v_L}$ is the velocity of the vortex line and, $\kappa = \frac{h}{2m_n}$ is the circulation quantum per vortex line directed along the rotation axis, where $2m_n$ represents the mass of a Cooper pair of superfluid neutrons.

The second is the *drag force*, $\boldsymbol{F_d}$, which arises from the scattering of charged particles off spontaneously magnetised vortex lines. Per unit length of a vortex line, the drag force is given by

$$\boldsymbol{F_d} = C\,(\boldsymbol{v_c} - \boldsymbol{v_L}) = \frac{\rho_c}{n_v \tau_v}\,(\boldsymbol{v_c} - \boldsymbol{v_L}), \tag{6.2}$$

where $C = \frac{\rho_c}{n_v \tau_v}$ is the drag coefficient, ρ_c is the mass density of the charged component, $n_v = \frac{2\Omega_n}{\kappa}$ is the number of vortex lines per unit area, τ_v is the relaxation time for the interaction between vortex lines and the charged component, and $\boldsymbol{v_c}$ is the velocity of the charged component.

Together, these two forces govern the motion and stability of vortex lines within the neutron star interior.

6.2 Rotational dynamics in the case of uniformly distributed vortices

In this section, we analyse how the local forces discussed above influence the dynamics of the uniformly distributed vortices and, in turn, the rotational behaviour of the star. Specifically, we calculate the dynamical coupling timescale of the superfluid and the crust under three different scenarios:

1. The angular velocity of the crust is held fixed, i.e., angular momentum conservation is not enforced. This calculation is reproduced from Alpar and Sauls (1988).
2. The angular velocity of the crust is allowed to evolve in time, with angular momentum conservation imposed, assuming an axisymmetric drag force acting on the vortices. This calculation is reproduced from Sidery and Alpar (2009).
3. Angular momentum conservation is imposed, but with a non-axisymmetric drag force acting on the vortices along the x- and y-axes. This calculation is developed here for the first time.

6.2.1 Dynamical coupling timescale with fixed crustal angular velocity

We begin by reproducing the calculation of the coupling timescale t_d for the neutron star's core superfluid and the crust, as presented by Alpar and Sauls (1988). In their model, angular momentum conservation was not considered, as the angular velocity of the crust was assumed to be constant.

The geometry is simplified to that of a rotating cylinder with angular velocity Ω_0, where vortices are uniformly distributed and aligned along the z-axis, which coincides with the axis of rotation. The charged component (the crust), which is initially co-rotating with the superfluid, acquires an angular velocity Ω. It is assumed that the crust always rotates rigidly.

Since the size of a vortex core is extremely small (on the order of 1 Å in superfluid ^{4}He), the inertial mass of a vortex is negligible. Thus, vortices may be considered effectively massless, and the force balance condition reduces to

$$\boldsymbol{F}_m + \boldsymbol{F}_d = 0. \tag{6.3}$$

Inserting the expressions for $\boldsymbol{F_m}$ and $\boldsymbol{F_d}$, given in equations (6.1) and (6.2), respectively, into equation (6.3) gives

$$C(\boldsymbol{v_c} - \boldsymbol{v_L}) = \rho_n \boldsymbol{\kappa} \times (\boldsymbol{v_n} - \boldsymbol{v_L}), \tag{6.4}$$

where $\boldsymbol{\kappa}$ is aligned with the rotation axis, chosen as the z-axis:

$$\boldsymbol{\kappa} = \kappa \hat{k}. \tag{6.5}$$

Rearranging equation (6.4) gives

$$\frac{C}{\rho_n \kappa} \boldsymbol{v_c} - \hat{k} \times \boldsymbol{v_n} = \frac{C}{\rho_n \kappa} \boldsymbol{v_L} - \hat{k} \times \boldsymbol{v_L}. \tag{6.6}$$

Taking the cross product of both sides of equation (6.6) with $\boldsymbol{\kappa}$ yields

$$\frac{C}{\rho_n \kappa} \hat{k} \times \boldsymbol{v_c} - \hat{k} \times (\hat{k} \times \boldsymbol{v_n}) = \frac{C}{\rho_n \kappa} \hat{k} \times \boldsymbol{v_L} - \hat{k} \times (\hat{k} \times \boldsymbol{v_L}). \tag{6.7}$$

Using the vector triple product identity,

$$\boldsymbol{A} \times (\boldsymbol{B} \times \boldsymbol{C}) = (\boldsymbol{A} \cdot \boldsymbol{C})\boldsymbol{B} - (\boldsymbol{A} \cdot \boldsymbol{B})\boldsymbol{C}, \tag{6.8}$$

equation (6.7) simplifies to

$$\frac{C}{\rho_n \kappa} \hat{k} \times \boldsymbol{v_c} + \boldsymbol{v_n} = \frac{C}{\rho_n \kappa} \hat{k} \times \boldsymbol{v_L} + \boldsymbol{v_L}. \tag{6.9}$$

Next, multiplying equation (6.6) by $\frac{C}{\rho_n \kappa}$ gives

$$\left(\frac{C}{\rho_n \kappa}\right)^2 \boldsymbol{v_c} - \frac{C}{\rho_n \kappa} \hat{k} \times \boldsymbol{v_n} = \left(\frac{C}{\rho_n \kappa}\right)^2 \boldsymbol{v_L} - \frac{C}{\rho_n \kappa} \hat{k} \times \boldsymbol{v_L}. \tag{6.10}$$

Adding equations (6.9) and (6.10), we obtain the vortex line velocity:

$$\boldsymbol{v_L} = \beta\, \hat{k} \times \boldsymbol{v_c} + \frac{\boldsymbol{v_n}}{1 + \left(\frac{C}{\rho_n \kappa}\right)^2} + \beta' \boldsymbol{v_c} - \beta \hat{k} \times \boldsymbol{v_n}, \tag{6.11}$$

where

$$\beta = \frac{\frac{C}{\rho_n \kappa}}{1 + \left(\frac{C}{\rho_n \kappa}\right)^2}, \qquad \beta' = \frac{\left(\frac{C}{\rho_n \kappa}\right)^2}{1 + \left(\frac{C}{\rho_n \kappa}\right)^2}. \tag{6.12}$$

The velocity of the charged component (the crust) is given by

$$\boldsymbol{v_c} = \Omega r \hat{e_\phi}, \tag{6.13}$$

and the velocity of the neutron superfluid is given by

$$\boldsymbol{v_n} = \Omega_n \hat{e_\phi}, \tag{6.14}$$

which can be expressed in terms of the initial angular velocity Ω_0 by noting that the total number of vortices enclosed within a radius $r(t)$ remains conserved. At $t = 0$, the number of vortices per unit area within a radius r_0 is

$$n_\nu(r_0) = \frac{N}{\pi r_0^2}, \tag{6.15}$$

where N is the total number of vortices within radius r_0. At time t, the vortex density is

$$n_\nu(r(t)) = \frac{N}{\pi r^2(t)}. \tag{6.16}$$

Equations (6.15) and (6.16) together give

$$n_\nu(r(t)) = \frac{n_\nu(r_0) r_0^2}{r^2(t)}. \tag{6.17}$$

Substituting equation (6.17) into the relation between the superfluid angular velocity Ω_n and the vortex density n_ν, as given in equation (5.20), yields

$$\Omega_n = \frac{\kappa n_\nu(r_0) r_0^2}{2r^2(t)}. \tag{6.18}$$

Using

$$\Omega_0 = \frac{\kappa n_\nu(r_0)}{2}, \tag{6.19}$$

equation (6.18) becomes

$$\Omega_n = \frac{\Omega_0 r_0^2}{r^2(t)}. \tag{6.20}$$

Substituting equation (6.18) into the expression for the neutron superfluid velocity, equation (6.14), gives

$$\boldsymbol{v_n} = \frac{\Omega_0 r_0^2}{r(t)} \hat{e_\phi}. \tag{6.21}$$

Finally, substituting the expressions for $\boldsymbol{v_c}$ from equation (6.13) and $\boldsymbol{v_n}$ from equation (6.21) into the expression for the vortex line velocity $\boldsymbol{v_L}$, equation (6.10), we obtain

the azimuthal and radial components of the vortex velocity:

$$\frac{d\phi}{dt} = -\frac{\rho_c}{r\rho_n n_v \tau_v \kappa}\frac{dr}{dt} + \frac{\Omega_0 r_0^2}{r^2}, \tag{6.22}$$

$$\frac{dr}{dt} = \frac{\rho_c r}{\rho_n n_v \tau_v \kappa}\left(\frac{d\phi}{dt} - \Omega\right). \tag{6.23}$$

Here, the crustal angular velocity Ω is fixed, meaning angular momentum conservation is not imposed.

Integrating equations (6.22) and (6.23) gives the following solutions:

$$\phi(t) = \phi_0 + \Omega t + \frac{\rho_n n_v \tau_v \kappa}{\rho_c}\log\left(\frac{r(t)}{r_0}\right), \tag{6.24}$$

$$r(t) = r_0\left[\frac{\Omega_0}{\Omega} + \left(1 - \frac{\Omega_0}{\Omega}\right)e^{-\frac{t}{t_d}}\right]^{\frac{1}{2}}, \tag{6.25}$$

where ϕ_0 and r_0 are the initial azimuthal and radial positions of the vortex line, and

$$t_d = \frac{1}{2\Omega}\left(\frac{\rho_c}{\rho_n n_v \tau_v \kappa} + \frac{\rho_n n_v \tau_v \kappa}{\rho_c}\right) \tag{6.26}$$

is the dynamical coupling timescale.

In the weak-drag limit ($\tau_v \to \infty$), the first term in equation (6.26) vanishes, while the second term diverges. In the strong-drag limit ($\tau_v \to 0$), the second term vanishes, while the first term diverges. In both cases, the timescale t_d tends to infinity. This behaviour is expected. In the weak-drag limit, the neutron vortices are unable to interact effectively with the charged component, and therefore it takes an indefinitely long time for the vortices to move outward in response to the changing angular velocity of the crust. In the strong-drag limit, the vortices are too tightly coupled to the charged component, which also prevents them from moving outward, and consequently it takes a long time for the angular velocity of the neutron superfluid to adjust to that of the crust.

Thus, we have reproduced the solutions for $\phi(t)$ and $r(t)$ given in equations (6.24) and (6.25), and we have also recovered the expression for the coupling timescale t_d as derived by Alpar and Sauls (1988). In the next subsection, we will investigate how the dynamical coupling timescale is modified when angular momentum conservation is taken into account.

6.2.2 Dynamical coupling timescale with the conservation of angular momentum in the case of symmetric drag force

In the previous section, angular momentum conservation was not imposed, since the angular velocity of the charged component Ω_c was kept fixed. In this section, we allow Ω_c to evolve with time and explicitly enforce angular momentum conservation. To do so, we adopt a rigid-body dynamics approach. We derive the time-evolution equations for the superfluid angular velocity Ω_n, the angular velocity of the charged component Ω_c, the lag $\omega = \Omega_n - \Omega_c$ between them, and the associated dynamical coupling timescale.

We consider a spherical two-component star consisting of a neutron superfluid and a charged component, the latter representing the crust. An initial lag is assumed between the two components, given by

$$\omega_0 = \Omega_{n,0} - \Omega_{c,0}, \tag{6.27}$$

where $\Omega_{n,0}$ and $\Omega_{c,0}$ denote the initial angular velocities of the neutron superfluid and the charged component, respectively. The initial lag is taken to be positive, representing the scenario immediately after a glitch.

Substituting expression of vortex line velocity v_L equation (6.11) into the expression for the Magnus force $\boldsymbol{F_m}$ in equation (6.1), we obtain

$$\boldsymbol{F_m} = \rho_n \kappa \beta' \hat{\kappa} \times (\boldsymbol{v_n} - \boldsymbol{v_c}) - \rho_n \kappa \beta (\boldsymbol{v_n} - \boldsymbol{v_c}). \tag{6.28}$$

We now assume that $\boldsymbol{v_n} - \boldsymbol{v_c}$ and $\boldsymbol{v_L}$ are perpendicular to $\hat{k}$. The force per unit length acting on a pinning site in the crust is $-\boldsymbol{F_d}$, which equals $\boldsymbol{F_m}$ according to equation (6.3). To obtain the force per unit volume of the crust, we multiply equation (6.28) by the number density of vortices n_v, giving

$$\tilde{\boldsymbol{F}}_{\boldsymbol{d}} = -\boldsymbol{F_d} = -n_v \rho_n \kappa \beta' r(\Omega_n - \Omega_c) - n_v \rho_n \kappa \beta r(\Omega_n - \Omega_c). \tag{6.29}$$

The negative sign in the first term arises from the cross product. The total torque $\boldsymbol{T}$ acting on the crust is

$$\boldsymbol{T} = I_c \dot{\Omega}_c = \int_V (\tilde{\boldsymbol{F}}_{\boldsymbol{d}} \times \boldsymbol{r})\, dV. \tag{6.30}$$

Inserting equation (6.29) into (6.30), we find

$$I_c \dot{\Omega}_c = \int_V n_v \rho_n \kappa \beta\, r^2 (\Omega_n - \Omega_c)\, dV. \tag{6.31}$$

After integrating and rewriting ρ_n in terms of the moment of inertia I_n, this becomes

$$I_c\dot{\Omega}_c = I_n n_v \kappa \beta (\Omega_n - \Omega_c). \tag{6.32}$$

Substituting expression of vortex density n_v equations (5.20) and β (6.12) into equation (6.32) yields

$$I_c\dot{\Omega}_c = 2I_n\Omega_n \left[\frac{\frac{C}{\rho_n\kappa}}{1+\left(\frac{C}{\rho_n\kappa}\right)^2} \right] (\Omega_n - \Omega_c). \tag{6.33}$$

Angular momentum conservation requires

$$I_n\Omega_{n,0} + I_c\Omega_{c,0} = I_n\Omega_n + I_c\Omega_c, \tag{6.34}$$

which implies

$$\dot{\Omega}_n = -\frac{I_c\dot{\Omega}_c}{I_n}. \tag{6.35}$$

Using equations (6.34) and (6.35), equation (6.33) becomes

$$\dot{\Omega}_n = 2\Omega_n \left[\frac{\frac{C}{\rho_n\kappa}}{1+\left(\frac{C}{\rho_n\kappa}\right)^2} \right] \left(\frac{I_n\Omega_{n,0} + I_c\Omega_{c,0} - I_n\Omega_n}{I_c} - \Omega_n \right). \tag{6.36}$$

This differential equation can be analysed in three different regimes, depending on the value of the drag coefficient C:

- weak-coupling regime,
- strong-coupling regime,
- general intermediate regime.

6.2.2.1 Weak-coupling regime

In the weak-coupling regime, the relaxation timescale τ_v between the neutron vortices and the charged component is very large, and hence the drag coefficient C is very small. In this regime,

$$C = \frac{\rho_c}{n_v\tau_v} \ll 1,$$

which allows us to approximate equation (6.36) as

$$\dot{\Omega}_n = \frac{2\Omega_n C}{\rho_n\kappa} \left(\frac{I_n\Omega_{n,0} + I_c\Omega_{c,0} - I_n\Omega_n}{I_c} - \Omega_n \right). \tag{6.37}$$

Using the expression for n_v given in equation (5.20), together with the expression for C, equation (6.37) can be rewritten as

$$\dot{\Omega}_n = \frac{\rho_c}{\rho_n \tau_v} \left(\frac{I_n \Omega_{n,0} + I_c \Omega_{c,0} - I_n \Omega_n}{I_c} - \Omega_n \right). \tag{6.38}$$

The analytic solution of equation (6.38) is

$$\Omega_n(t) = \frac{I_n \Omega_{n,0} + I_c \Omega_{c,0} - e^{-\frac{t}{t_d}} I_n (\Omega_{c,0} - \Omega_{n,0})}{I}, \tag{6.39}$$

where

$$t_d = \frac{\rho_n \tau_v}{\rho} \tag{6.40}$$

is the dynamical relaxation time and $\rho = \rho_n + \rho_c$ is the total density. Using $C = \frac{\rho_c}{n_v \tau_v}$ and $n_v = \frac{2\Omega_n}{\kappa}$, equation (6.40) becomes

$$t_d = \frac{\rho_c}{2\rho\,\Omega_n} \frac{\kappa \rho_n}{C}. \tag{6.41}$$

Using angular momentum conservation from equation (6.34), the angular velocity of the crust is

$$\Omega_c(t) = \frac{I_n \Omega_{n,0} + I_c \Omega_{c,0} + e^{-\frac{t}{t_d}} I_n (\Omega_{c,0} - \Omega_{n,0})}{I}, \tag{6.42}$$

and the lag is

$$\omega(t) = e^{-\frac{t}{t_d}} (\Omega_{n,0} - \Omega_{c,0}). \tag{6.43}$$

We also solved equation (6.38) numerically using Python and plotted the solutions, as shown in Fig. 6.2. A non-physical large value of the initial lag ω_0 was chosen for illustrative purposes, to better demonstrate the behaviour of the system.

Figure 6.2 shows the time evolution of Ω_n, Ω_c, and ω. As the star spins down, superfluid vortices move outward and transfer angular momentum to the crust, spinning it up. Since the typical ratio of $\frac{I_c}{I_n} \approx 0.05$ (as neutron star matter consists predominantly of neutrons), even a small transfer of angular momentum from the superfluid produces a relatively larger change in the angular velocity of the crust.

6.2.2.2 Strong-coupling regime

In the strong-coupling regime, the relaxation timescale τ_v between the neutron vortices and the charged component is very small, leading to the very large value of the drag coefficient C. In this regime,

$$C = \frac{\rho_c}{n_v \tau_v} \gg 1,$$

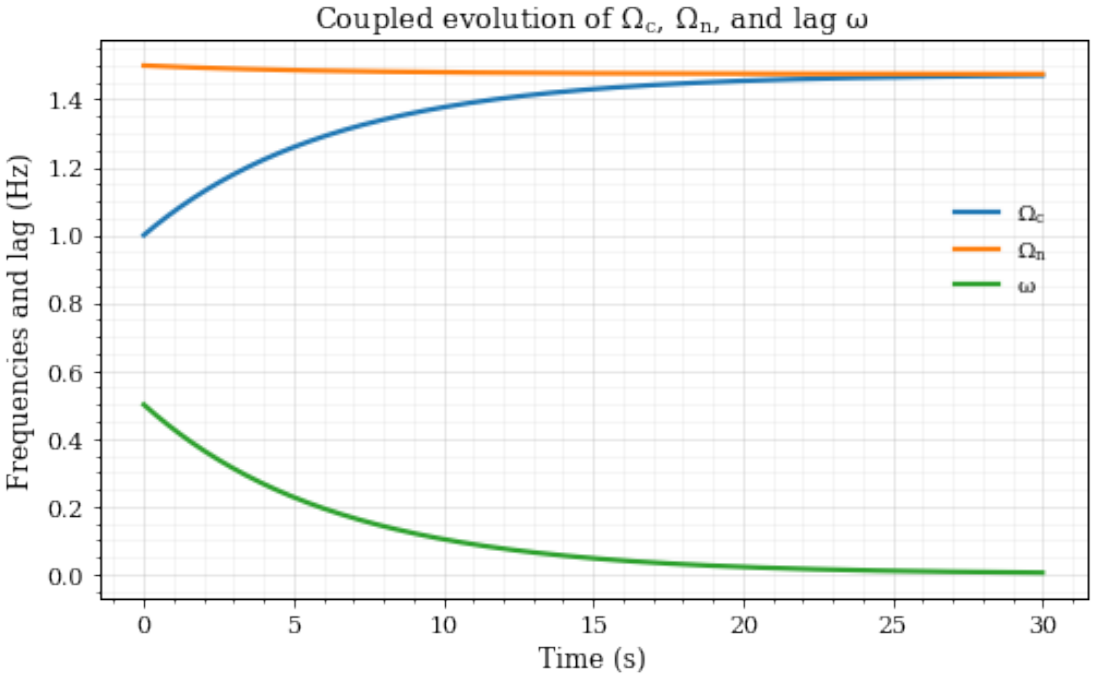

FIGURE 6.2: Time evolution of the superfluid angular velocity Ω_n, the charged component angular velocity Ω_c, and the lag ω in the weak-coupling regime.

and equation (6.36) simplifies to

$$\dot{\Omega}_n = 4\frac{\rho_n \tau_v}{\rho_c}\Omega_n^2 \left(\frac{I_n\Omega_{n,0} + I_c\Omega_{c,0} - I_n\Omega_n}{I_c} - \Omega_n \right). \tag{6.44}$$

The implicit analytic solution of equation (6.44) is

$$\frac{I^2}{(I_n\Omega_{n,0} + I_c\Omega_{c,0})^2} \ln\left[\frac{\Omega_n - \frac{I_n\Omega_{n,0} + I_c\Omega_{c,0}}{I}}{\Omega_n} \right] + \frac{I}{(I_n\Omega_{n,0} + I_c\Omega_{c,0})\Omega_n} = -\left(\frac{2\rho_n\tau_v\rho}{\rho_c^2} \right) t + C_1, \tag{6.45}$$

where C_1 is an integration constant.

To obtain an explicit solution, we assume that the fractional change in the superfluid angular velocity is small, i.e.

$$\Omega_n(t) = \Omega_{n,0} + \Delta\Omega_n, \tag{6.46}$$

with

$$\frac{\Delta\Omega_n(t)}{\Omega_{n,0}} \ll 1. \tag{6.47}$$

Rearranging equation (6.44) gives

$$\dot{\Omega}_n = \frac{2\rho_n\tau_v(I_n\Omega_{n,0} + I_c\Omega_{c,0})}{I_c\rho_c}\Omega_n^2 - \frac{2\rho_n\tau_v I}{I_c\rho_c}\Omega_n^3. \tag{6.48}$$

Substituting equation (6.46) into equation (6.48) and linearising yields

$$\Delta\dot{\Omega}_n = \frac{2\rho_n(I_n\Omega_{n,0} + I_c\Omega_{c,0})}{I_c C n_\nu}\Omega_{n,0}^2\left(1 + 2\frac{\Delta\Omega_n(t)}{\Omega_{n,0}}\right) - \frac{2\rho_n I}{I_c C n_\nu}\Omega_{n,0}^3\left(1 + 3\frac{\Delta\Omega_n(t)}{\Omega_{n,0}}\right). \tag{6.49}$$

Solving equation (6.49), we obtain the explicit solutions

$$\Omega_n(t) = \Omega_{n,0} + \frac{I_c\Omega_{n,0}\omega_0(e^{-\frac{t}{t_d}} - 1)}{I\Omega_{n,0} + 2I_c\omega_0}, \tag{6.50}$$

$$\Omega_c(t) = \Omega_{c,0} - \frac{I_n\Omega_{n,0}\omega_0(e^{-\frac{t}{t_d}} - 1)}{I\Omega_{n,0} + 2I_c\omega_0}, \tag{6.51}$$

and

$$\omega(t) = \omega_0 + \frac{I\Omega_{n,0}\omega_0(e^{-\frac{t}{t_d}} - 1)}{I\Omega_{n,0} + 2I_c\omega_0}, \tag{6.52}$$

where

$$t_d = \frac{I_c\rho_c}{2\rho_n\tau_\nu\Omega_{n,0}(I\Omega_{n,0} + 2I_c\omega_0)}. \tag{6.53}$$

We note that the lag ω does not vanish as $t \to \infty$ in equation (6.52). This discrepancy arises from the linearisation of equation (6.48) to obtain an explicit solution. However, if we assume the initial lag satisfies $\omega_0 \ll \Omega_{n,0}$, which is a reasonable approximation, then the lag does indeed vanish as $t \to \infty$.

Equation (6.44) was also solved numerically using Python, and the solutions are plotted in Fig. 6.4. In this case, the lag ω decays to zero at late times, as seen more clearly in the log-log plot of Fig. 6.5. The behaviour of Ω_n and Ω_c in Fig. 6.4 is similar to that obtained in the weak-coupling regime: because the ratio $\frac{I_c}{I_n} \approx 0.05$ is small, even a small transfer of angular momentum from the superfluid leads to a comparatively larger change in the angular velocity of the crust.

6.2.2.3 General regime

In the general regime, equation (6.36) cannot be simplified by assuming either a very large or very small relaxation time τ_ν. We therefore solve equation (6.36) directly, which yields an implicit solution of the same implicit type as that obtained in the strong-drag regime (see Eq. (6.45)). We do not present the intermediate steps here, as the procedure closely follows that used in the strong-drag case. As in the strong-coupling case, we assume that the fractional change in the superfluid angular velocity is small and linearise the ODE (6.36) to obtain analytic solutions. These are

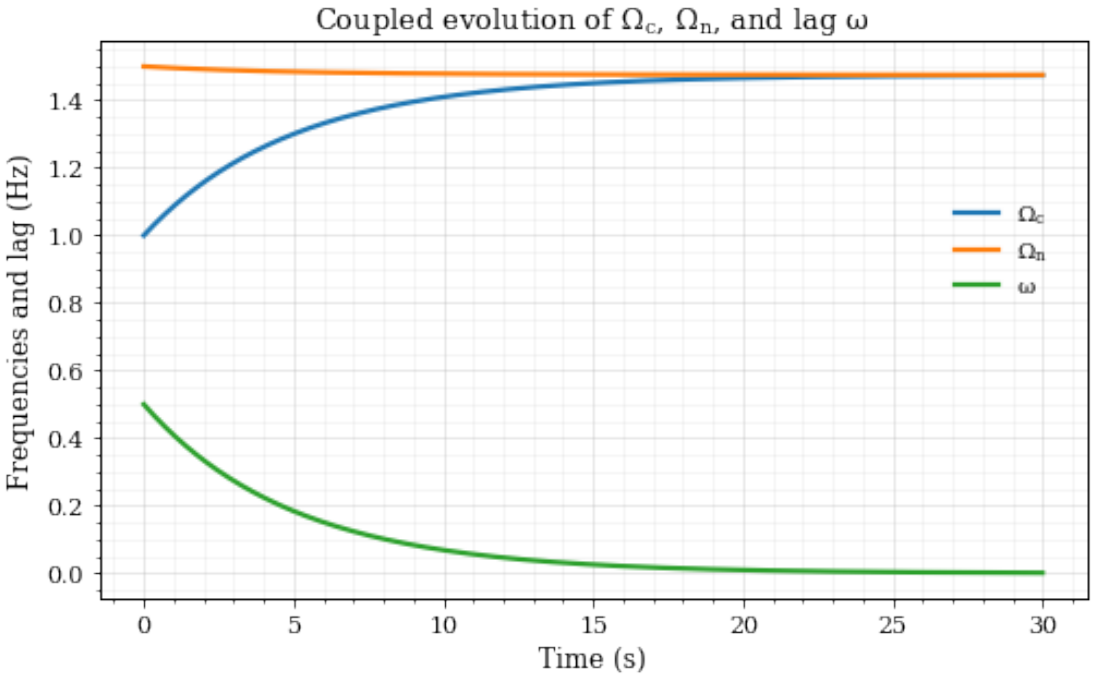

FIGURE 6.4: Time evolution of the superfluid angular velocity Ω_n, the charged component angular velocity Ω_c, and the lag ω in the strong-coupling regime.

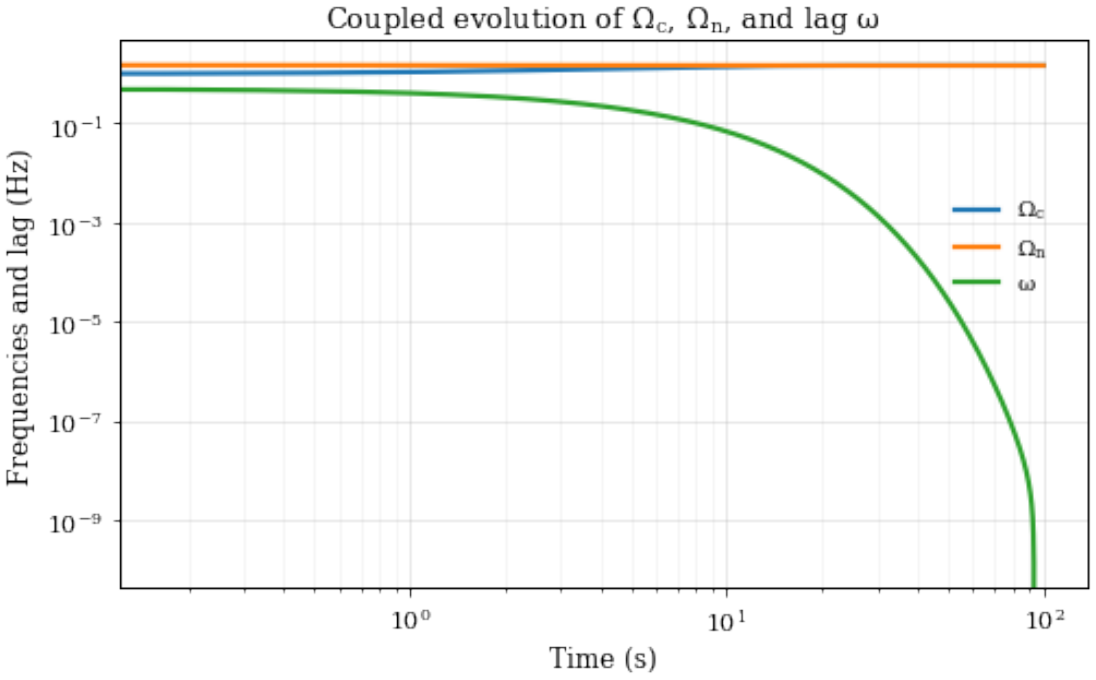

FIGURE 6.5: Log-log plot showing the decay of the lag ω in the strong-coupling regime.

$$\Omega_n(t) = \Omega_{n,0} + \frac{I_c\omega_0\Omega_{n,0}(4\rho_n^2\tau_\nu^2\Omega_{n,0}^2 + \rho_c^2)(e^{-\frac{t}{t_d}} - 1)}{\rho_c^2(I\Omega_{n,0} + I_c\omega_0) + 4I\rho_n^2\tau_\nu^2\Omega_{n,0}^3}, \tag{6.54}$$

$$\Omega_c(t) = \Omega_{c,0} - \frac{I_n\omega_0\Omega_{n,0}(4\rho_n^2\tau_\nu^2\Omega_{n,0}^2 + \rho_c^2)(e^{-\frac{t}{t_d}} - 1)}{\rho_c^2(I\Omega_{n,0} + I_c\omega_0) + 4I\rho_n^2\tau_\nu^2\Omega_{n,0}^3}, \tag{6.55}$$

and

$$\omega(t) = \omega_0 + \frac{I\omega_0\Omega_{n,0}(4\rho_n^2\tau_\nu^2\Omega_{n,0}^2 + \rho_c^2)(e^{-\frac{t}{t_d}} - 1)}{\rho_c^2(I\Omega_{n,0} + I_c\omega_0) + 4I\rho_n^2\tau_\nu^2\Omega_{n,0}^3}, \tag{6.56}$$

where

$$t_d = \frac{I_c(4\rho_n^2\tau_\nu^2\Omega_{n,0}^2 + \rho_c^2)^2}{4\rho_n\rho_c\tau_\nu\Omega_{n,0}\left[\rho_c^2(I\Omega_{n,0} + I_c\omega_0) + 4I\rho_n^2\tau_\nu^2\Omega_{n,0}^3\right]} \tag{6.57}$$

is the dynamical relaxation timescale.

As in the strong-coupling case, the lag ω in equation (6.56) does not appear to vanish as $t \to \infty$, which again is a consequence of the linearisation. If we assume $\omega_0 \ll \Omega_{n,0}$, then the lag simplifies to

$$\omega(t) = \omega_0 + \omega_0(e^{-\frac{t}{t_d}} - 1), \tag{6.58}$$

and it does vanish as $t \to \infty$.

Under the same assumption, the timescale in equation (6.57) reduces to

$$t_d = \frac{I_c(4\rho_n^2\tau_\nu^2\Omega_{n,0}^2 + \rho_c^2)}{4I\rho_n\rho_c\tau_\nu\Omega_{n,0}^2}. \tag{6.59}$$

We see that in the weak-drag limit ($\tau_\nu \to \infty$), the coupling timescale t_d tends to infinity. Similarly, in the strong-drag limit ($\tau_\nu \to 0$), t_d also tends to infinity. This behaviour is the same as that obtained in Section 6.2.1.

Equation (6.36) was also solved numerically, and the solutions are plotted in Fig. 6.6. Once again, we see that the lag ω decays to zero, which is more clearly visible in the log-log plot shown in Fig. 6.7.

We have therefore derived the time evolution of the crust and superfluid angular velocities using a rigid-body dynamics approach. Starting from a spinning-down system with a positive lag, we followed its evolution with time.

The plots in all three regimes display qualitatively similar behaviour. The key difference lies in the value of the dynamical coupling timescale t_d. In both the weak- and strong-coupling regimes, t_d is larger than in the general case. In the weak-coupling regime, the charged component couples only weakly to the superfluid, so the response time of the superfluid is long. In the strong-coupling regime, the interaction is so strong

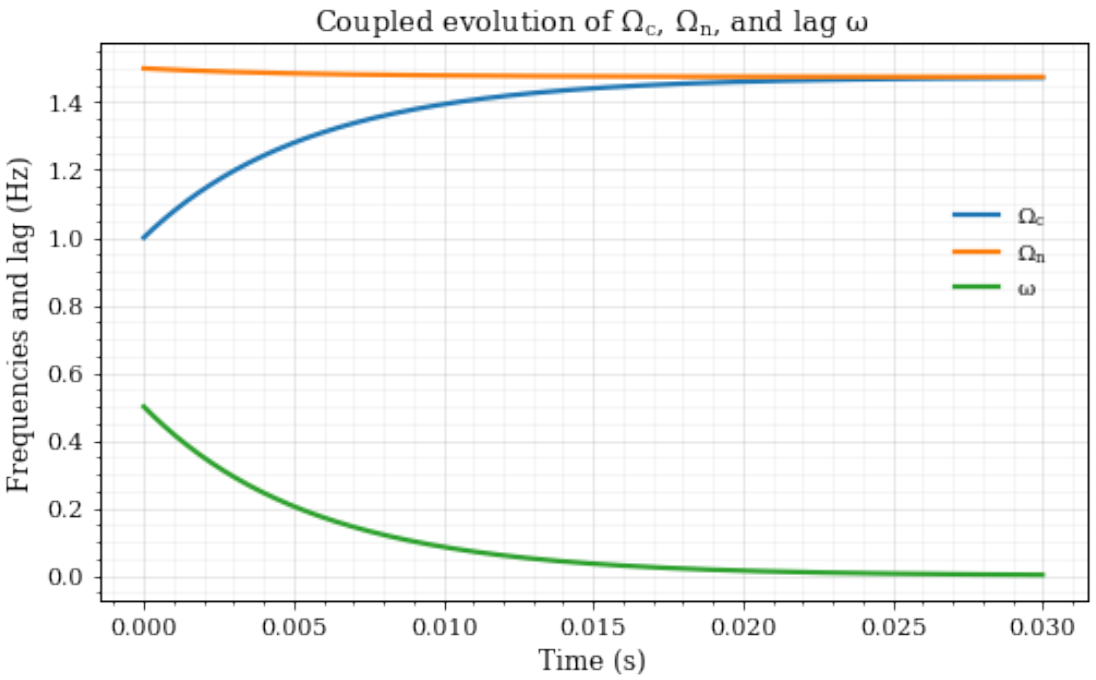

FIGURE 6.6: Time evolution of the superfluid angular velocity Ω_n, the charged component angular velocity Ω_c, and the lag ω in the general regime.

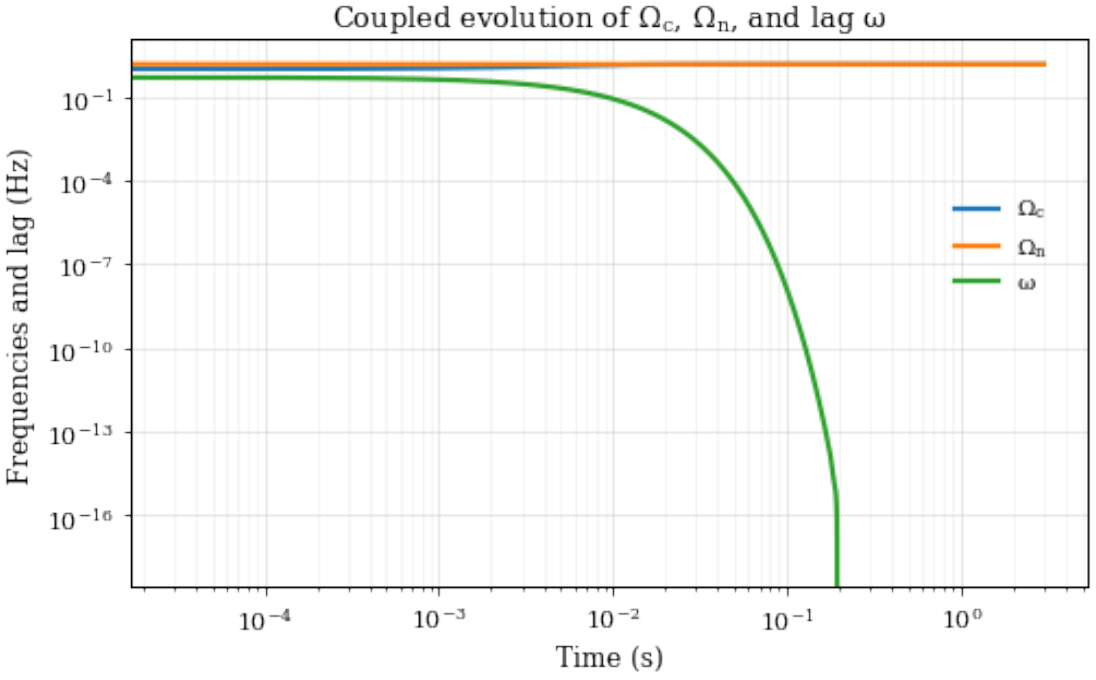

FIGURE 6.7: Log-log plot showing the decay of the lag ω in the general regime.

that vortex motion is suppressed, again resulting in a long coupling timescale. This behaviour is reflected in the expression for t_d in equation (6.59).

6.2.3 Dynamical coupling timescale with the conservation of angular momentum in the case of non-symmetric drag force

In this section, we calculate the dynamical coupling timescale while conserving angular momentum, but now considering a non-symmetric drag force, in contrast to the symmetric drag force treated in the previous section. To model the non-axisymmetric drag, we introduce distinct drag coefficients C_x and C_y along the x- and y-directions, respectively.

The force balance equations in the x- and y-directions are then written as

$$F_x = C_x(v_{c,x} - v_{l,x}) = -\rho_n \kappa (v_{n,y} - v_{l,y}), \tag{6.60}$$

$$F_y = C_y(v_{c,y} - v_{l,y}) = \rho_n \kappa (v_{n,x} - v_{l,x}), \tag{6.61}$$

where $(v_{c,x}, v_{c,y})$, $(v_{n,x}, v_{n,y})$, and $(v_{l,x}, v_{l,y})$ are the velocity components of the charged component, the neutron superfluid, and the vortex line, respectively.

We aim to express F_x and F_y solely in terms of $(v_{c,x}, v_{c,y})$ and $(v_{n,x}, v_{n,y})$, by eliminating the line velocity components $(v_{l,x}, v_{l,y})$. From equation (6.60), we obtain

$$v_{l,y} = v_{n,y} + \frac{C_x(v_{c,x} - v_{l,x})}{\rho_n \kappa}. \tag{6.62}$$

Substituting equation (6.62) into equation (6.61) and solving for $v_{l,x}$ gives

$$v_{l,x} = \frac{v_{n,x}}{1 + \frac{C_x C_y}{\rho_n^2 \kappa^2}} + \frac{\frac{C_y}{\rho_n \kappa}(v_{n,y} - v_{c,y})}{1 + \frac{C_x C_y}{\rho_n^2 \kappa^2}} + \frac{v_{c,x}}{1 + \frac{\rho_n^2 \kappa^2}{C_x C_y}}. \tag{6.63}$$

Inserting equation (6.63) into equation (6.62) yields

$$v_{l,y} = \frac{v_{n,y}}{1 + \frac{C_x C_y}{\rho_n^2 \kappa^2}} - \frac{\frac{C_x}{\rho_n \kappa}(v_{n,x} - v_{c,x})}{1 + \frac{C_x C_y}{\rho_n^2 \kappa^2}} + \frac{v_{c,y}}{1 + \frac{\rho_n^2 \kappa^2}{C_x C_y}}. \tag{6.64}$$

Next, substituting the expressions for $v_{l,x}$ and $v_{l,y}$ (equations (6.63)–(6.64)) into the force equations (6.60)–(6.61), we obtain

$$F_x = -\rho_n \kappa \left(\frac{(v_{n,y} - v_{c,y})}{1 + \frac{\rho_n^2 \kappa^2}{C_x C_y}} + \frac{\frac{C_x}{\rho_n \kappa}(v_{n,x} - v_{c,x})}{1 + \frac{C_x C_y}{\rho_n^2 \kappa^2}} \right), \tag{6.65}$$

$$F_y = \rho_n \kappa \left(\frac{(v_{n,x} - v_{c,x})}{1 + \frac{\rho_n^2 \kappa^2}{C_x C_y}} - \frac{\frac{C_y}{\rho_n \kappa}(v_{n,y} - v_{c,y})}{1 + \frac{C_x C_y}{\rho_n^2 \kappa^2}} \right). \tag{6.66}$$

To write the forces in terms of angular velocities, we define

$$\vec{v_n} = \Omega_n r \hat{e}_\phi, \qquad \vec{v_c} = \Omega_c r \hat{e}_\phi, \tag{6.67}$$

where in Cartesian coordinates

$$\hat{e}_\phi = -\sin\phi \hat{e}_x + \cos\phi \hat{e}_y. \tag{6.68}$$

This yields the Cartesian velocity components

$$v_{c,x} = -\Omega_c r \sin\phi, \qquad v_{c,y} = \Omega_c r \cos\phi, \tag{6.69}$$

$$v_{n,x} = -\Omega_n r \sin\phi, \qquad v_{n,y} = \Omega_n r \cos\phi. \tag{6.70}$$

It is crucial to note that the rigid-body dynamics analysis adopted here is valid only at $t = 0$, since beyond this time the distribution of vortices departs from its axisymmetric configuration due to the non-axisymmetric drag force acting on them. In this regime, the standard relation $\kappa n_v = 2\Omega$, which assumes a uniform and axisymmetric vortex array, is no longer valid. Consequently, the superfluid component no longer rotates as a rigid body.

Using (6.69) and (6.70), the forces reduce to

$$F_x = -\rho_n \kappa \left(\frac{(\Omega_n - \Omega_c)x}{1 + \frac{\rho_n^2 \kappa^2}{C_x C_y}} - \frac{\frac{C_x}{\rho_n \kappa}(\Omega_n - \Omega_c)y}{1 + \frac{C_x C_y}{\rho_n^2 \kappa^2}} \right), \tag{6.71}$$

$$F_y = -\rho_n \kappa \left(\frac{(\Omega_n - \Omega_c)y}{1 + \frac{\rho_n^2 \kappa^2}{C_x C_y}} + \frac{\frac{C_y}{\rho_n \kappa}(\Omega_n - \Omega_c)x}{1 + \frac{C_x C_y}{\rho_n^2 \kappa^2}} \right). \tag{6.72}$$

The torque acting on the neutron superfluid is then

$$I_n \dot{\Omega}_n = \int_V \boldsymbol{r} \times (F_x \hat{i} + F_y \hat{j})\, dV = \int_V (xF_y - yF_x)\, dV. \tag{6.73}$$

Terms proportional to xy vanish upon integration, leaving

$$I_n \dot{\Omega}_n = -\rho_n \kappa n_v (\Omega_n - \Omega_c) \int_V \left(\frac{\frac{C_x}{\rho_n \kappa} y^2}{1 + \frac{C_x C_y}{\rho_n^2 \kappa^2}} + \frac{\frac{C_y}{\rho_n \kappa} x^2}{1 + \frac{C_x C_y}{\rho_n^2 \kappa^2}} \right) dV. \tag{6.74}$$

Carrying out the integration gives

$$I_n\dot{\Omega}_n = -\rho_n\kappa n_v(\Omega_n - \Omega_c)\,\frac{4\pi R^5}{15}\left(\frac{\frac{C_x}{\rho_n\kappa}}{1+\frac{C_xC_y}{\rho_n^2\kappa^2}} + \frac{\frac{C_y}{\rho_n\kappa}}{1+\frac{C_xC_y}{\rho_n^2\kappa^2}}\right). \tag{6.75}$$

Using $\kappa n_v = 2\Omega_n$ and

$$I_n = \frac{2}{5}MR^2 = \frac{8}{15}\rho_n\pi R^5, \tag{6.76}$$

equation (6.75) can be rewritten as

$$I_n\dot{\Omega}_n = -I_n\Omega_n(\Omega_n - \Omega_c)\left(\frac{\frac{C_x}{\rho_n\kappa}}{1+\frac{C_xC_y}{\rho_n^2\kappa^2}} + \frac{\frac{C_y}{\rho_n\kappa}}{1+\frac{C_xC_y}{\rho_n^2\kappa^2}}\right). \tag{6.77}$$

From this expression, the characteristic timescale can be identified as

$$\tau_n = \frac{1+\frac{C_xC_y}{\rho_n^2\kappa^2}}{\Omega_n\left(\frac{C_x}{\rho_n\kappa}+\frac{C_y}{\rho_n\kappa}\right)}. \tag{6.78}$$

Note that the expression for τ_n is valid only at $t = 0$, since beyond this time the superfluid component no longer rotates rigidly. The lag $\omega = \Omega_n - \Omega_c$ evolves according to

$$\dot{\omega} = \dot{\Omega}_n - \dot{\Omega}_c. \tag{6.79}$$

Using equation (6.35), equation (6.79) becomes

$$\dot{\omega} = \dot{\Omega}_n - \frac{I_n}{I_c}\dot{\Omega}_n = \frac{I}{I_c}\dot{\Omega}_n = \frac{\rho}{\rho_c}\dot{\Omega}_n, \tag{6.80}$$

where ρ is the total mass density. Therefore, the coupling timescale at $t = 0$ is

$$\tau_d = \frac{\rho_c}{\rho\,\Omega_n}\frac{1+\frac{C_xC_y}{\rho_n^2\kappa^2}}{\frac{C_x}{\rho_n\kappa}+\frac{C_y}{\rho_n\kappa}}. \tag{6.81}$$

This result is new. If the drag is symmetric, such that $C_x = C_y = C$, then in the weak drag limit we obtain

$$\tau_{\text{weak}} = \frac{\rho_c}{2\rho\,\Omega_n}\frac{\kappa\rho_n}{C}, \tag{6.82}$$

which is the same as the result obtained in the previous section, given in equation (6.41). In the strong-drag limit, we find

$$\tau_{\text{strong}} = \frac{\rho_c}{2\rho\,\Omega_n}\frac{C}{\kappa\rho_n}. \tag{6.83}$$

It should be noted that equation (6.83) is not the same as the result in equation (6.53) from the previous section, since in that case we employed a linearisation by assuming that the fractional change in the neutron superfluid angular velocity is very small. Strictly speaking, equations (6.82) and (6.83) are valid only at $t = 0$. These results will be used in a later section to compare with the corresponding timescale in the case of perfect pinning of vortices in a single direction.

6.3 Dynamical coupling timescale in the case of vortex creep through nuclei in the crust

In this section, we consider a spherical two-component star consisting of a neutron superfluid and a charged component (the crust). We focus on the case of vortex creep through an axisymmetric distribution of nuclei in the crust and investigate its effect on the dynamical coupling timescales, before moving on to the non-axisymmetric interaction of vortices with flux tubes. This discussion is based on the phenomenological model proposed in Alpar et al. (1984), who suggested that vortices can pass through pinning sites (nuclei in the crust) due to thermal fluctuations.

We consider the case in which vortices encounter and pass through an axisymmetric distribution of nuclei in the crust, in the absence of any drag force acting on the vortices. This case is based entirely on Sidery and Alpar (2009). Alpar et al. (1984) proposed the following phenomenological expression for the radial creep velocity of vortex lines:

$$v_r = v_0 \left[\exp\left(-\frac{E_{p-out}}{kT} \right) - \exp\left(-\frac{E_{p-in}}{kT} \right) \right], \tag{6.84}$$

where v_0 is a characteristic velocity, k is Boltzmann's constant, and T is the temperature.

The pinning energy E_p is related to the critical lag by

$$E_p = b\xi F_{\text{critical}} = b\xi\rho_n\kappa r\omega_{\text{critical}}, \tag{6.85}$$

where b is the distance between pinning sites, ξ is the coherence length of the superfluid, r is the radius of the vortex core, and ω_{critical} is the critical lag. At a general lag $\omega \leq \omega_{\text{critical}}$, the pinning energy barrier E_p is modified by

$$\Delta E = b\xi F = b\xi\rho_n\kappa r\omega. \tag{6.86}$$

Hence, the effective outward and inward pinning energies are

$$E_{p-out} = E_p - \Delta E = E_p \left(1 - \frac{\omega}{\omega_{\text{critical}}} \right), \tag{6.87}$$

$$E_{p-in} = E_p + \Delta E = E_p \left(1 + \frac{\omega}{\omega_{\text{critical}}}\right). \tag{6.88}$$

Substituting equations (6.87) and (6.88) into equation (6.84), the creep velocity becomes

$$v_r = 2v_0 \exp\left(-\frac{E_p}{kT}\right) \sinh\left(\frac{E_p \omega}{kT\,\omega_{\text{critical}}}\right). \tag{6.89}$$

The force balance equation for the vortex lines is given by

$$\boldsymbol{F_p} + \boldsymbol{F_m} = 0, \tag{6.90}$$

where the pinning force is defined as

$$\boldsymbol{F_p} = -\boldsymbol{F_m} = -n_v \rho_n \kappa \times (\boldsymbol{v_n} - \boldsymbol{v_L}). \tag{6.91}$$

Here, $\boldsymbol{v_L}$ denotes the vortex line velocity. Since vortices move radially with the creep velocity v_r in the rotating frame, we identify

$$\boldsymbol{v_L} = \boldsymbol{v_c} + \boldsymbol{v_r} \tag{6.92}$$

in the inertial frame.

Inserting equation (6.92) into equation (6.91) and simplifying, we obtain

$$\boldsymbol{F_p} = \rho_n \kappa (v_n - v_c)\, \hat{e}_r + \rho_n \kappa v_r\, \hat{e}_\phi. \tag{6.93}$$

The torque acting on crust is therefore

$$I_c \dot{\Omega}_c = \int_V \boldsymbol{r} \times (-\boldsymbol{F_p})\, dV, \tag{6.94}$$

which simplifies to

$$I_c \dot{\Omega}_c = -\int_V r \sin\theta\, \rho_n \kappa n_v v_r\, dV. \tag{6.95}$$

Substituting equation (6.89) into equation (6.95) and performing the integration, we obtain

$$I_c \dot{\Omega}_c = -\rho_n \Omega_n R^4 \pi^2 \left[v_0 \exp\left(-\frac{E_p}{kT}\right) \sinh\left(\frac{E_p \omega}{kT\,\omega_{\text{critical}}}\right)\right]. \tag{6.96}$$

From conservation of angular momentum, we have

$$I_n \dot{\Omega}_n = \rho_n \Omega_n R^4 \pi^2 \left[v_0 \exp\left(-\frac{E_p}{kT}\right) \sinh\left(\frac{E_p \omega}{kT\,\omega_{\text{critical}}}\right)\right]. \tag{6.97}$$

We may write $I_n = \frac{2}{5} M_n R^2$ and $\rho_n = \frac{3M_n}{4\pi R^3}$, since the neutron fluid is modelled as a uniform-density sphere. Substituting these expressions into equation (6.97), we obtain

$$\dot{\Omega}_n = \frac{15\pi\Omega_n}{8R}\left[v_0 \exp\left(-\frac{E_p}{kT}\right)\sinh\left(\frac{E_p\omega}{kT\,\omega_{\text{critical}}}\right)\right]. \tag{6.98}$$

From equation (6.98), the characteristic timescale $\tau_{creep,n}$ can be identified as

$$\tau_{creep,n} = \frac{8R}{15\pi\left[v_0 \exp\left(-\frac{E_p}{kT}\right)\sinh\left(\frac{E_p\omega}{kT\,\omega_{\text{critical}}}\right)\right]}. \tag{6.99}$$

Finally, using the lag evolution equation (6.80), we obtain

$$\tau_{\text{creep}} = \frac{8\rho_c R}{15\pi\rho\left[v_0 \exp\left(-\frac{E_p}{kT}\right)\sinh\left(\frac{E_p\,\omega}{kT\,\omega_{\text{critical}}}\right)\right]}, \tag{6.100}$$

which gives the coupling timescale in the case of axisymmetric vortex creep with no drag force acting on the vortices. In the following section, we investigate the case of vortices pinning to flux tubes and experiencing a non-axisymmetric drag force, which may lead to a non-axisymmetric distribution of vortices as the system evolves with time.

6.4 Dynamical coupling timescale when flux tubes are present inside the NS

In this section, we study how the presence of both superconducting flux tubes and neutron superfluid vortices affects the rotational dynamics of the neutron star. We consider different cases of interaction between flux tubes and vortices. These interactions are of particular interest, as they may play an important role when we later investigate the case of Magnus mountains.

The calculations in this section are based on the analysis of Sidery and Alpar (2009). An important point to note is that the dynamical coupling timescale calculated in Sidery and Alpar (2009), when flux tubes are present, is valid only at $t = 0$. Beyond this time, the superfluid component no longer rotates rigidly, as the vortex distribution ceases to remain symmetric due to the asymmetry introduced by the flux tubes. Consequently, at later times the same expression cannot be directly interpreted as the dynamical coupling timescale.

Following Sidery and Alpar (2009), we adopt a simple setup in which flux tubes are aligned along the x-axis, while vortices are oriented along the z-axis (the rotation axis of the neutron star), as illustrated in Fig. 6.8. We then investigate two specific cases: 1)

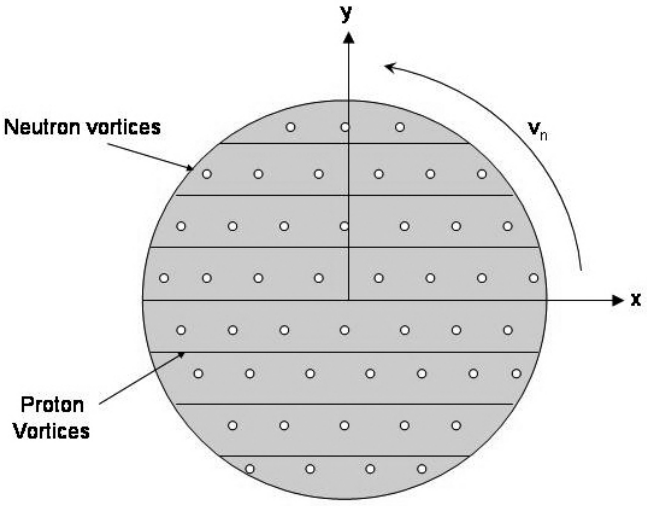

FIGURE 6.8: This figure, reproduced from Sidery and Alpar (2009), shows a cross-section of the x–y plane of a neutron star. The magnetic flux tubes are aligned along the x-axis, while the star rotates about the z-axis. The neutron superfluid vortices are oriented parallel to the z-axis.

perfect pinning of vortices along one axis, and 2) the inclusion of vortex creep instead of perfect pinning.

6.4.1 Case 1: Perfect pinning along one axis

We first consider the case of perfect pinning of vortices along the y-direction, while a drag force acts on the vortices. Since perfect pinning is assumed in the y-direction, the drag coefficient C_y tends to infinity, while in the x-direction vortices are free to move. The force balance equations in the x- and y-directions are then

$$F_x = C_x(v_{c,x} - v_{l,x}) = -\rho_n \kappa (v_{n,y} - v_{l,y}), \tag{6.101}$$

$$F_y = \rho_n \kappa (v_{n,x} - v_{l,x}). \tag{6.102}$$

The velocity of vortex lines in the inertial frame is

$$\boldsymbol{v_L} = \boldsymbol{\Omega_c} \times \boldsymbol{r} + \boldsymbol{v}_{\|}, \tag{6.103}$$

where $\boldsymbol{\Omega_c} \times \boldsymbol{r}$ gives the usual azimuthal component of the line velocity, and $\boldsymbol{v}_{\|}$ denotes the component of the line velocity parallel to the flux tubes, which lies entirely in the x-direction.

The x- and y-components of $\boldsymbol{v_n}$ are given by

$$v_{l,y} = \Omega_c r \cos\phi, \tag{6.104}$$

$$v_{l,x} = -\Omega_c r \sin\phi + v_{\parallel}. \tag{6.105}$$

The corresponding expressions for $v_{c,x}, v_{c,y}, v_{n,x}, v_{n,y}$ are given in equations (6.69)–(6.70). Substituting equations (6.104), (6.105), (6.69), and (6.70) into equation (6.101) and solving for $v_{\parallel}$ yields

$$v_{\parallel} = \frac{\rho_n \kappa}{C_x}\, \omega r \cos\phi. \tag{6.106}$$

Inserting equation (6.106) into the expression for $v_{l,x}$ gives

$$v_{l,x} = -\Omega_c r \sin\phi + \frac{\rho_n \kappa}{C_x}\, \omega r \cos\phi. \tag{6.107}$$

Substituting $v_{l,y}$ from equation (6.104) and $v_{n,y}$ from equation (6.70) into equation (6.101) yields

$$F_x = -\rho_n \kappa \eta_v (\Omega_n r \cos\phi - \Omega_c r \cos\phi) = -\rho_n \kappa \eta_v\, \omega x, \tag{6.108}$$

while substituting $v_{l,x}$ from equation (6.105) and $v_{n,x}$ from equation (6.70) into equation (6.102) gives

$$F_y = \rho_n \kappa \eta_v \left(-\Omega_n r \sin\phi - \left[-\Omega_c r \sin\phi + \frac{\rho_n \kappa}{C_x}\, \omega r \cos\phi \right] \right) = -\rho_n \kappa \eta_v\, \omega y - \frac{(\rho_n \kappa)^2 \eta_v}{C_x} \omega x. \tag{6.109}$$

The torque acting on the neutron superfluid is

$$I_n \dot{\Omega}_n = \int_V (x\hat{x} + y\hat{y}) \times (F_x \hat{x} + F_y \hat{y})\, dV. \tag{6.110}$$

Substituting equations (6.108) and (6.109) into equation (6.110) gives

$$I_n \dot{\Omega}_n = -\rho_n \kappa \eta_v \omega \int_V \left(xy + \frac{\rho_n \kappa}{C_x} x^2 - yx \right) \hat{z}\, dV, \tag{6.111}$$

which simplifies to

$$I_n \dot{\Omega}_n = -\rho_n \kappa \eta_v \omega \int_V \frac{\rho_n \kappa}{C_x} x^2\, dV. \tag{6.112}$$

Since

$$x = r \sin\theta \cos\phi, \tag{6.113}$$

equation (6.112) becomes

$$I_n \dot{\Omega}_n = -\rho_n\, 2\Omega_n \omega \frac{\rho_n \kappa}{C_x}\, \frac{4\pi R^5}{15}. \tag{6.114}$$

The moment of inertia of the sphere in terms of density is

$$I_n = \frac{2}{5} M R^2 = \frac{2}{5} \rho_n V R^2 = \frac{2}{5} \rho_n \frac{4\pi}{3} R^5. \tag{6.115}$$

Substituting equation (6.115) into equation (6.114) gives

$$I_n\dot{\Omega}_n = -\frac{2\Omega_n I_n \rho_n \kappa}{2C_x}\,\omega, \tag{6.116}$$

and hence

$$\dot{\Omega}_n = -\frac{\Omega_n \rho_n \kappa}{C_x}\,\omega. \tag{6.117}$$

By conservation of angular momentum, we then have

$$\dot{\Omega}_c = \frac{I_n}{I_c}\frac{\Omega_n \rho_n \kappa}{C_x}\,\omega. \tag{6.118}$$

Therefore, the lag evolution equation becomes

$$\dot{\omega} = \dot{\Omega}_n - \dot{\Omega}_c = \frac{\Omega_n I \rho_n \kappa}{I_c C_x}\,\omega. \tag{6.119}$$

From equation (6.119), the dynamical coupling timescale is directly read off as

$$\tau_{\rm pin} = \frac{I_c C_x}{\Omega_n I \rho_n \kappa} = \frac{\rho_c}{\Omega_n \rho}\frac{C_x}{\rho_n \kappa}. \tag{6.120}$$

We can recover the expression for $\tau_{\rm pin}$ in equation (6.120) by taking the limit $C_y \to \infty$ in the expression for the coupling timescale in the case of a non-axisymmetric drag force without flux tubes, as given in equation (6.81).

We now compare $\tau_{\rm pin}$ with the coupling timescales $\tau_{\rm weak}$ (6.82) and $\tau_{\rm strong}$ (6.83) in the weak and strong drag limits, respectively, when no flux tubes are present. In each case, the drag coefficient C_x is understood as the appropriate one for the regime under consideration, i.e. $C_x = C$ in the weak-drag limit and $C_x = C$ in the strong-drag limit.

Comparing equations (6.120) and (6.82), we find

$$\frac{\tau_{\rm pin}}{\tau_{\rm weak}} = 2\left(\frac{C}{\rho_n \kappa}\right)^2. \tag{6.121}$$

Sidery and Alpar (2009) provide the following range for $\frac{C}{\rho_n \kappa}$:

$$\frac{C}{\rho_n \kappa} = \frac{\rho_c}{2\rho_n \Omega \tau_\nu} \sim \frac{\rho_c}{\rho_n 4\pi(10-200)} \sim (4\times 10^{-4} - 2\times 10^{-5}). \tag{6.122}$$

To obtain this range, they assumed $\frac{\rho_c}{\rho_n} = 5\times 10^{-2}$ and $\tau_\nu = (10\text{–}200)P$, where P is the neutron star's rotation period. This gives

$$\frac{\tau_{\rm pin}}{\tau_{\rm weak}} = 2\left(\frac{C}{\rho_n \kappa}\right)^2 \sim (3.2\times 10^{-7} - 8\times 10^{-10}). \tag{6.123}$$

Equation (6.123) shows that absolute pinning in one direction reduces the coupling timescale significantly compared with the case of axisymmetric weak drag with no flux tubes.

Finally, comparing equations (6.120) and (6.83), we find

$$\frac{\tau_{\rm pin}}{\tau_{\rm strong}} = 2. \tag{6.124}$$

This demonstrates that the coupling timescale in the case of absolute pinning along one direction is almost the same as in the case of axisymmetric strong drag with no flux tubes, differing only by a factor of two.

6.4.2 Case 2: Vortex creep

In this section, we consider the case of vortex creep and examine its effect on the dynamical coupling timescales. Unlike the previous case, we now allow vortices to cut and pass through the flux tubes. This treatment follows the phenomenological model proposed by Sidery and Alpar (2009).

We focus on the non-axisymmetric case, where flux lines are aligned along the x-direction. Pinning is therefore provided only along the y-direction due to the flux lines. We ignore the drag force in the y-direction but retain it in the x-direction. The quantity ΔE modifies the pinning energy barrier along the y-axis, and to incorporate the resulting asymmetry, we introduce a factor $\hat{r}\cdot\hat{y} = \sin\phi$ in the expression. The pinning energy barriers for vortex motion in the positive and negative y-directions are then given by

$$E_{p+} = E_p\left(1 - \frac{\omega\sin\phi}{\omega_{\rm critical}}\right), \tag{6.125}$$

$$E_{p-} = E_p\left(1 + \frac{\omega\sin\phi}{\omega_{\rm critical}}\right). \tag{6.126}$$

The line velocity in the y-direction in the inertial frame is obtained as the sum of the crustal velocity and the creep velocity in the y-direction. The creep velocity is calculated by substituting E_{p+} and E_{p-} into the expression for v_r given in equation (6.84). This yields

$$v_{l,y} = v_{c,y} + v_r(\omega\sin\phi) = \Omega_c r\cos\phi + 2v_0\exp\left(-\frac{E_p}{kT}\right)\sinh\left(\frac{E_p\,\omega\sin\phi}{kT\,\omega_{\rm critical}}\right). \tag{6.127}$$

Next, we calculate the forces acting on the vortices in the x- and y-directions. The force balance equation in the x-direction is written as

$$F_x = C(v_{c,x} - v_{l,x}) = -\rho_n\kappa(v_{n,y} - v_{l,y}), \tag{6.128}$$

which can be rearranged to solve for $v_{l,x}$:

$$v_{l,x} = v_{c,x} + \frac{\rho_n \kappa}{C}(v_{n,y} - v_{l,y}). \tag{6.129}$$

Substituting the line velocity from equation (6.127) into equation (6.128) yields

$$F_x = -\rho_n \kappa n_v \left[\omega r \cos\phi - 2v_0 \exp\left(-\frac{E_p}{kT}\right) \sinh\left(\frac{E_p \omega \sin\phi}{kT\omega_{\text{critical}}}\right)\right]. \tag{6.130}$$

The force balance equation in the y-direction is

$$F_y = \boldsymbol{F_p} = \rho_n \kappa (v_{n,x} - v_{l,x}). \tag{6.131}$$

Substituting equation (6.129) into equation (6.131) gives

$$F_y = \rho_n \kappa \left[v_{n,x} - v_{c,x} - \frac{\rho_n \kappa}{C}(v_{n,y} - v_{l,y})\right]. \tag{6.132}$$

Further substituting equation (6.127) into equation (6.132) yields

$$F_y = -\rho_n \kappa \left[\omega r \sin\phi + \frac{\rho_n \kappa}{C}\left(\omega r \cos\phi - 2v_0 \exp\left(-\frac{E_p}{kT}\right) \sinh\left(\frac{E_p \omega \sin\phi}{kT\omega_{\text{critical}}}\right)\right)\right]. \tag{6.133}$$

The torque equation is written as

$$I_n \dot{\Omega}_n = \int_V \left[r \times (F_x + F_y)\right] dV, \tag{6.134}$$

which simplifies to

$$I_n \dot{\Omega}_n = \int_V \left[xF_y - yF_x\right] dV. \tag{6.135}$$

Substituting the expressions of F_x from equation (6.130) and F_y from equation (6.133) into equation (6.135) gives

$$I_n \dot{\Omega}_n = -\frac{\rho_n \Omega_n I_n \kappa \omega}{C} - \rho_n \kappa n_v \int_V y\, 2v_0 \exp\left(-\frac{E_p}{kT}\right) \sinh\left(\frac{E_p \omega \sin\phi}{kT\omega_{\text{critical}}}\right) dV. \tag{6.136}$$

Using equation (5.20) in equation (6.136), we obtain

$$I_n \dot{\Omega}_n = -\frac{\rho_n \Omega_n I_n \kappa \omega}{C} - \rho_n 2\Omega_n \int_V y\, 2v_0 \exp\left(-\frac{E_p}{kT}\right) \left(\frac{E_p \omega \sin\phi}{kT\omega_{\text{critical}}}\right) dV. \tag{6.137}$$

Performing the volume integral, we find

$$I_n \dot{\Omega}_n = -\frac{\rho_n \Omega_n I_n \kappa \omega}{C} - \rho_n 4\Omega_n v_0 \exp\left(-\frac{E_p}{kT}\right) \left(\frac{E_p \omega}{kT\omega_{\text{critical}}}\right) \frac{R^4}{4} \frac{\pi^2}{2}. \tag{6.138}$$

This simplifies to

$$\dot{\Omega}_n = -\frac{\rho_n \Omega_n \kappa \omega}{C} - \frac{15\pi}{16R}\Omega_n v_0 \exp\left(-\frac{E_p}{kT}\right)\left(\frac{E_p \omega}{kT\omega_{\text{critical}}}\right). \tag{6.139}$$

This result differs from the expression given in the literature (see equation (58) of Sidery and Alpar (2009)). Instead of the factor $\frac{15\pi}{16}$ in front of the second term of equation (6.139), the expression in Sidery and Alpar (2009) contains a factor of 2. It appears that Sidery and Alpar (2009) made a mistake in the calculation of the coefficient of the second term in equation (6.139).

As a next step, one would ideally study the case of non-axisymmetric creep in the presence of drag force. However, before proceeding, it is necessary to fully resolve the problem of axisymmetric creep with drag force, discussed earlier in Section **??**, which was only solved in the weak-drag limit. A complete treatment requires a detailed estimate of the pinning force F_p acting on vortices due to pinning sites, whether crustal nuclei or flux tubes. Such a microphysical analysis is beyond the scope of this thesis, and we do not pursue it further here.

Finally, it should be noted that the rigid-body analysis presented here, which was applied to the non-axisymmetric interaction between flux tubes and vortices, is valid only at $t = 0$. Beyond this initial time, rigid-body dynamics cannot be applied, since Ω_n does not evolve symmetrically with Ω_c. At later times, the calculation of Ω_n would require a more sophisticated numerical analysis of vortex motion and distribution. As this approach is considerably more complex, we do not pursue it here. Instead, in the next chapter, in order to study the formation of Magnus mountains, we assume an $m = 2$ distribution of vortices and prescribe an $m = 2$ velocity field by hand, without attempting to link it to the dynamics of the vortices and their interaction with the rest of the star.

Chapter 7

Formation of Magnus Mountains - Incompressible star

In this chapter, we adopt a simple model framework to investigate the possibility of forming a Magnus mountain. We consider a two-component neutron star model where one component is subjected to a non-axisymmetric velocity perturbation. Throughout this chapter, we assume the star to be incompressible; the effects of compressibility will be examined in the next chapter. Our goal is to estimate both the induced current multipole moment and the displacement field generated in response to the imposed velocity perturbation. We perform this analysis under two scenarios: first, using the Cowling approximation, where perturbations in the gravitational potential are neglected; and second, by relaxing the Cowling approximation and fully including gravitational potential perturbations.

7.1 Model Assumptions and Setup

The theory suggests that neutrons in the inner crust and outer core may exist in a superfluid state. As discussed in Chapter 5, a rotating superfluid mimics bulk rotation by forming quantised vortices. Similarly, protons in the inner core may exist in a type-II superconducting phase, which gives rise to quantised magnetic flux tubes due to the internal magnetic field (Baym et al., 1969; Haskell and Sedrakian, 2018; Chamel, 2017).

When a star spins up or spins down, the superfluid vortices move inward or outward, respectively, due to the Magnus force acting on them. This force arises from the velocity difference between the neutron vortex lines and neutron fluid (Sidery and Alpar, 2009).

In a spinning-down neutron star, vortices move outward and may become pinned either to crustal nuclei in the inner crust or to magnetic flux tubes in the core. In the case of pinning, the velocity of the neutron vortex line becomes equal to that of the crust.

Since the charged component of the star (primarily protons and electrons) is tightly coupled to the crust through electromagnetic interactions, the vortex line velocity—when pinned—also effectively matches the velocity of the proton fluid. Consequently, the Magnus force now arises due to the velocity difference between the proton fluid and the neutron fluid. If this pinning occurs in a non-axisymmetric manner, it results in a non-axisymmetric neutron superfluid velocity field. The pinned vortices experience an increasing Magnus force as the velocity difference between neutrons and protons grows: the superfluid retains its angular velocity because the vortices are stuck, while the charged component (tightly coupled to the crust) continues to slow down. This non-axisymmetric pinning leads to a non-axisymmetric Magnus force. The pinned vortices exert a reaction force on the crust, which may deform it in a non-axisymmetric way, thereby forming a " Magnus mountain" (Jones, 2002b).

A recent study, Haskell et al. (2022), investigated the mass and current multipoles generated by the non-axisymmetric pinning of vortices to flux tubes in the outer core of a neutron star. They considered a spherical two-fluid star consisting of a neutron superfluid (the "normal" component) and a charged component (proton + electron fluid). In their model, the neutron superfluid velocity was prescribed by hand in terms of Heaviside step functions. They did not solve the equations of motion to estimate the shape change of the star; instead, they calculated the current multipole for an incompressible star, which was found to be zero. In contrast, we consider an infinite cylindrical two-component star. In our model, the charged component has a non-zero shear modulus, and we solve the coupled equations of motion to calculate both the elastic response and the resulting shape change of the star. In this chapter, we focus on the incompressible case, while in Chapter 8 we extend our model to the compressible case.

In our model, we assume an infinitely long cylindrical star of finite radius R. This choice reflects the natural geometry of the vortices, which are aligned along the rotation axis. This simplifies the analysis and allows us to capture essential physics of vortex pinning and deformation while avoiding spherical complications at this stage. In this setup, the neutron superfluid and charged elastic components coexist. Our goal is to construct a simplified model for the formation of a Magnus mountain in a cylindrical star, with the intention of extending the analysis in future work to a more realistic spherical star possessing an elastic crust of finite thickness and a fluid core. The present thesis focuses exclusively on the cylindrical star case.

7.2 Background Star

The background star in our model is assumed to be an incompressible, constant-density configuration, providing a simplified baseline for studying the formation of mountains due to vortex pinning. In chapter 8, we will extend this framework to a compressible

stellar model. The background star is elastically relaxed, meaning that there are no pre-existing elastic stresses in the background configuration. The star consists of two interpenetrating fluids: a superfluid neutron component (fluid 1) and a charged fluid (fluid 2), composed of protons and electrons. Each fluid is taken to have a uniform, constant mass density, denoted by ρ_n and ρ_c, respectively, and we assume a common baryon mass m_B. The system rotates uniformly with angular velocity Ω about the z-axis, and due to the assumed cylindrical symmetry, all background quantities depend only on the radial coordinate r. Within this setup, we aim to solve for the chemical potentials $\mu_n(r)$ and $\mu_c(r)$, as well as the gravitational potential $\Phi(r)$, which together describe the equilibrium structure of the background star.

7.2.1 Equations of Motion in the Rotating Frame

We begin with the unperturbed Euler equations for each fluid component in the rotating frame of the star (Grosart, 2005; Andersson et al., 2008). These are the general equations, expressed in a frame rotating at the rate Ω.

For the neutron superfluid component, the Euler equation reads

$$\partial_t \vec{v}_n + \vec{v}_n \cdot \nabla \vec{v}_n + 2\vec{\Omega} \times \vec{v}_n + \vec{\Omega} \times (\vec{\Omega} \times \vec{r}) = -\nabla \tilde{\mu}_n - \nabla \Phi + \frac{\vec{F}^{mag}}{\rho_n}, \tag{7.1}$$

and for the charged component we have

$$\partial_t \vec{v}_c + \vec{v}_c \cdot \nabla \vec{v}_c + 2\vec{\Omega} \times \vec{v}_c + \vec{\Omega} \times (\vec{\Omega} \times \vec{r}) = -\nabla \tilde{\mu}_c - \nabla \Phi - \frac{\vec{F}^{mag}}{\rho_c}. \tag{7.2}$$

Here, $\vec{v}_c$ and $\vec{v}_n$ denote the velocity fields of the charged fluid and the neutron superfluid, respectively, as measured in the rotating frame. The quantities $\tilde{\mu}_c$ and $\tilde{\mu}_n$ are the corresponding reduced chemical potentials, defined by

$$\tilde{\mu}_c = \frac{\mu_c}{m_B}, \qquad \tilde{\mu}_n = \frac{\mu_n}{m_B}, \tag{7.3}$$

where m_B is the common baryon mass. The gravitational potential is denoted by Φ, while $\vec{\Omega}$ represents the angular velocity vector of the star. The position vector $\vec{r}$ is defined with respect to the corotating frame. The quantity

$$\vec{F}^{\text{mag}} = \rho_n \left(\nabla \times \vec{v}_n\right) \times \left(\vec{v}_n - \vec{v}_c\right) \tag{7.4}$$

represents the Magnus force acting on the neutron superfluid due to the presence of pinned vortices.

In the background configuration, the fluids are assumed to be co-rotating, so $\vec{v}_n = \vec{v}_c$. In the rotating frame, this implies $\vec{v}_n = \vec{v}_c = 0$, which immediately implies $\vec{F}^{mag} = 0$.

In this case, equations (7.1) and (7.2) reduce to the same form, which can be written in the unified notation

$$\partial_t \vec{v}_X + \vec{v}_X \cdot \nabla \vec{v}_X + 2\vec{\Omega} \times \vec{v}_X + \vec{\Omega} \times (\vec{\Omega} \times \vec{r}) = -\nabla \tilde{\mu}_X - \nabla \Phi, \quad X \in \{n, c\}, \tag{7.5}$$

where $X = n$ corresponds to the neutron component and $X = c$ to the charged component.

In the rotating frame, $\vec{v}_n = \vec{v}_c = 0$, which simplifies the Euler equation significantly. The steady-state Euler equations for each fluid component then reduce to:

$$\nabla \tilde{\mu}_X = -\nabla \Phi + \nabla \left(\frac{1}{2} |\vec{\Omega} \times \vec{r}|^2 \right), \tag{7.6}$$

where we have used the identity for the centrifugal term:

$$\vec{\Omega} \times (\vec{\Omega} \times \vec{r}) = -\nabla \left(\frac{1}{2} |\vec{\Omega} \times \vec{r}|^2 \right). \tag{7.7}$$

The term $\frac{1}{2}|\vec{\Omega} \times \vec{r}|^2$ represents the centrifugal potential. Equation (7.6) can be integrated with respect to r to find the chemical potential:

$$\tilde{\mu_X}(r) = -\Phi(r) + \frac{1}{2}\Omega^2 r^2 + \mu_{X,0}, \tag{7.8}$$

where $\mu_{X,0}$ is a constant of integration.

To determine the gravitational potential Φ, we solve the Poisson equation under the assumption of cylindrical symmetry:

$$\frac{1}{r}\frac{d}{dr}\left(r \frac{d\Phi}{dr} \right) = 4\pi G(\rho_n + \rho_c) = 4\pi G\rho, \tag{7.9}$$

where G denotes the gravitational constant and $\rho = \rho_n + \rho_c$ is the total mass density of the system, which is taken to be constant.

Multiplying both sides by r and integrating, we get:

$$\frac{d}{dr}\left(r \frac{d\Phi}{dr} \right) = 4\pi G\rho r, \tag{7.10}$$

$$r\frac{d\Phi}{dr} = 2\pi G\rho r^2 + A \quad \Rightarrow \quad \frac{d\Phi}{dr} = 2\pi G\rho r + \frac{A}{r}, \tag{7.11}$$

where A is a constant of integration. To avoid a singularity at $r = 0$, we set $A = 0$.

Integrating once more:

$$\Phi(r) = \int 2\pi G\rho r \, dr = \pi G\rho r^2 + \Phi_0, \tag{7.12}$$

where Φ_0 is a second constant of integration.

Substituting Equation (7.12) into Equation (7.8) yields:

$$\tilde{\mu_X}(r) = -(\pi G\rho r^2 + \Phi_0) + \frac{1}{2}\Omega^2 r^2 + \mu_{X,0}. \tag{7.13}$$

We impose the boundary condition that the chemical potential vanishes at the stellar surface (interpreted as the interface with vacuum):

$$\tilde{\mu_X}(R) = 0, \tag{7.14}$$

where R is the radius of the star.

Applying this boundary condition to Equation (7.13) at $r = R$, we obtain:

$$0 = -(\pi G\rho R^2 + \Phi_0) + \frac{1}{2}\Omega^2 R^2 + \mu_{X,0}, \tag{7.15}$$

which we solve for $\mu_{X,0}$:

$$\tilde{\mu_{X,0}} = (\pi G\rho R^2 + \Phi_0 - \frac{1}{2}\Omega^2 R^2). \tag{7.16}$$

Substituting Equation (7.16) back into Equation (7.13) gives the final expression for the chemical potential:

$$\tilde{\mu_X}(r) = \left[-\pi G\rho r^2 + \frac{1}{2}\Omega^2 r^2 + \pi G\rho R^2 - \frac{1}{2}\Omega^2 R^2\right]. \tag{7.17}$$

This can be written more compactly as:

$$\tilde{\mu_X}(r) = (R^2 - r^2)\left(\pi G\rho - \frac{1}{2}\Omega^2\right). \tag{7.18}$$

These results will serve as the unperturbed background quantities in our model and provide the foundation for studying perturbations due to pinned vortices and the resulting formation of mountains on neutron stars.

7.3 Superfluid Neutron Velocity Perturbation

In this section, we introduce a non-axisymmetric perturbation to the neutron superfluid velocity field on top of the background star. This perturbation is motivated by the non-axisymmetric pinning of vortices, which leads to a non-axisymmetric Magnus force. Such a force can deform the star in a non-axisymmetric manner, potentially giving rise to a "mountain." For the purposes of this study, we restrict our attention to azimuthal mode number $m = 2$, which corresponds to quadrupolar deformations most relevant for gravitational wave emission.

The neutron superfluid velocity perturbation field should ideally be calculated from first principles, taking into account the microphysical interactions of the vortices with the pinning potentials of flux tubes and lattice sites in the crust. One possible approach, indicated in Chapter 6, is to extend the model of asymmetric interactions between vortices and flux tubes presented by Sidery and Alpar (2009), and to solve the system numerically by carefully analysing the vortex motion and distribution. This detailed calculation lies beyond the scope of the present thesis and is planned as part of future work. In the current study, we therefore specify the velocity field by hand.

To simplify the analysis, we ignore perturbations along the z-axis, restricting our attention to two-dimensional perturbations in the r–ϕ plane. The perturbed velocity field is therefore given by:

$$\delta\vec{v}_n = v_r(r)e^{i2\phi}\,\hat{r} + v_\phi(r)e^{i2\phi}\,\hat{\phi}, \tag{7.19}$$

where v_r and v_ϕ are radial functions to be specified.

This velocity field must satisfy the incompressibility condition:

$$\nabla \cdot \delta\vec{v}_n = 0, \tag{7.20}$$

which ensures that the perturbed flow is divergence-free.

To obtain a Magnus force with $m = 2$ azimuthal symmetry (as illustrated in Figure 7.2), we require the velocity field to satisfy:

$$\nabla\Psi \cdot \delta\vec{v}_n = 0, \tag{7.21}$$

which implies that the fluid elements follow closed streamlines along level sets of a scalar streamfunction Ψ.

We define Ψ as:

$$\Psi(r,\phi) = \Psi(r)e^{i2\phi}, \tag{7.22}$$

Taking the gradient of Ψ, we obtain:

$$\nabla\Psi(r,\phi) = \frac{d\Psi(r,\phi)}{dr}\,\hat{r} + \frac{1}{r}\frac{\partial\Psi(r,\phi)}{\partial\phi}\,\hat{\phi}. \tag{7.23}$$

The velocity field $\delta\vec{v}_n$ must be perpendicular to $\nabla\Psi$, and hence must be proportional to $\hat{z}\times\nabla\Psi$:

$$\delta\vec{v}_n = f(r)\,\hat{z}\times\nabla\Psi, \tag{7.24}$$

where $f(r)$ is a scalar function to be determined. Substituting Equation (7.23) into Equation (7.24) gives:

$$\delta\vec{v}_n = f(r)\left(-\frac{1}{r}\frac{\partial\Psi}{\partial\phi}\,\hat{r} + \frac{d\Psi}{dr}\,\hat{\phi}\right). \tag{7.25}$$

Applying the incompressibility condition (Equation (7.20)) to this expression yields:

$$f(r) = \text{constant} = A', \tag{7.26}$$

so that the perturbed velocity becomes:

$$\delta\vec{v}_n = A'\left(-\frac{1}{r}\frac{\partial\Psi}{\partial\phi}\,\hat{r} + \frac{\partial\Psi}{\partial r}\,\hat{\phi}\right). \tag{7.27}$$

To ensure that the radial component of the perturbed velocity vanishes at the stellar surface (i.e., fluid elements remain inside the star), we choose:

$$\Psi(r,\phi) = \left(\frac{r^2}{R^2} - 1\right)\frac{r^2}{R^2}e^{2i\phi}. \tag{7.28}$$

The quadratic structure in Eq. (7.28) ensures that the function is regular at the origin. Additionally, this choice satisfies $\Psi = 0$ at both $r = 0$ and $r = R$, which implies that the streamlines are closed and remain entirely within the stellar domain.

Substituting Equation (7.28) into Equation (7.27), we obtain the explicit expression for the $m = 2$ perturbed superfluid velocity:

$$\delta\vec{v}_n = A'\left[-\frac{i2r}{R^2}\left(\frac{r^2}{R^2} - 1\right)e^{2i\phi}\,\hat{r} + \frac{2r}{R^2}\left(\frac{2r^2}{R^2} - 1\right)e^{2i\phi}\,\hat{\phi}\right]. \tag{7.29}$$

We get the required $m = 2$ superfluid neutron velocity perturbation that will source a corresponding $m = 2$ Magnus force.

In order to express the equations of motion (EOMs), derived later in this chapter, in a simplified and compact form, we rewrite Eq. (7.29) using two radial functions, $u(r)$ and $v(r)$, as follows:

$$\delta\vec{v}_n = -i\,u(r)\,e^{2i\phi}\,\hat{r} + v(r)\,e^{2i\phi}\,\hat{\phi}, \tag{7.30}$$

where the functions $u(r)$ and $v(r)$ are defined as:

$$u(r) = \frac{2A'r}{R^2}\left(\frac{r^2}{R^2} - 1\right), \tag{7.31}$$

$$v(r) = \frac{2A'r}{R^2}\left(\frac{2r^2}{R^2} - 1\right). \tag{7.32}$$

The vorticity associated with this perturbed velocity field is obtained by taking the curl:

$$\vec{\kappa} = \nabla \times \vec{v}_n = \frac{12A'r^2}{R^4} e^{2i\phi}\,\hat{z}, \tag{7.33}$$

which shows that the vorticity retains the $m = 2$ angular structure. Figure (7.1) shows the plots for the perturbed velocity field $\delta\vec{v}_n$ and the corresponding vorticity $\vec{\kappa}$.

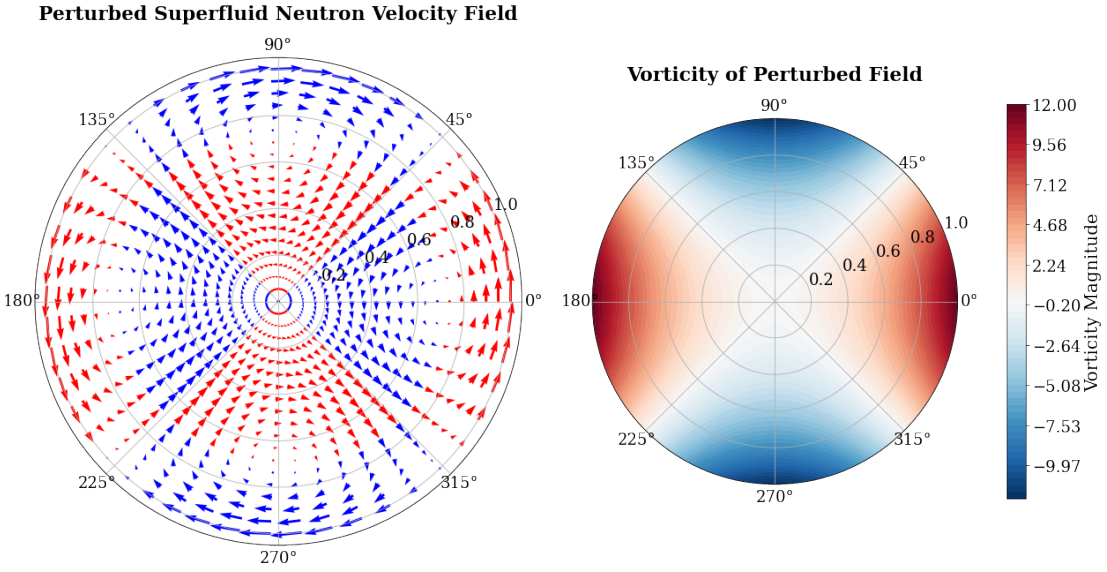

FIGURE 7.1: **Perturbed superfluid neutron velocity field and associated vorticity.** *Left panel:* Polar plot of the perturbed superfluid neutron velocity field. Arrow lengths reflect the local magnitude of the perturbation. Arrow colors indicate the sign of the azimuthal component at each location: red where the azimuthal velocity component is locally directed along increasing azimuthal angle, and blue where it is directed along decreasing azimuthal angle. *Right panel:* The corresponding vorticity field $\nabla \times \vec{v}_n$ exhibits the same $m = 2$ symmetry. Positive (red) and negative (blue) regions show the alternating pattern of vorticity that reflects spatial variation of the Magnus force. This perturbation may produce non-axisymmetric internal stresses, which may lead to elastic deformations ("mountains") on the neutron star crust.

7.4 Current Multipole

In this section, we evaluate the current multipole moment arising from the non-axisymmetric perturbed velocity field derived in the previous section. Specifically, we are interested in the $l = 2, m = 2$ component, which is relevant for gravitational wave emission from

quadrupolar fluid deformations. The current multipole will be evaluated over a finite cylindrical region bounded by $z = 0$ and $z = z_{\max}$.

The expression for the current multipole moment S_{22}, as defined by Thorne (1980), is

$$S_{22} = \frac{32\pi\sqrt{2}}{15} \int \delta\vec{v}_n \cdot \vec{Y}^*_{B,22}\, \rho\, r^2\, dV, \tag{7.34}$$

where ρ is the mass density, $\delta\vec{v}_n$ represents the perturbed velocity field of the neutron superfluid, and $\vec{Y}^*_{B,22}$ denotes the complex conjugate of the magnetic-type vector spherical harmonic:

$$\vec{Y}^*_{B,22} = \frac{1}{\sqrt{6}}\, \vec{r} \times \nabla Y^*_{22}, \tag{7.35}$$

where Y_{22} is the scalar spherical harmonic given by:

$$Y_{22} = \frac{1}{4}\sqrt{\frac{15}{2\pi}}\, \sin^2\theta\, e^{2i\phi}. \tag{7.36}$$

In the case of an incompressible fluid, the mass density ρ remains constant throughout the volume. This allows us to factor it out of the integral in Eq. (7.34). Consequently, the expression for the current multipole moment simplifies to:

$$S_{22} = \frac{32\pi\rho\sqrt{2}}{15} \int \delta\vec{v}_n \cdot \vec{Y}^*_{B,22}\, r^2\, dV. \tag{7.37}$$

To evaluate the current multipole in a cylindrical geometry, we express the standard spherical quantities in terms of cylindrical coordinates. We use the standard relations:

$$\varpi = r\sin\theta, \qquad z = r\cos\theta, \qquad r = \sqrt{\varpi^2 + z^2}, \tag{7.38}$$

$$\sin^2\theta = \frac{\varpi^2}{\varpi^2 + z^2}. \tag{7.39}$$

Substituting these into Equation (7.36), we obtain:

$$Y_{22} = \frac{1}{4}\sqrt{\frac{15}{2\pi}}\, \frac{\varpi^2}{\varpi^2 + z^2}\, e^{2i\phi}. \tag{7.40}$$

The gradient of Y_{22} is then computed as:

$$\nabla Y_{22} = \left(\frac{\sqrt{\frac{15}{2\pi}}\, r\, e^{2i\phi}}{2(r^2+z^2)} - \frac{\sqrt{\frac{15}{2\pi}}\, r^3\, e^{2i\phi}}{2(r^2+z^2)^2} \right) \hat{\varpi} + \frac{i\sqrt{\frac{15}{2\pi}}\, r\, e^{2i\phi}}{2(r^2+z^2)} \hat{\phi} - \frac{\sqrt{\frac{15}{2\pi}}\, r^2 z\, e^{2i\phi}}{2(r^2+z^2)^2} \hat{z}. \tag{7.41}$$

We express $\vec{r} = \varpi\hat{\varpi} + z\hat{z}$ and evaluate the vector spherical harmonic:

$$\vec{Y}_{B,22} = \frac{1}{\sqrt{6}}(\varpi\hat{\varpi} + z\hat{z}) \times \nabla Y_{22}. \tag{7.42}$$

Evaluating the cross product gives:

$$\vec{Y}_{B,22} = \frac{1}{\sqrt{6}}\left[-\frac{i\sqrt{\frac{15}{2\pi}}\varpi z e^{2i\phi}}{2(r^2+z^2)}\hat{\varpi} + \frac{\sqrt{\frac{15}{2\pi}}\varpi z e^{2i\phi}}{2(r^2+z^2)}\hat{\phi} + \frac{i\sqrt{\frac{15}{2\pi}}\varpi^2 e^{2i\phi}}{2(r^2+z^2)}\hat{z}\right]. \tag{7.43}$$

Taking the complex conjugate:

$$\vec{Y}^*_{B,22} = \frac{1}{\sqrt{6}}\left[\frac{i\sqrt{\frac{15}{2\pi}}\varpi z e^{-2i\phi}}{2(\varpi^2+z^2)}\hat{\varpi} + \frac{\sqrt{\frac{15}{2\pi}}\varpi z e^{-2i\phi}}{2(\varpi^2+z^2)}\hat{\phi} - \frac{i\sqrt{\frac{15}{2\pi}}\varpi^2 e^{-2i\phi}}{2(\varpi^2+z^2)}\hat{z}\right]. \tag{7.44}$$

Using the velocity field from Equation (7.29) and expressing it in terms of ϖ, we find:

$$\begin{aligned}\delta\vec{v}_n \cdot \vec{Y}^*_{B,22} &= \frac{A'}{\sqrt{6}}\left(\frac{\varpi^2}{R^2} - 1\right)\frac{\varpi^2}{R^2} \cdot \frac{\sqrt{\frac{15}{2\pi}}z}{(\varpi^2+z^2)} + \frac{A'}{\sqrt{6}}\left(\frac{2\varpi^2}{R^2} - 1\right)\frac{\varpi^2}{R^2} \cdot \frac{\sqrt{\frac{15}{2\pi}}z}{(\varpi^2+z^2)} \\ &= \frac{A'}{\sqrt{6}}\left(\frac{3\varpi^2}{R^2} - 2\right)\frac{\varpi^2}{R^2} \cdot \frac{\sqrt{\frac{15}{2\pi}}z}{(\varpi^2+z^2)}.\end{aligned} \tag{7.45}$$

Substituting into Equation (7.37) gives:

$$S_{22} = \frac{32\pi\rho\sqrt{2}}{15}\int_0^{z_{\max}}\int_0^{2\pi}\int_0^R \vec{v}_n \cdot \vec{Y}^*_{B,22}(\varpi^2+z^2)\varpi\, d\varpi\, d\phi\, dz. \tag{7.46}$$

This simplifies to:

$$S_{22} = A'\frac{32\pi\sqrt{\pi}z^2_{\max}\rho}{\sqrt{90}}\int_0^R\left(\frac{3\varpi^2}{R^2} - 2\right)\frac{\varpi^3}{R^2}\, d\varpi = 0. \tag{7.47}$$

Evaluating the integral, we find that it vanishes. Thus, the current multipole vanishes for this specific choice of velocity field.

To verify whether this vanishing result is a feature of the specific velocity profile or a more general outcome, we now consider a broader class of m=2 velocity perturbations expressed in cylindrical harmonics:

$$e^{i(m\phi+kz)}: \quad e^{i(m\phi+kz)}\hat{e}_r, \quad \hat{\nabla}e^{i(m\phi+kz)}, \quad \hat{e}_r \times \hat{\nabla}e^{i(m\phi+kz)}. \tag{7.48}$$

The general form of the perturbed velocity is:

$$\delta\vec{v}_n = u(\varpi)e^{i2\phi}\hat{e}_\varpi + i2v(\varpi)e^{i2\phi}\hat{e}_\phi. \tag{7.49}$$

Applying the incompressibility condition:

$$\vec{\nabla}\cdot\delta\vec{v}_n = 0 \quad \Rightarrow \quad \frac{u(\varpi)}{4} + \frac{\varpi}{4}\frac{du(\varpi)}{d\varpi} = v(\varpi). \tag{7.50}$$

The dot product becomes:

$$\delta\vec{v}_n \cdot \vec{Y}^*_{B,22} = \frac{i}{2\sqrt{6}}\frac{\sqrt{\frac{15}{2\pi}}\varpi z}{(\varpi^2+z^2)}\left(u(\varpi)+2v(\varpi)\right). \tag{7.51}$$

Substituting into Equation (7.37), we get:

$$\begin{aligned} S_{22} &= \frac{32\pi\rho\sqrt{2}}{15}\int \vec{v}_n\cdot\vec{Y}^*_{B,22}(\varpi^2+z^2)\varpi\, d\varpi\, d\phi\, dz \\ &= \frac{16\pi\sqrt{\pi}\rho}{\sqrt{90}}z^2_{\max}\int_0^R \left(u(\varpi)+2v(\varpi)\right)\varpi^2\, d\varpi. \end{aligned} \tag{7.52}$$

Using the incompressibility relation from Equation (7.50):

$$S_{22} = \frac{16\pi\sqrt{\pi}\rho}{\sqrt{90}}z^2_{\max}\int_0^R \left(\frac{3}{2}u(\varpi)\varpi^2 + \frac{\varpi^3}{2}\frac{du(\varpi)}{d\varpi}\right)d\varpi. \tag{7.53}$$

Integrating by parts:

$$\begin{aligned} S_{22} &= \frac{16\pi\sqrt{\pi}\rho}{\sqrt{90}}z^2_{\max}\left(\left[u(\varpi)\frac{\varpi^3}{2}\right]_0^R - \int_0^R \frac{\varpi^3}{2}\frac{du(\varpi)}{d\varpi}\,d\varpi + \int_0^R \frac{\varpi^3}{2}\frac{du(\varpi)}{d\varpi}\,d\varpi\right) \\ &= \frac{16\pi\sqrt{\pi}\rho}{\sqrt{90}}z^2_{\max}\left[u(\varpi)\frac{\varpi^3}{2}\right]_0^R. \end{aligned} \tag{7.54}$$

Imposing the boundary condition $u(R) = 0$, we finally find:

$$S_{22} = 0. \tag{7.55}$$

Thus, even for a general incompressible $m = 2$ velocity perturbation, the resulting current multipole moment vanishes under the imposed boundary conditions. This result arises primarily due to the vanishing radial perturbed velocity at the stellar surface. A more realistic perturbed velocity field, derived from detailed numerical simulations, may instead produce a non-zero current multipole moment.

In Melatos et al. (2015), the authors considered an infinitely long cylindrical star and calculated the current multipole arising from non-axisymmetric pinning of vortices in the crust. Instead of integrating from $z = z_1$ to $z = z_2$, they integrated over a spherical domain defined by $|z| \leq (R^{*2} - R^2)^{1/2}$, where R varies from 0 to R^* (the stellar radius). Following the same approach here would yield a non-zero current multipole. This indicates that the exact cancellation is likely a feature of the assumed cylindrical geometry, and that for a more realistic spherical star such a cancellation may not occur.

Nevertheless, despite the vanishing of the current multipole, it remains possible for the mass quadrupole moment to be non-zero. We therefore proceed to calculate the mass multipole moment by solving the coupled equations of motion. This will allow us to determine the deformation of the star from its equilibrium configuration in response to the perturbed velocity field.

7.5 Solving the Equations of Motion

In this section, we solve the linearised perturbed fluid and elastic equations of motion, coupled through the Magnus force, which is sourced by the perturbed velocity field defined in Equation (7.29).

7.5.1 Fluid Equations of Motion

We begin by perturbing the fluid equation of motion given in Equation (7.1). The neutron superfluid velocity perturbation is prescribed explicitly, as defined in Equation (7.29). We assume that the proton fluid velocity perturbation is zero. Our goal is to solve for the perturbed chemical potential of the neutron superfluid component. We restrict our analysis to linear perturbations and adopt the Cowling approximation, whereby perturbations in the gravitational potential are neglected. Furthermore, we consider only time-independent (stationary) perturbations. Under these assumptions, the perturbed Euler equation becomes:

$$2\vec{\Omega} \times \delta\vec{v}_n = -\nabla \delta\mu_n + \delta\vec{F}^{mag}, \tag{7.56}$$

where the perturbed Magnus force is given by:

$$\delta\vec{F}^{mag} = \rho_n \left(\nabla \times \vec{v}_n + \nabla \times \delta\vec{v}_n \right) \times \delta\vec{v}_n = \rho_n (2\vec{\Omega} \times \delta\vec{v}_n) + \rho_n (\nabla \times \delta\vec{v}_n) \times \delta\vec{v}_n. \tag{7.57}$$

This expression captures the Magnus force acting on the neutron superfluid, sourced by the perturbed velocity field. Since we are working within a linear perturbation

framework, we retain only the first-order term and discard the nonlinear contribution:

$$\delta\vec{F}^{mag} \approx \rho_n(2\vec{\Omega} \times \vec{\delta v}_n). \tag{7.58}$$

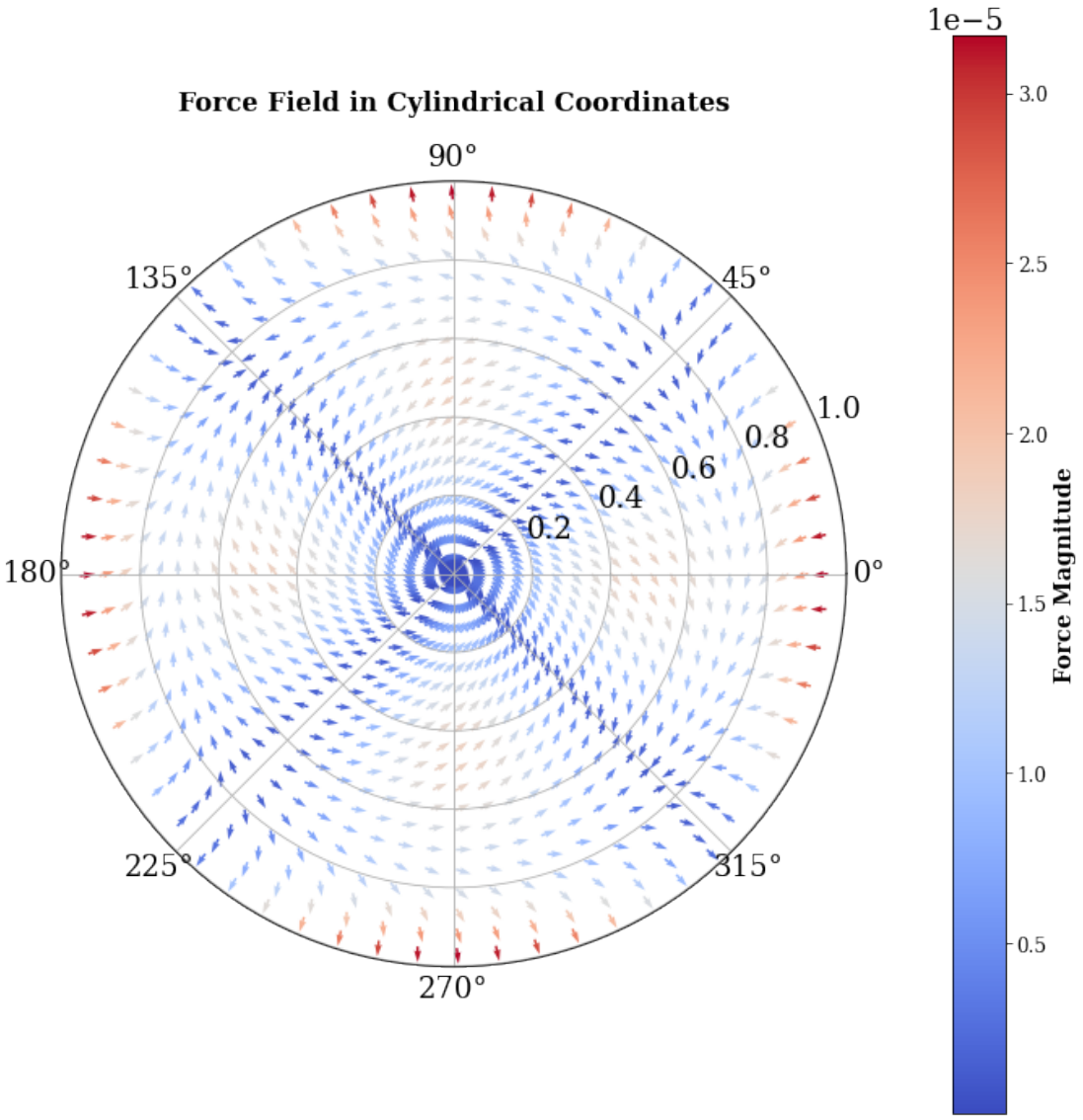

FIGURE 7.2: This figure shows the resulting $m = 2$ Magnus force field corresponding to the perturbed velocity field given in Equation (7.29), plotted in a z = constant plane.

Figure 7.2 shows the Magnus force field map. By substituting Equation (7.58) into the perturbed Euler equation (7.56), we obtain:

$$2\vec{\Omega} \times \vec{\delta v}_n = -\nabla\delta\mu_n + 2\vec{\Omega} \times \vec{\delta v}_n. \tag{7.59}$$

We observe that the Coriolis force on the left-hand side of the equation exactly balances

the Magnus force on the right-hand side. Canceling these terms on both sides of Equation (7.59) yields the following:

$$\nabla\delta\mu_n = 0 \quad \Rightarrow \quad \delta\mu_n = \text{constant}. \tag{7.60}$$

At the stellar surface, the Lagrangian perturbation condition for the chemical potential is:

$$\Delta\mu_n = \delta\mu_n + \xi_r\nabla_r\mu_n = 0, \tag{7.61}$$

which implies:

$$\text{constant} = -\xi_r\nabla_r\mu_n. \tag{7.62}$$

If we assume a free surface perturbation of the form:

$$\xi_r = f(r)\cos(2\phi), \tag{7.63}$$

then the right-hand side of Equation (7.62) varies as $\cos(2\phi)$, while the left-hand side is constant. This condition can only be satisfied if:

$$\xi_r = 0. \tag{7.64}$$

Hence, we conclude:

$$\delta\mu_n = 0. \tag{7.65}$$

We therefore find that the perturbed chemical potential $\delta\mu_n$ vanishes under the set of assumptions we have made. These include the linearity of perturbations, the use of the Cowling approximation (where perturbations in the gravitational potential are neglected), the incompressibility of the neutron superfluid, and the condition of a free fluid surface at the stellar boundary. The resulting solution is not entirely trivial. The Coriolis force associated with the prescribed velocity perturbation $\delta\vec{v}_n$ is exactly balanced by the Magnus force. There is no force associated with the gradient of a perturbed chemical potential.

In the calculations presented thus far, we have not included the effects of entrainment. Entrainment is a fundamental feature of multi-fluid systems such as neutron stars, wherein the motion of one fluid component influences the momentum of the other. The full calculation incorporating entrainment is not presented here, as its contribution vanishes to first order in the perturbation. However, for completeness, we briefly summarise the approach adopted. The fluid equations of motion, accounting for entrainment effects, were solved in the rotating frame of reference. In the unperturbed background, the neutron and charged fluids were assumed to co-rotate, meaning their velocities were equal and the relative velocity vanished. As a result, the background

Magnus force was zero. Upon introducing perturbations, we found that the entrainment terms did not contribute at linear order in the perturbed neutron velocity. Their contribution arose only at second order, which lies beyond the scope of our present linear analysis. Consequently, the linearised equations of motion in the rotating frame reduced to a balance between the Coriolis force and the Magnus force, leading to the condition that the gradient of the perturbed chemical potential vanishes. The subsequent analysis then proceeded identically to that of the non-entrained case discussed previously. We therefore conclude that, to linear order, entrainment has no effect on the neutron fluid dynamics in our setup.

7.5.2 Elastic Equation of Motion

In this section, we solve the equation of motion for the elastic (charged) component. We assume a constant shear modulus throughout the star. The elastic EOM is coupled to the fluid EOM via the Magnus force acting on vortices. Pinned vortices exert a reaction force on the elastic component, equal in magnitude and opposite in direction to the Magnus force.

The unperturbed equation of motion for the elastic component is given by Passamonti and Andersson (2012) as:

$$\rho_c \left(\partial_t v^c_b + v^c_a \nabla^a v^c_b + 2\epsilon_{bcd}\Omega^c v^d_c + (\vec{\Omega} \times (\vec{\Omega} \times \vec{r}))_b \right) = \nabla^a \tau_{ab} - \rho_c \nabla_b \Phi - F^{mag}_b. \quad (7.66)$$

Here, the Latin indices a and d are summed over according to the Einstein summation convention, while the index b is a free spatial index specifying the vector component of the equation. The superscript c denotes the charged component of the fluid and is a label rather than an index; it does not participate in index contraction. The tensor τ_{ab} represents the elastic stress tensor.

Since $\vec{v}_c = 0$ in the rotating frame, equation (7.66) simplifies to:

$$(\vec{\Omega} \times (\vec{\Omega} \times \vec{r}))_b = \frac{\nabla^a \tau_{ab}}{\rho_c} - \nabla_b \Phi - \frac{F^{mag}_b}{\rho_c}. \quad (7.67)$$

In the background star, we have $F^{mag}_b = 0$, as both components are co-rotating. Assuming further that the background star is elastically relaxed, the stress tensor satisfies:

$$\nabla^a \tau_{ab} = -\rho_c \nabla_b \tilde{\mu}_c, \quad (7.68)$$

which implies:

$$\tau_{ab} = -\rho_c \, \tilde{\mu}_c \, g_{ab}. \quad (7.69)$$

We will use this result later when applying the boundary conditions on the perturbed traction at the stellar surface.

To find the dynamics of perturbations, we now perturb Equation (7.67). Assuming the Cowling approximation (neglecting perturbations in the gravitational potential), the perturbed EOM becomes:

$$\nabla^a \delta\tau_{ab} - \delta F_b^{mag} = 0, \tag{7.70}$$

where $-\delta F_b^{mag}$ is the reaction force due to the Magnus force acting on pinned vortices. Using the expression for δF_b^{mag} from Equation (7.58), the equation becomes:

$$\nabla^a \delta\tau_{ab} = \rho_n 2(\Omega \times \delta\vec{v}_n)_b, \tag{7.71}$$

or equivalently,

$$\nabla^a \delta\tau_{ab} = \rho_n 2\Omega \epsilon_{bzd} \delta v_n^d. \tag{7.72}$$

Here, $\delta\vec{v}_n$ is the perturbed neutron velocity field defined in Equation (7.29). The perturbed stress tensor is given by:

$$\delta\tau_{ab} = -\rho_c \delta\tilde{\mu}_c g_{ab} + \mu(\nabla_a \xi_b + \nabla_b \xi_a - \frac{2}{3} g_{ab} \nabla^c \xi_c), \tag{7.73}$$

where the Lagrangian displacement is:

$$\xi^a = \xi_r C_{mk} \hat{r}^a + \xi_\perp r \nabla^a C_{mk}, \tag{7.74}$$

with the harmonic factor defined as:

$$C_{mk} = e^{im\phi} e^{ikz}. \tag{7.75}$$

In Ushomirsky et al. (2000), the authors expressed the perturbed stress tensor in terms of the perturbed tractions $\delta\tau_{rr}$ and $\delta\tau_{r\perp}$ in spherical coordinates, which facilitated applying boundary conditions at the surface. Inspired by this approach, we write a general form of the perturbed stress tensor in cylindrical coordinates:

$$\delta\tau_{ab} = g_{ab}\delta\tau_{rr} C_{mk} + w_{ab} 2\mu \frac{\xi_r}{r} C_{mk} - e_{ab} 2\mu \frac{d\xi_r}{dr} C_{mk} + f_{ab}\delta\tau'_{r\phi} + \tilde{f}_{ab}\delta\tau'_{rz} + \Lambda_{ab} 2\mu \frac{\xi_\perp}{r}, \tag{7.76}$$

with component definitions:

$$\delta\tau_{rr} = -\rho_c\delta\tilde{\mu}_c + \mu\left(\frac{4}{3}\frac{d\xi_r}{dr} - \frac{2}{3}\frac{\xi_r}{r} + \frac{2}{3}m^2\frac{\xi_\perp}{r} + \frac{2}{3}k^2\xi_\perp r\right), \tag{7.77}$$

$$\delta\tau'_{r\phi} = \mu\left(\frac{d\xi_\perp}{dr} - \frac{\xi_\perp}{r} + \frac{\xi_r}{r}\right), \tag{7.78}$$

$$\delta\tau'_{rz} = \mu\left(r\frac{d\xi_\perp}{dr} + \xi_\perp + \xi_r\right), \tag{7.79}$$

$$f_{ab} = r(\hat{r}_a\nabla_b C_{mk} + \hat{r}_b\nabla_a C_{mk} - \hat{r}_a\hat{z}_b ikC_{mk} - \hat{r}_b\hat{z}_a ikC_{mk}), \tag{7.80}$$

$$\tilde{f}_{ab} = \hat{r}_a\nabla_b C_{mk} + \hat{r}_b\nabla_a C_{mk} - \frac{\hat{r}_a\hat{\phi}_b imC_{mk}}{r} - \frac{\hat{r}_b\hat{\phi}_a imC_{mk}}{r}, \tag{7.81}$$

$$\Lambda_{ab} = r^2\nabla_a\nabla_b C_{mk} + f_{ab}, \tag{7.82}$$

$$e_{ab} = g_{ab} - \hat{r}_a\hat{r}_b, \tag{7.83}$$

$$w_{ab} = e_{ab} - \hat{z}_a\hat{z}_b. \tag{7.84}$$

In our specific model, we do not include perturbations along the z-axis. Therefore, the expressions simplify to:

$$\delta\tau_{ab} = g_{ab}\delta\tau_{rr}e^{im\phi} + w_{ab}2\mu\frac{\xi_r}{r}e^{im\phi} - e_{ab}2\mu\frac{d\xi_r}{dr}e^{im\phi} + f_{ab}\delta\tau'_{r\phi} + \Lambda_{ab}2\mu\frac{\xi_\perp}{r}, \tag{7.85}$$

where:

$$\delta\tau_{rr} = -\rho_c\delta\tilde{\mu}_c + \mu\left(\frac{4}{3}\frac{d\xi_r}{dr} - \frac{2}{3}\frac{\xi_r}{r} + \frac{2}{3}m^2\frac{\xi_\perp}{r}\right), \tag{7.86}$$

$$\delta\tau'_{r\phi} = \mu\left(\frac{d\xi_\perp}{dr} - \frac{\xi_\perp}{r} + \frac{\xi_r}{r}\right), \tag{7.87}$$

$$f_{ab} = r(\hat{r}_a\nabla_b e^{im\phi} + \hat{r}_b\nabla_a e^{im\phi}), \tag{7.88}$$

$$\xi^a = \xi_r e^{im\phi}\hat{r}^a + \xi_\perp r\nabla^a e^{im\phi}. \tag{7.89}$$

Finally, substituting the expression for the perturbed stress tensor from Equation (7.85) into the perturbed EOM (7.72), we obtain:

$$\nabla^a\left(g_{ab}\delta\tau_{rr}e^{im\phi} + w_{ab}2\mu\frac{\xi_r}{r}e^{im\phi} - e_{ab}2\mu\frac{d\xi_r}{dr}e^{im\phi} + f_{ab}\delta\tau'_{r\phi} + \Lambda_{ab}2\mu\frac{\xi_\perp}{r}\right) = \rho_n 2\Omega\epsilon_{bzd}\delta v_n^d. \tag{7.90}$$

Inserting (7.82), (7.83), (7.84) and (7.88) into (7.90) gives,

$$\begin{aligned}\nabla^a(g_{ab}\delta\tau_{rr}e^{im\phi} + g_{ab}e^{im\phi}2\mu(\frac{\xi_r}{r} - \frac{d\xi_r}{dr}) - \hat{r}_a\hat{r}_b e^{im\phi}2\mu(\frac{\xi_r}{r} - \frac{d\xi_r}{dr}) - \hat{z}_a\hat{z}_b 2\mu e^{im\phi}\frac{\xi_r}{r} \\ + r(\hat{r}_a\nabla_b e^{im\phi} + \hat{r}_b\nabla_a e^{im\phi})(\delta\tau'_{r\phi} + 2\mu\frac{\xi_\perp}{r}) + r^2\nabla_a\nabla_b C_{mk}2\mu\frac{\xi_\perp}{r}) = \rho_n 2\Omega\epsilon_{bzd}\delta v_n^d\end{aligned} \tag{7.91}$$

To simplify Eq. (7.91), we break the left-hand side into the following components. These simplifications rely on standard vector calculus identities and cylindrical coordinate basis properties:

1. Divergence of the isotropic radial stress:

$$\nabla^a(g_{ab}\delta\tau_{rr}e^{im\phi}) = \delta\tau_{rr}\nabla^b e^{im\phi} + e^{im\phi}\frac{d\delta\tau_{rr}}{dr}\hat{r}^b, \tag{7.92}$$

2. Divergence of the isotropic elastic term:

$$\nabla^a(g_{ab}e^{im\phi}2\mu(\frac{\xi_r}{r} - \frac{d\xi_r}{dr})) = 2\mu(\frac{\xi_r}{r} - \frac{d\xi_r}{dr})\nabla^b e^{im\phi} + 2\mu e^{im\phi}\frac{d}{dr}(\frac{\xi_r}{r} - \frac{d\xi_r}{dr})\hat{r}^b, \tag{7.93}$$

3. Divergence of the anisotropic radial component:

$$\nabla^a(\hat{r}_a\hat{r}_b e^{im\phi}2\mu(\frac{\xi_r}{r} - \frac{d\xi_r}{dr})) = \frac{1}{r}e^{im\phi}2\mu(\frac{\xi_r}{r} - \frac{d\xi_r}{dr})\hat{r}^b + 2\mu e^{im\phi}\frac{d}{dr}(\frac{\xi_r}{r} - \frac{d\xi_r}{dr})\hat{r}^b, \tag{7.94}$$

using

$$\nabla^a\hat{r}_a = \frac{1}{r}, \quad \hat{r}^a\nabla_a\hat{r}_b = \frac{1}{r}\left(\delta_{ab} - \hat{z}_a\hat{z}_b - \hat{r}_a\hat{r}_b\right)\hat{r}^a. \tag{7.95}$$

4. The vertical (z-axis) term vanishes:

$$\nabla^a(\hat{z}_a\hat{z}_b e^{im\phi}2\mu\frac{\xi_r}{r}) = 0, \tag{7.96}$$

5. The mixed radial-angular terms:

$$\nabla^a(r\hat{r}_a\nabla_b e^{im\phi}(\delta\tau'_{r\phi} + 2\mu\frac{\xi_\perp}{r})) = \nabla_b e^{im\phi}\delta\tau'_{r\phi} + r\nabla_b e^{im\phi}\frac{d\delta\tau'_{r\phi}}{dr} + \nabla_b e^{im\phi}2\mu\frac{d\xi_\perp}{dr}, \tag{7.97}$$

$$\nabla^a(r\hat{r}_b\nabla_a e^{im\phi}(\delta\tau'_{r\phi} + 2\mu\frac{\xi_\perp}{r})) = \nabla_b e^{im\phi}\delta\tau'_{r\phi} + \nabla_b e^{im\phi}2\mu\frac{\xi_\perp}{r} - m^2\frac{\delta\tau'_{r\phi}}{r}e^{im\phi}\hat{r}_b - m^2\frac{2\mu\xi_\perp}{r^2}e^{im\phi}\hat{r}_b, \tag{7.98}$$

6. The Laplacian angular term:

$$\nabla^a(2\mu\xi_\perp r\nabla_a\nabla_b e^{im\phi}) = -2\mu\frac{d\xi_\perp}{dr}\nabla_b e^{im\phi} - 2\mu\frac{\xi_\perp}{r}\nabla_b e^{im\phi} - m^2 2\mu\frac{\xi_\perp}{r}\nabla_b e^{im\phi} + m^2 4\mu\frac{\xi_\perp}{r^2}e^{im\phi}, \tag{7.99}$$

using the identity:

$$\nabla_a \nabla^a \nabla_b e^{im\phi} = -m^2 \nabla_b \left(\frac{e^{im\phi}}{r^2} \right). \tag{7.100}$$

Substituting Eqs. (7.92)–(7.99) back into Eq. (7.91), and projecting along $\hat{r}$ and $\hat{\phi}$ directions, we obtain two components of the perturbed equation of motion:

$$\hat{r} : \left(\frac{d\delta\tau_{rr}}{dr} - \frac{2\mu}{r} \left(\frac{\xi_r}{r} - \frac{d\xi_r}{dr} \right) - \frac{m^2}{r} \delta\tau'_{r\phi} + m^2 2\mu \frac{\xi_\perp}{r^2} \right) e^{im\phi} = -\rho_n 2\Omega v(r) e^{im\phi}, \tag{7.101}$$

$$\hat{\phi} : \left(\delta\tau_{rr} + 2\mu \left(\frac{\xi_r}{r} - \frac{d\xi_r}{dr} \right) + r \frac{d\delta\tau'_{r\phi}}{dr} + 2\delta\tau'_{r\phi} - m^2 2\mu \frac{\xi_\perp}{r} \right) \nabla_\phi e^{im\phi} = -2i\rho_n \Omega u(r) e^{im\phi}. \tag{7.102}$$

These equations describe the core dynamics of the perturbed elastic medium coupled to vortex motion. In our model, we consider only the $m = 2$ perturbation. For $m = 2$, Eqs. (7.101) and (7.102) simplify to:

$$\hat{r} : \left(\frac{d\delta\tau_{rr}}{dr} - \frac{2\mu}{r} \left(\frac{\xi_r}{r} - \frac{d\xi_r}{dr} \right) - \frac{4}{r} \delta\tau'_{r\phi} + 8\mu \frac{\xi_\perp}{r^2} \right) e^{i2\phi} = -\rho_n 2\Omega v(r) e^{i2\phi}, \tag{7.103}$$

$$\hat{\phi} : \left(\delta\tau_{rr} + 2\mu \left(\frac{\xi_r}{r} - \frac{d\xi_r}{dr} \right) + r \frac{d\delta\tau'_{r\phi}}{dr} + 2\delta\tau'_{r\phi} - 8\mu \frac{\xi_\perp}{r} \right) \nabla_\phi e^{i2\phi} = -2i\rho_n \Omega u(r) e^{i2\phi}. \tag{7.104}$$

Taking the real part of both sides leads to:

$$\frac{d\delta\tau_{rr}}{dr} - \frac{2\mu}{r} \left(\frac{\xi_r}{r} - \frac{d\xi_r}{dr} \right) - \frac{4}{r} \delta\tau'_{r\phi} + 8\mu \frac{\xi_\perp}{r^2} = -\rho_n 2\Omega v(r), \tag{7.105}$$

$$\delta\tau_{rr} + 2\mu \left(\frac{\xi_r}{r} - \frac{d\xi_r}{dr} \right) + r \frac{d\delta\tau'_{r\phi}}{dr} + 2\delta\tau'_{r\phi} - 8\mu \frac{\xi_\perp}{r} = -r\rho_n \Omega u(r). \tag{7.106}$$

In addition, we have the incompressibility condition $\nabla \cdot \vec{\xi} = 0$, which gives:

$$\frac{d\xi_r}{dr} - 4\frac{\xi_\perp}{r} + \frac{\xi_r}{r} = 0. \tag{7.107}$$

We now have three variables, ξ_r, $\xi_\perp$, and $\delta\tilde{\mu}_c$, which can be determined by solving Eqs. (7.105), (7.106), and (7.107).

First, we substitute Eqs. (7.86) and (7.87) into Eq. (7.105), yielding:

$$\frac{2\mu d^2\xi_r}{dr^2} + \frac{2\mu d\xi_r}{rdr} - \frac{6\mu\xi_r}{r^2} + \frac{12\mu\xi_\perp}{r^2} - \frac{4\mu d\xi_\perp}{rdr} - \frac{\rho_c d\delta\tilde{\mu}_c}{dr} = -2\rho_n\Omega v(r). \tag{7.108}$$

Using Eq. (7.107) to eliminate $\xi_\perp$ gives:

$$\frac{\mu d^2\xi_r}{dr^2} + \frac{3\mu d\xi_r}{rdr} - \frac{3\mu\xi_r}{r^2} - \frac{\rho_c d\delta\tilde{\mu}_c}{dr} = -2\rho_n\Omega v(r). \tag{7.109}$$

Next, substituting Eqs. (7.86) and (7.87) into Eq. (7.106), we obtain:

$$-\rho_c\delta\tilde{\mu}_c + \frac{3\mu\xi_r}{r} + \frac{\mu d\xi_r}{dr} - \frac{9\mu\xi_\perp}{r} + \frac{\mu d\xi_\perp}{dr} + \mu r\frac{d^2\xi_\perp}{dr^2} = -\rho_n\Omega r u(r). \tag{7.110}$$

Applying Eq. (7.107) again simplifies this to:

$$\rho_c\delta\tilde{\mu}_c = \rho_n\Omega r u(r) + \frac{3\mu\xi_r}{4r} - \frac{3\mu d\xi_r}{4dr} + \mu r\frac{d^2\xi_r}{dr^2} + \frac{\mu r^2 d^3\xi_r}{4dr^3}. \tag{7.111}$$

Differentiating this expression gives:

$$\frac{\rho_c d\delta\tilde{\mu}_c}{dr} = \rho_n\Omega\frac{d(ru(r))}{dr} - \frac{3\mu\xi_r}{4r^2} + \frac{3\mu d\xi_r}{4rdr} + \frac{\mu d^2\xi_r}{4dr^2} + \frac{3\mu r d^3\xi_r}{2dr^3} + \frac{\mu r^2 d^4\xi_r}{4dr^4}. \tag{7.112}$$

Substituting Eq. (7.112) into Eq. (7.109) results in a fourth-order differential equation for ξ_r:

$$-\frac{r^2 d^4\xi_r}{4dr^4} - \frac{3r d^3\xi_r}{2dr^3} + \frac{3d^2\xi_r}{4dr^2} + \frac{9d\xi_r}{4rdr} - \frac{9\xi_r}{4r^2} = \frac{\rho_n\Omega}{\mu}\left[r\frac{du(r)}{dr} + u(r) - 2v(r)\right]. \tag{7.113}$$

The right-hand side vanishes due to the incompressibility condition:

$$\frac{u(r)}{2} + \frac{r}{2}\frac{\partial u(r)}{\partial r} = v(r). \tag{7.114}$$

Thus, Eq. (7.113) simplifies to the homogeneous form:

$$-\frac{r^2 d^4\xi_r}{4dr^4} - \frac{3r d^3\xi_r}{2dr^3} + \frac{3d^2\xi_r}{4dr^2} + \frac{9d\xi_r}{4rdr} - \frac{9\xi_r}{4r^2} = 0. \tag{7.115}$$

Assuming a power-law solution $\xi_r = r^n$ and substituting into Eq. (7.115) leads to the characteristic equation:

$$(n-1)(9+9n-n^2-n^3) = 0, \tag{7.116}$$

with solutions $n = 1, -1, 3, -3$. Discarding negative powers to ensure regularity at $r = 0$, we obtain the general solution:

$$\xi_r = C_0 r + C_1 r^3, \tag{7.117}$$

which leads to

$$\xi_\perp = \frac{C_0 r}{2} + C_1 r^3. \tag{7.118}$$

From Eq. (7.111) we get:

$$\delta\tilde{\mu}_c = \frac{6\mu C_1}{\rho_c} r^2 + \frac{2\rho_n \Omega A'}{\rho_c}\left(\frac{r^4}{R^4} - \frac{r^2}{R^2}\right). \tag{7.119}$$

We now apply boundary conditions. At surface, the radial traction condition $\Delta\tau_{rr} = 0$ gives:

$$\Delta\tau_{rr} = \delta\tau_{rr} + \xi_r \nabla^r \tau_{rr} = 0. \tag{7.120}$$

Substituting Eqs. (7.69), (7.86), (7.117), (7.118), and (7.119) into Eq. (7.120) yields:

$$2C_0\left(\mu - \frac{(\Omega^2 - 2\pi\rho_c G)}{3} R^2 \rho_c\right) = 0. \tag{7.121}$$

Similarly, the tangential traction condition $\Delta\tau_{r\phi} = 0$ gives:

$$C_0 + 3C_1 R^2 = 0, \tag{7.122}$$

which implies $C_0 = 0$ and $C_1 = 0$. Therefore,

$$\xi_r = \xi_\perp = 0, \tag{7.123}$$

and Eq. (7.119) reduces to:

$$\delta\tilde{\mu}_c(r,\phi) = \frac{\rho_n \Omega A'}{\rho_c}\left(\frac{r^4}{R^4} - \frac{r^2}{R^2}\right) e^{i2\phi}. \tag{7.124}$$

Thus, we find that the displacement field in the elastic component of the star vanishes. We have also previously found $\xi_r^F = 0$. Therefore, the shape of the star remains unchanged. This outcome is somewhat surprising, as one would generally expect a non-axisymmetric deforming force acting on the crust to produce a corresponding distortion of the stellar shape. However, the Magnus force acting on the superfluid neutrons is exactly balanced by the Coriolis force, while the corresponding reaction force on the elastic component is entirely compensated by the gradient of the perturbed reduced chemical potential.

7.6 Solving the Equations of Motion Without the Cowling Approximation

We now proceed to solve the full problem, dropping the Cowling approximation and including perturbations to the gravitational potential alongside the fluid and elastic perturbations. This step is motivated by the question of whether relaxing the Cowling approximation leads to a non-zero displacement field and, consequently, to a change in the shape of the star—unlike the result obtained in Section 7.5.

7.6.1 Fluid EOM

We first perturb the fluid equations of motion in the rotating frame, starting from the unperturbed Euler equation. After linearizing, and noting that in the rotating frame the Coriolis force balances the Magnus force for steady perturbations, we obtain the following perturbed EOM:

$$\nabla(\delta\tilde{\mu_n} + \delta\Phi) = 0. \tag{7.125}$$

Next, we focus on determining the perturbed gravitational potential $\delta\Phi$. The perturbation satisfies Poisson's equation:

$$\nabla^2\delta\Phi = 0, \tag{7.126}$$

in the bulk of the star where the density perturbation vanishes. However, because of surface displacements in both the fluid and elastic components, there will be nonzero

density perturbations localized at the surface. These will enter through the boundary conditions.

Assuming no dependence on the z-coordinate, we rewrite Poisson's equation in cylindrical coordinates as:

$$\frac{1}{r}\frac{\partial}{\partial r}\left(r\frac{\partial \delta\Phi}{\partial r}\right)+\frac{1}{r^2}\frac{\partial^2 \delta\Phi}{\partial \phi^2}=0. \tag{7.127}$$

We solve this using separation of variables, setting $\delta\Phi(r,\phi)=\varsigma(r)\Theta(\phi)$. Substituting this into the equation yields two separate ordinary differential equations, one for $\Theta(\phi)$ and one for $\varsigma(r)$.

The angular equation takes the form:

$$\frac{\partial^2\Theta(\phi)}{\partial\phi^2}=-m^2\Theta(\phi), \tag{7.128}$$

whose solution is:

$$\Theta(\phi)=A\cos(m\phi)+B\sin(m\phi). \tag{7.129}$$

The radial equation is a Cauchy-Euler differential equation:

$$\frac{d^2\varsigma}{dr^2}+\frac{1}{r}\frac{d\varsigma}{dr}=\frac{m^2}{r^2}\varsigma, \tag{7.130}$$

which has general solution:

$$\varsigma(r)=Cr^m+Dr^{-m}. \tag{7.131}$$

For the $m=2$ mode of interest, the interior solution becomes:

$$(\delta\Phi)_{int}=r^2(A_1\cos 2\phi+B_1\sin 2\phi), \tag{7.132}$$

and the exterior solution is:

$$(\delta\Phi)_{ext}=\frac{1}{r^2}(A_2\cos 2\phi+B_2\sin 2\phi). \tag{7.133}$$

To determine the constants A_1, B_1, A_2, B_2, we apply boundary conditions at $r=R$. The first condition is continuity of the gravitational potential:

$$(\delta\Phi)_{int} = (\delta\Phi)_{ext}. \tag{7.134}$$

The second condition comes from integrating Poisson's equation across the surface, accounting for surface density perturbations induced by the radial displacements ξ_r^F and ξ_r^E of the fluid and elastic components, respectively. This leads to the jump condition:

$$\frac{\partial(\delta\Phi)_{ext}}{\partial r} - \frac{\partial(\delta\Phi)_{int}}{\partial r} = 4\pi G\left[\rho_c \xi_r^E(R,\phi) + \rho_n \xi_r^F(R,\phi)\right]. \tag{7.135}$$

Solving these boundary conditions yields:

$$A_1 = -\frac{\pi G[\rho_c \xi_r^E(R) + \rho_n \xi_r^F(R)]}{R}, \tag{7.136}$$

$$A_2 = -\pi G[\rho_c \xi_r^E(R) + \rho_n \xi_r^F(R)]R^3, \tag{7.137}$$

$$B_1 = B_2 = 0. \tag{7.138}$$

Thus, the internal perturbed gravitational potential becomes:

$$(\delta\Phi)_{int} = -\frac{r^2\pi G[\rho_c \xi_r^E(R) + \rho_n \xi_r^F(R)]}{R}\cos 2\phi. \tag{7.139}$$

Substituting this back into the perturbed Euler equation shows that:

$$\left(\delta\tilde{\mu_n}(r) - \frac{r^2\pi G\left[\rho_c\, \xi_r^E(R) + \rho_n\, \xi_r^F(R)\right]}{R}\right)\cos 2\phi = \text{constant}. \tag{7.140}$$

Since the left-hand side of equation (7.140) contains a factor of $\cos 2\phi$, the only possible value for the constant is zero. Hence, we obtain:

$$\delta\tilde{\mu_n}(r) = \frac{r^2\pi G\left[\rho_c\, \xi_r^E(R) + \rho_n\, \xi_r^F(R)\right]}{R}. \tag{7.141}$$

We now apply the Lagrangian boundary condition for the chemical potential perturbation at the stellar surface, which relates $\delta\tilde{\mu_n}$ to the radial displacement ξ_r^F as:

$$\Delta\tilde{\mu_n}(R,\phi) = \delta\tilde{\mu_n}(R,\phi) + \xi_r^F(R,\phi)\,\nabla_r\tilde{\mu_n}(r)\big|_{r=R} = 0. \tag{7.142}$$

Inserting equation (7.141) and the radial derivative of the background chemical potential from equation (7.18) into the surface boundary condition (7.142), we obtain the

following relation between $\xi_r^F(R)$ and $\xi_r^E(R)$:

$$\xi_r^F(R) = \frac{-\pi G\rho_c}{\pi G\rho_n + (\Omega^2 - 2\pi G\rho)}\,\xi_r^E(R). \tag{7.143}$$

This relation will be used as an input when solving the elastic equations of motion.

7.6.2 Elastic EOM

We now focus on solving the elastic equations of motion (EOM) in the presence of the perturbed gravitational potential. The perturbed EOM can be written as:

$$\nabla^a \delta\tau_{ab} = \rho_c \nabla_b \delta\Phi + \rho_n \kappa \epsilon_{bzd} v_n^d. \tag{7.144}$$

Here, $\delta\tau_{ab}$ is the perturbed stress tensor, $\delta\Phi$ is the perturbed gravitational potential, and the final term represents the Magnus force acting on the elastic component.

The expression for $\delta\Phi$ is given by Eq. (7.139). We now decompose the EOM into radial and azimuthal components. The radial component becomes:

$$\frac{d\delta\tau_{rr}}{dr} - \frac{2\mu}{r}\left(\frac{\xi_r}{r} - \frac{d\xi_r}{dr}\right) - \frac{4}{r}\delta\tau'_{r\phi} + 8\mu\frac{\xi_\perp}{r^2} = -\frac{2r\pi G\rho_c[\rho_c\xi_r^E(R) + \rho_n\xi_r^F(R)]}{R} - 2\rho_n\Omega v(r). \tag{7.145}$$

The azimuthal component reads:

$$\delta\tau_{rr} + 2\mu\left(\frac{\xi_r}{r} - \frac{d\xi_r}{dr}\right) + r\frac{d\delta\tau'_{r\phi}}{dr} + 2\delta\tau'_{r\phi} - 8\mu\frac{\xi_\perp}{r} = -\frac{r^2\pi G\rho_c[\rho_c\xi_r^E(R) + \rho_n\xi_r^F(R)]}{R} - r\rho_n\Omega u(r). \tag{7.146}$$

Next, we substitute the definitions of $\delta\tau_{rr}$ and $\delta\tau'_{r\phi}$ into Eq. (7.145). This leads to:

$$2\mu\frac{d^2\xi_r}{dr^2} + 2\mu\frac{d\xi_r}{rdr} - \frac{6\mu\xi_r}{r^2} + \frac{12\mu\xi_\perp}{r^2} - \frac{4\mu d\xi_\perp}{rdr} - \rho_c\frac{d\delta\tilde{\mu}_c}{dr} = -\frac{2r\pi G\rho_c[\rho_c\xi_r^E(R) + \rho_n\xi_r^F(R)]}{R} - 2\rho_n\Omega v(r). \tag{7.147}$$

Applying the incompressibility condition $\frac{d\xi_r}{dr} - 2\frac{\xi_\perp}{r} + \frac{\xi_r}{r} = 0$, we eliminate $\xi_\perp$ to obtain:

$$\mu\frac{d^2\xi_r}{dr^2}+3\mu\frac{d\xi_r}{rdr}-\frac{3\mu\xi_r}{r^2}-\rho_c\frac{d\delta\tilde{\mu}_c}{dr}=-\frac{2r\pi G\rho_c[\rho_c\xi_r^E(R)+\rho_n\xi_r^F(R)]}{R}-2\rho_n\Omega v(r). \quad (7.148)$$

We now turn to Eq. (7.146). After substituting for $\delta\tau_{rr}$ and $\delta\tau'_{r\phi}$, we obtain:

$$-\rho_c\delta\tilde{\mu}_c+\frac{3\mu\xi_r}{r}+\mu\frac{d\xi_r}{dr}-\frac{9\mu\xi_\perp}{r}+\mu\frac{d\xi_\perp}{dr}+\mu r\frac{d^2\xi_\perp}{dr^2}=-\frac{r^2\pi G\rho_c[\rho_c\xi_r^E(R)+\rho_n\xi_r^F(R)]}{R}-\rho_n\Omega ru(r). \quad (7.149)$$

Eliminating $\xi_\perp$ using the incompressibility condition leads to:

$$-\rho_c\delta\tilde{\mu}_c+\frac{3\mu\xi_r}{4r}-\frac{3\mu d\xi_r}{4dr}+\mu r\frac{d^2\xi_r}{dr^2}+\frac{\mu r^2d^3\xi_r}{4dr^3}=-\frac{r^2\pi G\rho_c[\rho_c\xi_r^E(R)+\rho_n\xi_r^F(R)]}{R}-\rho_n\Omega ru(r). \quad (7.150)$$

Rearranging gives an expression for $\delta\tilde{\mu}_c$:

$$\rho_c\delta\tilde{\mu}_c=\frac{r^2\pi G\rho_c[\rho_c\xi_r^E(R)+\rho_n\xi_r^F(R)]}{R}+\rho_n\Omega ru(r)+\frac{3\mu\xi_r}{4r}-\frac{3\mu d\xi_r}{4dr}+\mu r\frac{d^2\xi_r}{dr^2}+\frac{\mu r^2d^3\xi_r}{4dr^3}. \quad (7.151)$$

Differentiating Eq. (7.151) gives:

$$\frac{\rho_c d\delta\tilde{\mu}_c}{dr}=\frac{2r\pi G\rho_c[\rho_c\xi_r^E(R)+\rho_n\xi_r^F(R)]}{R}+\rho_n\Omega\frac{d(ru(r))}{dr}-\frac{3\mu\xi_r}{4r^2}+\frac{3\mu d\xi_r}{4rdr}+\frac{\mu d^2\xi_r}{4dr^2}+\frac{3\mu rd^3\xi_r}{2dr^3}+\frac{\mu r^2d^4\xi_r}{4dr^4}. \quad (7.152)$$

Substituting Eq. (7.152) into Eq. (7.148), we obtain a fourth-order differential equation for ξ_r:

$$-\frac{r^2d^4\xi_r}{4dr^4}-\frac{3rd^3\xi_r}{2dr^3}+\frac{3d^2\xi_r}{4dr^2}+\frac{9d\xi_r}{4rdr}-\frac{9\xi_r}{4r^2}=\frac{1}{\mu}\left(\frac{2r\pi G\rho_c[\rho_c\xi_r^E(R)+\rho_n\xi_r^F(R)]}{R}-\frac{2r\pi G\rho_c[\rho_c\xi_r^E(R)+\rho_n\xi_r^F(R)]}{R}\right)+\frac{\rho_n\Omega}{\mu}\left[r\frac{du(r)}{dr}+u(r)-2v(r)\right]. \quad (7.153)$$

The terms on the right-hand side cancel out due to the incompressibility condition:

$$\frac{u(r)}{2} + \frac{r}{2}\frac{du(r)}{dr} = v(r). \tag{7.154}$$

Thus, Eq. (7.153) reduces to the homogeneous form:

$$-\frac{r^2 d^4\xi_r}{4dr^4} - \frac{3rd^3\xi_r}{2dr^3} + \frac{3d^2\xi_r}{4dr^2} + \frac{9d\xi_r}{4rdr} - \frac{9\xi_r}{4r^2} = 0. \tag{7.155}$$

Assuming a power-law solution $\xi_r = r^n$, we substitute into Eq. (7.155) and obtain the characteristic equation:

$$(n-1)(9+9n-n^2-n^3) = 0. \tag{7.156}$$

The physically acceptable solutions are $n = 1$ and $n = 3$, giving the general solution:

$$\xi_r = C_0 r + C_1 r^3. \tag{7.157}$$

Using the incompressibility condition again yields:

$$\xi_\perp = \frac{C_0 r}{2} + C_1 r^3. \tag{7.158}$$

We now substitute ξ_r into Eq. (7.151) to find:

$$\rho_c \delta\tilde{\mu}_c = 6\mu C_1 r^2 + \frac{r^2 \pi G \rho_c [\rho_c \xi_r^E(R) + \rho_n \xi_r^F(R)]}{R} - \rho_n \Omega A \left(\frac{r^7}{R^6} - \frac{r^4}{R^3}\right). \tag{7.159}$$

Finally, we apply boundary conditions at $r = R$ to determine C_0 and C_1. The first condition comes from $\Delta\tau_{rr} = 0$:

$$C_0 + 3C_1 R^2 = 0. \tag{7.160}$$

The second condition $\Delta\tau_{r\phi} = 0$ gives:

$$2\mu C_0 - R\pi G\rho_c[\rho_c \xi_r^E(R) + \rho_n \xi_r^F(R)] = \rho_c(C_0 R + C_1 R^3)(\Omega^2 - 2\pi G\rho). \tag{7.161}$$

Solving these equations, we obtain:

$$C_0 = \frac{3R\pi G\rho_c[\rho_c\xi_r^E(R) + \rho_n\xi_r^F(R)]}{6\mu - 2R^2\rho_c(\Omega^2 - 2\pi G\rho)}, \tag{7.162}$$

$$C_1 = -\frac{\pi G\rho_c[\rho_c\xi_r^E(R) + \rho_n\xi_r^F(R)]}{6R\mu - 2R^3\rho_c(\Omega^2 - 2\pi G\rho)}. \tag{7.163}$$

Substituting back, we have:

$$\xi_r = \frac{\pi G\rho_c[\rho_c\xi_r^E(R) + \rho_n\xi_r^F(R)](3R^2r - r^3)}{6R\mu - 2R^3\rho_c(\Omega^2 - 2\pi G\rho)}, \tag{7.164}$$

and

$$\xi_\perp = \frac{\pi G\rho_c[\rho_c\xi_r^E(R) + \rho_n\xi_r^F(R)](3R^2r - 2r^3)}{2(6R\mu - 2R^3\rho_c(\Omega^2 - 2\pi G\rho))}. \tag{7.165}$$

Evaluating ξ_r at $r = R$, we obtain:

$$\xi_r^E(R) = \frac{2\pi G\rho_c R^2[\rho_c\xi_r^E(R) + \rho_n\xi_r^F(R)]}{6\mu - 2R^2\rho_c(\Omega^2 - 2\pi G\rho)}. \tag{7.166}$$

Rearranging gives:

$$\xi_r^F(R) = \frac{6\mu - 2R^2\rho_c(\Omega^2 - 2\pi G\rho) - 2\pi G\rho_c^2R^2}{2\pi G\rho_c\rho_n R^2}\xi_r^E(R). \tag{7.167}$$

Finally, comparing this relation with the one obtained earlier from the fluid EOM shows that both are compatible only if $\xi_r^F(R) = \xi_r^E(R) = 0$. Therefore, even when including the perturbed gravitational potential, the system cannot support a non-axisymmetric deformation, and no mountain is generated. The entire perturbation is absorbed into the chemical potential gradient.

Thus, both approaches — with and without the Cowling approximation — lead to the same conclusion: no non-axisymmetric deformation or mountain formation occurs in the incompressible model under the present assumptions. There is a possibility that the assumption of incompressibility inhibits the star from developing a sustained shape deformation in response to the imposed Magnus force. It is important to note, however, that realistic neutron stars are not strictly incompressible; their compressibility may allow for more complex responses. In the next chapter, we will relax the incompressibility assumption and explore whether compressibility can enable the formation of non-axisymmetric deformations — potentially opening a viable path for mountain formation and continuous gravitational wave emission.

Chapter 8

Formation of Magnus mountains - Compressible star

In this chapter, we extend our investigation of Magnus mountain formation by considering a compressible neutron star model. The overall set-up follows closely the framework established previously in Chapter 7, where the formation of mountains was studied in the incompressible limit. As before, we consider a star composed of coexisting superfluid neutrons and a charged component (consisting of protons and electrons) that occupy the same volume throughout the star.

The central mechanism remains the same: we introduce a non-axisymmetric perturbation in the superfluid neutron velocity field. This perturbation arises from the non-axisymmetric pinning of vortices inside the star. As a consequence, a non-axisymmetric Magnus force is generated, which couples the superfluid and the charged components, potentially deforming the star.

The primary difference in this chapter lies in relaxing the incompressibility assumption. By allowing the star to be compressible, we explore how the star's response to the same class of perturbations may change. We will employ the Cowling approximation in this analysis. The equations of motion for the system will now involve the full compressible hydrodynamics and elasticity, and we will solve the resulting coupled ordinary differential equations (ODEs) numerically.

A key step in this investigation will be the careful derivation of regularity conditions at the stellar center, as well as boundary conditions at the surface, both of which are essential for the numerical solution of the system. We will also compute appropriate forms of the perturbed neutron superfluid velocity field consistent with bulk compressibility of the star.

In addition to the fully compressible cylindrical star model, we will also investigate an alternative configuration: an annular model, consisting of a fluid core, an elastic crust,

and a thin surface ocean layer. For this layered model, we will again define a non-axisymmetric velocity perturbation and carefully analyze the boundary and interface conditions at each transition layer. We will investigate whether such configurations can sustain a non-zero current multipole moment and whether they allow for the formation of a non-axisymmetric mountain.

The goal of this chapter is to systematically assess whether compressibility and realistic multi-layered structures enable the formation of non-axisymmetric mountains under the action of the Magnus force generated by pinned superfluid vortices.

8.1 Background Star

We now construct the background configuration for a compressible star, which forms the equilibrium state upon which the perturbations will be introduced. The overall model setup remains the same as outlined earlier in Section 7.2, with both the superfluid neutrons and the charged component coexisting throughout the volume of an infinitely long cylindrical star. However, in contrast to the incompressible case, we now allow for compressibility. Our goal in this section is to derive the equilibrium gravitational and chemical potentials for this compressible background star.

We adopt a simple two-fluid polytropic equation of state (EOS) where each fluid obeys an independent $n = 1$ polytrope. The total internal energy density is given by:

$$\epsilon = \frac{1}{2}K_n n_n^2 + \frac{1}{2}K_c n_c^2, \tag{8.1}$$

where n_n and n_c are the neutron and proton number densities, and K_n, K_c are the respective polytropic constants. We neglect any interaction terms between the two components.

The chemical potentials for each component are obtained by differentiating the energy density with respect to the corresponding number density:

$$\mu_n = \left(\frac{d\epsilon}{dn_n}\right)_{n_c} = K_n n_n, \tag{8.2}$$

$$\mu_c = \left(\frac{d\epsilon}{dn_c}\right)_{n_n} = K_c n_c. \tag{8.3}$$

We rewrite these relations in terms of the mass densities $\rho_n = m_n n_n$ and $\rho_c = m_p n_c$, yielding:

$$\mu_n = \frac{K_n}{m_n}\rho_n, \tag{8.4}$$

$$\mu_c = \frac{K_c}{m_p}\rho_c. \tag{8.5}$$

Defining the reduced chemical potentials as:

$$\tilde{\mu}_n = \frac{K_n}{m_n^2}\rho_n, \tag{8.6}$$

$$\tilde{\mu}_c = \frac{K_c}{m_p^2}\rho_c, \tag{8.7}$$

we can invert these to obtain the mass densities as:

$$\rho_n = \frac{m_n^2}{K_n}\tilde{\mu}_n = a_n\tilde{\mu}_n, \tag{8.8}$$

$$\rho_c = \frac{m_p^2}{K_c}\tilde{\mu}_c = a_c\tilde{\mu}_c. \tag{8.9}$$

Thus, the total mass density becomes:

$$\rho = \rho_n + \rho_c = a_n\tilde{\mu}_n + a_c\tilde{\mu}_c. \tag{8.10}$$

We now turn to the equations of motion (EOM) for the background configuration. Since the system is time-independent and we are working in the rotating frame where $\vec{v}_X = 0$, the steady-state Euler equations simplify to:

$$\nabla\tilde{\mu}_X + \nabla\Phi - \nabla\left(\frac{1}{2}\Omega^2 r^2\right) = 0, \tag{8.11}$$

where $X = n, c$. Integrating this yields:

$$\tilde{\mu}_n + \Phi - \frac{1}{2}\Omega^2 r^2 = C_n, \tag{8.12}$$

$$\tilde{\mu}_c + \Phi - \frac{1}{2}\Omega^2 r^2 = C_c. \tag{8.13}$$

Since both fluids share a common surface, we impose that $\tilde{\mu}_n = \tilde{\mu}_c = 0$ at the surface, yielding $C_n = C_c = C_0$. Therefore, throughout the interior of the star, both fluids share a common reduced chemical potential:

$$\tilde{\mu}_n = \tilde{\mu}_c \equiv \tilde{\mu}_0. \tag{8.14}$$

Thus, Eq. (8.12) becomes:

$$\tilde{\mu}_0 + \Phi - \frac{1}{2}\Omega^2 r^2 = C_0. \tag{8.15}$$

We now substitute this relation into Poisson's equation to determine $\tilde{\mu}_0$. The Poisson equation reads:

$$\nabla^2\Phi = 4\pi G\rho = 4\pi G(a_n + a_c)\tilde{\mu}_0. \tag{8.16}$$

We define

$$A = 4\pi G(a_n + a_c), \tag{8.17}$$

which allows us to rewrite equation (8.16) as

$$\nabla^2\Phi = A\tilde{\mu}_0. \tag{8.18}$$

Using Eq. (8.15) in Eq. (8.18), we obtain:

$$\nabla^2\tilde{\mu}_0 + A\tilde{\mu}_0 = 2\Omega^2. \tag{8.19}$$

In cylindrical coordinates, this becomes:

$$\frac{d^2\tilde{\mu}_0}{dr^2} + \frac{1}{r}\frac{d\tilde{\mu}_0}{dr} + A\tilde{\mu}_0 = 2\Omega^2. \tag{8.20}$$

This is a non-homogeneous Bessel differential equation. The homogeneous solution is given by:

$$\tilde{\mu}_0^{(h)}(r) = C_1 J_0(\sqrt{A}r), \tag{8.21}$$

where J_0 is the Bessel function of the first kind of order zero. For the particular solution, we assume $\tilde{\mu}_0^{(p)} = B$, leading to:

$$B = \frac{2\Omega^2}{A}. \tag{8.22}$$

Thus, the full solution for $\tilde{\mu}_0$ is:

$$\tilde{\mu}_0(r) = C_1 J_0(\sqrt{A}r) + \frac{2\Omega^2}{A}. \tag{8.23}$$

The boundary condition at the stellar surface requires $\tilde{\mu}_0(R) = 0$, which gives:

$$C_1 J_0(\sqrt{A}R) + \frac{2\Omega^2}{A} = 0. \tag{8.24}$$

Rearranging this yields:

$$J_0(\sqrt{A}R) = -\frac{2\Omega^2}{AC_1}. \tag{8.25}$$

From Eq. (8.15), the gravitational potential becomes:

$$\Phi(r) = \frac{1}{2}\Omega^2 r^2 - C_1 J_0(\sqrt{A}r) - \frac{2\Omega^2}{A} + C_0. \tag{8.26}$$

We determine C_0 and C_1 by matching the interior and exterior potentials at the surface. Using Gauss's law for a cylinder, we obtain the exterior solution:

$$\Phi_{\text{ext}}(r) = 2G\lambda \ln\left(\frac{r}{R}\right), \tag{8.27}$$

where λ is the mass per unit length. Without loss of generality, we set $\Phi_{\text{ext}}(R) = 0$.

Applying the continuity of potential at $r = R$ gives:

$$\frac{1}{2}\Omega^2 R^2 - C_1 J_0(\sqrt{A}R) - \frac{2\Omega^2}{A} + C_0 = 0. \tag{8.28}$$

Since $C_1 J_0(\sqrt{A}R) + \frac{2\Omega^2}{A} = 0$, it follows that:

$$C_0 = -\frac{1}{2}\Omega^2 R^2. \tag{8.29}$$

Another boundary condition applied at the surface is the continuity of the derivative of the gravitational potential at $r = R$, which gives:

$$\Omega^2 R + C_1\sqrt{A} J_1(\sqrt{A}R) = \frac{2G\lambda}{R}, \tag{8.30}$$

which rearranges to:

$$C_1 = \frac{2G\lambda - \Omega^2 R^2}{R\sqrt{A} J_1(\sqrt{A}R)}. \tag{8.31}$$

Substituting back into Eq. (8.23) yields the final expression for the reduced chemical potential:

$$\tilde{\mu}_0(r) = \frac{2G\lambda - \Omega^2 R^2}{R\sqrt{A} J_1(\sqrt{A}R)} J_0(\sqrt{A}r) + \frac{2\Omega^2}{A}. \tag{8.32}$$

The corresponding internal gravitational potential becomes:

$$\Phi(r) = \frac{1}{2}\Omega^2(r^2 - R^2) - \frac{2G\lambda - \Omega^2 R^2}{R\sqrt{A} J_1(\sqrt{A}R)} J_0(\sqrt{A}r) - \frac{2\Omega^2}{A}. \tag{8.33}$$

Using the relations from Eqs. (8.8) and (8.9), the neutron and proton mass densities can be written as:

$$\rho_n(r) = \frac{m_n^2}{K_n}\left(\frac{2G\lambda - \Omega^2 R^2}{R\sqrt{A} J_1(\sqrt{A}R)} J_0(\sqrt{A}r) + \frac{2\Omega^2}{A}\right) \tag{8.34}$$

and

$$\rho_c(r) = \frac{m_p^2}{K_p}\left(\frac{2G\lambda - \Omega^2 R^2}{R\sqrt{A}J_1(\sqrt{A}R)}J_0(\sqrt{A}r) + \frac{2\Omega^2}{A}\right). \tag{8.35}$$

We can express these densities in terms of the dimensionless radial coordinate, $\hat{r} \to \frac{r}{R}$, which yields

$$\rho_n(\hat{r}) = \frac{m_n^2}{K_n}\left(\frac{2G\lambda - \Omega^2 R^2}{R\sqrt{A}J_1(\sqrt{A}R)}J_0(\sqrt{A}R\hat{r}) + \frac{2\Omega^2}{A}\right) \tag{8.36}$$

and

$$\rho_c(\hat{r}) = \frac{m_p^2}{K_p}\left(\frac{2G\lambda - \Omega^2 R^2}{R\sqrt{A}J_1(\sqrt{A}R)}J_0(\sqrt{A}R\hat{r}) + \frac{2\Omega^2}{A}\right). \tag{8.37}$$

The density profiles $\rho_n(\hat{r})$ and $\rho_c(\hat{r})$ are shown in Figure 8.1 as functions of the dimensionless radial coordinate $\hat{r}$. Both curves display a monotonic decrease as $\hat{r}$ increases from the centre towards the surface of the star.

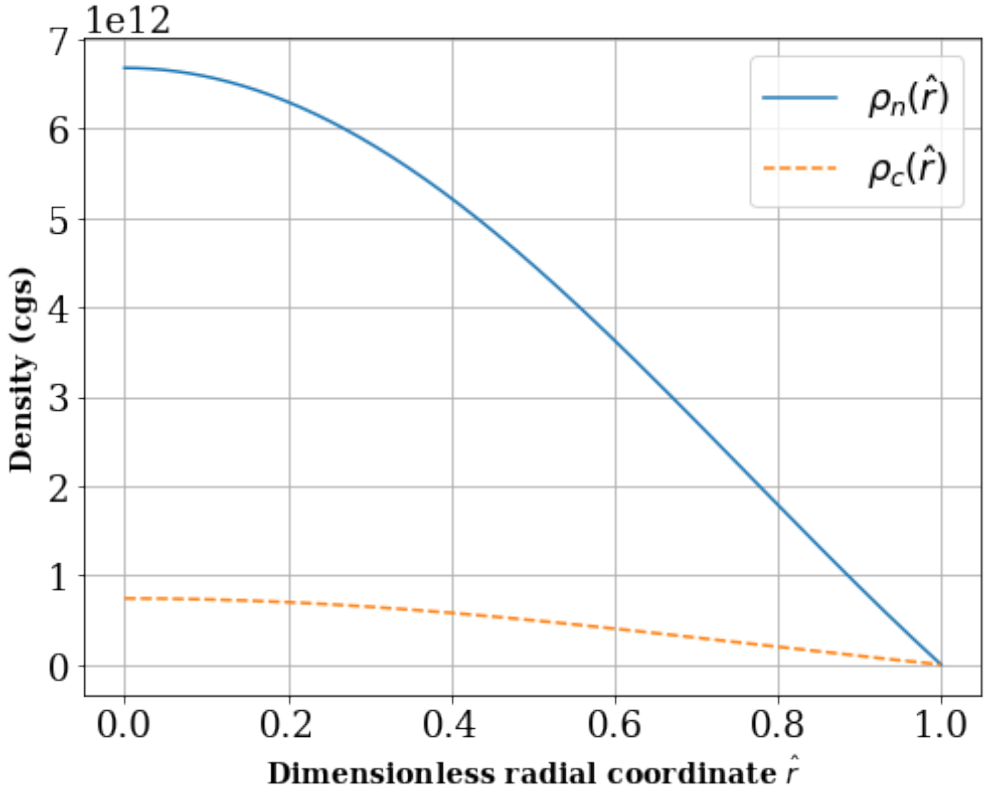

FIGURE 8.1: Plot of $\rho_n(\hat{r})$ and $\rho_c(\hat{r})$ as functions of the dimensionless radial coordinate $\hat{r}$. We assume $\lambda = 10^{25}\,\mathrm{g\,cm^{-1}}$ and $R = 10^6\,\mathrm{cm}$. The values of K_n and K_p are given in equations (B.14) and (B.15), respectively, in Appendix D, where we consider a 9 : 1 ratio between neutron and charged mass per unit lengths.

This completes the derivation of the background equilibrium configuration of the star. In the next sections, we will introduce perturbations on top of this background and solve the corresponding perturbed equations of motion to investigate the star's response.

8.2 Superfluid Neutron Velocity Perturbation

In this section, we introduce a non-axisymmetric $m = 2$ perturbed superfluid neutron velocity field for the compressible star. The overall construction follows the same logic as previously described in Section 7.3 for the incompressible case. However, due to compressibility, we will modify the condition on the velocity field using the full continuity equation.

We begin by expressing the perturbed velocity field in terms of a scalar streamfunction Ψ, such that the fluid elements follow the level sets of a scalar streamfunction Ψ. Specifically, we write:

$$\vec{\delta v}_n = g(r)\hat{z} \times \nabla\Psi. \tag{8.38}$$

Unlike the incompressible case, where we imposed the condition $\nabla \cdot \vec{\delta v}_n = 0$, for the compressible case we begin with the full continuity equation for a general flow:

$$\frac{\partial \rho_n}{\partial t} + \nabla \cdot (\rho_n \vec{v}_n) = 0. \tag{8.39}$$

Perturbing Eq. (8.39) yields:

$$\frac{\partial \delta\rho_n}{\partial t} + \nabla \cdot (\rho_n \vec{\delta v}_n) + \nabla \cdot (\delta\rho_n \, \vec{v}_n) = 0. \tag{8.40}$$

We now consider the flow of fluid elements that are stationary in the rotating frame. Under this assumption, the first term in Eq. (8.40) vanishes. Furthermore, since we are working in the rotating frame, the background velocity is zero, i.e., $\vec{v}_n = 0$. As a result, the third term also vanishes, and the continuity equation reduces to:

$$\nabla \cdot (\rho_n \vec{\delta v}_n) = 0. \tag{8.41}$$

Substituting Eq. (8.38) into Eq. (8.41) leads to:

$$g(r) = \frac{B_*}{\rho_n(r)} \ , \tag{8.42}$$

where B_* is a constant. Substituting (8.42) into (8.38) gives:

$$\vec{\delta v}_n = \frac{B_*}{\rho_n(r)} \hat{z} \times \nabla\Psi. \tag{8.43}$$

We now specify the streamfunction Ψ to ensure that the radial component of the perturbed velocity vanishes at the stellar surface while keeping the azimuthal component

finite. We adopt:

$$\Psi(r,\phi) = \frac{r^2}{R^2}\frac{\rho_n^2(r)}{\rho_{n,0}^2}e^{i2\phi}. \tag{8.44}$$

The quadratic dependence on r in Eq. (8.44) ensures that the streamfunction is regular at the origin. The background neutron density $\rho_n(r)$, derived earlier from the background equilibrium solution, is written in compact form as:

$$\rho_n(r) = DJ_0(\sqrt{A}r) + E, \tag{8.45}$$

where the constants D and E are defined as:

$$D = \frac{m_n^2}{K_n}\left(\frac{2G\lambda - \Omega^2R^2}{R\sqrt{A}J_1(\sqrt{A}R)}\right), \tag{8.46}$$

$$E = \frac{m_n^2}{K_n}\frac{2\Omega^2}{A}. \tag{8.47}$$

We substitute Eqs. (8.44) and (8.45) into Eq. (8.43), which yields the explicit form for the perturbed velocity components. The radial component becomes:

$$\delta v_{n,r} = -\frac{2iB_*r\rho_n(r)}{\rho_{n,0}^2R^2}e^{i2\phi}, \tag{8.48}$$

and the azimuthal component is:

$$\delta v_{n,\phi} = \left(\frac{2B_*r\rho_n(r)}{\rho_{n,0}^2R^2} - \frac{2B_*r^2D\sqrt{A}J_1(\sqrt{A}r)}{\rho_{n,0}^2R^2}\right)e^{i2\phi}. \tag{8.49}$$

Thus, the total perturbed velocity field can be written as:

$$\vec{\delta v}_n = -\frac{2iB_*r\rho_n(r)}{\rho_{n,0}^2R^2}e^{i2\phi}\,\hat{r} + \left(\frac{2B_*r\rho_n(r)}{\rho_{n,0}^2R^2} - \frac{2B_*r^2D\sqrt{A}J_1(\sqrt{A}r)}{\rho_{n,0}^2R^2}\right)e^{i2\phi}\,\hat{\phi}. \tag{8.50}$$

For convenience, we introduce a compact notation by defining radial functions $\tilde{u}(r)$ and $\tilde{v}(r)$ as:

$$\tilde{u}(r) = \frac{2B_*r\rho_n(r)}{\rho_{n,0}^2R^2}, \tag{8.51}$$

$$\tilde{v}(r) = \frac{2B_*r\rho_n(r)}{\rho_{n,0}^2R^2} - \frac{2B_*r^2D\sqrt{A}J_1(\sqrt{A}r)}{\rho_{n,0}^2R^2}. \tag{8.52}$$

Thus, Eq. (8.50) can be rewritten compactly as:

$$\vec{\delta v}_n = -i\tilde{u}(r)e^{i2\phi}\,\hat{r} + \tilde{v}(r)e^{i2\phi}\,\hat{\phi}. \tag{8.53}$$

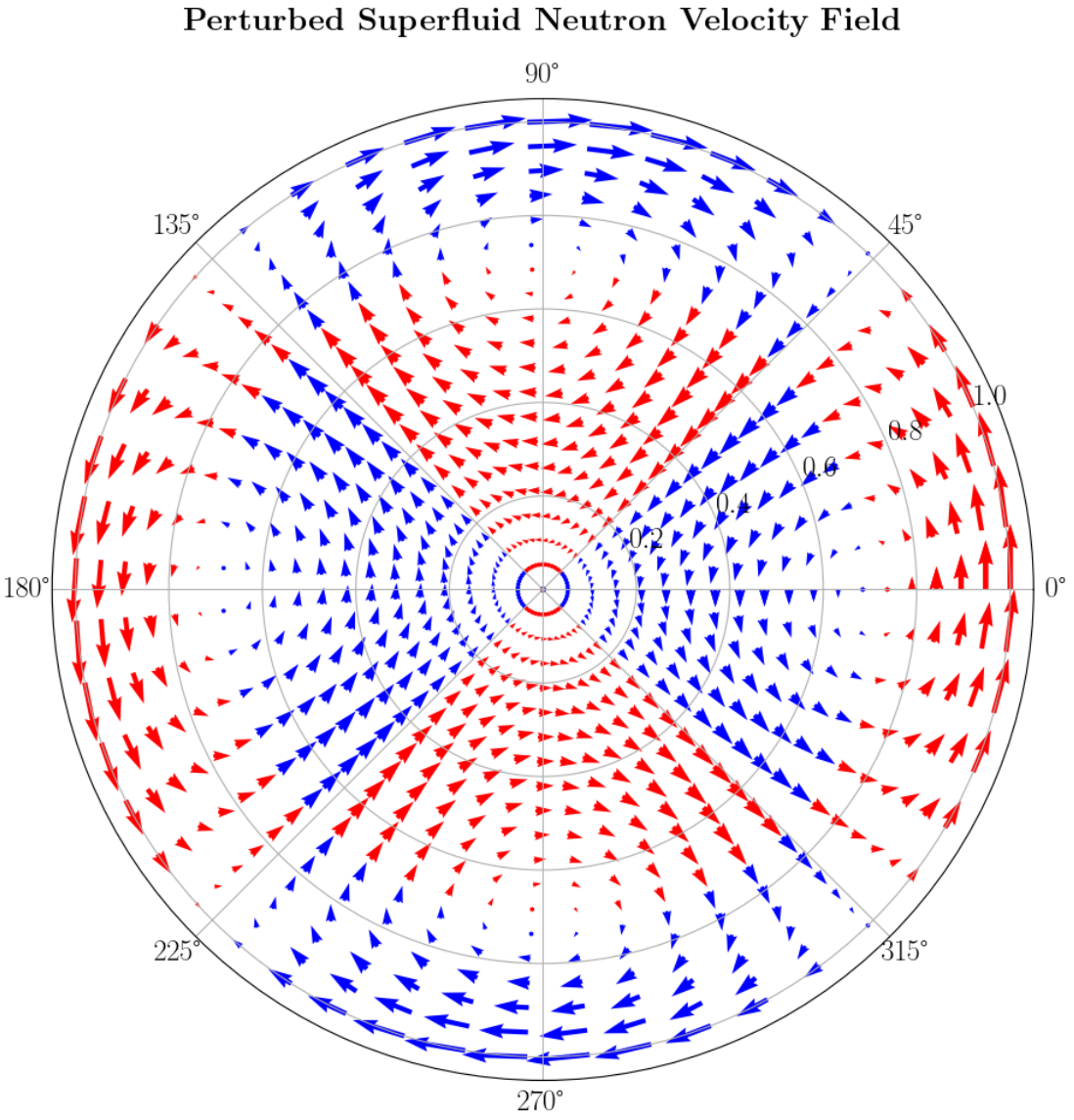

FIGURE 8.2: This figure shows the $m = 2$ perturbed velocity field corresponding to Equation (8.50).

We have now successfully constructed an $m = 2$ perturbed superfluid neutron velocity field appropriate for the compressible background configuration. Figure 8.2 shows a visualisation of this perturbed velocity field. In the following sections, we will use this velocity perturbation to compute the resulting current multipole moment and solve for the elastic displacement field that arises in response to this perturbation.

8.3 Current Multipole

In this section, we compute the current multipole moment S_{22} using the perturbed superfluid neutron velocity derived in Section 8.2 for the compressible star. The expression for S_{22} remains the same as previously defined in Eq. (7.34).

As before, we follow the derivation steps from Eqs. (7.35) through (7.49) that transform the multipole definition into cylindrical coordinates. These steps are identical to those described in Section 7.4. The final expression for the $l = 2$, $m = 2$ current multipole in cylindrical coordinates, but now applied to the compressible star, reads:

$$S_{22} = \frac{32\pi\sqrt{2}}{15} \int_0^z \int_0^{2\pi} \int_0^R \rho_n \, \vec{\delta v}_n \cdot \vec{Y}^*_{B,22} (\varpi^2 + z^2) \varpi \, d\varpi \, d\phi \, dz. \tag{8.54}$$

Unlike the incompressible case, the density ρ_n now varies with radius, and therefore appears inside the integral.

In order to evaluate the current multipole moment for the compressible case, we use the general expression for an $m = 2$ perturbed velocity field. This approach allows us to compute the current multipole without committing to a specific velocity profile. We recall the general form of the perturbed velocity from Eq. (7.49), written in terms of two unknown radial functions $u(\varpi)$ and $v(\varpi)$ as:

$$\vec{\delta v}_n = u(\varpi) e^{i2\phi} \hat{e}_\varpi + i2v(\varpi) e^{i2\phi} \hat{e}_\phi. \tag{8.55}$$

Substituting Eq. (8.55) into the continuity equation (8.41) gives the following relation between between $u(\varpi)$ and $v(\varpi)$:

$$v(\varpi) = \frac{1}{4\rho_n} \frac{d}{d\varpi} \left(\rho_n \varpi u(\varpi) \right). \tag{8.56}$$

Substituting these expressions into Eq. (8.54), and integrating over ϕ and z, we arrive at:

$$S_{22} = \frac{32\pi\sqrt{2}}{15} \int_0^z \int_0^{2\pi} \int_0^R \rho_n \vec{\delta v}_n \cdot \vec{Y}^*_{B,22} (\varpi^2 + z^2) \varpi \, d\varpi \, d\phi \, dz \tag{8.57}$$

$$= \frac{16\pi\sqrt{\pi}}{\sqrt{90}} z^2 \int_0^R \rho_n \left(u(\varpi) + 2v(\varpi) \right) \varpi^2 \, d\varpi. \tag{8.58}$$

Using Eq. (8.56), this becomes:

$$S_{22} = \frac{16\pi\sqrt{\pi}}{\sqrt{90}} z^2 \int_0^R \left(\rho_n u(\varpi) \varpi^2 + \frac{\varpi^2}{2} \frac{d}{d\varpi} (\varpi u(\varpi) \rho_n) \right) d\varpi. \tag{8.59}$$

We now do integration by parts. The integral becomes:

$$S_{22} = \frac{16\pi\sqrt{\pi}}{\sqrt{90}} z^2 \left[\left(\rho_n u(\varpi) \frac{\varpi^3}{2} \right)_0^R - \int_0^R \frac{\varpi^2}{2} \frac{d}{d\varpi} (\varpi u(\varpi) \rho_n) d\varpi + \int_0^R \frac{\varpi^2}{2} \frac{d}{d\varpi} (\varpi u(\varpi) \rho_n) d\varpi \right]. \tag{8.60}$$

The last two integrals cancel each other exactly, leaving:

$$S_{22} = \frac{16\pi\sqrt{\pi}}{\sqrt{90}} z^2 \left[\rho_n(R) u(R) \frac{R^3}{2} \right]. \tag{8.61}$$

As we require the radial component of the perturbed velocity to vanish at the stellar surface (i.e., $u(R) = 0$), this directly leads to:

$$S_{22} = 0. \tag{8.62}$$

Thus, even for the compressible star model, the $m = 2$ current multipole moment vanishes under the constructed perturbation. The reason is once again that the surface boundary condition $u(R) = 0$ ensures that the surface integral gives no contribution, just as we found in the incompressible case. It is possible that the vanishing current multipole arises from the assumed cylindrical geometry, and that realistic spherical stars may yield a non-trivial current multipole value.

8.4 Solving the equations of motion

In this section, we solve for the perturbed equations of motion (EOMs) for both the fluid and elastic components of the compressible star. These two components are coupled through the Magnus force, which acts on the superfluid neutrons due to the non-axisymmetric vortex pinning, and through the equal but opposite reaction forces that act on the elastic component as a result of the pinned vortices. Throughout this analysis, we apply the Cowling approximation. This simplifies the problem while still capturing the essential physics of the mutual coupling between the fluids and the elastic crust.

8.4.1 Solving Fluid Equations of Motion

We now proceed to solve the equations of motion for the fluid component of the compressible star in the rotating frame. As in the incompressible case, the perturbed fluid equation of motion (EOM) retains the same form as given previously in Eq. (7.56). The only difference is that the perturbed velocity field entering the equation is now given by Eq. (8.50), appropriate for the compressible case. As in the previous chapter, the Magnus force $\delta\vec{F}_m$ is again balanced exactly by the Coriolis force to leading order, which leaves:

$$\nabla \delta\tilde{\mu}_n = 0. \tag{8.63}$$

This indicates that the perturbed chemical potential must be spatially constant:

$$\delta\tilde{\mu}_n = \text{constant}. \tag{8.64}$$

To determine the value of this constant, we apply the boundary condition at the stellar surface. The appropriate boundary condition is that the Lagrangian perturbation of the chemical potential vanishes at the surface as given in (7.142). This allows us to express the constant as:

$$\text{constant} = -\xi_r \frac{\partial\tilde{\mu}_n}{\partial r}. \tag{8.65}$$

Next, we specify the functional form of the surface displacement. Assuming the perturbed displacement at the surface has an $m = 2$ angular dependence, we write:

$$\xi_r = f(r)\cos(2\phi). \tag{8.66}$$

Substituting Eq. (8.66) into Eq. (8.65), we observe that the right-hand side contains a $\cos(2\phi)$ dependence, while the left-hand side must be a constant. The only way these two can be equal for all azimuthal angles is if the coefficient of $\cos(2\phi)$ vanishes. This implies:

$$\xi_r = 0. \tag{8.67}$$

Thus, we find that the perturbed radial displacement of the fluid vanishes at the surface. Substituting this result back into Eq. (8.65) gives:

$$\delta\tilde{\mu}_n = 0. \tag{8.68}$$

Therefore, even in the compressible case, we reach the same conclusion as in the incompressible model: the perturbed chemical potential vanishes.

8.4.2 Solving Elastic Equations of Motion

In this section, we solve the equations of motion (EOM) for the elastic component of a compressible star. We begin by perturbing the elastic EOM from Eq. (7.67), as described earlier in Section 7.5.2. Under the Cowling approximation and assuming a compressible stellar model, the perturbed EOM takes the form:

$$\nabla^a\delta\tau_{ab} - \frac{\delta\rho_c}{\rho_c}\nabla^a\tau_{ab} - \delta F_b^{mag} = 0, \tag{8.69}$$

where $-\delta F^{mag}$ represents the reaction force due to the Magnus force acting on pinned vortices. To express the background stress tensor τ_{ab}, we insert the density–chemical

potential relation from Eq. (8.9) into the general expression for the stress tensor gradient in Eq. (7.68). Upon integration, we obtain:

$$\tau_{ab} = -\frac{a_c \tilde{\mu}_c^2}{2} g_{ab}. \tag{8.70}$$

Let us define,

$$\Psi = \frac{a_c \tilde{\mu}_c^2}{2}, \tag{8.71}$$

so that Eq. (8.70) can be written as:

$$\tau_{ab} = -\Psi g_{ab}. \tag{8.72}$$

Substituting the expression for δF^{mag} from Eq. (7.58) and the background stress tensor from Eq. (8.70) into Eq. (8.69) yields:

$$\nabla^a \delta\tau_{ab} + \delta\rho_c \nabla_b \tilde{\mu}_c = \rho_n 2\Omega \times \vec{\delta v}_n, \tag{8.73}$$

which can equivalently be written in index notation as:

$$\nabla^a \delta\tau_{ab} + \delta\rho_c \nabla_b \tilde{\mu}_c = \rho_n 2\Omega \epsilon_{bzd} \delta v_n^d. \tag{8.74}$$

Here, the perturbed stress tensor is given by

$$\delta\tau_{ab} = -\rho_c \delta\tilde{\mu}_c g_{ab} + \mu \left(\nabla_a \xi_b + \nabla_b \xi_a - \frac{2}{3} g_{ab} \nabla^c \xi_c \right), \tag{8.75}$$

which is structurally similar to Eq. (7.73) used in the incompressible model, but with the shear modulus μ and the charged-fluid density ρ_c now treated as functions of r. We adopt the expression for the shear modulus $\mu(r)$ from equation (13) of Strohmayer et al. (1991), which is

$$\mu(r) = C^* \, \tilde{\mu}_c^{\frac{4}{3}}, \tag{8.76}$$

where the constant C^* is defined as

$$C^* = 0.1194 \, e^2 \left(\frac{4\pi}{3} \right)^{\frac{1}{3}} \left(\frac{m_p}{K_p} \right)^{\frac{4}{3}}, \quad \text{(CGS units)}. \tag{8.77}$$

Here, the electron charge e is expressed in CGS units (statcoulomb). The reduced chemical potential $\tilde{\mu}_c$ is also expressed in CGS units in Eq. (8.76). In the original reference, the shear modulus was written in terms of the density ρ_c. In this work, we re-express the shear modulus in terms of the reduced chemical potential $\tilde{\mu}_c$ using the relation given in Eq. (8.7), as this provides a natural extension to the two-fluid formalism.

Inserting Eqs. (8.75) and (8.53) into Eq. (8.74), and following the same steps as outlined in Eqs. (7.77) through (7.104), we obtain the radial and azimuthal components of the EOM as:

$$\frac{d\delta\tau_{rr}}{dr} - \frac{2\mu}{r}\left(\frac{\xi_r}{r} - \frac{d\xi_r}{dr}\right) - \frac{4}{r}\delta\tau'_{r\phi} + 8\mu\frac{\xi_\perp}{r^2} + \delta\rho_c\frac{d\tilde{\mu}_c}{dr} = -\rho_n 2\Omega\tilde{v}(r), \tag{8.78}$$

$$\delta\tau_{rr} + 2\mu\left(\frac{\xi_r}{r} - \frac{d\xi_r}{dr}\right) + r\frac{d\delta\tau'_{r\phi}}{dr} + 2\delta\tau'_{r\phi} - 8\mu\frac{\xi_\perp}{r} = -r\rho_n\Omega\tilde{u}(r). \tag{8.79}$$

Interestingly, although the shear modulus μ varies with radius in this compressible case, the left-hand sides (LHS) of Eqs. (8.78) and (8.79) match exactly with those derived in the incompressible case, i.e., Eqs. (7.105) and (7.106), except for the additional term $\delta\rho_c\frac{d\tilde{\mu}_c}{dr}$ in the radial component arising from the $\delta\rho_c\nabla_b\tilde{\mu}_c$ contribution in the compressible EOM. This happens because all additional terms resulting from the radial dependence of μ cancel out. On the right-hand sides (RHS) of the equations the velocity profiles $\tilde{u}(r)$ and $\tilde{v}(r)$ replace the $u(r)$ and $v(r)$ profiles used in the incompressible case.

The form of the perturbed stress tensor components in the present compressible model is identical to that derived for the incompressible case, Eqs. (7.86) and (7.87); however, in this model, both the density and the shear modulus are functions of r.

We aim to solve the EOMs (8.78) and (8.79). First, we substitute the expressions for the perturbed stress tensor components, Eqs. (7.86) and (7.87), into Eq. (8.78), obtaining:

$$\frac{4\mu}{3}\frac{d^2\xi_r}{dr^2} + \frac{4}{3}\frac{d\xi_r}{dr}\left(\frac{d\mu}{dr} + \frac{\mu}{r}\right) - \frac{2\xi_r}{3r}\left(\frac{d\mu}{dr} + \frac{8\mu}{r}\right) + \frac{4\xi_\perp}{3r}\left(\frac{2\,d\mu}{dr} + \frac{7\mu}{r}\right) - \frac{4\mu}{3r}\frac{d\xi_\perp}{dr}$$
$$- \rho_c\frac{d\delta\tilde{\mu}_c}{dr} - \delta\tilde{\mu}_c\left(\frac{d\rho_c}{dr} + DJ_1(\sqrt{A}r)\right) = -2\rho_n\Omega\tilde{v}(r). \tag{8.80}$$

Similarly, substituting Eqs. (7.86) and (7.87) into Eq. (8.79) yields:

$$\mu\frac{d^2\xi_\perp}{dr^2} + \frac{d\xi_\perp}{dr}\left(\frac{d\mu}{dr} + \frac{7\mu}{3r}\right) - \frac{\xi_\perp}{r}\left(\frac{d\mu}{dr} + \frac{19\mu}{3r}\right) + \frac{\mu}{3r}\frac{d\xi_r}{dr} + \frac{\xi_r}{r}\left(\frac{d\mu}{dr} + \frac{7\mu}{3r}\right) - \frac{\rho_c\delta\tilde{\mu}_c}{r}$$
$$= -\Omega\rho_n\tilde{u}(r). \tag{8.81}$$

In addition to the second-order EOMs (8.80) and (8.81), we also consider the continuity equation:

$$\delta\rho_c + \nabla\cdot(\rho_c\vec{\xi}) = 0, \tag{8.82}$$

which simplifies to:

$$\xi_\perp = \frac{\delta\tilde{\mu}_c\, r}{4\tilde{\mu}_c} + \frac{r\xi_r}{4\rho_c}\frac{d\rho_c}{dr} + \frac{\xi_r}{4} + \frac{r}{4}\frac{d\xi_r}{dr}. \tag{8.83}$$

Our goal is to solve Eqs. (8.80), (8.81), and (8.83) to determine the functions ξ_r, $\xi_\perp$, and $\delta\tilde{\mu}_c$. Due to the coupling and complexity of these equations, an analytical solution is no longer feasible as in the incompressible case. Instead, we follow a numerical approach similar to that described in Ushomirsky et al. (2000), converting the second-order ODEs into first-order form. For this purpose, we introduce the following new variables:

$$z_1 = \frac{\xi_r}{r}, \tag{8.84}$$

$$z_2 = \frac{\Delta\tau_{rr}}{\Psi_o} = \frac{\delta\tau_{rr}}{\Psi_o} - \frac{z_1}{\Psi_o}\frac{d\Psi}{d\ln r}, \tag{8.85}$$

$$z_3 = \frac{\xi_\perp}{r}, \tag{8.86}$$

$$z_4 = \frac{\Delta\tau'_{r\phi}}{\Psi_o} = \frac{\delta\tau'_{r\phi}}{\Psi_o}, \tag{8.87}$$

$$z_5 = \frac{\Delta\tilde{\mu}_c}{\tilde{\mu}_o} = \frac{\delta\tilde{\mu}_c}{\tilde{\mu}_o} + \frac{z_1}{\tilde{\mu}_o}\frac{d\tilde{\mu}_c}{d\ln r}. \tag{8.88}$$

Here,

$$\tilde{\mu}_o = C_1 + C_2, \tag{8.89}$$

which is the value of $\tilde{\mu}_c(r)$ at the origin, and

$$\Psi_o = \frac{a_c\tilde{\mu}_o^2}{2} = \frac{a_c(C_1+C_2)^2}{2}, \tag{8.90}$$

is the central value of Ψ. The constant C_1 is the same as defined in Eq. (8.31), and

$$C_2 = \frac{2\Omega^2}{A}. \tag{8.91}$$

To simplify the analysis of the system, we introduce the dimensionless radius

$$\hat{r} = \frac{r}{R}, \tag{8.92}$$

and three dimensionless parameters:

$$\varepsilon_\mu = \frac{\mu_0}{\Psi_0}, \tag{8.93}$$

$$\varepsilon_\Omega = \frac{\Omega^2}{2\pi G(\rho_{n,0}+\rho_{c,0})}, \tag{8.94}$$

$$\varepsilon_{mag} = \frac{B_*\Omega}{\Psi_0}. \tag{8.95}$$

Using the definitions of z_2 and z_4, and substituting from Eqs. (7.86), (7.87), and (8.71), we obtain two first-order differential equations:

$$\frac{dz_1}{d\ln\hat{r}} = -\frac{z_1}{2} + \frac{3}{4\alpha_1}z_2 - 2z_3 + \frac{3\alpha_3}{2\alpha_1}z_5, \tag{8.96}$$

$$\frac{dz_3}{d\ln\hat{r}} = \frac{z_4}{\alpha_1} - z_1. \tag{8.97}$$

Here,

$$\alpha_1 = \hat{\rho}\,\varepsilon_\mu, \tag{8.98}$$

$$\alpha_3 = \hat{\rho}, \tag{8.99}$$

where

$$\hat{\rho} = \frac{\rho_n}{\rho_{n,0}} = \frac{\rho_c}{\rho_{c,0}} = \varepsilon_\Omega + J_0(\sqrt{A}R\hat{r})(1-\varepsilon_\Omega) \tag{8.100}$$

We now rewrite the EOMs (8.78), (8.79), and the continuity equation (8.83) in terms of z_i, obtaining:

$$\frac{dz_2}{d\ln\hat{r}} = z_1(\alpha_1 - \frac{\Gamma}{2} - \gamma + \frac{\alpha_4^2}{2}) - z_2\frac{3}{4}\frac{\alpha_2}{\alpha_1} + 2z_3(\Gamma - 2\alpha_1) + 4z_4 - \left[\frac{3}{2}\frac{\alpha_2\alpha_3}{\alpha_1} + \alpha_4\right]z_5 + \tilde{V}, \tag{8.101}$$

$$\frac{dz_4}{d\ln\hat{r}} = -z_1(\alpha_1 + \Gamma) + \frac{z_2}{2} + 4\alpha_1 z_3 - 2z_4 + 3\alpha_3 z_5 + \tilde{U}, \tag{8.102}$$

$$\frac{dz_1}{d\ln\hat{r}} = -2z_1 + 4z_3 - \frac{z_5}{\alpha_3}. \tag{8.103}$$

where

$$\Gamma = -2\hat{r}\hat{\rho}(1-\varepsilon_\Omega)\sqrt{A}RJ_1(\sqrt{A}R\hat{r}), \tag{8.104}$$

$$\alpha_2 = \Gamma + 2\alpha_1, \tag{8.105}$$

$$\gamma = \hat{r}^2\frac{d^2(\hat{\rho})^2}{d\hat{r}^2}, \tag{8.106}$$

$$\alpha_4 = 2\frac{d\hat{\rho}}{dr}, \tag{8.107}$$

$$\tilde{V} = -4\varepsilon_{mag}\hat{r}^2\left(\hat{\rho}^2 + \frac{\Gamma}{2}\right), \tag{8.108}$$

$$\tilde{U} = -2\varepsilon_{mag}\hat{r}^2\hat{\rho}^2. \tag{8.109}$$

Equating Eqs. (8.96) and (8.103) allows expressing z_5 in terms of the other variables:

$$z_5 = \left(\frac{2\alpha_3}{3\alpha_5 + 2}\right)\left(-\frac{3}{2}z_1 - \frac{3}{4\alpha_1}z_2 + 6z_3\right), \tag{8.110}$$

where

$$\alpha_5 = \frac{\alpha_3^2}{\alpha_1} = \frac{\hat{\rho}^{2/3}}{\varepsilon_\mu}. \tag{8.111}$$

Substituting Eq. (8.110) into Eqs. (8.96), (8.97), (8.101), and (8.102) leads to:

$$\frac{dz_1}{d\ln r} = -z_1\left[\frac{6\alpha_5+1}{3\alpha_5+2}\right] + \frac{3z_2}{2(3\alpha_3^2+2\alpha_1)} + 4z_3\left[\frac{3\alpha_5-1}{3\alpha_5+2}\right], \tag{8.112}$$

$$\frac{dz_2}{d\ln r} = z_1\left[2\alpha_1\left(\frac{6\alpha_5+1}{3\alpha_5+2}\right) + \Gamma - 2\alpha_3\beta\right] - z_2\frac{3}{(3\alpha_5+2)} - z_3\left[4\Gamma + 8\alpha_1\left(\frac{6\alpha_5+1}{3\alpha_5+2}\right)\right] + 4z_4 + \tilde{V}, \tag{8.113}$$

$$\frac{dz_3}{d\ln r} = \frac{z_4}{\alpha_1} - z_1, \tag{8.114}$$

$$\frac{dz_4}{d\ln r} = -z_1\left[\Gamma + \frac{2\alpha_1(6\alpha_5+1)}{(3\alpha_5+2)}\right] + z_2\left[\frac{1-3\alpha_5}{3\alpha_5+2}\right] + 8\alpha_1 z_3\left[\frac{6\alpha_5+1}{3\alpha_5+2}\right] - 2z_4 + \tilde{U}. \tag{8.115}$$

Here,

$$\beta = -\frac{\hat{r}^2(\sqrt{A}R)^2(1-\varepsilon_\Omega)\left[J_0(\sqrt{A}R\hat{r}) - J_2(\sqrt{A}R\hat{r})\right]}{2}. \tag{8.116}$$

Equations (8.112)–(8.115) define a coupled system of four first-order ODEs in the variables z_1, z_2, z_3, and z_4, where $\tilde{U}$ and $\tilde{V}$ are source terms.

To solve this system, we require four boundary conditions.

1. **Surface Traction-Free Conditions:** At the stellar surface ($\hat{r} = 1$), the normal and tangential components of stress must vanish:

$$\Delta\tau_{rr}(1) = 0, \tag{8.117}$$

$$\Delta\tau_{r\phi}(1) = 0. \tag{8.118}$$

2. **Regularity Conditions at the Origin:** The solution must remain finite at $\hat{r} \to 0$. We obtain three regularity conditions, given in equation (C.60) in Appendix C, expressed in terms of a common parameter, $z_{1,0} = \varepsilon_\mu$, which is the value of z_1 at $\hat{r} = 0$.

   At first sight, the appearance of three regularity conditions may seem unexpected, since only two are typically required for a second-order system. However, one is always free to seek a unique, physically regular solution even if the problem appears to admit an additional boundary condition. We implement the problem using the `solve_bvp` Python solver, which allows all three regularity conditions to be imposed consistently because they are not independent but are linked through

the single parameter ε_μ. The regularity conditions are

$$z_{2,0} = 2\varepsilon_\mu z_{1,0}, \tag{8.119}$$

$$z_{3,0} = \frac{1}{2} z_{1,0}, \tag{8.120}$$

$$z_{4,0} = \varepsilon_\mu z_{1,0}. \tag{8.121}$$

These boundary conditions allow us to numerically solve the system of first-order ODEs.

8.4.2.1 Parametrised dimensionless quantities and back-of-the-envelope estimates

In this section, we write the three dimensionless parameters ε_μ, ε_Ω, and $\varepsilon_{\rm mag}$, as defined in Eqs. (8.93), (8.94), and (8.95), in parametrised form.

Using the relation $\rho_{c,0} = \rho_{n,0}/9$, so that $\rho_{n,0} + \rho_{c,0} = (10/9)\rho_{n,0}$, the rotational parameter may be written in the parametrised form

$$\varepsilon_\Omega \simeq 2.15 \times 10^{-5}\, \Omega_{100}^2\, \rho_{15}^{-1}, \tag{8.122}$$

where $\Omega_{100} = \Omega/(100\ {\rm rad\,s^{-1}})$ and $\rho_{15} = \rho_{n,0}/(10^{15}\ {\rm g\,cm^{-3}})$.

We set $\delta v_n \approx 10^4\ {\rm cm\,s^{-1}}$ at $r = 0.95R$, based on Figure 15 of Seveso et al. (2015). The figure shows a maximum critical lag of order 10^{-2} at $r \approx 0.95R$, which, when multiplied by the stellar radius, corresponds to a critical unpinning velocity of approximately $10^4\ {\rm cm\,s^{-1}}$.

Using Eq. (8.50), which relates δv_n and B_*, we obtain

$$\delta v_n \approx \frac{2\rho_n B_*}{\rho_{n,0}^2\, R} \approx \frac{2 \times 10^{-1} B_*}{\rho_{n,0}\, R}, \tag{8.123}$$

where we have taken $\rho_n(r = 0.95R)/\rho_{n,0} \approx 0.1$.

This leads to

$$\varepsilon_{\rm mag} = \frac{\rho_{n,0} R\Omega\, \delta v_n}{2 \times 10^{-1}\, \Psi_0} \simeq 10^{-8}\, \frac{\rho_{15}\, R_6\, \Omega_{100}\, (\delta v_n)_4}{\Psi_{35}}, \tag{8.124}$$

where $R_6 = R/(10^6\ {\rm cm})$, $(\delta v_n)_4 = \delta v_n/(10^4\ {\rm cm\,s^{-1}})$, and $\Psi_{35} = \Psi_0/(10^{35}\ {\rm erg\,cm^{-3}})$.

Finally, the elastic parameter may be written as

$$\varepsilon_\mu = 10^{-5}\, \frac{\mu_{30}}{\Psi_{35}}, \tag{8.125}$$

with $\mu_{30} = \mu_0/(10^{30}\ \mathrm{erg\,cm^{-3}})$.

Next, we present a brief calculation to estimate the approximate magnitude of the dimensionless displacement fields z_1 and z_3, by balancing the Magnus force with the elastic restoring force. The Magnus force per unit volume is given in Eq. (7.58), and the elastic restoring force per unit volume is approximated by $\mu\vec{\xi}/r^2$, where μ is the shear modulus and $\vec{\xi}$ is the displacement field.

By equating these two forces, we obtain

$$2\rho_{n,0}\,\vec{\Omega} \times \vec{v}_n = \mu_0 \frac{\vec{\xi}}{R^2}. \tag{8.126}$$

Solving Eq. (8.126) for the magnitude of the displacement field $\vec{\xi}$, we find

$$z_1 \approx z_3 \approx \frac{\xi}{R} \approx \frac{2\Omega\,\rho_{n,0}\,v_n\,R}{\mu_0}. \tag{8.127}$$

Substituting Eq. (8.123), we obtain

$$z_1 \approx z_3 \approx \frac{4\rho_n \Omega\,B_*}{\rho_{n,0}\,\mu_0} \approx \frac{4\times10^{-1}\Omega\,B_*}{\mu_0}, \tag{8.128}$$

where we have taken $\rho_n(r = 0.95R)/\rho_{n,0} \approx 0.1$. Multiplying both the numerator and denominator of Eq. (8.128) by Ψ_0, and using the definitions of the dimensionless parameters $\varepsilon_{\mathrm{mag}}$ and ε_μ, we obtain

$$z_1 \approx z_3 \approx \frac{4\times10^{-1}\varepsilon_{\mathrm{mag}}}{\varepsilon_\mu}. \tag{8.129}$$

Finally, for $\varepsilon_{\mathrm{mag}} = 10^{-8}$ and $\varepsilon_\mu = 10^{-5}$, Eq. (8.129) gives

$$z_1 \approx z_3 \approx 4\times10^{-4}. \tag{8.130}$$

This estimate serves as a useful cross-check for validating the numerical solutions obtained for the displacement variables z_1 and z_3 in the main analysis.

8.4.2.2 Numerical Results

We have obtained a system of four first-order ordinary differential equations (ODEs), accompanied by five boundary conditions, three of which are expressed in terms of a common parameter ε_μ. This system is solved numerically using the `solve_bvp` function from the `scipy.integrate` Python package.

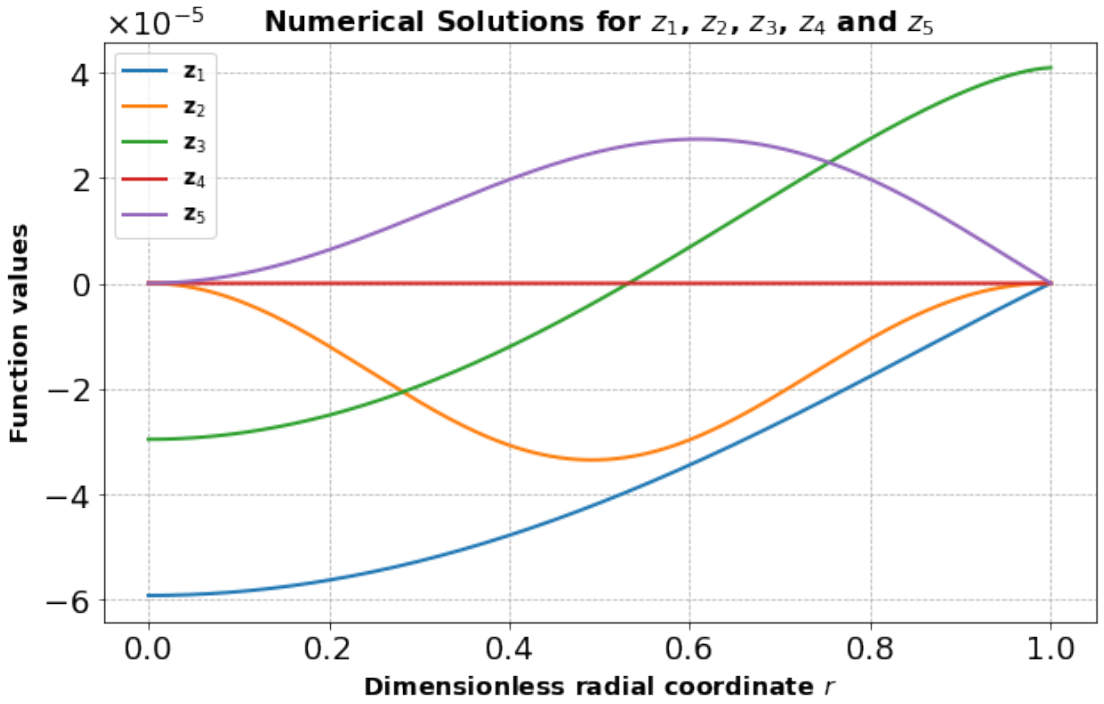

FIGURE 8.3: Solutions for $z_1(\hat{r})$, $z_2(\hat{r})$, $z_3(\hat{r})$, $z_4(\hat{r})$ and $z_5(\hat{r})$ as functions of the dimensionless cylindrical radial coordinate $\hat{r}$.

For the numerical implementation, we assigned specific values to $\varepsilon_\mu = 10^{-5}$. we fix $\varepsilon_\Omega = 10^{-4}$ and $\varepsilon_{\text{mag}} = 10^{-8}$, both parameterised by the stellar angular velocity Ω, which is taken to be 100 rad s^{-1}. We fix $r_{\text{min}} = 10^{-6}$ and $r_{\text{max}} = 1$.

The solutions for $z_1(\hat{r})$, $z_2(\hat{r})$, $z_3(\hat{r})$, $z_4(\hat{r})$ and $z_5(\hat{r})$ are shown in Figure 8.3. All four functions exhibit smooth behaviour across the domain. To verify the validity of the numerical solution, we compare the computed values of z_1 and z_3 at a representative point in the star with an analytical back-of-the-envelope estimate. Specifically, at the midpoint of the star, $\hat{r} = 0.5$, the numerical results yield:

- $z_1(0.5) = -4 \times 10^{-5}$
- $z_3(0.5) = -3 \times 10^{-6}$

The corresponding back-of-the-envelope estimate, as derived in section 8.4.2.1, gives:

$$\frac{\zeta}{R} \approx 4 \times 10^{-4}. \tag{8.131}$$

Since the numerical results differ from the back-of-the-envelope (BOTE) estimate by one to two orders of magnitude, the agreement is not sufficiently close to be fully convincing. However, the BOTE estimate predicts that the solutions $z_1(0.5)$ and $z_3(0.5)$ scale inversely with the shear parameter ε_μ, as indicated by Eq. (8.129). This scaling

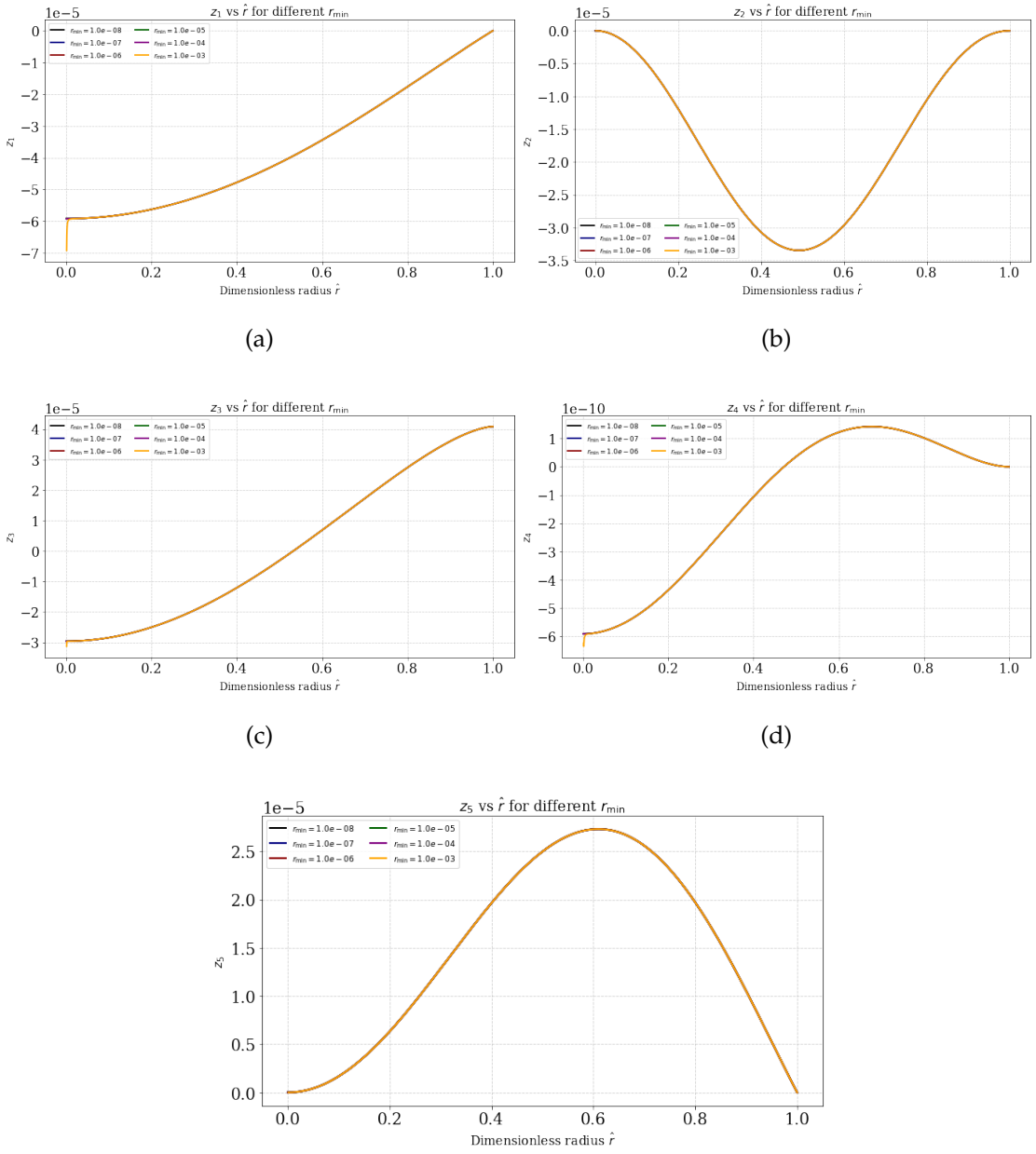

FIGURE 8.4: This figure shows the variation of the modulus of z_1, z_2, z_3, z_4, and z_5 with $\hat{r}$ for different choices of $r_{\rm min}$. The horizontal axis is plotted on a logarithmic scale. Throughout, we fix $\varepsilon_\Omega = 10^{-4}$ and $\varepsilon_{\rm mag} = 10^{-8}$, both parameterized by the stellar angular velocity Ω, which is taken to be 100 rad s^{-1}.

behaviour is borne out by the numerical results: in the log–log plots of $z_1(0.5)$ and $z_3(0.5)$ as functions of ε_μ, we observe an approximately linear trend with a slope close to -1, as shown in Fig. 8.6(a) and Fig. 8.6(c). The clear consistency in this scaling provides reassurance that the numerical solutions capture the correct underlying physical behaviour. Moreover, we find that $z_2(1)$ and $z_4(1)$ vanish at the stellar surface, as required by the imposed boundary conditions.

The values of $z_1(1)$ and $z_3(1)$, when multiplied by R, yield the values of the radial and perpendicular displacements, ξ_r and $\xi_\perp$, respectively. The values of ξ_r and $\xi_\perp$ are not unique, but scale proportionally with the free parameter ϵ_{mag} of the model.

Figures 8.4 and 8.5 illustrate how the solutions behave for different choices of $r_{\min}$ and $r_{\max}$, respectively.

In Fig. 8.4, we vary $r_{\min}$ from 10^{-8} to 10^{-3}. We observe the appearance of spikes near the origin in the cases of z_1, z_3, and z_4, while the overall radial profiles remain similar across the rest of the domain. These spikes become prominent for larger values of $r_{\min}$, particularly for $r_{\min} \gtrsim 10^{-3}$. In our numerical implementation, we choose $r_{\min} = 10^{-6}$, which is a standard and well-behaved choice for most physics problems. It is clear from Eqs. (8.112)–(8.115) that we cannot take $r_{\min} = 0$, since expanding the $\ln(r)$ term on the left-hand side introduces factors of r in the numerator, which, when transferred to the right-hand side, appear in the denominator and lead to singular behaviour.

In our numerical implementation, we set $r_{\max} = 1$, even though two coefficients constructed from background functions in Eqs. (8.112) and (8.114) diverge at $r_{\max} = 1$. However, when the system is solved numerically, the resulting solutions remain finite and well behaved at the outer boundary. This behaviour was not obvious beforehand and was confirmed only through numerical experimentation.

To check the reliability of this choice, we vary $r_{\max}$ between 0.99 and 1, as shown in Fig. 8.5. The solutions are found to be almost identical over this range, indicating that the results are not sensitive to the precise choice of the outer boundary within this interval. Based on this test, we set $r_{\max} = 1$ in all numerical calculations.

To perform a sanity check on our numerical results, we examine the behaviour of the displacement field of the star as the shear modulus parameter ε_μ is varied. Physically, increasing the shear modulus makes the star more resistant to deformation, and we therefore expect a monotonic decrease in the magnitudes of z_1 and z_3. This behaviour is also predicted by the back-of-the-envelope analysis in Eq. (8.129). Taking the logarithm of both sides of Eq. (8.129), we expect a slope of -1 in the log–log plots of $|z_1|$ and $|z_3|$ versus ε_μ. This behaviour is indeed observed, as shown in Fig. 8.6 (a) and Fig. 8.6 (c), respectively.

In Fig. 8.6 (a), we present three curves corresponding to $|z_1|$ evaluated at the centre, midpoint, and surface of the star. All three exhibit a slope close to -1, consistent with

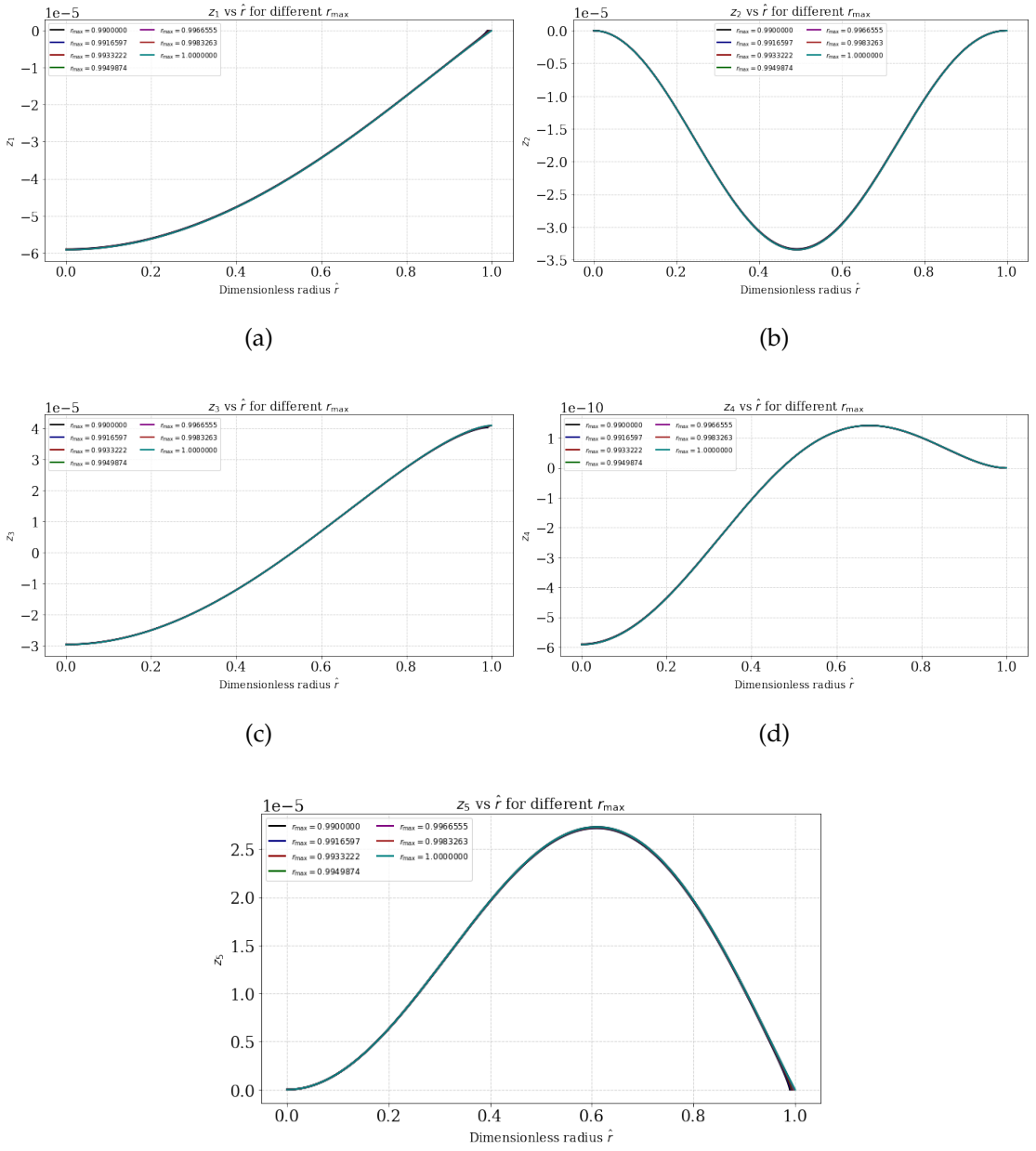

FIGURE 8.5: This figure shows the variation of the modulus of z_1, z_2, z_3, z_4, and z_5 with $\hat{r}$ for different choices of r_{max}. The horizontal axis is plotted on a logarithmic scale. Throughout, we fix $\varepsilon_\Omega = 10^{-4}$ and $\varepsilon_{mag} = 10^{-8}$, both parameterized by the stellar angular velocity Ω, which is taken to be 100 rad s^{-1}.

the inverse proportionality between z_1 and ε_μ predicted by a back-of-the-envelope estimate. One exception occurs for $|z_1|$ at the surface, which remains approximately constant with increasing ε_μ up to $\varepsilon_\mu = 10^{-1}$. Beyond this value, the surface solution also exhibits a slope close to -1.

The dip visible in the blue curve arises because we plot the modulus $|z_1|$; the numerical solution for z_1 changes sign in this interval, which appears as a dip in the $|z_1|$ curve. The same explanation applies to the dips seen in the other curves in Fig. 8.6.

For $|z_3|$, we find that the slope is approximately -1 at the centre, midpoint, and surface over the entire range of ε_μ, as shown in Fig. 8.6 (c). The corresponding log–log plots of $|z_2|$, $|z_4|$, and $|z_5|$ as functions of ε_μ are shown in Fig. 8.6 (b), Fig. 8.6 (d), and Fig. 8.6 (e) respectively.

We also examine the behaviour of z_1 and z_3 as functions of the stellar spin frequency, $f = \Omega/(2\pi)$. A back-of-the-envelope estimate suggests that both z_1 and z_3 should scale linearly with the angular velocity Ω, as shown in Eq. (8.128). We consider spin frequencies up to $f = 1700$ Hz, corresponding to the break-up frequency of the star.

The top panels of Fig. 8.7 show the behaviour of z_1 as a function of spin frequency at the midpoint and the surface of the star. For each value of Ω, the parameters ε_Ω and $\varepsilon_{\rm mag}$ are recalculated, since both are parameterised by Ω. The relative critical velocity is fixed at 10^4 cm s^{-1}, and we take $\varepsilon_\mu = 10^{-5}$, as shown in Eqs. (8.124) and (8.125), respectively.

As shown in Fig. 8.7(a), z_1 at the midpoint increases almost linearly with spin frequency, in agreement with the back-of-the-envelope estimate.Close to the break-up frequency, the deviation from linearity is not as significant as near the surface, because the presence of a non-zero pressure gradient in the stellar interior continues to provide a restoring force.

At the surface, z_1 remains linear over most of the spin-frequency range but deviates significantly near the break-up frequency, as shown in Fig. 8.7(b). This behaviour arises because the restoring force effectively vanishes at the surface when the gravitational acceleration is nearly balanced by the centrifugal acceleration, so that even a small perturbation leads to a disproportionately large displacement.

We expect z_3 to exhibit behaviour similar to that of z_1; however, we observe the opposite trend. As shown in Figs. 8.7(c) and (d), z_3 at the midpoint deviates significantly from linearity near the break-up frequency, whereas at the surface it remains almost linear over the entire range of spin frequencies. This behaviour cannot be explained using a simple back-of-the-envelope estimate and likely reflects the more complex coupling present in the full system of equations, leading to a non-trivial response of z_3 at rapid rotation.

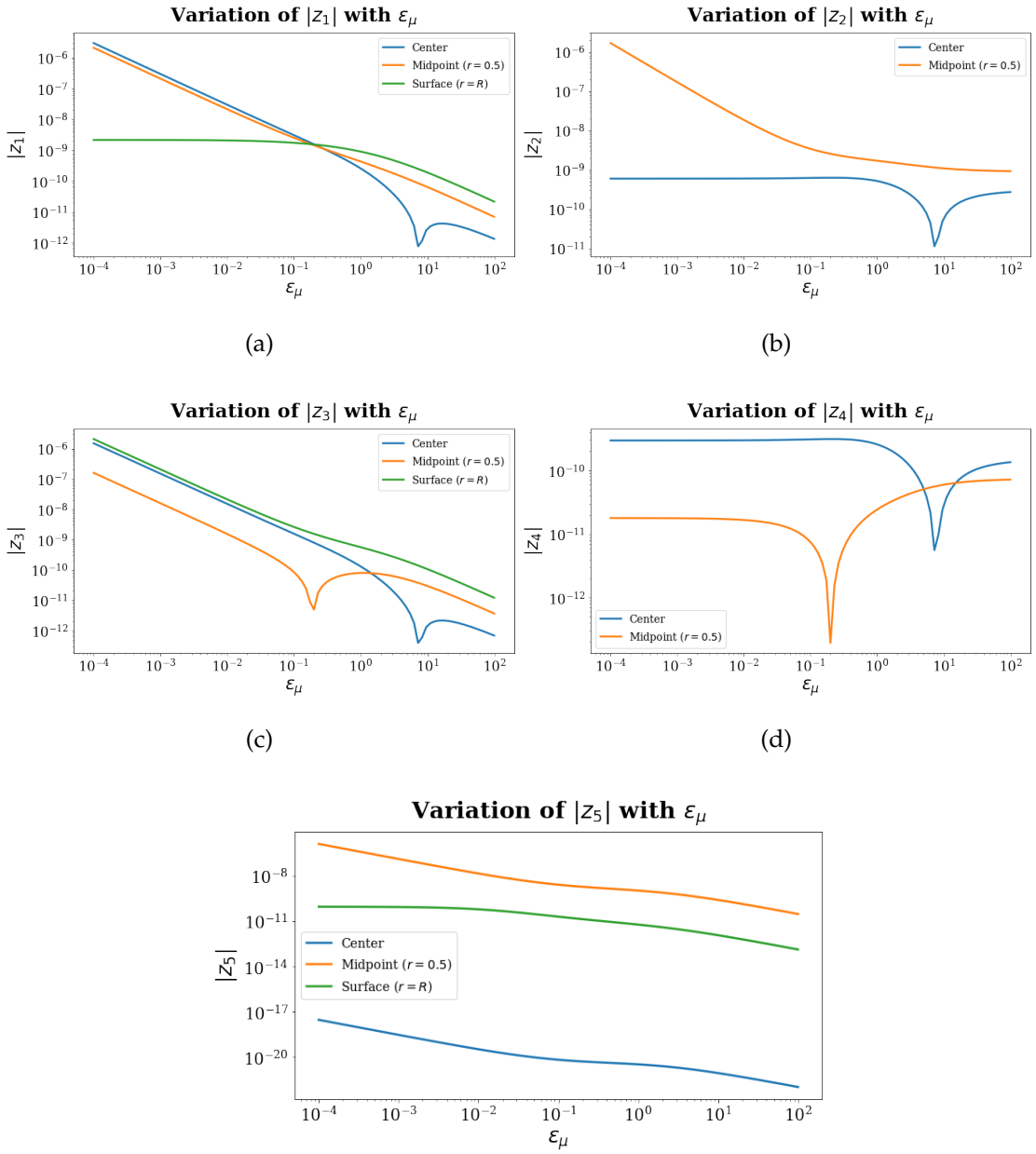

FIGURE 8.6: This figure shows the variation of modulus of z_1, z_2, z_3, z_4, and z_5 with the dimensionless shear parameter ε_μ at the centre (blue), midpoint (orange) and surface (green), shown in panels (a), (b), (c), (d), and (e), respectively. The source term in the perturbation equations is taken to be the Magnus force. Both the horizontal and vertical axes are plotted on logarithmic scales. Throughout, we fix $\varepsilon_\Omega = 10^{-4}$ and $\varepsilon_{\text{mag}} = 10^{-8}$, both parameterised by the stellar angular velocity Ω, which is taken to be 100 rad s^{-1}.

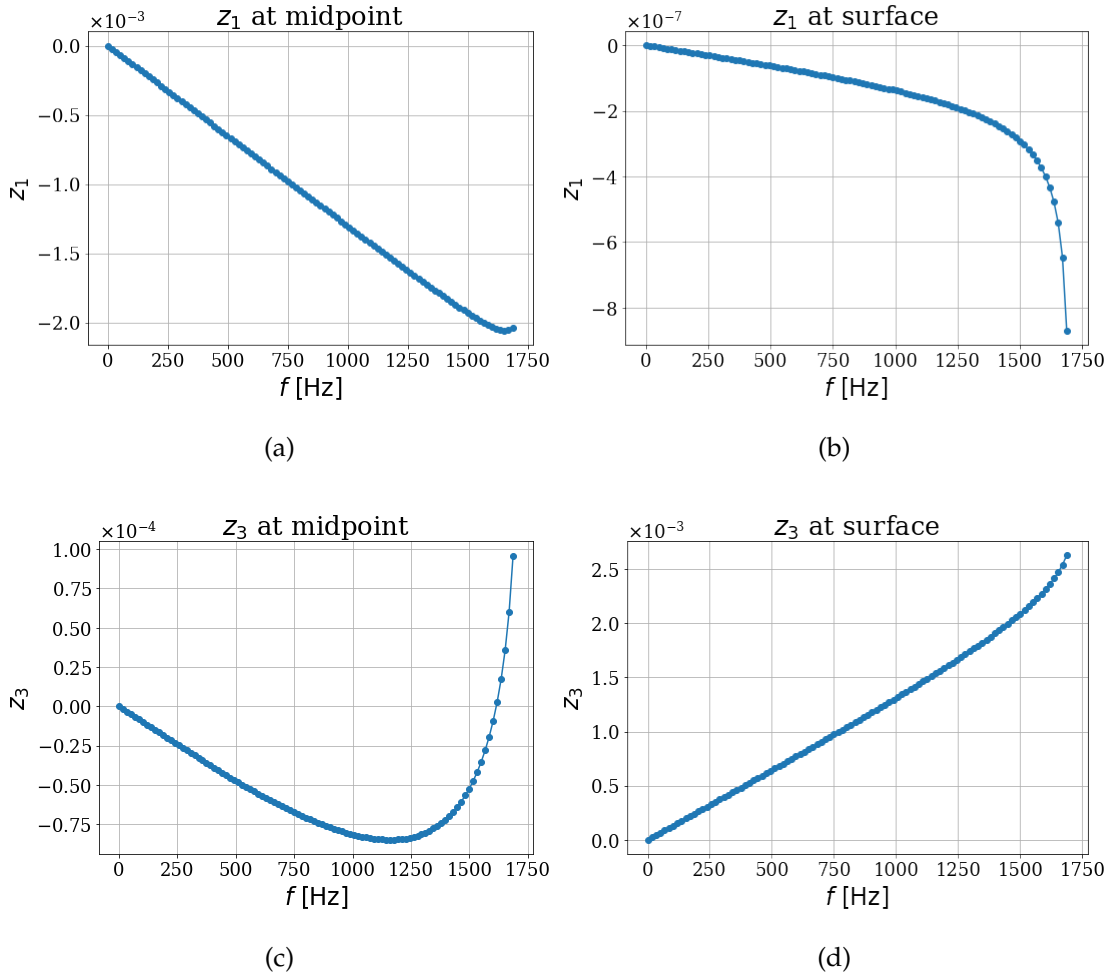

FIGURE 8.7: This figure shows the variation of z_1 and z_3 at the midpoint and the surface of the star as functions of the spin frequency. The top row, panels (a) and (b), corresponds to z_1 evaluated at the midpoint and the surface, respectively, while the bottom row, panels (c) and (d), shows the corresponding results for z_3. In all panels, $\varepsilon_\mu = 10^{-5}$.

In the next section to further develop our intuition and sanity check our code, we examine the same system with the tidal force acting as the source term and compare the resulting displacement behaviour with that obtained in the Magnus-force case.

8.5 Tidal force as source term

In this section we investigate how the star deforms when the source term is tidal force and compare it with the results obtained in the magnus force source term. To investigate this, we make two modifications to the two-fluid model: (i) we consider a single-component star instead of a two-component star, and (ii) we replace the Magnus force with a tidal force as the new source term. All other model assumptions remain the same as in the two-fluid star case.

Physically, the tidal force may be regarded as arising from another cylinder placed parallel to the original one. However, we do not explicitly consider these details, since quantities such as the mass per unit length of the new cylinder and the separation between the cylinders are absorbed into a single prefactor B^{tidal} in the expression for the tidal force (see Equation (8.136) below).

The background star is rotating and is elastically relaxed. We can map the calculation of the two-fluid background star, given in Section 8.1, into the single-fluid case. The expressions for the chemical potential and gravitational potential for the background star remain the same as those in equations (8.32) and (8.33), respectively, except that A, as defined in equation (8.17), is now given by

$$A = 4\pi G \frac{m_0^2}{K_0}, \tag{8.132}$$

where m_0 is the mass of the particles that make up the star, and K_0 is the polytropic constant in the equation of state for the $n = 1$ polytrope.

The perturbed equation of motion is similar to the two-fluid case in equation (8.69), but with a different source term. It is given by

$$\nabla^a \delta\tau_{ab} - \frac{\delta\rho_0}{\rho_0} \nabla^a \tau_{ab} + F_b^{\text{tidal}} = 0, \tag{8.133}$$

where we have replaced the term $-\delta F^{\text{mag}}$, representing the reaction force due to the Magnus force acting on pinned vortices, with the tidal force $+F^{\text{tidal}}$ acting directly on the elastic component of the star. We have

$$F^{\text{tidal}} = -\rho_0 \boldsymbol{\nabla} \Phi^{\text{tidal}}, \tag{8.134}$$

where Φ^{tidal} is given by

$$\Phi^{\text{tidal}} = B^{\text{tidal}} r^2 e^{2i\phi}. \tag{8.135}$$

Inserting equation (8.135) into equation (8.134) gives

$$F^{\text{tidal}} = -\rho_0 B^{\text{tidal}} \left[2r\hat{r} + 2ir\hat{\phi}\right] e^{2i\phi}. \tag{8.136}$$

The perturbed equation of motion (8.133) can be cast into four single order ODEs in terms of the variables z_1, z_2, z_3, and z_4, as defined in equations (8.84) - (8.87), following

the same steps as in the two-fluid star discussed in Section 8.4.2. These are:

$$\frac{dz_1}{d\ln r} = -z_1\left[\frac{6\alpha_5+1}{3\alpha_5+2}\right] + \frac{3z_2}{2(3\alpha_3^2+2\alpha_1)} + 4z_3\left[\frac{3\alpha_5-1}{3\alpha_5+2}\right], \tag{8.137}$$

$$\frac{dz_2}{d\ln r} = z_1\left[2\alpha_1\left(\frac{6\alpha_5+1}{3\alpha_5+2}\right)+\Gamma-2\alpha_3\beta\right] - z_2\frac{3}{(3\alpha_5+2)} - z_3\left[4\Gamma+8\alpha_1\left(\frac{6\alpha_5+1}{3\alpha_5+2}\right)\right] + 4z_4 + \tilde{V}^*, \tag{8.138}$$

$$\frac{dz_3}{d\ln r} = \frac{z_4}{\alpha_1} - z_1, \tag{8.139}$$

$$\frac{dz_4}{d\ln r} = -z_1\left[\Gamma + \frac{2\alpha_1(6\alpha_5+1)}{(3\alpha_5+2)}\right] + z_2\left[\frac{1-3\alpha_5}{3\alpha_5+2}\right] + 8\alpha_1 z_3\left[\frac{6\alpha_5+1}{3\alpha_5+2}\right] - 2z_4 + \tilde{U}^*. \tag{8.140}$$

The definitions of all coefficients appearing in z_1, z_2, z_3, and z_4 are identical to those given in Section 8.4.2. The only difference in the present case arises in the source terms, which are given by

$$\tilde{V}^* = 2\varepsilon_{\rm tidal} r^2, \tag{8.141}$$

and

$$\tilde{U}^* = \varepsilon_{\rm tidal} r^2, \tag{8.142}$$

where

$$\varepsilon_{\rm tidal} = \frac{\rho_0 B^{\rm tidal} R^2}{\Psi_0}, \tag{8.143}$$

is a new dimensionless parameter. This can be written in the parameterised form as

$$\varepsilon_{\rm tidal} = 10^{-1}\,\frac{\rho_{15}\,R_6^2\,B_{14}^{\rm tidal}}{\Psi_{35}}, \tag{8.144}$$

where $B_7^{\rm tidal} \equiv B^{\rm tidal}/(10^7\,{\rm s}^{-2})$. Here, $B^{\rm tidal}$ is chosen to be $10^7\,{\rm s}^{-2}$ in order to bring the system into a regime where the dimensionless tidal parameter satisfies $\varepsilon_{\rm tidal} \sim 0.1$, thereby allowing us to clearly study the system's response. The definitions of ε_μ and ε_Ω remain the same as those given in Eqs. (8.93) and (8.94), respectively.

The surface boundary condition is the same as that given in Eq. (8.117), corresponding to vanishing traction at the surface. The regularity conditions at the origin are also identical to those given in Eqs. (8.119), (8.120), and (8.121). This is because the only difference in the present case lies in the source term, whose leading-order contribution is quadratic in r, whereas the regularity conditions involve only zeroth-order terms in r.

We numerically solve the ODEs (8.137)–(8.140). Figure 8.8 shows the solutions for z_1, z_2, z_3, z_4, and z_5 as functions of the dimensionless radial coordinate $\hat{r}$. The solutions are smooth and well behaved throughout the stellar interior. Unless otherwise stated, we set $\varepsilon_{\rm tidal} = 10^{-1}$, $\varepsilon_\mu = 10^{-5}$, and $\varepsilon_\Omega = 10^{-4}$.

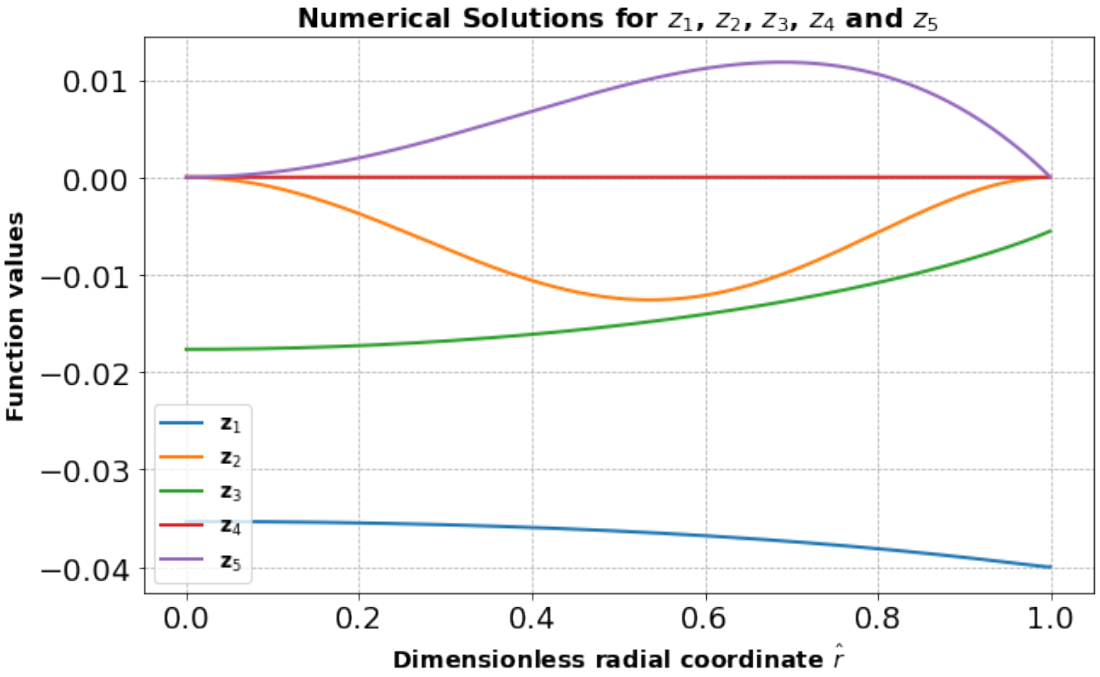

FIGURE 8.8: Solutions for $z_1(\hat{r})$, $z_2(\hat{r})$, $z_3(\hat{r})$, $z_4(\hat{r})$ and $z_5(\hat{r})$ as functions of the dimensionless cylindrical radial coordinate $\hat{r}$ with the tidal force acting as the source term.

Before commenting on the numerical solutions, we first present a back-of-the-envelope estimate obtained by balancing the elastic stress against the tidal force. At $r = R$, this balance may be written as

$$\rho_0 B^{\text{tidal}}\, 2R = \mu \frac{\xi}{R^2}, \tag{8.145}$$

which leads to

$$\frac{\xi}{R} = \frac{\rho_0 B^{\text{tidal}}\, 2R^2}{\mu} \approx \frac{\varepsilon_{\text{tidal}}}{\varepsilon_\mu}. \tag{8.146}$$

For $\varepsilon_{\text{tidal}} = 10^{-1}$ and $\varepsilon_\mu = 10^{-5}$, this estimate yields

$$\frac{\xi}{R} = z_1 \approx z_3 \approx 10^4. \tag{8.147}$$

Numerically, however, we obtain surface values of z_1 and z_3 of order 10^{-2}. There is a clear physical reason for this mismatch. For sufficiently small values of ε_μ, we find that the values of z_1 and z_3 saturate to finite values. In this regime, shear forces become negligible, and the tidal force is instead balanced by pressure gradients within the stellar interior. This behaviour is illustrated in Fig. 8.9 (a) and Fig. 8.9 (c).

In the range $\varepsilon_\mu \lesssim 1$, where the solutions plateau, the numerical results therefore do not agree with the back-of-the-envelope estimate. It is only for larger values of the shear modulus parameter, $\varepsilon_\mu \gtrsim 1$, that the numerical solutions begin to follow the scaling predicted by the simple force-balance argument.

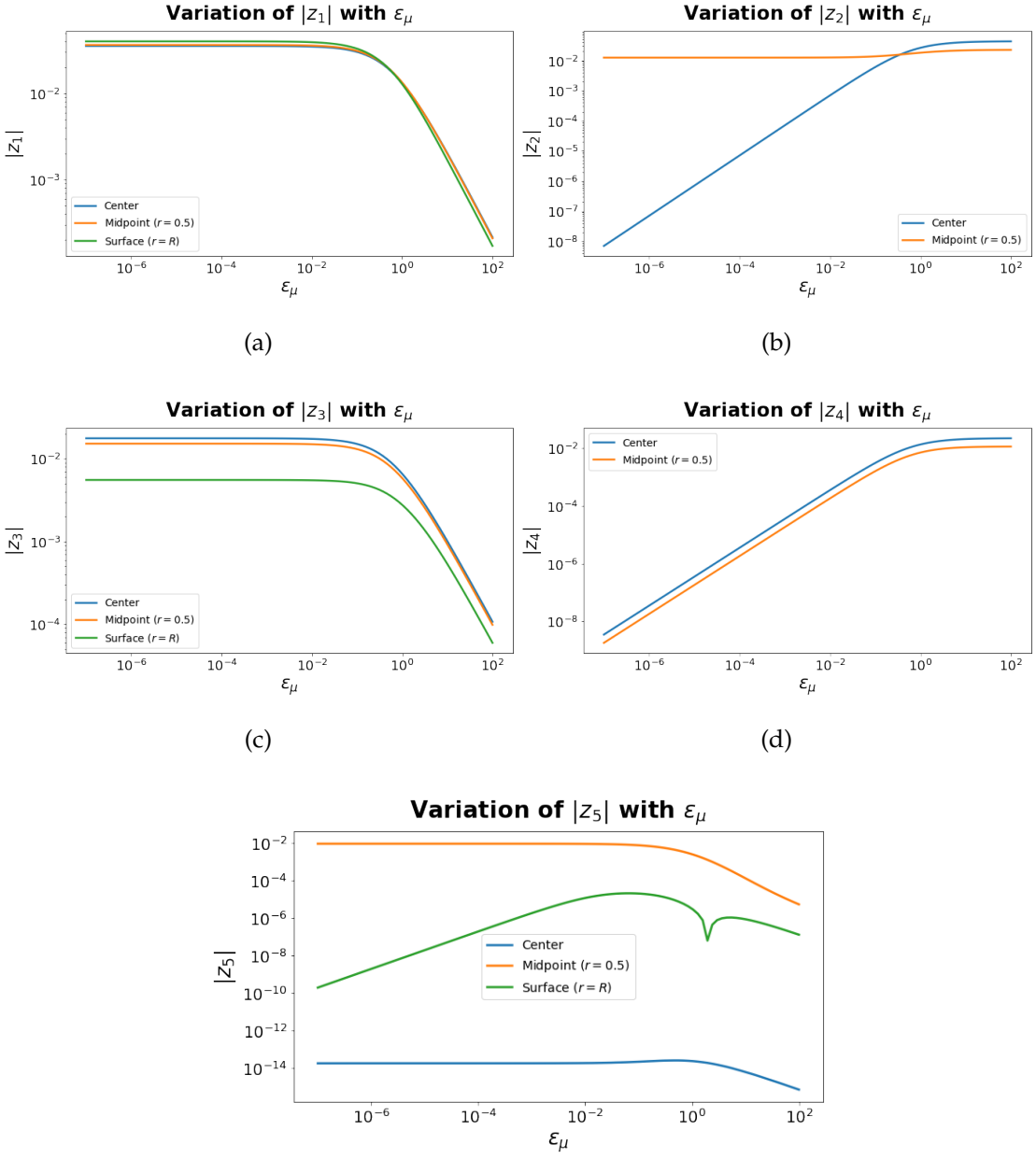

FIGURE 8.9: This figure shows the variation of z_1, z_2, z_3, z_4, and z_5 with the dimensionless shear parameter ε_μ at the centre (blue), midpoint (orange) and surface (green), shown in panels (a), (b), (c), (d), and (e), respectively. The source term in the perturbation equations is the tidal force. Both the horizontal and vertical axes are plotted on logarithmic scales. Throughout, we fix $\varepsilon_\Omega = 10^{-4}$ and $\varepsilon_{\text{mag}} = 10^{-8}$, both parameterised by the stellar angular velocity Ω, which is taken to be 100 rad s^{-1}.

For $\varepsilon_{\text{tidal}} = 10^{-1}$ and $\varepsilon_\mu = 1$, Eq. (8.146) gives

$$\frac{\xi}{R} = z_1 \approx z_3 \approx 10^{-1}. \tag{8.148}$$

Numerically, for $\varepsilon_{\text{tidal}} = 10^{-1}$, $\varepsilon_\mu = 1$, and $\varepsilon_\Omega = 10^{-4}$, we obtain surface values of z_1 and z_3 of order 10^{-2}, which are much closer to the back-of-the-envelope estimate of 10^{-1}.

Overall, we find that the back-of-the-envelope estimate begins to agree with the numerical solutions only for sufficiently large values of the shear modulus parameter, specifically for $\varepsilon_\mu \gtrsim 1$. This behaviour is clearly illustrated in the log–log plots of z_1 and z_3 as functions of ε_μ, shown in Fig. 8.9 (a) and Fig. 8.9 (c), evaluated at the centre, midpoint, and surface. From these plots, it is evident that the slopes of the curves for z_1 and z_3 approach approximately -1 for $\varepsilon_\mu \gtrsim 10^{-1}$, which corresponds to the regime in which the back-of-the-envelope estimate provides a reasonable approximation to the numerical results.

We also plot z_2, z_4, and z_5 as functions of ε_μ. The quantities z_2 and z_4 are shown only at the centre and midpoint, since they vanish at the surface due to the imposed boundary conditions.

Fig. 8.9 (a) and Fig. 8.9 (c) show that, as the system moves towards the fluid regime, i.e. towards smaller values of ε_μ, the solutions for z_1 and z_3 saturate and approach a plateau. This behaviour is in contrast to the Magnus-force–driven case, where the displacement continues to increase in the fluid regime.

The origin of this difference lies in the nature of the force balance. In the tidal case, the tidal force can be balanced by the hydrodynamic force, and therefore a well-defined fluid limit exists. This behaviour is reflected in Fig. 8.9 (a) and Fig. 8.9 (c). In contrast, in the Magnus-force case, the Magnus force cannot be balanced by hydrodynamic forces alone, since the hydrodynamic force is the gradient of a scalar, whereas the Magnus force is not. As a result, an elastic restoring force is always required to balance the Magnus force, and the displacement therefore continues to grow as the shear modulus of the star is reduced.This behaviour is reflected in Fig. 8.6 (a) and Fig. 8.6 (c).

8.6 Annulus Neutron Star

In this section, we consider an alternative configuration of the neutron star, again modeled as an infinite cylinder in cylindrical coordinates (r, ϕ, z). As before, the two components—the neutron superfluid and the charged component—coexist throughout the star. However, in this case, the charged component possesses a non-zero shear modulus confined only to an **annular region** between the inner radius $R_{\text{in}} = 0.9$ and the

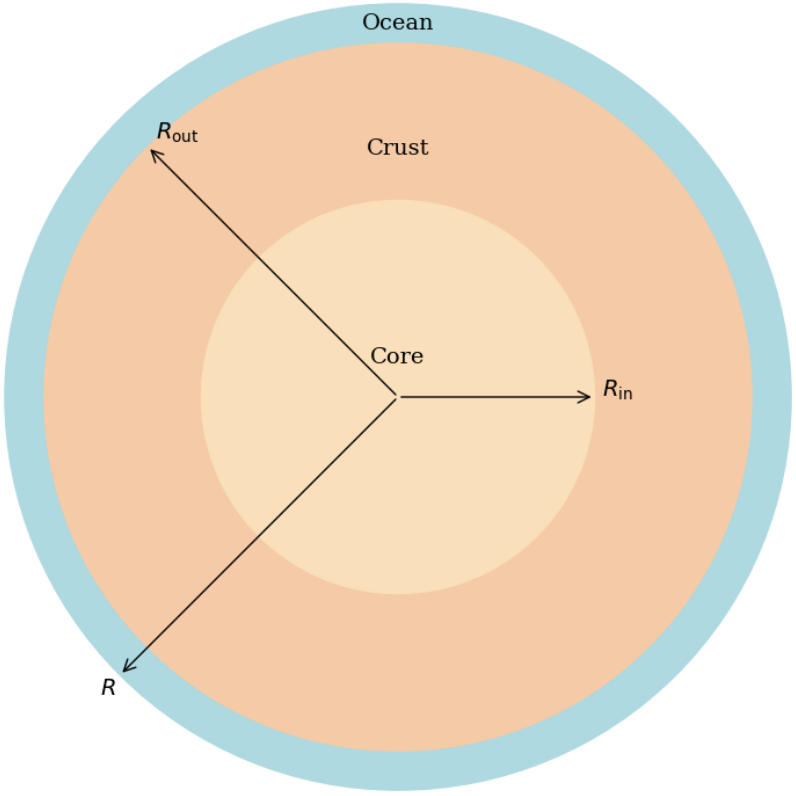

FIGURE 8.10: Schematic of the annular crust model. The fluid core lies inside R_{in}, the elastic crust spans $R_{in} < r < R_{out}$, and the outer ocean lies beyond R_{out}.

outer radius $R_{out} = 0.99$, in dimensionless units where the total radius of the star is set to $R = 1$. This configuration is illustrated in Figure 8.10.

Since the background star is assumed to be elastically relaxed, the analysis presented in Section 8.1 for the background structure remains applicable here as well. Velocity perturbations are introduced via non-axisymmetric pinning of vortices in the star. We consider two scenarios for the location of the pinning:

1. Pinning only in the crust and
2. Pinning in both the crust and the core.

These two configurations are schematically represented in Figure 8.11. We now discuss each case one by one.

8.6.1 Pinning only in the crust

In this case, we consider pinning of neutron superfluid vortices only at the crustal nuclei. This means that the velocity purturbation is confined only in the crust.

The general formulation of velocity perturbations remains largely as described in Section 8.2, with one key difference: the ansatz for the streamfunction Ψ must now be modified to ensure that the perturbation vanishes at the crust-core and crust-ocean boundary. The new ansatz is given by:

$$\Psi = \left(\frac{r^2}{R_{\text{in}}^2} - 1\right)\left(\frac{r^2}{R_{\text{out}}^2} - 1\right)\frac{r^2}{R^2}e^{2i\phi}. \tag{8.149}$$

Substituting Equation (8.149) into the general expression for the velocity perturbation, as given in Equation (8.43), we obtain:

$$\begin{aligned}\vec{\delta v}_n = &-\frac{2iB_*}{\rho_n}\frac{r}{R^2}\left(\frac{r^2}{R_{\text{out}}^2} - 1\right)\left(\frac{r^2}{R_{\text{in}}^2} - 1\right)e^{2i\phi}\hat{r} \\ &+ \frac{B_*}{\rho_n}\left(\frac{6r^5}{R^2R_{\text{out}}^2R_{\text{in}}^2} - \frac{4r^3}{R^2R_{\text{out}}^2} - \frac{4r^3}{R^2R_{\text{in}}^2} + \frac{2r}{R^2}\right)e^{2i\phi}\hat{\phi}.\end{aligned} \tag{8.150}$$

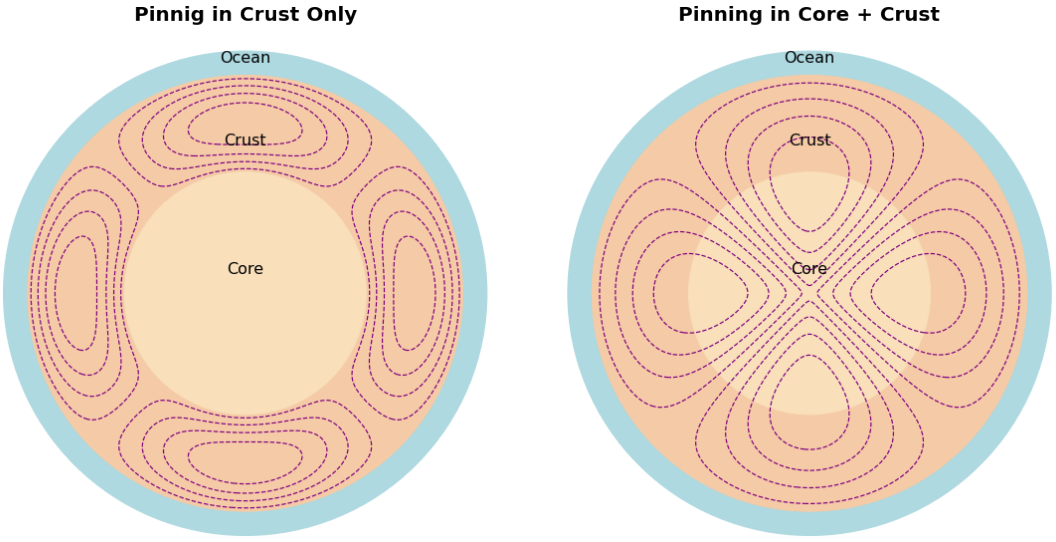

FIGURE 8.11: This figure shows two different cases of pinning regions. The left panel illustrates the case where pinning occurs only in the crust region, with the perturbation in the neutron velocity field confined accordingly. The right panel shows the scenario where pinning is present in both the crust and the core, and the corresponding velocity perturbation extends through both regions.

This yields the desired neutron superfluid velocity perturbation field, as shown in Figure 8.12, which we now use to solve the perturbed equations of motion for the fluid and elastic components.

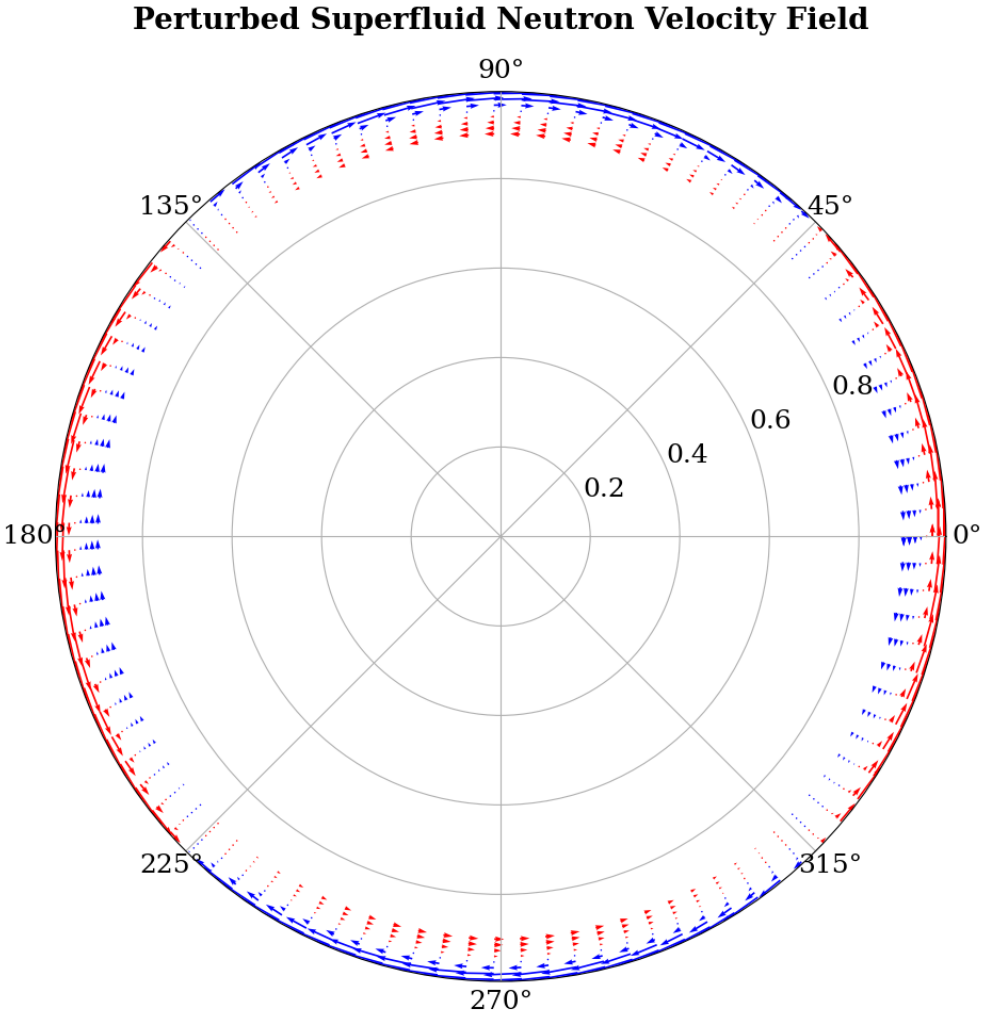

FIGURE 8.12: This figure shows the $m = 2$ perturbed velocity field corresponding to Equation (8.150). The velocity field is confined only in the crust.

8.6.1.1 Solving the Equations of Motion: Pinning Confined to the Crust

Since we adopt the Cowling approximation and assume that the velocity perturbation is confined entirely to the crust, there are no perturbations of the form $\delta f\, e^{im\phi}$ with $m \neq 0$ in the core and ocean regions of the star, where f denotes a fluid variable. This can be seen explicitly from the perturbed equations of motion (EOMs) in the fluid core and ocean for the neutron superfluid and the charged fluid.

To see this, recall that the unperturbed equations of motion (EOMs) for the neutron superfluid and the charged fluid are given by Equations 7.1 and 7.2, respectively. If we do not adopt the Cowling approximation, then upon perturbation, Equations 7.1 and 7.2 reduce to

$$\nabla(\delta\mu_X + \delta\phi) = 0, \quad X \in \{n, c\}, \tag{8.151}$$

where $\delta\mu_X$ is the perturbed chemical potential for each component and $\delta\phi$ is the perturbed gravitational potential. Since we consider the perturbed velocity field only in

the crust, there are no velocity perturbations in the core or ocean. In this case, the perturbed gravitational potential exactly balances the perturbed chemical potential for each component, and therefore $\delta\mu_X$ can admit perturbation components with $m \neq 0$.

If we instead adopt the Cowling approximation, then upon perturbation, Equations 7.1 and 7.2 reduce to

$$\nabla(\delta\mu_X) = 0, \tag{8.152}$$

which follows directly from the absence of velocity perturbations together with the neglect of the perturbed gravitational potential. We can see that the Cowling approximation introduces a significant difference: under this assumption, $\delta\mu_X$ cannot contain perturbation components with $m \neq 0$. A similar argument, formulated in terms of the pressure perturbation, was presented by Ushomirsky et al. (2000). Therefore, for the $m = 2$ source term, we solve the perturbed equations of motion only within the annular crustal region.

The solution for the fluid EOM remains identical to that described in Section 8.4.1. In this case, the Magnus force on the right-hand side is exactly balanced by the Coriolis force on the left-hand side, resulting in:

$$\delta\tilde{\mu_n} = 0. \tag{8.153}$$

The radial and azimuthal components of the elastic EOMs are again given by Eqs. (8.78) and (8.79), respectively, but with slightly modified source terms, since the velocity field used here, given in Eq. (8.150), is slightly different. Eqs. (8.78) and (8.79), together with the continuity equation (8.83), are solved numerically using the same setup discussed in Section 8.4.2.

We numerically solve the four first-order ODEs given by Eqs. (8.112)–(8.115). Note that the source terms in (8.113) and (8.115) differ from those in the earlier case, as the velocity field is slightly different here. To obtain a solution, we require four boundary conditions. We have exactly four unique boundary conditions: two at the crust-core interface and two at the crust-ocean interface. These are outlined below.

1. At the crust-core boundary ($r = R_{\text{in}}$):

   (a) The first condition enforces the vanishing of the Lagrangian perturbation of the tangential traction component in both the fluid and elastic regions at the interface:

   $$\Delta\tau^E_{r\phi} = \Delta\tau^F_{r\phi} = 0, \tag{8.154}$$

   where the superscripts E and F refer to the elastic and fluid components, respectively. (8.154) can be written in terms of the z_4 variable as:

   $$z_4 = 0. \tag{8.155}$$

(b) The second condition involves the Lagrangian perturbation of the radial traction component at the inetrface:

$$\Delta\tau_{rr}^{E} = \Delta\tau_{rr}^{F}. \tag{8.156}$$

For the fluid component, the Lagrangian perturbation of the radial traction can be expressed as

$$\Delta\tau_{rr}^{F} = \delta\tau_{rr}^{F} + \xi_{F}^{r}\nabla_{r}\tau_{rr}^{F}, \tag{8.157}$$

where the background stress tensor τ_{rr}^{F} is given by

$$\tau_{rr}^{F} = -\frac{a_c\tilde{\mu_c}^2}{2}, \tag{8.158}$$

following the same reasoning used in the derivation of equation (8.70).
Taking the Eulerian perturbation of equation (8.158) yields

$$\delta\tau_{rr}^{F} = -a_c\delta\tilde{\mu_c}^{F}. \tag{8.159}$$

Substituting equation (8.159) into equation (8.157) and applying the condition from equation (8.156), we obtain

$$\Delta\tau_{rr}^{E} = -a_c\delta\tilde{\mu_c}^{F} + \xi_{F}^{r}\nabla_{r}\tau_{rr}^{F}. \tag{8.160}$$

Since $\xi_{F}^{r} = \xi_{E}^{r}$ (the radial displacement must be the same at the interface for both components) and $\delta\tilde{\mu_c}^{F} = 0$ at the crust–core interface (due to the absence of $l \neq 0$ perturbations in the fluid core), this simplifies to

$$\Delta\tau_{rr}^{E} = \xi_{E}^{r}\nabla_{r}\tau_{rr}^{F}. \tag{8.161}$$

Inserting (8.158) into Eq. (8.161) and differentiating gives:

$$\Delta\tau_{rr}^{E} = -\xi_{E}^{r}a_c\tilde{\mu_c}\frac{d\tilde{\mu_c}}{dr}\bigg|_{r=R_{\rm in}}. \tag{8.162}$$

Dividing both sides by Ψ_o yields:

$$\frac{\Delta\tau_{rr}^{E}}{\Psi_o} = -\frac{\xi_{E}^{r}a_c\tilde{\mu_c}}{\Psi_o}\frac{d\tilde{\mu_c}}{dr}\bigg|_{r=R_{\rm in}}. \tag{8.163}$$

This can be written in terms of the variables z_1 and z_2 as:

$$z_2 = -z_1\frac{R_{\rm in}a_c\tilde{\mu_c}}{\Psi_o}\frac{d\tilde{\mu_c}}{dr}\bigg|_{r=R_{\rm in}}. \tag{8.164}$$

These boundary conditions, given by Equations (8.155) and (8.164), are similar to those presented in Equation (47) of Ushomirsky et al. (2000). In their case, however, the analysis was carried out for spherical stars.

2. Similarly, at the crust-ocean boundary ($r = R_{\rm out}$):

   (a) The tangential traction must vanish:

   $$z_4 = 0. \tag{8.165}$$

   (b) The radial traction condition is:

   $$z_2 = -z_1 \frac{R_{\rm out} a_c \tilde{\mu}_c}{\Psi_o} \frac{d\tilde{\mu}_c}{dr}\bigg|_{r=R_{\rm out}}. \tag{8.166}$$

This provides four unique boundary conditions: two applied at the crust-core interface and two at the crust-ocean interface, sufficient to solve the system of four coupled first-order ODEs.

8.6.1.2 Numerical Results

We use the boundary conditions given in Equations (8.154)–(8.166), together with the system of four first-order ODEs described in Equations (8.112)–(8.115), to numerically solve for the variables z_i. The numerical setup remains the same as discussed in Section 8.4.2.2. Here, the domain of the cylindrical radial coordinate r, over which the system of ODEs is solved is restricted to the annular region from $R_{\rm in} = 0.9$ to $R_{\rm out} = 0.99$. We fixed $\varepsilon_\mu = 10^{-5}$, $\varepsilon_\Omega = 10^{-4}$ and $\varepsilon_{\rm mag} = 10^{-8}$.

Figure 8.13 shows the numerical solutions for $z_1(\hat{r})$, $z_2(\hat{r})$, $z_3(\hat{r})$, $z_4(\hat{r})$ and $z_5(\hat{r})$ as functions of the cylindrical dimensionless radial coordinate $\hat{r}$.

All four solutions are smooth and well behaved across the entire radial domain. As a sanity check on these results, we select a representative radial location within the crust, specifically at $r = 0.95\,R$, and examine the variation of z_1 with respect to the shear modulus. The resulting behaviour is shown in Fig. 8.14. As expected, we again observe that z_1 decreases with increasing shear modulus.

Figures 8.14 (a)– 8.14(e) show log–log plots of z_1, z_2, z_3, z_4, and z_5, evaluated at $r_{\rm min}$, the midpoint of the crust, and $r_{\rm out}$. The quantity z_4 is plotted only at the midpoint of the crust, since it vanishes at both boundaries due to the imposed boundary conditions.

Unlike the full elastic configuration, the slopes of z_1 and z_3 are approximately -1 throughout the explored parameter range. For $\varepsilon_\mu = 10^{-5}$, $\varepsilon_\Omega = 10^{-4}$, and $\varepsilon_{\rm mag} = 10^{-8}$, the back-of-the-envelope estimate remains the same as that given in Eq. (8.129), namely

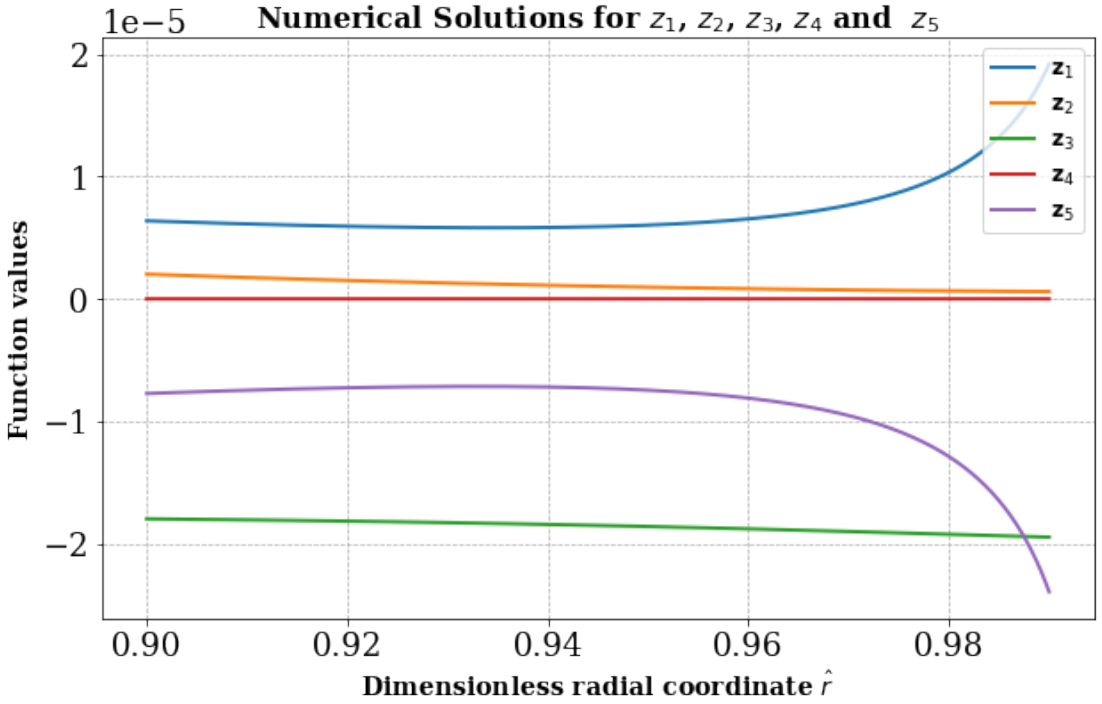

FIGURE 8.13: Solutions for $z_1(\hat{r})$, $z_2(\hat{r})$, $z_3(\hat{r})$, $z_4(\hat{r})$ and $z_5(\hat{r})$ as functions of the cylindrical dimensionless radial coordinate $\hat{r}$.

4×10^{-4}. The corresponding numerical solutions are of order 10^{-6} and 10^{-5} for $z_1(0.5)$ and $z_3(0.5)$, respectively. As in the fully elastic case, the numerical solution differs from the back-of-the-envelope estimate by one to two orders of magnitude.

Next, we plot the variation of z_1 and z_3 at the midpoint of the crust and at the outer boundary r_{out} as functions of the stellar spin frequency. Throughout this analysis, we fix $\varepsilon_\mu = 10^{-5}$. The parameter ε_{mag} is recomputed for each spin frequency, with the relative critical velocity set to $10^4\,\text{cm}\,\text{s}^{-1}$.

In the annulus configuration, z_1 and z_3 exhibit similar behaviour. Over most of the explored range, both quantities vary linearly with the spin frequency, as expected from the back-of-the-envelope estimate. Significant deviations from this linear trend appear as the star approaches the break-up spin frequency.

The back-of-the-envelope estimate is therefore able to capture most of the relevant physics in the annulus case. In realistic neutron stars, the interior typically consists of a fluid core, a thin ocean layer, and a kilometre-thick crust. The displacement field predicted in the annulus configuration provides a closer approximation to the expected behaviour in realistic neutron star models.

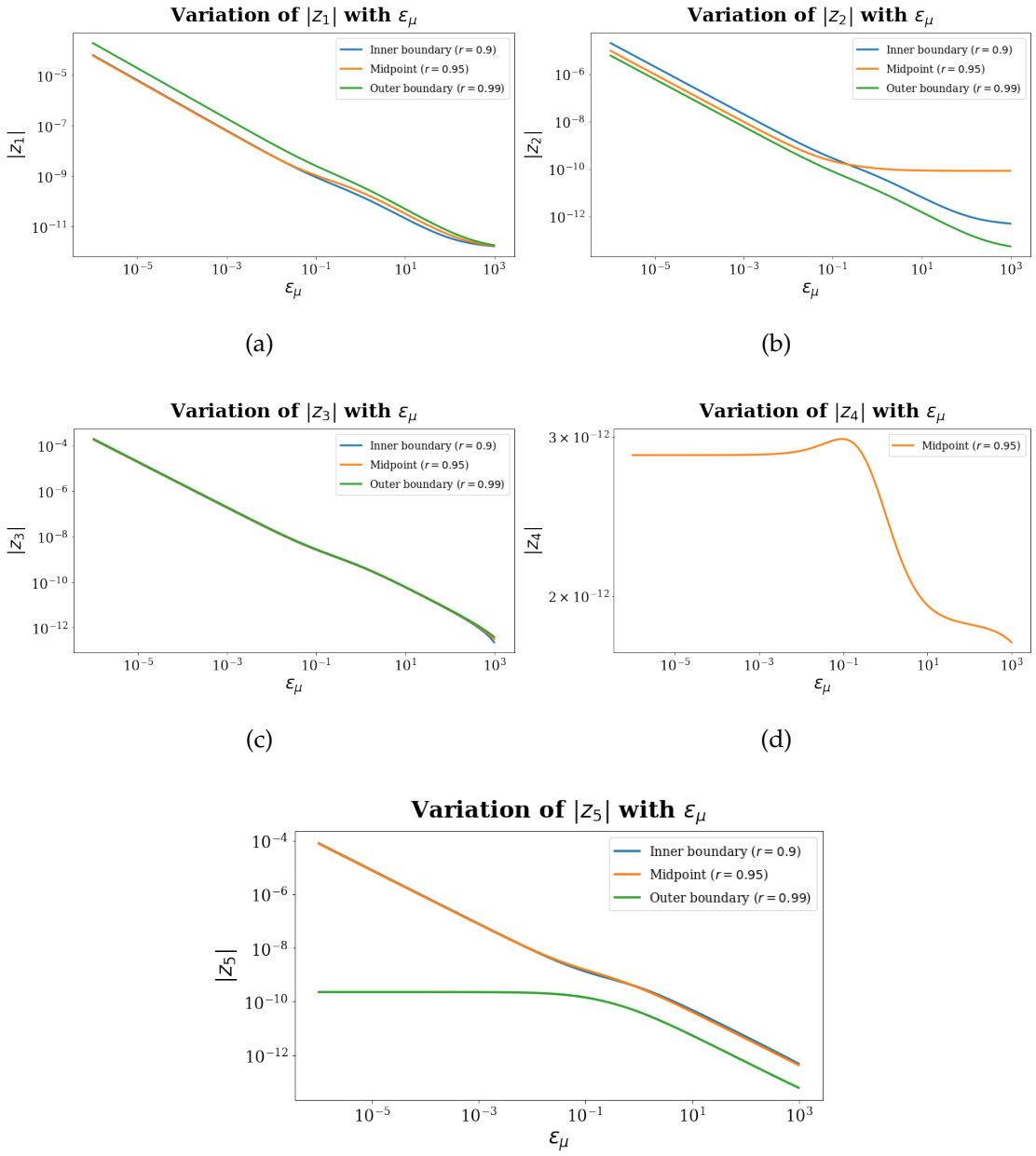

FIGURE 8.14: This figure shows the variation of z_1, z_2, z_3, z_4, and z_5 with the dimensionless shear parameter ε_μ at the inner crust boundary (blue), midpoint of the crust (orange) and outer crust boundary (green), shown in panels (a), (b), (c), (d), and (e), respectively. The source term in the perturbation equations is taken to be the Magnus force. Both the horizontal and vertical axes are plotted on logarithmic scales. Throughout, we fix $\varepsilon_\Omega = 10^{-4}$ and $\varepsilon_{\text{mag}} = 10^{-8}$, both parameterised by the stellar angular velocity Ω, which is taken to be 100 rad s^{-1}.

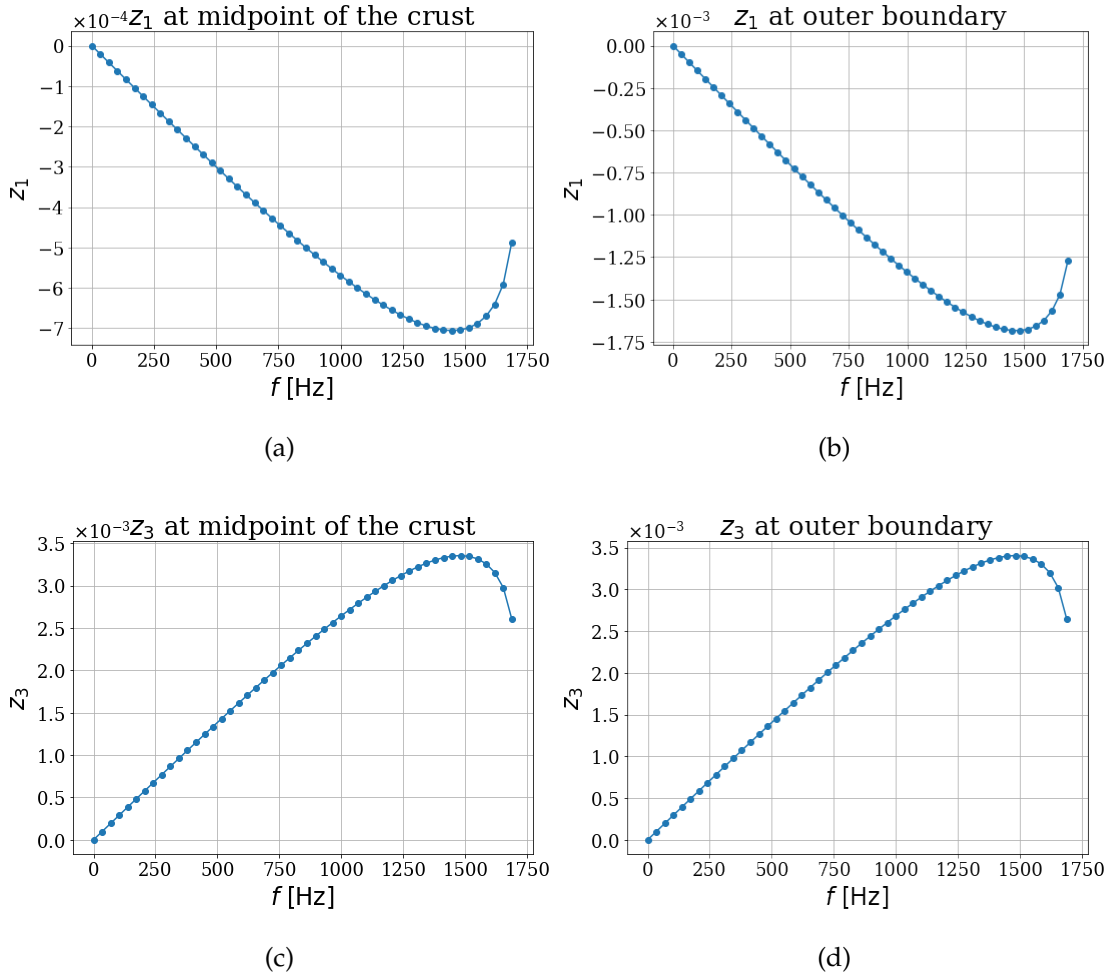

FIGURE 8.15: This figure shows the variation of z_1 and z_3 at the midpoint and the outer boundary of the crust as functions of the spin frequency. The top row, panels (a) and (b), corresponds to z_1 evaluated at the midpoint and the surface, respectively, while the bottom row, panels (c) and (d), shows the corresponding results for z_3. In all panels, $\varepsilon_\mu = 10^{-5}$.

8.6.2 Pinning in the Crust and Core

In this case, we consider pinning of neutron superfluid vortices both at the crustal nuclei and at the flux tubes in the core. This implies that the neutron superfluid velocity perturbation exists only in the crust and the core, and is absent in the ocean. The modified ansatz for the streamfunction Ψ to ensure that the perturbation vanishes at the crust-ocean boundary is given by:

$$\Psi = \frac{r^2}{R^2}\left(\frac{r^2}{R_{\text{out}}^2} - 1\right) e^{i2\phi}. \tag{8.167}$$

Substituting Equation (8.167) into the general expression for the velocity perturbation, as given in Equation (8.43), we obtain:

$$\delta\vec{v}_n = -\frac{2iB_*}{\rho_n}\frac{r}{R^2}\left(\frac{r^2}{R_{\text{out}}^2}-1\right)e^{2i\phi}\hat{r} + \frac{B_*}{\rho_n}\left(\frac{4r^3}{R^2R_{\text{out}}^2}-2\frac{r}{R^2}\right)e^{2i\phi}\hat{\phi}. \tag{8.168}$$

This gives the neutron superfluid velocity perturbation field, which we now use to solve the perturbed equations of motion for the fluid and elastic components.

8.6.2.1 Solving the Perturbed Fluid EOM

In the case of neutron fluid, the formulation of perturbed EOM remains the same as discussed in Section 8.4.1. In the neutron fluid, the Magnus force is balanced by the Coriolis force, and we again obtain $\delta\mu_n = 0$.

In the core, we also have the proton fluid, which experiences a reaction force opposite to the Magnus force. The perturbed equation of motion for the proton fluid is:

$$\vec{\nabla}\delta\tilde{\mu}_c = \frac{\rho_n}{\rho_c}2\vec{\Omega}\times\delta\vec{v}_n. \tag{8.169}$$

Equation (8.169) is obtained by perturbing the unperturbed fluid EOM, originally given in Equation (7.5). In this equation, the left-hand side is the gradient of a scalar, whereas the right-hand side involves the Coriolis force term, which is not expressible as a gradient of a scalar field. Consequently, these forces cannot balance each other. Dropping the Cowling approximation would not help in this case, as the inclusion of gravitational potential terms would still result in scalar gradients and hence not contribute to the non-conservative force required on the right-hand side.

We suggest that in a more realistic neutron star, the reaction force on the proton fluid might be counteracted by magnetic tension forces associated with flux tubes. However, such magnetic effects are beyond the scope of the present simplified model. We need a more detailed investigation in future studies, possibly involving the inclusion of magnetic field effects in the core.

Chapter 9

Concluding Remarks

In this thesis, we have examined two distinct models for the formation of elastic mountains on spinning neutron stars. In the first model, we investigated the formation of an elastic mountain within the framework of the starquake model. In the second, we explored the superfluid vortex pinning model. Below, we summarise our analysis, conclusions, and outline possible refinements for both models.

9.1 Mountain Formation in the Starquake Model

To study the formation of the elastic mountain and to determine how large a mountain can be supported, we extended the energy minimisation argument in the starquake model, originally presented by Baym and Pines (1971), from axisymmetric crust-breaking with $l = 2, m = 0$ to non-axisymmetric crust-breaking with $l = 2, m = 2$.

Following the starquake, in order to obtain a precise relation between the relaxed zero-strain shape of the star and its equilibrium shape, it is necessary to determine the constants constants A_{22}, as given in equation (3.152), and B_{22}, as given in equation (3.129). These constants relate the star's equatorial ellipticity to the perturbed gravitational and elastic strain energies, respectively.

We explicitly calculated the constants A_{22} and B_{22} and found that their values are almost identical to those of A_{20} and B_{20}, differing only by constant numerical factors of $\frac{1}{3}$ and $\frac{25}{57}$, respectively, as given in equations (3.153) and (3.130). These results confirm that the non-axisymmetric coefficients retain the same functional dependence as their axisymmetric counterparts, with only minor numerical differences.

When first calculating the perturbed gravitational energy, δE_g, using the method described in Friedman and Schutz (1978), we obtained a negative result. Such a negative value of δE_g is unphysical, as it implies that the spherical configuration does not

correspond to the minimum gravitational potential energy. Furthermore, we found a non-zero perturbed internal energy, δU, despite assuming an incompressible star. This issue was also highlighted in a recent study by Yim and Jones (2022). We attribute the underlying cause to the fact that the displacement field employed enforces incompressibility only to first order, whereas the leading-order contributions to δE_g and δU are of second order.

To enforce incompressibility at second order, we introduced an additional second-order term into the displacement vector field by hand, as given in equation (3.80). This modification yielded a positive value for δE_g. We further verified this value using two independent methods described in Chandrasekhar (1969) and Shapiro and Teukolsky (1983) for the $l = 2, m = 2$ perturbation. As expected for an incompressible star, we also found $\delta U = 0$.

Finally, we demonstrated that no cross-energy terms appear in the total energy expression, equation (3.225), when both symmetric ($l = 2, m = 0$) and asymmetric ($l = 2, m = 2$) perturbations are present simultaneously. The two modes remain decoupled in energy to second order.

We confirmed that the effect of elasticity is small for non-axisymmetric crustal strains, just as it is for axisymmetric ones. Quantitatively, the non-axisymmetric ellipticity ϵ_{22} of a star with zero-strain shape $\epsilon_{22,0}$ is given by

$$\epsilon_{22} \approx \frac{B_{22}}{A_{22}}\epsilon_{22,0} \approx 3.005 \times 10^{-5}\epsilon_{22,0}\frac{\mu_{30}R_6^3\Delta R_5}{M_{1.4}^2}, \tag{9.1}$$

implying that the crust must possess a very large zero-strain distortion to generate a significant gravitational-wave-emitting mountain. This result was anticipated, but our calculation provided the explicit coefficients A_{22} and B_{22} for the non-axisymmetric case for the first time; previously, only the axisymmetric counterparts A_{20} and B_{20} had been computed.

As an application of our formalism, we considered a non-rotating, elastically relaxed star spun up to high rotation rates and subsequently undergoing a single large starquake, as studied in Fattoyev et al. (2018) and Giliberti and Cambiotti (2022). We parameterised the quake by two free parameters: $\Delta\epsilon_{20,0}$ and $\Delta\epsilon_{22,0}$, corresponding to changes in the zero-strain shapes of the $m = 0$ and $m = 2$ perturbations, respectively. We identified the region in this parameter space consistent with angular momentum and energy conservation ($\Delta J = 0, \Delta E < 0$). We then showed that the maximum mountain that can be built, subject only to these constraints, is

$$\epsilon_{22}^{\max} = \frac{\sqrt{B_{22}B_{20}}}{A_{22}}\epsilon_{20} = \frac{\sqrt{57}}{5}\frac{B_{22}}{A_{22}}\epsilon_{20}, \tag{9.2}$$

where, in the final equality, we used equation (3.130). Here, ϵ_{20} denotes the rotational oblateness of the pre-quake star. We found this value to be roughly a factor of 4 larger than that predicted by the particular fracture scenario of Giliberti and Cambiotti (2022). Furthermore, we demonstrated that mountain formation necessarily involves a change in the axisymmetric shape; axisymmetric energy must be sacrificed to build a non-axisymmetric mountain.

We also provided a rough estimate for the size of the maximum mountain (4.46), limited by the crust's finite breaking strain. By setting $\epsilon_\Omega = \sigma_{\text{break}}$ in equation (2.14), we obtained the maximum spin frequency f_{break} up to which a star can be spun before fracturing. This allowed us to estimate the maximum mountain size achievable if a non-rotating neutron star is spun up to the crust-breaking threshold.

The results of Chapters 3 and 4 have been compiled into a paper (Gangwar and Jones, 2024).

9.1.1 Future Directions

The simple model we constructed in Chapter 4, of course, is highly idealised and can be improved in several key areas:

1. We assumed that all crustal strain arises from centrifugal forces. In realistic glitch models, the neutron superfluid component plays a crucial role. Pinned superfluid vortices generate additional strain in the crust via the Magnus force as discussed in chapters 7 and 8. A more accurate model would incorporate strain contributions from both centrifugal and Magnus forces (Ruderman, 1991).

2. We employed a star model with an incompressible fluid core, uniform density, and a uniform shear modulus for the outer crust. This should be generalised to include a realistic equation of state.

3. For the non-axisymmetric perturbation, we adopted a "Kelvin mode" displacement field, appropriate only for incompressible stars. Exploring a broader class of non-axisymmetric quadrupolar deformations, motivated by realistic crust-failure mechanisms, would be beneficial.

4. Our treatment was Newtonian. A more refined approach would involve general relativity (see, e.g., Gittins and Andersson (2021)).

5. In accreting stars, the accretion process itself drives continuous compression of the crust. A model incorporating this effect could reveal whether it mitigates strain build-up due to centrifugal forces.

6. We followed Fattoyev et al. (2018) and Giliberti and Cambiotti (2022) in considering the spin-up of a spherical, unstrained star. This made the application of perturbation theory straightforward. However, in reality, a pre-quake star would already possess at least an $(l = 2, m = 0)$ relaxed shape. Modelling an isolated neutron star spinning down under electromagnetic torques, and developing perturbation theory on such a background, would be a significant improvement.

In summary, until now, starquakes have only been modelled under the assumption of symmetric crust breaking. We have demonstrated that non-axisymmetric starquakes are energetically permitted. Future work should therefore develop comprehensive models of asymmetric crust breaking. Beyond their relevance to continuous gravitational-wave emission, non-axisymmetric shape changes could also have important implications for glitch modelling. We therefore suggest that a unified glitch model incorporating both crust fractures and superfluid unpinning represents a promising avenue for future research.

9.2 Mountain formation under the vortex pinning model

In the second half of this thesis, we investigated another mechanism for the formation of elastic mountains, arising from the non-axisymmetric pinning of superfluid vortices to crustal nuclei or magnetic flux tubes within the neutron star. Before developing the simplified models presented in Chapters 7 and 8, we examined the analysis of Sidery and Alpar (2009), which constitutes the most relevant study of non-axisymmetric interactions between vortices and flux tubes. We explored this study in detail to understand how such non-axisymmetric interactions influence the rotational dynamics of the neutron star and the formation of mountains. Our observations on this analysis are summarised in the following section.

9.2.1 Rotational dynamics of neutron stars

We began by considering a symmetric distribution of vortices without any inetraction with flux tubes and crustal nuclei. In this case, we reproduced the expression for the coupling timescale, t_d, of the neutron star's core superfluid to the crust, as given in Alpar and Sauls (1988), in the absence of angular momentum conservation. We then studied the time evolution of the superfluid angular velocity, $\Omega_n(t)$, the charged-component angular velocity, $\Omega_c(t)$, and the lag, $\omega(t)$, incorporating angular momentum conservation and accounting for both symmetric and non-axisymmetric drag forces acting on the vortices. The calculation including the non-axisymmetric drag force is presented here for the first time.

Next, we examined the effect on the dynamical coupling timescales when both magnetic flux tubes and superfluid vortices are present in the neutron star interior. We considered a simple configuration, as presented in Sidery and Alpar (2009), in which flux tubes are aligned along the x-axis, while vortices are oriented along the z-axis, which we also take to be the rotation axis of the star. We then studied the case of perfect pinning of the vortices to the flux tubes in one direction and calculated the corresponding dynamical coupling timescale. Our analysis reproduced, and independently verified, the result obtained in Sidery and Alpar (2009): namely, that the coupling timescale, $\tau_{\rm pin}$, associated with absolute pinning in one direction is 10^{-7}–10^{-10} times smaller than the coupling timescale in the weak-drag limit in the absence of flux tubes. This result appears counterintuitive, as one might expect that absolute pinning in a single direction would restrict the motion of the vortices and therefore increase the coupling timescale. However, the analysis shows the opposite behaviour. Furthermore, we found that $\tau_{\rm pin}$ differs by only a factor of 2 when compared with the coupling timescale in the strong-drag limit with no flux tubes present.

We then investigated axisymmetric and non-axisymmetric creep of vortices, with pinning to crustal nuclei and flux tubes respectively, in the absence of drag forces and derived the corresponding dynamical coupling timescales. For non-axisymmetric creep without drag, we obtained an expression for the time evolution of Ω_n whose form differs from that given in Sidery and Alpar (2009).

Although Sidery and Alpar (2009) considered the non-axisymmetric interaction of vortices and flux tubes, their analysis, which relies on rigid-body dynamics in the case of perfect pinning in one direction, is valid only at $t = 0$. Beyond $t = 0$, rigid-body dynamics no longer applies because the vortices deviate from their initial axisymmetric distribution, and the neutron superfluid ceases to rotate rigidly with the charged component. Consequently, it is not possible to obtain an analytic expression for the non-axisymmetric average superfluid velocity, which would act as the source of the non-axisymmetric Magnus force on the pinning sites responsible for mountain formation. While it is possible to extend the analysis of Sidery and Alpar (2009) beyond $t = 0$, this would require a detailed microphysical numerical study, which I intend to pursue as part of future work, but it lies beyond the scope of this thesis.

9.2.2 Model for Magnus mountain

In Chapters 7 and 8, we constructed a simple model for the formation of a Magnus mountain, in which the non-axisymmetric Magnus force acting on pinned superfluid vortices serves as the source of a non-zero quadrupolar ellipticity. This non-axisymmetric Magnus force arises from the non-axisymmetric global average superfluid velocity field

associated with the non-axisymmetric distribution of pinned vortices. Due to the absence of an analytic expression for this non-axisymmetric superfluid velocity field derived from first principles, we manually introduced an $m = 2$ velocity field and applied it within our model to estimate the size of the resulting mountain.

We began with a two-component, incompressible, infinitely long star with both components co-rotating, adopting the Cowling approximation. We specified an $m = 2$ neutron superfluid velocity perturbation. First, we calculated the current multipole associated with this velocity perturbation, which unexpectedly turned out to be zero. In general, a non-zero current multipole is expected for an $m = 2$ velocity perturbation because the current multipole moment is sourced by non-axisymmetric mass currents inside the star. An $m = 2$ perturbation corresponds to a quadrupolar azimuthal structure, which produces a time-varying, non-axisymmetric flow pattern. Such a flow naturally generates a quadrupolar current distribution, and therefore a non-zero S_{22}. However, our result indicates otherwise.

Next, for the same stellar configuration described in the preceding paragraph, we solved the coupled fluid and elastic perturbed equations of motion (EOMs). In the fluid component, the Magnus force acting on the neutron superfluid was found to be balanced by the Coriolis force, while in the elastic component it was balanced by the gradient of the perturbed chemical potential of the charged component. No shape change of the star was observed, as indicated by a vanishing displacement field in both the fluid and elastic components. Thus, no mountain was formed in this configuration.

The fluid and elastic components are coupled not only through the Magnus force but also via the common gravitational potential. To investigate whether this coupling alters the results obtained under the Cowling approximation, we removed the Cowling approximation and solved the coupled perturbed EOMs for the fluid and elastic components again. The displacement field remained zero, indicating no shape change.

We then considered a compressible, infinitely long cylindrical star with co-rotating components under the Cowling approximation. We specified an $m = 2$ velocity perturbation throughout the star, which again yielded a zero current multipole. This suggests that the vanishing current multipole is unrelated to the compressibility or incompressibility assumption and may instead result from the form of the velocity perturbation we have specified. It is possible that a velocity perturbation derived from first principles would yield a non-zero current multipole, or that the zero result is a consequence of the infinite cylindrical geometry, which might not hold in a spherical configuration. Haskell et al. (2022) considered a spherical star and obtained a zero current multipole.

To evaluate shape changes, we numerically solved the coupled perturbed EOMs for both components. This time, we obtained a non-zero displacement field, whose amplitude is controlled by a free parameter in the velocity perturbation that sets the magnitude of the source term. Using estimated values of the average superfluid velocity

in neutron stars, $\sim 10^4\,\mathrm{cm/s}$, we found that the resulting surface radial displacement field amplitude $\sim 10^{-5}$, agrees to within an order of magnitude with the back-of-the-envelope estimate of $\sim 10^{-4}\,\mathrm{cm}$.

The numerical solutions for the displacement field were smooth across the radial profile of the star. To verify their validity, we performed a consistency check by varying the shear modulus of the star over a wide range (10^{-4} to 10^2 times the baseline value) and examining the effect on the displacement field at a representative point in the star, $r = R/2$. Increasing the shear modulus should make the crust harder to deform, resulting in a monotonically decreasing value of the displacement. We indeed observe this result.

After checking that the solutions behave as expected, we plot the variables z_1 and z_3 at the midpoint of the crust and at the stellar surface as functions of the spin frequency, up to the break-up spin frequency. The behaviour of z_1 is broadly consistent with physical expectations. At the surface, z_1 remains linear over most of the spin-frequency range, but deviates from linearity as the break-up frequency is approached. This deviation occurs because, near break-up, the centrifugal force increasingly balances gravity, leaving no effective restoring force. In contrast, z_1 evaluated at the midpoint of the crust remains linear over almost the entire range of spin frequencies, even close to the break-up limit, since pressure gradients continue to provide a restoring force in this region.

The behaviour of z_3 is more counterintuitive. At the surface, z_3 remains approximately linear across nearly the entire range of spin frequencies. However, at the midpoint, it deviates from linear behaviour as the break-up spin frequency is approached.

In this work, we are primarily interested in the surface value of z_1, as z_1 can be interpreted as a rough measure of the stellar ellipticity. For a spin frequency of approximately 700 Hz, corresponding to the fastest known spinning neutron star, the surface value of z_1 is found to be of order 10^{-7}. This value therefore provides an estimate of the upper limit on the ellipticity achievable within the Magnus-mountain formation model.

We repeated the analysis of mountain formation with the tidal force acting as the deforming agent. Since the qualitative behaviour of solutions in the tidal case is well understood, running the numerical code with the tidal force as the source term provided an important validation check and increased our confidence in its correctness.

We solved the system with the tidal force as the source term and found that the solutions behaved smoothly, as expected. As the shear modulus was varied, both z_1 and z_3, evaluated at a representative point $r = R/2$, decreased monotonically, consistent with physical expectations. For sufficiently small values of the shear parameter ε_μ, both z_1 and z_3 approached finite limiting values, in contrast to the behaviour observed in the Magnus-mountain case.

This difference arises because, in the tidal case, a well-defined fluid limit exists. The tidal force can be balanced purely by hydrostatic forces, allowing the elastic contribution to vanish in the limit of zero shear modulus. In contrast, no such fluid limit exists for the Magnus-mountain scenario. The Magnus force cannot be balanced solely by hydrodynamic forces, and as a result an elastic contribution to the equations of motion is always required. Consequently, the displacement continues to grow as the shear modulus is decreased in the Magnus-mountain case.

As a final analysis, we repeated the study of Magnus mountain formation for an annular stellar configuration consisting of a fluid core, an overlying elastic crust extending from $0.9R$ to $0.99R$, and a thin outer ocean. This configuration is closer to a realistic model of a neutron star. In this case, we obtained four explicit boundary conditions—two at the inner crust–core interface and two at the outer crust–ocean interface—consistent with the approach of Ushomirsky et al. (2000). The velocity perturbation was confined entirely to the crustal region.

We again solved the coupled perturbed equations of motion numerically for both components. The solutions were smooth and well behaved. Taking $r = 0.95R$ as a representative point within the crust, we find that increasing the shear parameter ε_μ leads to a monotonic decrease in both z_1 and z_3, as expected.

Next, we plot z_1 and z_3 at the outer crustal boundary ($r = 0.99R$) and at the midpoint of the crust ($r = 0.95R$) as functions of the spin frequency, up to the breakup frequency. At both locations, z_1 and z_3 remain approximately linear over most of the spin-frequency range and deviate from linear behaviour only near the breakup frequency.

At the outer boundary, for a spin frequency of approximately 700 Hz, we find $z_1 \sim 10^{-7}$. Since z_1 can be interpreted as a rough measure of the stellar ellipticity, this value provides an estimate of the maximum ellipticity achievable within the Magnus-mountain formation model. This constitutes our key result.

9.2.3 Future Directions

Several open questions remain to be addressed in future analyses, along with potential modifications and enhancements to the proposed setup. These are outlined below:

1. In this study, we specified a $m = 2$ perturbed neutron superfluid velocity field by hand. A key direction for future work is to evaluate this velocity field from first principles by considering the microphysical interaction of the vortices with the pinning potentials associated with flux tubes and crustal nuclei. This would allow us to investigate how the system evolves over time to generate such a non-axisymmetric velocity field. In Chapter 6, we examined the non-axisymmetric

interaction of vortices with flux tubes as described in Sidery and Alpar (2009). Their rigid-body analysis is valid only at $t = 0$; however, this analysis can be extended numerically to study the time evolution of the vortex distribution. A recent study by Cheunchitra et al. (2024) observed a non-axisymmetric distribution of vortices after multiple glitches. While they did not calculate the velocity field corresponding to this distribution, it is certainly feasible to do so in future work.

2. The analysis should be extended to a realistic spherical configuration of the star. The infinite cylindrical configuration was chosen for simplicity, as it aligns with the natural geometry of the vortices, with no perturbations along the z-axis. However, in a spherical geometry, this assumption no longer holds. Moreover, it is necessary to consider a spherical configuration to determine whether it may give rise to a non-zero current multipole. A spherical configuration of the star would require careful investigation, particularly in terms of boundary conditions.

3. Once the model is extended to the spherical configuration, a further refinement could involve conducting the analysis within the framework of General Relativity (GR) instead of Newtonian mechanics. This would provide a more accurate description of the star's behavior, particularly under extreme gravitational fields.

Appendix A

Bessel's Function

In this appendix, we discuss the general solution of the Bessel differential equation and list useful identities for the differentiation and integration of Bessel functions. The general Bessel differential equation of order n is given by:

$$x^2\frac{d^2y}{dx^2} + x\frac{dy}{dx} + \left(x^2 - n^2\right)y = 0. \tag{A.1}$$

For $n = 0$, this reduces to the Bessel differential equation of zeroth order:

$$x^2\frac{d^2y}{dx^2} + x\frac{dy}{dx} + x^2y = 0, \tag{A.2}$$

which can be rewritten as:

$$\frac{d^2y}{dx^2} + \frac{1}{x}\frac{dy}{dx} + y = 0. \tag{A.3}$$

The general solution of the Bessel differential equation is:

$$y = C_1J_0(x) + C_2Y_0(x), \tag{A.4}$$

where $J_0(x)$ and $Y_0(x)$ are the Bessel functions of the first and second kinds of order zero, respectively. The series expansion for $J_0(x)$ is:

$$J_0(x) = \sum_{k=0}^{\infty}\frac{(-1)^k}{(k!)^2}\left(\frac{x}{2}\right)^{2k}, \tag{A.5}$$

and for $Y_0(x)$:

$$Y_0(x) = \frac{2}{\pi}\left(\ln\left(\frac{x}{2}\right) + \gamma\right)J_0(x) - \frac{1}{\pi}\sum_{k=0}^{\infty}\frac{(-1)^k}{(k!)^2}\left(\frac{x}{2}\right)^{2k}\left(\psi(k+1) - \ln(x)\right), \tag{A.6}$$

where γ is the Euler-Mascheroni constant, and $\psi(k+1)$ is the digamma function.

For small values of x, the functions behave as:

$$J_0(x) \approx 1 - \frac{x^2}{4} + \frac{x^4}{64} - \cdots, \tag{A.7}$$

and

$$Y_0(x) \approx \frac{2}{\pi}\left(\ln\left(\frac{x}{2}\right) + \gamma\right). \tag{A.8}$$

At $x = 0$, $J_0(x)$ is finite, but $Y_0(x)$ diverges. Therefore, in our analysis, we consider only the finite solution:

$$y = C_1 J_0(x). \tag{A.9}$$

The differentiation identity for the Bessel function of the first kind, $J_n(x)$, is:

$$\frac{d}{dx}\left[J_n(x)\right] = \frac{n}{x}J_n(x) - J_{n+1}(x). \tag{A.10}$$

For $n = 0$, this simplifies to:

$$\frac{d}{dx}\left[J_0(x)\right] = -J_1(x). \tag{A.11}$$

We used this identity in our calculations.

The integration identity for $xJ_n(x)$ is given by:

$$\int xJ_n(x)\,dx = xJ_{n+1}(x) - nJ_n(x) + C, \tag{A.12}$$

where C is the constant of integration. For $n = 0$, this becomes:

$$\int xJ_0(x)\,dx = xJ_1(x) + C. \tag{A.13}$$

We also used this specific identity in our analysis.

Appendix B

Estimate of K_n and K_p.

For a rough estimate of the values of K_n and K_p, we fix the radius of the star as $R = 10\,\text{km}$. Using the ratio of λ_n to λ_p, we write:

$$\frac{\lambda_n}{\lambda_p} = \frac{\int_0^R \rho_n r\, dr\, d\phi}{\int_0^R \rho_p r\, dr\, d\phi} = \frac{2\pi \frac{m_n^2}{K_n} \int_0^R \tilde{\mu_0} r\, dr}{2\pi \frac{m_p^2}{K_p} \int_0^R \tilde{\mu_0} r\, dr} = \frac{m_n^2 K_p}{m_p^2 K_n}. \tag{B.1}$$

In a typical neutron star, we assume the following ratio of neutron mass density to proton mass density (Lattimer and Prakash (2004)):

$$\frac{\lambda_n}{\lambda_p} = 9. \tag{B.2}$$

Using this ratio, we get:

$$\frac{9}{1} = \frac{m_n^2 K_p}{m_p^2 K_n}. \tag{B.3}$$

Assuming $m_n \approx m_p$, this simplifies to:

$$\frac{K_p}{K_n} = 9, \tag{B.4}$$

$$K_p = 9K_n. \tag{B.5}$$

Now, using the expression of chemical potential in the absence of rotation:

$$\tilde{\mu_0} = \frac{2G\lambda}{R\sqrt{A} J_1(\sqrt{A}R)} J_0(\sqrt{A}r), \tag{B.6}$$

we impose the surface condition $\tilde{\mu_0} = 0$:

$$\frac{2G\lambda}{R\sqrt{A}J_1(\sqrt{A}R)}J_0(\sqrt{A}R) = 0. \tag{B.7}$$

Since the prefactor is non-zero, we require:

$$J_0(\sqrt{A}R) = 0, \tag{B.8}$$

where

$$A = 4\pi G\left(\frac{m_n^2}{K_n} + \frac{m_p^2}{K_p}\right). \tag{B.9}$$

Using the first root of the Bessel function (Weisstein (2024)):

$$\sqrt{A}R \approx 2.4048, \tag{B.10}$$

and squaring both sides gives:

$$AR^2 \approx 5.78. \tag{B.11}$$

Substituting A:

$$4\pi G\left(\frac{m_n^2}{K_n} + \frac{m_p^2}{K_p}\right)R^2 \approx 5.78. \tag{B.12}$$

Given $R = 10\,\text{km} = 10^6\,\text{cm}$, and using $K_p = 9K_n$, we get:

$$4\pi G\left(\frac{m_n^2}{K_n} + \frac{m_p^2}{9K_n}\right)10^{12} \approx 5.78. \tag{B.13}$$

With $m_n \approx m_p \approx 1.67 \times 10^{-24}\,\text{g}$, we obtain:

$$K_n \approx 4.49 \times 10^{-43}\,\text{g}\cdot\text{cm}^5\cdot\text{s}^{-2}, \tag{B.14}$$

$$K_p \approx 4.04 \times 10^{-42}\,\text{g}\cdot\text{cm}^5\cdot\text{s}^{-2}. \tag{B.15}$$

These values of K_n and K_p are then used to plot the density profiles ρ_n and ρ_c of the background star.

Appendix C

Regularity conditions around the origin

In this appendix, we derive the regularity conditions at the origin by Taylor expanding the ODEs (8.112) to (8.115) up to r^2. To achieve this, we systematically expand all the coefficient functions appearing in the four ODEs.

Taylor Expansion of $\alpha_1(r)$

We begin by expanding the function $\alpha_1(r)$, defined as:

$$\alpha_1(r) = \frac{\mu(r)}{\Psi_0}. \tag{C.1}$$

From Eq. (8.76), we know that $\mu(r)$ is proportional to the reduced chemical potential $\tilde{\mu}_c(r)$, given by:

$$\tilde{\mu}_c(r) = C_1 J_0(\sqrt{A}r) + C_2, \tag{C.2}$$

where C_1 and C_2 are constants defined in Eqs. (8.31) and (8.91), respectively.

To obtain the Taylor expansion of $\alpha_1(r)$, we expand the Bessel function $J_0(\sqrt{A}r)$ around $r = 0$. Using the series expansion for the Bessel function of the first kind of order zero, we get:

$$J_0(\sqrt{A}r) = 1 - \frac{Ar^2}{4} + \mathcal{O}(r^4). \tag{C.3}$$

Substituting Equation (C.3) into Equation (C.2), we get:

$$\tilde{\mu}_c(r) = (C_1 + C_2) - \frac{C_1 A r^2}{4} + \mathcal{O}(r^4). \tag{C.4}$$

Define:

$$M = C_1 + C_2, \quad N = \frac{AC_1}{4}, \tag{C.5}$$

then

$$\tilde{\mu}_c(r) = M - Nr^2 + \mathcal{O}(r^4). \tag{C.6}$$

Substituting into $\mu(r)$:

$$\mu(r) = C^*(M - Nr^2)^{4/3}, \tag{C.7}$$

which expands via the binomial theorem:

$$\mu(r) = C^* M^{4/3} \left(1 - \frac{4}{3} \cdot \frac{Nr^2}{M} + \mathcal{O}(r^4)\right). \tag{C.8}$$

Thus,

$$\mu(r) \approx C^* M^{4/3} - \frac{4}{3} C^* M^{1/3} N r^2 + \mathcal{O}(r^4). \tag{C.9}$$

Given that

$$\Psi_o = \frac{a_c M^2}{2}, \tag{C.10}$$

we obtain:

$$\alpha_1(r) = \frac{2C^*}{a_c M^{2/3}} - \frac{8C^* N r^2}{3a_c M^{5/3}} + \mathcal{O}(r^4). \tag{C.11}$$

Substituting $N = \frac{AC_1}{4}$ and $M = C_1 + C_2$,

$$\alpha_1(r) = \frac{2C^*}{a_c (C_1 + C_2)^{2/3}} - \frac{2C^* A C_1 r^2}{3a_c (C_1 + C_2)^{5/3}} + \mathcal{O}(r^4). \tag{C.12}$$

Taylor Expansion of $\frac{1}{\alpha_1(r)}$ up to r^2

We begin by rewriting the expression for $\alpha_1(r)$, as obtained in Eq. (C.12), in the form of a Taylor series around $r = 0$. Let us define:

$$\alpha_{10} = \frac{2C^*}{a_c M^{2/3}}, \quad \alpha_{20} = -\frac{2C^* A C_1}{3a_c M^{5/3}}, \tag{C.13}$$

where $M = C_1 + C_2$. Then, the function $\alpha_1(r)$ can be written as:

$$\alpha_1(r) = \alpha_{10} + \alpha_{20} r^2 + \mathcal{O}(r^4). \tag{C.14}$$

To obtain the reciprocal of $\alpha_1(r)$, we use the standard expansion for the inverse of a function expanded around a small parameter:

$$\frac{1}{\alpha_1(r)} = \frac{1}{\alpha_{10} + \alpha_{20} r^2} + \mathcal{O}(r^4). \tag{C.15}$$

Applying the binomial expansion to Eq. (C.15), we find:

$$\frac{1}{\alpha_1(r)} = \frac{1}{\alpha_{10}}\left(1 - \frac{\alpha_{20}r^2}{\alpha_{10}} + \mathcal{O}(r^4)\right). \tag{C.16}$$

Substituting the expressions from Eq. (C.13) into Eq. (C.16), we obtain:

$$\frac{1}{\alpha_1(r)} = \frac{a_c M^{2/3}}{2C^*} + \frac{A a_c C_1 r^2}{6C^* M^{\frac{1}{3}}} + \mathcal{O}(r^4). \tag{C.17}$$

Finally, by replacing M with its explicit expression $M = C_1 + C_2$, we arrive at:

$$\frac{1}{\alpha_1(r)} = \frac{a_c (C_1 + C_2)^{2/3}}{2C^*} + \frac{A a_c C_1 r^2}{6C^* (C_1 + C_2)^{\frac{1}{3}}} + \mathcal{O}(r^4). \tag{C.18}$$

This completes the Taylor expansion of $\frac{1}{\alpha_1(r)}$ up to order r^2.

Taylor Expansion of $\frac{6\alpha_5(r)+1}{3\alpha_5(r)+2}$, $\frac{3\alpha_5(r)-1}{3\alpha_5(r)+2}$ and $\frac{1}{3\alpha_5(r)+2}$.

Using Eqs. (8.89) and (C.4), we can write the following expression for $\alpha_3(r)$:

$$\alpha_3(r) = \frac{\tilde{\mu}_c(r)}{\tilde{\mu}_o} = 1 - \frac{C_1 A r^2}{4(C_1 + C_2)} + \mathcal{O}(r^4), \tag{C.19}$$

$$\alpha_3^2(r) = 1 - \frac{C_1 A r^2}{2(C_1 + C_2)} + \mathcal{O}(r^4). \tag{C.20}$$

We now use the definition of $\alpha_5(r)$, given as $\alpha_5(r) = \frac{\alpha_3^2(r)}{\alpha_1(r)}$. Substituting the expressions for $\alpha_3^2(r)$ (C.20) and $\alpha_1(r)$ (C.14) into this definition, we obtain:

$$\alpha_5(r) = \left(1 - \frac{C_1 A r^2}{2(C_1 + C_2)}\right)\left(\frac{a_c (C_1 + C_2)^{2/3}}{2C^*} + \frac{A a_c C_1 r^2}{6C^* (C_1 + C_2)^{\frac{1}{3}}}\right) + \mathcal{O}(r^4). \tag{C.21}$$

Expanding the product in the above expression yields:

$$\alpha_5(r) = \frac{a_c (C_1 + C_2)^{2/3}}{2C^*} - \frac{A a_c C_1 r^2}{12C^* (C_1 + C_2)^{\frac{1}{3}}} + \mathcal{O}(r^4). \tag{C.22}$$

Let us define:

$$\alpha_{50} = \frac{a_c(C_1+C_2)^{2/3}}{2C^*}, \tag{C.23}$$

$$\alpha_{52} = -\frac{Aa_cC_1r^2}{12C^*(C_1+C_2)^{\frac{1}{3}}}. \tag{C.24}$$

With these definitions, the function $f(r)$ becomes:

$$f(r) = \frac{6\alpha_5(r)+1}{3\alpha_5(r)+2} = \frac{6\alpha_{50}+1+6\alpha_{52}r^2}{3\alpha_{50}+2+3\alpha_{52}r^2} + \mathcal{O}(r^3). \tag{C.25}$$

Using the binomial expansion to simplify the above expression, we get:

$$f(r) = \frac{6\alpha_{50}+1}{3\alpha_{50}+2} + \frac{6\alpha_{50}+1}{3\alpha_{50}+2}\left(\frac{6\alpha_{52}}{6\alpha_{50}+1} - \frac{3\alpha_{52}}{3\alpha_{50}+2}\right)r^2 + \mathcal{O}(r^3). \tag{C.26}$$

Substituting (C.22) into (C.26) and simplifying gives,

$$\frac{6\alpha_5(r)+1}{3\alpha_5(r)+2} = \frac{2C^*+6a_c(C_1+C_2)^{\frac{2}{3}}}{4C^*+3a_c(C_1+C_2)^{\frac{2}{3}}} - \frac{3a_cC^*AC_1r^2}{(C_1+C_2)^{\frac{1}{3}}(4C^*+3a_c(C_1+C_2)^{\frac{2}{3}})^2} + \mathcal{O}(r^3). \tag{C.27}$$

Similarly, we can expand the function $\dfrac{3\alpha_5(r)-1}{3\alpha_5(r)+2}$ using the same definitions:

$$\frac{3\alpha_5(r)-1}{3\alpha_5(r)+2} = \frac{3\alpha_{50}-1}{3\alpha_{50}+2} + \frac{3\alpha_{50}-1}{3\alpha_{50}+2}\left(\frac{3\alpha_{52}}{3\alpha_{50}-1} - \frac{3\alpha_{52}}{3\alpha_{50}+2}\right)r^2 + \mathcal{O}(r^4). \tag{C.28}$$

Substituting (C.22) into (C.28) and simplifying give

$$\frac{3\alpha_5(r)-1}{3\alpha_5(r)+2} = \frac{3a_c(C_1+C_2)^{\frac{2}{3}}-2C^*}{4C^*+3a_c(C_1+C_2)^{\frac{2}{3}}} - \frac{3a_cC^*AC_1r^2}{(C_1+C_2)^{\frac{1}{3}}(4C^*+3a_c(C_1+C_2)^{\frac{2}{3}})^2} + \mathcal{O}(r^3). \tag{C.29}$$

Finally, we also expand the reciprocal function $\dfrac{1}{3\alpha_5(r)+2}$:

$$\frac{1}{3\alpha_5(r)+2} = \frac{1}{3\alpha_{50}+2} - \frac{1}{3\alpha_{50}+2}\left(\frac{3\alpha_{52}}{3\alpha_{50}+2}\right)r^2 + \mathcal{O}(r^4). \tag{C.30}$$

Substituting (C.22) into (C.30) and simplifying give

$$\frac{1}{3\alpha_5(r)+2} = \frac{2C^*}{4C^* + 3a_c(C_1+C_2)^{\frac{2}{3}}} - \frac{a_c C^* A C_1 r^2}{(C_1+C_2)^{\frac{1}{3}}(4C^* + 3a_c(C_1+C_2)^{\frac{2}{3}})^2} + \mathcal{O}(r^3). \tag{C.31}$$

Taylor Expansion of $f(r) = \dfrac{1}{3\alpha_3^2(r) + 2\alpha_1(r)}$

To expand the function $f(r) = \dfrac{1}{3\alpha_3^2(r) + 2\alpha_1(r)}$ about $r = 0$, we use the earlier Taylor expansions for $\alpha_3^2(r)$ from Eq. (C.20) and $\alpha_1(r)$ from Eq. (C.12). Substituting these into the expression for $f(r)$, we obtain:

$$3\alpha_3^2(r) + 2\alpha_1(r) = \left(3 + \frac{4C^*}{a(C_1+C_2)^{2/3}}\right) - \left(\frac{3C_1 A}{2(C_1+C_2)} + \frac{4C^* A C_1}{3a(C_1+C_2)^{5/3}}\right) r^2 + \mathcal{O}(r^4). \tag{C.32}$$

We define the following constants to simplify the notation:

$$D_0 = 3 + \frac{4C^*}{a_c(C_1+C_2)^{2/3}}, \tag{C.33}$$

$$D_2 = \frac{3C_1 A}{2(C_1+C_2)} + \frac{4C^* A C_1}{3a_c(C_1+C_2)^{5/3}}. \tag{C.34}$$

Then, the expression for $f(r)$ becomes:

$$f(r) = \frac{1}{D_0 - D_2 r^2 + \mathcal{O}(r^4)}. \tag{C.35}$$

Applying the binomial expansion to the reciprocal yields:

$$f(r) = \frac{1}{D_0} + \frac{D_2 r^2}{D_0^2} + \mathcal{O}(r^4). \tag{C.36}$$

Finally, substituting Eqs. (C.33) and (C.34) into Eq. (C.36), we obtain:

$$\frac{1}{3\alpha_3^2(r)+2\alpha_1(r)} = \frac{1}{3+\dfrac{4C^*}{a_c(C_1+C_2)^{2/3}}} + \frac{\dfrac{3C_1A}{2(C_1+C_2)}+\dfrac{4C^*AC_1}{3a_c(C_1+C_2)^{5/3}}}{\left(3+\dfrac{4C^*}{a_c(C_1+C_2)^{2/3}}\right)^2}r^2+\mathcal{O}(r^4). \tag{C.37}$$

Simplifying (C.37) gives

$$\frac{1}{3\alpha_3^2(r)+2\alpha_1(r)} = \frac{a_c(C_1+C_2)^{\frac{2}{3}}}{4C^*+3a_c(C_1+C_2)^{\frac{2}{3}}} + \frac{a_cAC_1(8C^*+9a_c(C_1+C_2)^{\frac{2}{3}})r^2}{6(C_1+C_2)^{\frac{1}{3}}(4C^*+3a_c(C_1+C_2)^{\frac{2}{3}})^2}+\mathcal{O}(r^4). \tag{C.38}$$

Expansion of Γ

Using Eqs. (8.90) and (8.71) in Eq. (8.104), we obtain:

$$\Gamma = 2\frac{r\tilde{\mu}_c}{\tilde{\mu}_o^2}\frac{d\tilde{\mu}_c}{dr}. \tag{C.39}$$

To compute this, we first differentiate Eq. (C.4), which gives:

$$\frac{d\tilde{\mu}_c}{dr} = -\frac{C_1Ar}{2}+\mathcal{O}(r^3). \tag{C.40}$$

Substituting Eqs. (8.89), (C.4), and (C.40) into Eq. (C.39), we find:

$$\Gamma = \frac{2r\left(-\frac{C_1Ar}{2}\right)\left((C_1+C_2)-\frac{C_1Ar^2}{4}+\mathcal{O}(r^4)\right)}{(C_1+C_2)^2}, \tag{C.41}$$

which simplifies to:

$$\Gamma = -\frac{C_1Ar^2}{C_1+C_2}+\mathcal{O}(r^4). \tag{C.42}$$

Taylor Expansion of β

The expression for β is given in Eq. (8.116). To perform a Taylor expansion, we first compute the first derivative of $\tilde{\mu}_c(r)$. We have the following:

$$\frac{d}{dr}\tilde{\mu}_c(r) = C_1\frac{d}{dr}J_0(\sqrt{A}r) = -C_1\sqrt{A}J_1(\sqrt{A}r). \tag{C.43}$$

Differentiating once again gives the following.

$$\frac{d^2}{dr^2}\tilde{\mu}_c(r) = -C_1\sqrt{A}\frac{d}{dr}J_1(\sqrt{A}r). \tag{C.44}$$

Using the identity for the derivative of J_1:

$$\frac{d}{dr}J_1(\sqrt{A}r) = \frac{J_0(\sqrt{A}r) - J_1(\sqrt{A}r)}{2}\sqrt{A}, \tag{C.45}$$

we obtain:

$$\frac{d^2}{dr^2}\tilde{\mu}_c(r) = -C_1 A\frac{(J_0(\sqrt{A}r) - J_1(\sqrt{A}r))}{2}. \tag{C.46}$$

We now expand the Bessel functions around $r = 0$. Using Eq. (C.3) and the expansion:

$$J_1(\sqrt{A}r) = \frac{\sqrt{A}r}{2} - \frac{Ar^3}{16} + \mathcal{O}(r^5), \tag{C.47}$$

we find:

$$\frac{d^2\tilde{\mu}_c}{dr^2} = -\frac{C_1 A}{2}\left(1 - \frac{\sqrt{A}r}{2} - \frac{Ar^2}{4} + \frac{Ar^3}{16} + \mathcal{O}(r^4)\right). \tag{C.48}$$

Finally, substituting Eqs. (C.48) and (8.89) into Eq. (8.116) and simplifying, we obtain the Taylor expansion of β as:

$$\beta = \frac{-C_1 Ar^2}{2(C_1 + C_2)} + \mathcal{O}(r^3). \tag{C.49}$$

Expansion of $\tilde{U}(r)$ and $\tilde{V}(r)$

We now derive the leading-order Taylor expansions of the functions $\tilde{U}(r)$ and $\tilde{V}(r)$ near the origin. These functions appear in the driving terms of the perturbed equations of motion.

First, by substituting Eqs. (8.51), (8.90), (8.89), and (C.4) into Eq. (8.109), we obtain:

$$\tilde{U}(r) = \frac{4a_n^2\Omega B_*}{a_c R^2}r^2 + \mathcal{O}(r^4), \tag{C.50}$$

which gives the leading-order behaviour of $\tilde{U}(r)$ up to $\mathcal{O}(r^2)$.

Similarly, inserting Eqs. (8.52), (8.90), (8.89), and (C.4) into Eq. (8.108) yields:

$$\tilde{V}(r) = \frac{8a_n^2 \Omega B_*}{a_c R^2} r^2 + \mathcal{O}(r^4). \tag{C.51}$$

Thus, both $\tilde{U}(r)$ and $\tilde{V}(r)$ scale as r^2 near the origin.

Taylor Expansion of z_1, z_2, z_3, z_4

We begin by expanding each function as a Taylor series about the origin $r = 0$, up to second order in r:

The expansion of $z_1(r)$ is:

$$z_1(r) = z_{1,0} + z_{1,1} r + \frac{z_{1,2}}{2!} r^2 + \mathcal{O}(r^3), \tag{C.52}$$

The expansion of $z_2(r)$ is:

$$z_2(r) = z_{2,0} + z_{2,1} r + \frac{z_{2,2}}{2!} r^2 + \mathcal{O}(r^3), \tag{C.53}$$

The expansion of $z_3(r)$ is:

$$z_3(r) = z_{3,0} + z_{3,1} r + \frac{z_{3,2}}{2!} r^2 + \mathcal{O}(r^3), \tag{C.54}$$

The expansion of $z_4(r)$ is:

$$z_4(r) = z_{4,0} + z_{4,1} r + \frac{z_{4,2}}{2!} r^2 + \mathcal{O}(r^3). \tag{C.55}$$

Focusing on the zeroth-order terms (i.e., constant terms), we derive the following system of algebraic equations:

$$0 = -z_{1,0}(6 + \alpha_{10}) + \frac{3}{2} z_{2,0} + 4 z_{3,0}(3 - \alpha_{10}), \tag{C.56}$$

$$0 = 2\alpha_{10}(6 + \alpha_{10}) z_{1,0} - 3\alpha_{10} z_{2,0} - 8\alpha_{10}(6 + \alpha_{10}) z_{3,0} + 4(3 + 2\alpha_{10}) z_{4,0}, \tag{C.57}$$

$$z_{4,0} = \alpha_{10} z_{1,0}, \tag{C.58}$$

$$0 = -2\alpha_{10}(6 + \alpha_{10}) z_{1,0} + (\alpha_{10} - 3) z_{2,0} + 8\alpha_{10}(6 + \alpha_{10}) z_{3,0} - 2(3 + 2\alpha_{10}) z_{4,0}. \tag{C.59}$$

Solving the system given by Eqs. (C.56)–(C.59), we express $z_{2,0}, z_{3,0}, z_{4,0}$ in terms of the single free parameter $z_{1,0}$ and the parameter α_{10}:

$$z_{2,0} = 2\alpha_{10} z_{1,0}, \quad z_{3,0} = \frac{1}{2} z_{1,0}, \quad z_{4,0} = \alpha_{10} z_{1,0}. \tag{C.60}$$

These relations provide the regularity conditions near the origin in terms of a single free parameter $z_{1,0}$.

Furthermore, substituting the series expansions into the system of differential equations governing z_1, z_2, z_3, and z_4, and collecting terms of equal powers of r, we find that at first order

$$z_{1,1} = z_{2,1} = z_{3,1} = z_{4,1} = 0.$$

Appendix D

Numerical Solution of Coupled ODEs

In this section, we provide the details of the numerical method used to solve the system of four coupled ordinary differential equations (ODEs), given in Equations (8.112)–(8.115), subject to specific boundary conditions: Equations (8.117)–(8.121) for the case where both elastic and fluid components coexist throughout the star (as discussed in Section 8.4.2), and Equations (8.155), (8.164), (8.165), and (8.166) for the annulus case discussed in Section 8.6.1.1. The implementation is done using Python's scientific computing libraries, including NumPy, SciPy, and Matplotlib. To simplify the analysis, we introduce the dimensionless radial coordinate:

$$\hat{r} = \frac{r}{R},$$

where r is the radial distance and R is the radius of the star.

Physical Constants and Parameters

The code begins by defining the fundamental dimensionless parameters necessary for the computations. We assume an angular velocity of $\Omega = 100\,\mathrm{rad\,s^{-1}}$, which corresponds to $\varepsilon_\Omega = 10^{-4}$ and $\varepsilon_{\mathrm{mag}} = 10^{-8}$. The relative critical velocity is set to $10^4\,\mathrm{cm\,s^{-1}}$. We also adopt $\varepsilon_\mu = 10^{-5}$, which is representative of a realistic neutron star.

Once the parameters are fixed, we define the background functions $\alpha_1(r)$, $\alpha_3(r)$, $\alpha_5(r)$, Γ, and β, along with the source terms $\tilde{V}(r)$ and $\tilde{U}(r)$ appearing in the ODEs (8.112)–(8.115).

To solve for the variables z_1, z_2, z_3, and z_4, we use the boundary value problem (BVP) solver `solve_bvp` from the `scipy.integrate` module. This method is suitable for problems with boundary conditions specified at more than one point. The boundary conditions are implemented in the function `bc(ya, yb)`.

Initial Guess and Mesh

An initial mesh for r is defined using `np.linspace` from $r_{\min} = 1 \times 10^{-6}$ to $r_{\max} = 1$, with 10,000 points for adequate resolution. The range of $r_{\min}$ and $r_{\max}$ will change in the annulus problem, where it is taken to be from 0.9 to 0.99.

The initial guess for the solution y is a zero array of shape $(4, \text{number of mesh points})$, which helps the solver converge.

Solving the boundary value problem

The `solve_bvp` function is called with the following inputs:

- `system`: the function defining the ODE system,
- `bc`: the function defining the boundary conditions,
- `r_vals`: the radial mesh points,
- `y_guess`: the initial guess for the solution,
- `tol=1e-8`: the convergence tolerance.

The solver returns an object `sol` containing:

- `sol.x`: the mesh points,
- `sol.y`: the solution values at those mesh points.

Post-processing and Visualisation

The solution components $z_1(r)$, $z_2(r)$, $z_3(r)$, and $z_4(r)$ are extracted from `sol.y` and plotted against $\hat{r}$ to visualise their behaviour, as shown in Figure 8.3.

References

B. P. Abbott and et al. Observation of gravitational waves from a binary black hole merger. *Phys. Rev. Lett.*, 116:061102, Feb 2016. . URL https://link.aps.org/doi/10.1103/PhysRevLett.116.061102.

B. P. Abbott, R. Abbott, T. D. Abbott, F. Acernese, and K. Ackley. Multi-messenger observations of a binary neutron star merger. *The Astrophysical Journal*, 848(2):L12, oct 2017. URL https://doi.org/10.3847%2F2041-8213%2Faa91c9.

K. Abe, others, and Super-Kamiokande Collaboration. Search for Neutrinos in Super-Kamiokande Associated with the GW170817 Neutron-star Merger. , 857(1):L4, April 2018. .

Mark G. Alford, Andreas Schmitt, Krishna Rajagopal, and Thomas Schäfer. Color superconductivity in dense quark matter. *Rev. Mod. Phys.*, 80:1455–1515, Nov 2008. . URL https://link.aps.org/doi/10.1103/RevModPhys.80.1455.

J. F. Allen and A. D. Misener. Flow of liquid helium ii. *Nature*, 141(3558):75, 1938. .

M. A. Alpar and J. A. Sauls. On the Dynamical Coupling between the Superfluid Interior and the Crust of a Neutron Star. *The Astrophysical Journal*, 327:723, April 1988. URL https://ui.adsabs.harvard.edu/abs/1988ApJ...327..723A. Provided by the SAO/NASA Astrophysics Data System.

M. A. Alpar, D. Pines, P. W. Anderson, and J. Shaham. Vortex creep and the internal temperature of neutron stars. I - General theory. , 276:325–334, January 1984. .

M. Ali Alpar. Pinning and Threading of Quantized Vortices in the Pulsar Crust Superfluid. , 213:527–530, April 1977. .

P. W. Anderson and N. Itoh. Pulsar glitches and restlessness as a hard superfluidity phenomenon. , 256(5512):25–27, July 1975. .

P. W. Anderson, M. A. Alpar, D. Pines, and J. Shaham. Pulsar glitches: Superfluid unpinning. *Symposium - International Astronomical Union*, 95:299–300, 1981. .

N. Andersson, T. Sidery, and G. L. Comer. Waves and instabilities in dissipative rotating superfluid neutron stars. *Mon. Not. R. Astron. Soc.*, 385:335–348, 2008. .

N. Andersson, C. Krüger, G. L. Comer, and L. Samuelsson. A minimal model for finite temperature superfluid dynamics. *Class. Quant. Grav.*, 30:235025, 2013. .

Nils Andersson. A superfluid perspective on neutron star dynamics. *Universe*, 7(1), 2021. ISSN 2218-1997. . URL https://www.mdpi.com/2218-1997/7/1/17.

J.F. Annett. *Superconductivity, Superfluids and Condensates*. Oxford Master Series in Physics. OUP Oxford, 2004. ISBN 9780198507550. URL https://books.google.co.uk/books?id=-wiHrgEACAAJ.

ATLAS Collaboration. Evidence for the spin-0 nature of the higgs boson using atlas data. *Physics Letters B*, 726(1):120–144, 2013. ISSN 0370-2693. . URL https://www.sciencedirect.com/science/article/pii/S0370269313006527.

W. Baade and F. Zwicky. Cosmic Rays from Super-novae. *Proceedings of the National Academy of Science*, 20(5):259–263, May 1934. .

M. Baldo and H. J. Schulze. Proton pairing in neutron stars. *Phys. Rev. C*, 75:025802, 2007. .

G. Baym, C. Pethick, and D. Pines. Superfluidity in neutron stars. *Nature*, 224(5215): 673–674, 1969. .

Gordon Baym and David Pines. Neutron starquakes and pulsar speedup. *Annals of Physics*, 66(2):816–835, 1971. ISSN 0003-4916. URL https://www.sciencedirect.com/science/article/pii/0003491671900844.

Werner Becker, Michael Kramer, and Alberto Sesana. Pulsar timing and its application for navigation and gravitational wave detection. *Space Science Reviews*, 214(1), jan 2018. URL https://doi.org/10.1007%2Fs11214-017-0459-0.

Lars Bildsten. Gravitational radiation and rotation of accreting neutron stars. *The Astrophysical Journal*, 501(1):L89–L93, jul 1998. URL https://doi.org/10.1086%2F311440.

Annette Bussmann-Holder and Hugo Keller. High-temperature superconductors: underlying physics and applications. *Zeitschrift für Naturforschung B*, 75(1-2):3–14, 2020. URL https://doi.org/10.1515/znb-2019-0103.

Nicolas Chamel. Superfluidity and superconductivity in neutron stars. *Journal of Astrophysics and Astronomy*, 38:1–14, 2017.

S. Chandrasekhar. *Ellipsoidal figures of equilibrium*. Yale University Press, 1969. URL https://books.google.co.uk/books?id=z4LBjgEACAAJ.

T. Cheunchitra, A. Melatos, J. B. Carlin, and G. Howitt. Persistent gravitational radiation from glitching pulsars – ii. updated scaling with vortex number. *Monthly Notices of the Royal Astronomical Society*, 528(2):1360–1371, 2024. .

Albert Einstein. Approximative Integration of the Field Equations of Gravitation. *Sitzungsber. Preuss. Akad. Wiss. Berlin (Math. Phys.)*, 1916:688–696, 1916.

Richard I. Epstein and Bennett Link. Starquake-induced glitches in pulsars. *Astrophys. Space Sci. Libr.*, 254:95–104, 2000. .

EPTA Collaboration and InPTA Collaboration. The second data release from the european pulsar timing array - iii. search for gravitational wave signals. *Astronomy Astrophysics*, 678(A50), 2023. . URL https://doi.org/10.1051/0004-6361/202346844.

B P Abbott et al. Exploring the sensitivity of next generation gravitational wave detectors. *Classical and Quantum Gravity*, 34(4):044001, Jan 2017. URL https://dx.doi.org/10.1088/1361-6382/aa51f4.

F. J. Fattoyev, C. J. Horowitz, and Hao Lu. Crust breaking and the limiting rotational frequency of neutron stars. *never published*, 4 2018.

C. S. Flanagan. Twelve years of Glitches in the VELA Pulsar. In S. Johnston, M. A. Walker, and M. Bailes, editors, *IAU Colloq. 160: Pulsars: Problems and Progress*, volume 105 of *Astronomical Society of the Pacific Conference Series*, page 103, January 1996. URL https://ui.adsabs.harvard.edu/abs/1996ASPC..105..103F.

Lucia M. Franco, Bennett Link, and Richard I. Epstein. Quaking neutron stars. *The Astrophysical Journal*, 543(2):987–994, nov 2000. URL https://doi.org/10.1086/317121.

J. L. Friedman and B. F. Schutz. Lagrangian perturbation theory of nonrelativistic fluids. *The Astrophysical Journal*, 221:937–957, May 1978. URL https://ui.adsabs.harvard.edu/abs/1978ApJ...221..937F.

Yashaswi Gangwar and David Ian Jones. Applying the starquake model to study the formation of elastic mountains on spinning neutron stars. *Monthly Notices of the Royal Astronomical Society*, 532(2):2763–2777, 07 2024. ISSN 0035-8711. . URL https://doi.org/10.1093/mnras/stae1671.

A. Gezerlis, C. J. Pethick, and A. Schwenk. Pairing and superfluidity of nucleons in neutron stars. 6 2014.

E Giliberti and G Cambiotti. Starquakes in millisecond pulsars and gravitational waves emission. *Monthly Notices of the Royal Astronomical Society*, 511(3):3365–3376, jan 2022. URL https://doi.org/10.1093%2Fmnras%2Fstac245.

Vitalii L Ginzburg. Superfluidity and superconductivity in the universe. *Soviet Physics Uspekhi*, 12(2):241, feb 1969. . URL https://dx.doi.org/10.1070/PU1969v012n02ABEH003935.

F Gittins, N Andersson, and D I Jones. Modelling neutron star mountains. *Monthly Notices of the Royal Astronomical Society*, 500(4):5570–5582, November 2020. ISSN 1365-2966. . URL http://dx.doi.org/10.1093/mnras/staa3635.

Fabian Gittins and Nils Andersson. Modelling neutron star mountains in relativity. *Monthly Notices of the Royal Astronomical Society*, 507(1):116–128, 07 2021. ISSN 0035-8711. . URL https://doi.org/10.1093/mnras/stab2048.

K. Glampedakis and Leonardo Gualtieri. *Gravitational Waves from Single Neutron Stars: An Advanced Detector Era Survey*, pages 673–736. Springer International Publishing, Cham, 2018. ISBN 978-3-319-97616-7. URL https://doi.org/10.1007/978-3-319-97616-7_12.

K. Glampedakis, D. I. Jones, and L. Samuelsson. Gravitational waves from color-magnetic "mountains" in neutron stars. *Phys. Rev. Lett.*, 109:081103, Aug 2012. URL https://link.aps.org/doi/10.1103/PhysRevLett.109.081103.

Kirsty Grosart. *Oscillations and Stability of Rotating Superfluids*. PhD thesis, University of Southampton, 2005. URL https://eprints.soton.ac.uk/466010/. PhD thesis.

B. Haskell and A. Melatos. Models of pulsar glitches. *International Journal of Modern Physics D*, 24(3):1530008, 2015. .

B. Haskell, D. I. Jones, and N. Andersson. Mountains on neutron stars: accreted versus non-accreted crusts. *Monthly Notices of the Royal Astronomical Society*, 373(4):1423–1439, 11 2006. ISSN 0035-8711. . URL https://doi.org/10.1111/j.1365-2966.2006.10998.x.

B. Haskell, M. Priymak, A. Patruno, M. Oppenoorth, A. Melatos, and P. D. Lasky. Detecting gravitational waves from mountains on neutron stars in the advanced detector era. *Monthly Notices of the Royal Astronomical Society*, 450(3):2393–2403, 05 2015. ISSN 0035-8711. URL https://doi.org/10.1093/mnras/stv726.

Brynmor Haskell and Armen Sedrakian. Superfluidity and superconductivity in neutron stars. In *The Physics and Astrophysics of Neutron Stars*, pages 401–454. Springer International Publishing, 2018. URL https://doi.org/10.1007%2F978-3-319-97616-7_8.

Brynmor Haskell, Marco Antonelli, and Pierre Pizzochero. Continuous gravitational wave emissions from neutron stars with pinned superfluids in the core. *Universe*, 8 (12), 2022. ISSN 2218-1997. URL https://www.mdpi.com/2218-1997/8/12/619.

A. Heger, C. L. Fryer, S. E. Woosley, N. Langer, and D. H. Hartmann. How massive single stars end their life. *The Astrophysical Journal*, 591(1):288–300, 2003. .

A Hewish, S J Bell, J D.H. Pilkington, P F Scott, and R A Collins. Observation of a rapidly pulsating radio source. *Nature (London), 217: 709-13(Feb. 24, 1968).* URL https://www.osti.gov/biblio/4555886.

C. J. Horowitz and Kai Kadau. Breaking Strain of Neutron Star Crust and Gravitational Waves. , 102(19):191102, May 2009. .

Nathan K. Johnson-McDaniel and Benjamin J. Owen. Maximum elastic deformations of relativistic stars. *Phys. Rev. D*, 88:044004, Aug 2013. . URL https://link.aps.org/doi/10.1103/PhysRevD.88.044004.

D I Jones. Gravitational waves from rotating strained neutron stars. *Classical and Quantum Gravity*, 19(7):1255, mar 2002a. . URL https://dx.doi.org/10.1088/0264-9381/19/7/304.

D I Jones. Gravitational waves from rotating strained neutron stars. *Classical and Quantum Gravity*, 19(7):1255–1265, mar 2002b. URL https://doi.org/10.1088%2F0264-9381%2F19%2F7%2F304.

D. I. Jones. Gravitational wave emission from rotating superfluid neutron stars. *Monthly Notices of the Royal Astronomical Society*, 402(4):2503–2519, 03 2010. ISSN 0035-8711. URL https://doi.org/10.1111/j.1365-2966.2009.16059.x.

D. I. Jones. Parameter choices and ranges for continuous gravitational wave searches for steadily spinning neutron stars. , 453(1):53–66, October 2015. .

P. Kapitza. Viscosity of liquid helium below the λ-point. *Nature*, 141(3558):74, 1938. .

Lucy Keer. *Neutron star oscillations from starquakes*. PhD thesis, University of Southampton, January 2014. URL https://eprints.soton.ac.uk/363269/.

A D Kerin and A Melatos. Mountain formation by repeated, inhomogeneous crustal failure in a neutron star. *Monthly Notices of the Royal Astronomical Society*, 514(2):1628–1644, 05 2022. ISSN 0035-8711. . URL https://doi.org/10.1093/mnras/stac1351.

Reinhold Kleiner, Dieter Koelle, Frank Ludwig, and John Clarke. Superconducting Quantum Interference Devices: State of the Art and Applications. *IEEE Proceedings*, 92(10):1534–1548, January 2004. .

P. D. Lasky. Gravitational waves from neutron stars: A review. *Publications of the Astronomical Society of Australia*, 32:e034, 2015. .

J. M. Lattimer and M. Prakash. The physics of neutron stars. *Science*, 304:536–542, 2004. .

A.E.H. Love. *A Treatise on the Mathematical Theory of Elasticity*. New York: Dover Publications, 4th edition, 1944. ISBN 9781107618091.

Andrew G. Lyne and Francis Graham-Smith. *Pulsar Astronomy*, volume 48 of *Cambridge Astrophysics Series*. Cambridge University Press, Cambridge, 4th edition, 2012. ISBN 9780521764919. .

Michele Maggiore, Chris Van Den Broeck, Nicola Bartolo, Enis Belgacem, Daniele Bertacca, Marie Anne Bizouard, Marica Branchesi, Sebastien Clesse, Stefano Foffa, Juan García-Bellido, Stefan Grimm, Jan Harms, Tanja Hinderer, Sabino Matarrese, Cristiano Palomba, Marco Peloso, Angelo Ricciardone, and Mairi Sakellariadou. Science case for the einstein telescope. *Journal of Cosmology and Astroparticle Physics*, 2020 (03):050, mar 2020. URL https://dx.doi.org/10.1088/1475-7516/2020/03/050.

W. Meissner and R. Ochsenfeld. Ein neuer effekt bei eintritt der supraleitfähigkeit. *Naturwissenschaften*, 21:787–788, 1933. .

A. Melatos, J. A. Douglass, and T. P. Simula. Persistent gravitational radiation from glitching pulsars. *The Astrophysical Journal*, 807(2):132, jul 2015. . URL https://doi.org/10.1088/0004-637X/807/2/132.

Débora Peres Menezes. A neutron star is born. *Universe*, 7(8):267, jul 2021. URL https://doi.org/10.3390.

A.B. Migdal. Superfluidity and the moments of inertia of nuclei. *Nuclear Physics*, 13(5): 655–674, 1959. ISSN 0029-5582. . URL https://www.sciencedirect.com/science/article/pii/0029558259902640.

J A Morales and C J Horowitz. Neutron star crust can support a large ellipticity. *Monthly Notices of the Royal Astronomical Society*, 517(4):5610–5616, 10 2022. ISSN 0035-8711. . URL https://doi.org/10.1093/mnras/stac3058.

Joonas Nättilä and Jari J. E. Kajava. Fundamental physics with neutron stars. In *Handbook of X-ray and Gamma-ray Astrophysics*, pages 1–53. Springer Nature Singapore, nov 2022. URL https://doi.org/10.1007%2F978-981-16-4544-0_105-1.

E L Osborne and D I Jones. Gravitational waves from magnetically induced thermal neutron star mountains. *Monthly Notices of the Royal Astronomical Society*, 494(2):2839–2850, 03 2020. ISSN 0035-8711. URL https://doi.org/10.1093/mnras/staa858.

A. Passamonti and N. Andersson. Towards real neutron star seismology: accounting for elasticity and superfluidity. *Monthly Notices of the Royal Astronomical Society*, 419 (1):638–656, 2012. .

Jean Jú nio Mendes Pimenta, Lucas Francisco Bosso Belussi, Érica Regina Takano Natti, and Paulo Laerte Natti. O bóson de higgs. *Revista Brasileira de Ensino de Física*, 35(2), jun 2013. URL https://doi.org/10.1590%2Fs1806-11172013000200006.

G. W. Rayfield and F. Reif. Evidence for the creation and motion of quantized vortex rings in superfluid helium. *Phys. Rev. Lett.*, 11:305–308, Oct 1963. . URL https://link.aps.org/doi/10.1103/PhysRevLett.11.305.

M. Ruderman. Neutron Starquakes and Pulsar Periods. *Nature*, 223(5206):597–598, August 1969. URL https://ui.adsabs.harvard.edu/abs/1969Natur.223..597R.

M. Ruderman. Neutron Star Crustal Plate Tectonics. I. Magnetic Dipole Evolution in Millisecond Pulsars and Low-Mass X-Ray Binaries. , 366:261, January 1991. .

Siti Fatimah Saipuddin, Azhan Hashim, and Nurbaisyatul Ermiza Suhaimi. *Type I and Type II Superconductivity*, pages 123–146. Springer Nature Singapore, Singapore, 2022. ISBN 978-981-19-1211-5. URL https://doi.org/10.1007/978-981-19-1211-5_5.

J Robert Schrieffer. *Theory of superconductivity*. CRC press, 2018.

S. Seveso, P. M. Pizzochero, F. Grill, and B. Haskell. Mesoscopic pinning forces in neutron star crusts. *Monthly Notices of the Royal Astronomical Society*, 455(4):3952–3967, 12 2015. ISSN 0035-8711. . URL https://doi.org/10.1093/mnras/stv2579.

Shapiro and Teukolsky. *Shapiro and Teukolsky*. John Wiley Sons, Ltd, 1983. ISBN 9783527617661. URL https://onlinelibrary.wiley.com/doi/abs/10.1002/9783527617661.ch7.

Trevor Sidery and M. Ali Alpar. The effect of quantized magnetic flux lines on the dynamics of superfluid neutron star cores. *Monthly Notices of the Royal Astronomical Society*, 400:1859–1867, 2009. URL https://api.semanticscholar.org/CorpusID:18485662.

Magdalena Sieniawska and Michał Bejger. Continuous gravitational waves from neutron stars: Current status and prospects. *Universe*, 5(11):217, oct 2019. URL https://doi.org/10.3390%2Funiverse5110217.

T. E. Strohmayer, S. Ogata, H. Iyetomi, S. Ichimaru, and H. M. Van Horn. The shear modulus of the Neutron Star crust and nonradial Oscillations of Neutron Stars. *Astrophysical Journal*, 375:679–686, 1991.

Yuan Tang, Wei Guo, Hiromichi Kobayashi, Satoshi Yui, Makoto Tsubota, and Toshiaki Kanai. Imaging quantized vortex rings in superfluid helium to evaluate quantum dissipation. *Nature Communications*, 14(1):1–8, December 2023. . URL https://ideas.repec.org/a/nat/natcom/v14y2023i1d10.1038_s41467-023-38787-w.html.

Kip S. Thorne. Multipole expansions of gravitational radiation. *Reviews of Modern Physics*, 52:299–339, 1980. .

K.S. Thorne and R.D. Blandford. *Modern Classical Physics: Optics, Fluids, Plasmas, Elasticity, Relativity, and Statistical Physics*. Princeton University Press, 2017. ISBN 9781400848898. URL https://books.google.co.uk/books?id=U1S6BQAAQBAJ.

Michael Tinkham. *Introduction to superconductivity*. Courier Corporation, 2004.

Greg Ushomirsky, Curt Cutler, and Lars Bildsten. Deformations of accreting neutron star crusts and gravitational wave emission. *Monthly Notices of the Royal Astronomical Society*, 319(3):902–932, 2000. URL https://doi.org/10.1046%2Fj.1365-8711.2000.03938.x.

Francisco Hernandez Vivanco, Rory Smith, Eric Thrane, Paul D. Lasky, Colm Talbot, and Vivien Raymond. Measuring the neutron star equation of state with gravitational waves: The first forty binary neutron star merger observations. *Physical Review D*, 100 (10), nov 2019. URL https://doi.org/10.1103%2Fphysrevd.100.103009.

Eric W. Weisstein. "bessel function zeros". https://mathworld.wolfram.com/BesselFunctionZeros.html, 2024. Accessed July 28, 2025.

E. J. Yarmchuk, M. J. V. Gordon, and R. E. Packard. Observation of stationary vortex arrays in rotating superfluid helium. *Phys. Rev. Lett.*, 43:214–217, Jul 1979. . URL https://link.aps.org/doi/10.1103/PhysRevLett.43.214.

G Yim and D I Jones. Gravitational radiation back-reaction from f-modes on neutron stars. *Monthly Notices of the Royal Astronomical Society*, 511(2):1942–1960, jan 2022. URL https://doi.org/10.1093%2Fmnras%2Fstac009.

Garvin Yim. *Gravitational waves from timing irregularities of radio pulsars*. PhD thesis, University of Southampton, February 2022. URL https://eprints.soton.ac.uk/467267/.